ABSTRACT

Title of dissertation: MAGNETIC AND STRUCTURAL CHARACTERIZATION OF Fe–Ga USING KERR MICROSCOPY AND NEUTRON SCATTERING

Chaitanya Mudivarthi,
Doctor of Philosophy, 2010

Dissertation directed by: Professor Alison B. Flatau and
Professor Manfred Wuttig
Dept. of Materials Science and Engineering

Fe–Ga alloys belong to a class of smart materials called magnetostrictive materials. Magnetostrictive materials show dimensional (magnetostriction) and magnetization changes in response to magnetic and elastic fields. These effects can be utilized for transduction purposes. Most widely used magnetostrictive materials like Tb-Dy-Fe (Terfenol-D) show giant magnetostriction ($\sim 2000\ \mu\epsilon$) but suffer from low modulus of elasticity, low tensile strength and are extremely brittle, limiting their usage to applications involving only axial loads. Fe–Ga alloys have recently been discovered to show an extraordinary enhancement in magnetostriction (from 36 $\mu\epsilon$ to 400 $\mu\epsilon$) with the addition of the nonmagnetic element, Ga. Though their magnetostriction is less than that of Terfenol-D, they boast superior properties such as ductile-like behavior, high tensile strengths ($\sim$ 400 MPa), low hysteresis, and low saturation fields ($\sim$ 10 mT). Understanding the origin of the magnetostriction enhancement in these alloys is technologically and scientifically important because it

will aid in our quest to discover alloys with higher magnetostriction (as Terfenol-D) and better mechanical properties (as Fe–Ga).

With the goal of elucidating the nature of this unusually large magnetostriction enhancement, Fe–Ga solid solutions have recently been the focus of intense studies. All the studies so far, show the existence of nanoscale heterogeneities embedded in the cubic matrix but the experimental means to correlate the presence of nanoscale heterogeneities to the magnetostriction enhancement is lacking.

In this work, Fe–Ga alloys of various compositions and heat treatments were probed at different length scales - lattice level, nano-, micro-, and macro-scales. Neutron diffraction was used to probe the alloy at the lattice level to identify the existence of different phases. Small-Angle Neutron Scattering (SANS) experiments were used to study the nanoscale heterogeneities and their response to the applied magnetic and elastic fields. Ultra small-angle neutron scattering (USANS), magnetic force and Kerr microscopy were used to investigate the response of magnetic domains under externally applied magnetic and elastic fields. Piecing the results from lattice level, nano-, micro-, and macro-scales together with the macroscopic magnetostriction measurements, the nature of the magnetostriction in Fe–Ga alloys was uncovered. No evidence could be found that directly relates the presence of heterogeneities to the enhanced magnetostriction. Further, it was found that the observed heterogeneities were possibly of DO3 phase and are detrimental to the magnetostriction.

MAGNETIC AND STRUCTURAL CHARACTERIZATION OF Fe–Ga USING KERR MICROSCOPY AND NEUTRON SCATTERING

by

Chaitanya Mudivarthi

Dissertation submitted to the Faculty of the Graduate School of the
University of Maryland, College Park in partial fulfillment
of the requirements for the degree of
Doctor of Philosophy
2010

Advisory Committee:
Professor Alison B. Flatau, Chair/Advisor
Professor Manfred Wuttig, Co-Advisor
Professor James Cullen
Dr. Mark Laver
Professor Lourdes Salamanca-Riba
Professor Norman M. Wereley

गुरुर्ब्रह्मा गुरुर्विष्णुः गुरुर्देवो महेश्वरः ।

गुरुर्साक्षात् परभ्रह्म तस्मै श्रीगुरवे नमः ॥

Gurur BrahmA Gurur Vishnu Gurur Devo MaheshvarA,

Guru sAkshAt ParaBrahma tasmai Shri Guruve namah.

- Aadi Shankara (788 - 820 CE)

"*Guru (teacher) is truly a representative of Brahma the creator, Vishnu the protector, Maheshvara the destroyer because Guru creates, sustains knowledge and destroys the weeds of ignorance. Guru is the supreme spirit him/herself. I salute such a Guru.*" This dissertation is dedicated to everyone who imparted knowledge and made me what I am today.

Acknowledgments

I owe my gratitude to all the people who have made this thesis possible and because of whom my graduate experience has been one that I will cherish forever.

First and foremost I'd like to thank my advisors, Professor Alison Flatau and Professor Manfred Wuttig. Many thanks to Prof. Alison Flatau for giving me an invaluable opportunity to work on various challenging projects over past 5 years. I am very thankful to her for her unwavering support and confidence she showed in me, throughout my stay here. I am especially thankful to her for being so supportive when I shifted to materials science and engineering from aerospace engineering after two and half years into graduate school. She has been an excellent mentor who always pushed me to *think* with her positive criticisms. I am also thankful to her for being such an awesome person and teaching me how to balance life with work and fun.

I am extremely thankful to Prof. Manfred Wuttig who readily accepted to co-advise me on this dissertation. I am grateful to him for being available whenever I knocked on his door to discuss and teach me the toughest of the concepts. I throughly enjoyed talking to him not only on the subject matters but also about the life in general. His remarkable knowledge in materials science and unbiased way of looking at things influenced me a lot.

I would also like to thank Dr. Mark Laver for his exceptional guidance and contribution to this dissertation. I have been very lucky to get an opportunity to work with him on the neutron scattering experiments using state-of-the-art instru-

ments at NIST and PSI. I am also extremely thankful to him for giving me the opportunity to visit Switzerland and work at PSI for five months. His quick thinking, exceptional experimental skills, and friendly nature made my stay at PSI an enriching experience. I must also thank him for teaching me skiing in the beautiful Swiss Alps.

I am grateful to all the committee members, Prof. Cullen, Prof. Salamanca-Riba, and Prof. Wereley. Prof. Cullen has been very helpful throughout with his suggestions. His strong theoretical background and wonderful nature made all our interactions very pleasant learning experiences. I am thankful to Prof. Salamanca-Riba from whom I learned the fundamental materials science concepts as part of three of her courses. Thanks also to Prof. Wereley for readily agreeing to serve as the dean's representative. I am also thankful to Prof. Dasgupta who served as dean's representative during the proposal defense.

I would like to acknowledge the financial support of the US office of Naval Research through MURI grant # N000140610530. I am also grateful to all the members who are part of the MURI research. I would like to especially thank Dr. Thomas Lograsso, and Dr. Deborah Schlagel of Materials Preperation Center, Ames for providing samples on a collaborative basis. I would also like to thank Dr. Clark, Dr. Hathaway, Dr. Wun-Fogle of NSWC, Carderock for stimulation discussions during our meetings at conferences and funding reviews.

Special thanks to David Cogswell of the Physics machine shop for carefully cutting all the single crystals. Thanks to Dr. Phil Piccoli who helped conduct EDS analysis to measure composition of all our samples. I am very thankful to Dr.

Suok-Min Na and Hyunsuk Chun who helped me learn the art of polishing. Thanks also to Dr. Chen and Shannon Watson of NIST who helped in neutron polarization experiments. Dr. Jurg Schaefer and Dr. Oksana Zaharko of PSI also must be thanked for their help on TriCS instrument at PSI. Dr. Rudolf Schaefer deserves a special mention. I am grateful to have been trained by him on Kerr microscope. His expertise in magnetism and magnetic domain visualization techniques helped immensely in interpreting the magnetic domain study results. I have gained vast knowledge from his book, magnetic domains, and from our interactions.

I am hankful to all my colleagues in our research group, Dr. Jin Yoo, Dr. Supratik Datta, Dr. Atulasimha Jayasimha, Dr. Patrick Downey, Frank Graham, Rupal Jain, Zohaib Hasnain, Lina Castano, Michael Marana, Ganesh Raghunath for helping me various times throughout my graduate studies. I especially want to thank Dr. Supratik Datta for being my mentor, friend, house-mate, and office-mate. Working with him was a pleasure and a wonderful experience. I want to also thank Dr. Atulasimha Jayasimha from whom I gained most of my magnetic materials knowledge through discussions. I would also like to thank Rupal Jain whose friendship, positive criticisms, and thin film knowledge helped my transition from aerospace enegineering to materials science a pleasant one. My professional and personal relationships with Dr. Supratik Datta, Dr. Atulasimha Jayasimha, and Rupal Jain have been excellent. I hope they continue into future, as they currently are.

I would also like to thank my personal friends: Gaurav Chawla, Pragati Godbole Chaudhary, Smita Bhadra, Anshu Sarje, Doug Galagate, Tony Rogers, Kather-

ine Cecilia Sequeira, Mustafa Dajani, Annabelle Pascua, Gary Paradee, Adam Karcz, Paris Alexander, Krista Cosert, Keith Gregorczyk, Konde Kartheek Reddy who made my stay at Maryland a memorable one.

Finally, I would like to thank my parents who inculcated the scientific way of looking at things right from my childhood, which indubitably helped me pursue knowledge throughout my life. I am also thankful to them for being supportive and showing belief that I can succeed no matter what I pursue.

Table of Contents

List of Tables ix

List of Figures x

1 Introduction 1
1.1 Physics of Magnetism . . . 1
1.1.1 Atomic magnetic moments . . . 2
1.1.2 Diamagnetism . . . 4
1.1.3 Paramagnetism . . . 6
1.1.4 Ferromagnetism . . . 7
1.2 Magnetostriction . . . 10
1.3 Magnetic domains . . . 18
1.4 Magnetostrictive materials . . . 20
1.5 Iron-Gallium (Fe–Ga) alloys . . . 21
1.6 Research objectives . . . 30

2 Macroscale characterization 33
2.1 Overview . . . 33
2.2 Sample specimens . . . 33
2.3 Magnetization . . . 34
2.4 Magnetostriction . . . 38
2.4.1 Experimental procedure . . . 38
2.4.2 Remanent state calculation . . . 39
2.4.3 Results and Discussion . . . 40
2.5 Summary . . . 45

3 Magnetic domains 48
3.1 Overview . . . 48
3.2 Background . . . 48
3.2.1 Magnetic Force Microscopy (MFM) . . . 52
3.2.2 Kerr microscopy . . . 54
3.2.2.1 Magneto-Optic Kerr effect . . . 54
3.2.2.2 Wide-field Kerr microscopy . . . 57
3.2.3 Expected domain structure in Fe–Ga . . . 59
3.2.4 Literature review . . . 61
3.3 Experimental procedure . . . 64
3.4 Magnetic domains at remanence . . . 64
3.4.1 Conventional polishing . . . 64
3.4.2 Additional silica gel polishing . . . 67
3.4.3 Discussion . . . 72
3.5 Magnetic domains under magnetic and elastic fields . . . 74
3.5.1 Experimental setup . . . 75
3.5.2 Domains under magnetic field . . . 76

3.5.3 Domains under elastic field . . . 86
3.6 Discussion and conclusions . . . 90

4 Neutron Scattering 94
4.1 Overview . . . 94
4.2 Background . . . 94
4.2.1 Nuclear Scattering . . . 95
4.2.1.1 Scattering Cross Section . . . 97
4.2.2 Magnetic Scattering . . . 99
4.2.2.1 Unpolarized Neutrons . . . 104
4.2.2.2 Polarized Neutrons . . . 105
4.2.3 Small-Angle Neutron Scattering . . . 106
4.2.3.1 Contrast . . . 108
4.2.4 Neutron Diffraction by Crystals . . . 110
4.2.5 Optimal thickness . . . 111
4.3 Setup . . . 112
4.3.1 Small-Angle Neutron Scattering (SANS) . . . 112
4.3.2 Ultra Small-Angle Neutron Scattering (USANS) . . . 115
4.3.3 Single Crystal Neutron Diffraction . . . 116
4.4 Unpolarized SANS . . . 118
4.4.1 Under magnetic field . . . 119
4.4.2 Under elastic field . . . 156
4.5 Polarized SANS . . . 161
4.6 Ultra Small-Angle Neutron Scattering . . . 164
4.7 Neutron Diffraction . . . 171
4.8 Discussion and conclusions . . . 176

5 Conclusions 195
5.1 Summary of Research . . . 196
5.2 Contributions of this research . . . 202
5.3 Recommendations and future work . . . 205

List of Tables

2.1 Sample specimens 35
2.2 Magnetostriction at $H = 800$ mT 46
2.3 Remanent states 47

4.1 Scattering Length Densities (SLDs) 109
4.2 30m NG3SANS Characteristics 113
4.3 Summary of unpolarized SANS results under magnetic field 155
4.4 lattice parameter 173
4.5 Saturation magnetic fields in mT 189
4.6 Comparison of SANS and neutron diffraction results with the magnetostriction 192

List of Figures

1.1 Ferromagnetic spins on a simple cubic lattice . . . 9
1.2 A spin pair with variable bond length $\boldsymbol{r}$. Arrows indicate direction of the spin . . . 11
1.3 (a) Single domain with high magnetostatic energy, (b) forming two domains reduces the magnetostatic energy, (c) forming multiple domains reduces the magnetostatic energy further, (d) formation of closure domains results in zero magnetostatic energy . . . 19
1.4 Bitter patterns in Fe-Si that is, (a) mechanically polished, (b) electrochemically polished or annealed. . . . 20
1.5 Magnetostrictive constants for Fe–Ga (single crystal) alloys for different at% Ga. Two peaks in magnetostriction correspond to ∼20 at% Ga and ∼28 at% respectively. . . . 22
1.6 (a) Equilibrium phase diagram of Fe–Ga. (b) Metastable phase diagram of Fe–Ga. . . . 23
1.7 Structure of different phases in Fe–Ga . . . 24
1.8 Lattice parameter of Fe–Ga . . . 25
1.9 (a) Magnetic anisotropy constant K_1 and (b) Magnetic anisotropy constant K_2 as a function of Ga at% in Fe–Ga. . . . 26
1.10 Shear elastic constants $c' = \frac{1}{2}(c_{11} - c_{12})$ and c_{44} as a function Ga at% 27
1.11 Mechanism of intrinsic magnetostriction. The magnetostriction arises within the atomic bond due to spin-orbit coupling. . . . 27
1.12 Mechanism of extrinsic magnetostriction. The magnetostriction arises due to the reorientation of tetragonal clusters in the presence of a magnetic field. The cluster shape itself is depicted to be tetragonal for illustrative purposes. The phase of the cluster is tetragonal and it can be in any shape. . . . 28

2.1 Magnetization of 15S vs. azimuthal angle . . . 35
2.2 Magnetization of 15S (left) and 18S (right) . . . 36
2.3 Magnetization of 19Qe . . . 37
2.4 Magnetization vs Temperature @$H_x = 2$ T for 19Qe . . . 38
2.5 Magnetostriction of 15S under H applied along $\hat{\boldsymbol{x}}$ (left) and $\hat{\boldsymbol{y}}$ (right) 41
2.6 Magnetostriction of 17S under H applied along $\hat{\boldsymbol{x}}$ (left) and $\hat{\boldsymbol{y}}$ (right) 41
2.7 Magnetostriction of 17Q under H applied along $\hat{\boldsymbol{x}}$ (left) and $\hat{\boldsymbol{y}}$ (right) 42
2.8 Magnetostriction of 18S under H applied along $\hat{\boldsymbol{x}}$ (left) and $\hat{\boldsymbol{y}}$ (right) 42
2.9 Magnetostriction of 19Qe under H applied along $\hat{\boldsymbol{x}}$ (left) and $\hat{\boldsymbol{y}}$ (right) 43
2.10 Magnetostriction of 20S under H applied along $\hat{\boldsymbol{x}}$ (left) and $\hat{\boldsymbol{y}}$ (right) 43
2.11 Magnetostriction of 20Q under H applied along $\hat{\boldsymbol{x}}$ (left) and $\hat{\boldsymbol{y}}$ (right) 44
2.12 Magnetostriction of 18Q under H applied along $\hat{\boldsymbol{x}}$ (left) and $\hat{\boldsymbol{y}}$ (right) 44

3.1 Magnetic domains on (001) Fe-Si showing 180° and 90° domain walls. 49
3.2 (a) Straight 180° domain wall leads to minimal magnetostatic energy (b) 180° domain wall that is not straight costs magnetostatic energy . 49

3.3 Possible curvature of a 180° domain wall in a material with uniaxial anisotropy . . . 50
3.4 Maze domain structure with curved domain walls in polycrystalline Ni thin film with out-of-plane anisotropy . . . 51
3.5 *Fir tree* magnetic domain pattern in (100) Fe-Al that is slightly misoriented. . . . 51
3.6 Illustration of the elementary magneto-optical interaction for the longitudinal Kerr effect. The sample with in-plane magnetization is illuminated using light that is polarized parallel to the plane of incidence 54
3.7 Illustration of the elementary magneto-optical interaction for the transverse Kerr effect. The sample with in-plane magnetization is illuminated using light that is polarized at 45° to the plane of incidence. . . 56
3.8 Kerr microscope setup . . . 57
3.9 Subtracting the background enhances the contrast . . . 58
3.10 A magnetic domain image (left) with four kinds of domains and its histogram (right) showing peaks corresponding to the domains . . . 59
3.11 MFM images of Fe-19 at. %Ga upon applying a step-increased field normal to the sample surface, (a) as-grown state, (b) H = 400 Oe, (c) H = 1000 Oe, and (d) H = 2600 Oe. . . . 61
3.12 Kerr image of (001) surface of 17S in (a) longitudinal mode and (b) polar mode. . . . 65
3.13 MFM image of (001) surface of 17S, showing maze pattern with out-of-plane magnetization. . . . 66
3.14 MFM image of (001) surface of (a) 17Q and (b) 19Qe, showing maze pattern with out-of-plane magnetization. . . . 66
3.15 Etching in Nital for more than 4 minutes . . . 68
3.16 (a) Highly stressed surface layer with effective thickness d_1 after polishing with alumina powder. (b,c) Reduction of the stressed layer thickness with silica gel polishing. (d) Extremely smooth surface with stressed layer thickness $d_2 \ll d_1$. . . . 69
3.17 Domain structure of 17S as a function of silica gel polishing time (a) t = 0, (b) t = 20 min, (c) t = 50 min, (d) 75 min. . . . 70
3.18 No domain structure visible in 17S with MFM even at the maximum scan size . . . 71
3.19 MFM images after additional polishing with colloidal silica. . . . 71
3.20 Typical Kerr images after additional polishing with colloidal silica. The domains show 90° and 180° domain walls with domains oriented along [100], [$\bar{1}$00], [010] and [0$\bar{1}$0]. . . . 72
3.21 High magnification MFM scan of 19Qe showing 90° and 180° domain walls . . . 72
3.22 Domain splitting near areas of stress concentration in 17Q (left) and 17S (right). Inset shows a magnified view of the maze domain structure within the scratch. . . . 73

3.23 An electromagnet that can be rotated was used to apply magnetic field along $\pm\hat{\boldsymbol{x}}$ or $\pm\hat{\boldsymbol{y}}$. Due to space constraints between the poles of the electromagnet, stress could be applied only along $\pm\hat{\boldsymbol{y}}$. 75
3.24 Device built from high strength aluminum to apply compressive stresses. Samples are squeezed between 1 and 2 by manually turning the screw. 76
3.25 Magnetic domain structure evolution in 19Qe with magnetic field applied along $\hat{\boldsymbol{x}}$ 77
3.26 Magnetization measure in 19Qe from Kerr microscope with magnetic field applied along $\hat{\boldsymbol{x}}$ 78
3.27 Magnetic domain structure evolution in 17S with magnetic field applied along $-\hat{\boldsymbol{x}}$ 79
3.28 Magnetization measure in 17S from Kerr microscope with magnetic field applied along $\hat{\boldsymbol{x}}$ 80
3.29 Magnetic domain structure evolution in 17S (backside) with magnetic field applied along $-\hat{\boldsymbol{x}}$ 81
3.30 Magnetization measure in 17S (backside) from Kerr microscope with magnetic field applied along $\hat{\boldsymbol{x}}$ 82
3.31 Magnetic domain structure evolution in 17Q with magnetic field applied along $-\hat{\boldsymbol{x}}$ 83
3.32 Magnetization measure in 17Q from Kerr microscope with magnetic field applied along $\hat{\boldsymbol{x}}$ 84
3.33 Magnetic domain structure evolution in 17Q (back side) with magnetic field applied along $-\hat{\boldsymbol{y}}$ 85
3.34 Magnetization measure in 17Q (backside) from Kerr microscope with magnetic field applied along $\hat{\boldsymbol{x}}$ 86
3.35 Magnetic domain structure evolution in 19Qe with compressive elastic field applied along $\hat{\boldsymbol{y}}$ 87
3.36 Magnetic domain structure evolution in 17S with compressive elastic field applied along $\hat{\boldsymbol{y}}$ 88
3.37 Magnetic domain structure evolution in 17S with an elastic pre-strain $\epsilon_0 = -1140\,\mu\epsilon \parallel \hat{\boldsymbol{y}}$ and magnetic field applied along $\hat{\boldsymbol{x}}$ 89

4.1 Schematic showing the elastic scattering of the neutron from a fixed nucleus 96
4.2 Geometry of a scattering experiment 98
4.3 Schematic of Small-Angle Neutron Scattering (SANS) 112
4.4 Schematic of Ultra Small-Angle Neutron Scattering (USANS) 116
4.5 Circles represent iso-intensity contours from isotropic small angle scattering. The Narrow slit represents the scattered region collected by the BT5 analyzer. 117
4.6 Schematic of triple axes single crystal neutron diffractometer (left). TriCS intrument at Paul Scherrer Institut, Switzerland (right) 118
4.7 19Qe SANS lowq images for $H_x = 0.07$ mT and 30 mT. Streaks along 0, 90, and ± 45 degrees to the $\hat{\boldsymbol{x}}$ are due to the 90° and 180° domains walls 120

4.8 19Qe SANS lowq images under magnetic field after pre-treating the sample with $H = -1.3$ T. Streaks along 0, 90, and ± 45 degrees to the $\hat{\boldsymbol{x}}$ are due to the 90° and 180° domains walls . . . 121
4.9 19Qe SANS lowq (lower) images. In addition the top surface of the sample was finely polished such that magnetic domains are visible. Streaks along 0, 90, and ± 45 degrees to the $\hat{\boldsymbol{x}}$ are more clearly visible. 122
4.10 19Qe SANS highq images under magnetic field after pre-treating the sample with $H = -1.3$ T. Strong anisotropy in the scattering suggests presence of heterogeneities . . . 124
4.11 19Qe SANS highq (higher) images under magnetic field after pre-treating the sample with $H = -1.3$ T. Detector was moved to cover even higher q values. . . . 125
4.12 19Qe SANS I vs. q averaged along a 30 degree horizontal sector (left) and a 30 degree vertical sector (right) . . . 126
4.13 Azimuthal angle θ dependence of the SANS intensity averaged over $0.021 \leq |q| \leq 0.057$ Å^{-1} for 19Qe . . . 126
4.14 18SLowQ . . . 128
4.15 SANS highq images of 18S subjected to magnetic field. Very weak anisotropy can be discerned from the scattering image at $H = 1.3$ T. 130
4.16 Azimuthal angle θ dependence of the SANS intensity averaged over $0.039 \leq |q| \leq 0.15$ Å^{-1} for 18S . . . 131
4.17 Merging lowq and highq data in 18S sample. The misalignment of the intensity curves is possibly due to the multiple scattering effect . 131
4.18 18S SANS I vs. $|q|$ circularly averaged in all directions. No peak is perceptible. . . . 132
4.19 SANS lowq images of 18Q under magnetic field . . . 133
4.20 SANS highq images of 18Q under magnetic field . . . 134
4.21 Azimuthal angle θ dependence of the SANS intensity averaged over $0.039 \leq |q| \leq 0.15$ Å^{-1} for 18Q . . . 134
4.22 18Q SANS I vs. $|q|$ circularly averaged in all directions. No peak is perceptible. . . . 135
4.23 SANS lowq images of 15S under magnetic field. Scattering at $H = 1.5$ T indicates nuclear scattering due to crystalline imperfections . . . 136
4.24 SANS highq images of 15S under magnetic field . . . 137
4.25 Azimuthal angle θ dependence of the SANS intensity averaged over $0.041 \leq |q| \leq 0.17$ Å^{-1} for 15S. Strong nuclear scattering leads to deviation from the sine squared dependence. . . . 138
4.26 Azimuthal angle θ dependence of the SANS intensity averaged over $0.041 \leq |q| \leq 0.17$ Å^{-1} for 15S. Nuclear scattering, which is field independent was removed by subtracting $H = -3.4$ mT scattering image from $H = 1.5$ T image. . . . 139
4.27 15S SANS I vs. $|q|$, circularly averaged in all directions. . . . 139
4.28 SANS lowq images of 17S under magnetic field. . . . 140
4.29 SANS highq images of 17S under magnetic field. . . . 142

4.30 Azimuthal angle θ dependence of the SANS intensity averaged over $0.045 \leq |q| \leq 0.14$ Å^{-1} for 17S. . . . 143
4.31 17S SANS I vs. $|q|$, circularly averaged in all directions. . . . 143
4.32 SANS lowq images of 17Q under magnetic field. . . . 144
4.33 SANS highq images of 17Q under magnetic field. . . . 145
4.34 Azimuthal angle θ dependence of the SANS intensity averaged over $0.045 \leq |q| \leq 0.14$ Å^{-1} for 17Q. . . . 146
4.35 17Q SANS I vs. $|q|$, circularly averaged in all directions. . . . 147
4.36 20S lowq SANS images under decreasing magnetic field . . . 148
4.37 20S highq SANS images under decreasing magnetic field . . . 149
4.38 Azimuthal angle θ dependence of the SANS intensity averaged over $0.029 \leq |q| \leq 0.14$ Å^{-1} for 20S. . . . 150
4.39 20S SANS I vs. $|q|$, circularly averaged in all directions. . . . 150
4.40 20Q lowq SANS images under decreasing magnetic field . . . 151
4.41 20Q highq SANS images under decreasing magnetic field . . . 152
4.42 Azimuthal angle θ dependence of the SANS intensity averaged over $0.029 \leq |q| \leq 0.14$ Å^{-1} for 20Q. . . . 153
4.43 Azimuthal angle θ dependence of the SANS intensity of 20Q. Intensity at remanence was subtracted from the intensity at $H = 1.6$ T and averaged over $0.029 \leq |q| \leq 0.14$ Å^{-1}. . . . 153
4.44 20Q SANS I vs. $|q|$, circularly averaged in all directions. . . . 154
4.45 Device used to apply compressive elastic load to the sample. A resistive strain gage bonded to the sample was used to quantify the applied load . . . 156
4.46 19Qe lowq SANS images under elastic field . . . 157
4.47 19Qe highq SANS images under elastic field . . . 158
4.48 Azimuthal angle θ dependence of the SANS intensity averaged over $0.02 \leq |q| \leq 0.051$ Å^{-1} for 19Qe under elastic field . . . 159
4.49 SANS I vs. $|q|$ of 19Qe under increasing compressive elastic field along $\hat{\boldsymbol{y}}$, averaged along a 30 degree horizontal sector (left) and a 30 degree vertical sector (right). . . . 160
4.50 19Qe non-spin-flip scattering (left) and spin-flip scattering (right) images at $H = 1.3$ T . . . 161
4.51 Azimuthal angle dependence of non-spin-flip and spin-flip scattering in comparison to scattering of unpolarized neutrons for 19Qe at $H = 1.3$ T. Intensity was averaged for $0.02 \leq q \leq 0.057$ Å^{-1}. . . . 162
4.52 Schematic of depolarized neutron beam due to the presence of magnetic domains and polarized neutron beam at saturation. . . . 163
4.53 Neutron polarization with increasing magnetic field for 19Qe. . . . 164
4.54 USANS transmission measurements for 19Qe, 20S, 17Q, and 17S. I_{SAS} was measured at $q = 1.7 \times 10^{-4}$ Å^{-1}. . . . 165
4.55 19Qe USANS intensity curves for increasing magnetic fields . . . 166
4.56 20S USANS intensity curves for increasing magnetic fields . . . 167
4.57 17Q USANS intensity curves for increasing magnetic fields . . . 167
4.58 17S USANS intensity curves for increasing magnetic fields . . . 168

4.59 USANS transmission measurements of 17Q and 17S after they polishing them both sides. I_{SAS} was measured at $q = 1.7 \times 10^{-4}$ Å^{-1}. . . 169
4.60 17Q USANS intensity curves for increasing magnetic fields after top and bottom surfaces were polished . . . 170
4.61 17S USANS intensity curves for increasing magnetic fields after top and bottom surfaces were polished . . . 170
4.62 Rocking curves for (200) reciprocal point. Multiple peaks were observed in all the samples that show the samples were not perfect crystals but contain more than one crystal that are slightly misoriented. . . . 172
4.63 (h00) reciprocal line scans. 19Qe and 20S show sharp (100) peaks. 17S, 17Q, 18Q, 20Q show weak or diffuse (100) peaks. 15S shows no peak at all. . . . 174
4.64 Gaussian fits to the (100) peaks with background subtracted and normalized to the (200) peak intensity. 19Qe and 20S show sharp + diffuse (100) peaks, 17Q shows weak + diffuse (100) peak, 18Q shows weak (100) peak, 17S and 20Q show diffuse (100) peaks and 15S shows no (100) peak. . . . 175
4.65 (hhh) reciprocal line scans. 20S shows sharp (1/2 1/2 1/2) peak. 17Q shows weak (1/2 1/2 1/2) peak. 17S shows a diffuse (1/2 1/2 1/2) peak. . . . 176
4.66 Gaussian fits to the (1/2 1/2 1/2) peaks with background subtracted and normalized to the (200) peak intensity. 20S shows sharp (1/2 1/2 1/2) peak. 17Q shows weak (1/2 1/2 1/2) peak. 17S shows a diffuse (1/2 1/2 1/2) peak. . . . 177
4.67 19Qe lowq, highq SANS comparison with magnetostriction. Highq SANS was averaged along 30° sectors between $0.025 < q < 0.05$ Å^{-1}. Lowq SANS was circularly averaged between $0.0069 < q < 0.0195$ Å^{-1}. 178
4.68 18S lowq, highq SANS comparison with magnetostriction. Highq SANS was averaged along 30° sectors between $0.039 < q < 0.15$ Å^{-1}. Lowq SANS was circularly averaged between $0.0049 < q < 0.023$ Å^{-1}. 179
4.69 18Q lowq, highq SANS comparison with magnetostriction. Highq SANS was averaged along 30° sectors between $0.041 < q < 0.17$ Å^{-1}. Lowq SANS was circularly averaged between $0.006 < q < 0.039$ Å^{-1}. . . 179
4.70 15S lowq, highq SANS comparison with magnetostriction. Lowq SANS was circularly averaged between $0.0056 < q < 0.04$ Å^{-1}. Highq SANS was dominated by nuclear scattering from crystalline imperfections . . . 180
4.71 17Q lowq, highq SANS comparison with magnetostriction. Highq SANS was averaged along 30° sectors between $0.045 < q < 0.14$ Å^{-1}. Lowq SANS was circularly averaged between $0.001 < q < 0.015$ Å^{-1}. . 180
4.72 17S lowq, highq SANS comparison with magnetostriction. Highq SANS was averaged along 30° sectors between $0.045 < q < 0.14$ Å^{-1}. Lowq SANS was circularly averaged between $0.001 < q < 0.015$ Å^{-1}. . 181

4.73 20S lowq, highq SANS comparison with magnetostriction. Highq SANS was averaged along 30° sectors between $0.029 < q < 0.14$ Å^{-1}. Lowq SANS was circularly averaged between $0.001 < q < 0.015$ Å^{-1}. . 181
4.74 20Q lowq, highq SANS comparison with magnetostriction. Highq SANS was averaged along 30° sectors between $0.029 < q < 0.14$ Å^{-1}. Lowq SANS was circularly averaged between $0.001 < q < 0.015$ Å^{-1}. . 182
4.75 19Qe lowq, highq SANS response to elastic field. Highq SANS was averaged along 30° sectors between $0.019 < q < 0.051$ Å^{-1}. Lowq SANS was circularly averaged between $0.0069 < q < 0.0195$ Å^{-1}. . . . 183
4.76 19Qe neutron polarization data superimposed on to the data shown in figure 4.67. . . . 183
4.77 Comparison of USANS intensity at $q = 1.7 \times 10^{-4}$ Å^{-1} and magnetostriction of 19Qe . . . 185
4.78 Comparison of USANS intensity at $q = 1.7 \times 10^{-4}$ Å^{-1} and magnetostriction of 20S . . . 185
4.79 Comparison of USANS intensity at $q = 1.7 \times 10^{-4}$ Å^{-1} and magnetostriction of 17Q . . . 186
4.80 Comparison of USANS intensity at $q = 1.7 \times 10^{-4}$ Å^{-1} and magnetostriction of 17S . . . 186
4.81 Comparison of USANS intensity at $q = 1.7 \times 10^{-4}$ Å^{-1} and magnetostriction of 17Q that was polished on both sides . . . 188
4.82 Comparison of USANS intensity at $q = 1.7 \times 10^{-4}$ Å^{-1} and magnetostriction of 17S that was polished on both sides . . . 188
4.83 Magnetostriction of slow-cooled (SC) and quenched (Q) Fe-Ga. First four data points were used for quadratic fit. . . . 194

Chapter 1

Introduction

This dissertation attempts to unravel the origins of magnetostriction in Fe–Ga alloys. These ferromagnetic alloys, also known as Galfenol, belong to the class of smart materials, which can be used in novel devices for robust transduction purposes, both as actuators and sensors. The knowledge thus gained will aid us in our quest to find alloy systems that demonstrate higher magnetostriction and better mechanical properties.

This chapter introduces the concepts necessary to fully appreciate the motivation and contribution of this dissertation. In the next sections, a brief introduction to magnetism explaining the physics behind ferromagnetism is provided. In the next section, fundamentals of magnetostriction are discussed. In the subsequent section, a brief introduction to magnetostrictive materials followed by an overview of magnetostriction in Fe–Ga alloys is provided. Following that, the research objectives of this dissertation are stated.

1.1 Physics of Magnetism

Magnetism is the behavior of materials that respond to the applied magnetic field. This phenomenon arises due to the magnetic moments of the atoms.

1.1.1 Atomic magnetic moments

The magnetic moment of the atom arises due to the angular momentum of the electrons. If the electron, which has a charge e, rotates around the nucleus in an orbit of radius r at an angular velocity of ω then its motion constitutes a current of $i = -e\omega/2\pi$. The magnetic moment generated by this electric current is given by

$$\boldsymbol{\mu} = -i(\pi r^2) = -\frac{e\boldsymbol{\omega} r^2}{2} \tag{1.1}$$

Since the angular momentum of the moving electron is given by

$$\boldsymbol{P} = m\boldsymbol{\omega} r^2, \tag{1.2}$$

where m is the mass of the electron, the magnetic moment can be expressed as

$$\boldsymbol{\mu} = -\frac{e}{2m}\boldsymbol{P}. \tag{1.3}$$

The magnetic moment is thus proportional to the angular momentum of the electron and is in the opposite direction.

Although the above expression was derived using classical mechanics, it accurately describes the relationship between the angular momentum of the electron and the corresponding magnetic moment due to this angular momentum. From quantum mechanics, the electron has two kinds of angular momentum - orbital angular momentum ($\boldsymbol{L}$) and spin angular momentum or spin ($\boldsymbol{S}$). In classical perspective, orbital momentum can be thought of the momentum due to electron's motion in its orbital. Spin angular momentum is purely quantum mechanical effect and has no analogy in classical mechanics. The total angular momentum of the electron is

$\boldsymbol{J} = \boldsymbol{L}+\boldsymbol{S}$. As many other quantities of subatomic particles, the angular momentum of the electron is also quantized. The quantized angular momentum of the electron are expressed as $L = \sqrt{\ell(\ell+1)}\ \hbar$ and $S = \sqrt{s(s+1)}\ \hbar$, where ℓ and s are orbital quantum number and spin quantum number respectively. The allowed values for ℓ are integers and for s are $\pm\frac{1}{2}$, called *up* and *down* spin states.

The magnetic moment associated with the orbital angular momentum is

$$\boldsymbol{\mu}_L = -\mu_B \boldsymbol{L} \tag{1.4}$$

and that with the spin angular momentum is

$$\boldsymbol{\mu}_S = -2\mu_B \boldsymbol{S}, \tag{1.5}$$

where

$$\mu_B = \frac{e\hbar}{2m} \tag{1.6}$$

is the Bohr magneton.

Using these the total magnetic moment associated with the electron can be expressed as

$$\boldsymbol{\mu} = -\mu_B(\boldsymbol{L} + 2\boldsymbol{S}). \tag{1.7}$$

Pauli's exclusion principle states that no two electrons can have the same set of quantum numbers. As a consequence, electrons pair up i.e., the electrons are so stacked that within the same orbital if one electron has *spin up* (s = +1/2) then the other will have *spin down* (s = -1/2). This leads to the cancellation of the magnetic moments resulting in a net zero magnetic moment. Therefore, an atom has a magnetic moment only when there are unpaired electrons. Another quantum mechanical rule called Hund's rule governs the arrangement of the electrons. According

to this rule the electrons are arranged such that (1) the resulting spin $\boldsymbol{S}$ is as large as possible within the restrictions of the Pauli's principle. The reason for this is that the electrons tend to take different orbits to minimize the Coulomb repulsion. Moreover, the intra-atomic spin-spin interaction tends to align their spins parallel to each other. (2) The resulting orbital angular momentum $\boldsymbol{L}$ is as large as possible within the restrictions of the Pauli's principle and condition (1). The reason for this is that the electrons tend to align their magnetic moment due to the orbital angular momentum parallel to each other so as to minimize the Coulomb repulsion. As a consequence of Hund's rule, some of the elements with $3d$ and $4f$ shell electrons have more than one unpaired electrons leading to strong atomic moments.

1.1.2 Diamagnetism

Diamagnetism occurs in materials with no atomic magnetic moments, i.e. those materials in which all the electrons are paired up. The susceptibility of these materials is small and negative, typically $\chi \approx -10^{-5}$. The negative sign means the induced magnetization is opposite in direction to the magnetic field. The mechanism by which this happens is the acceleration of the orbital electrons by electromagnetic induction. According to Lenz's law, the magnetic flux produced by this acceleration is always opposite to the change in the external magnetic field.

If one assumes a circular orbit of radius r for simplicity then the electric field E produced due to the magnetic field H applied perpendicular to the orbital plane

is

$$E = -\frac{r}{2}\frac{dH}{dt}. \tag{1.8}$$

The electron is accelerated because of this electric field resulting in a change of its velocity by Δv in time Δt, which is given by

$$\Delta v = -\frac{e}{m}E\Delta t = \frac{er}{2m}\Delta H. \tag{1.9}$$

Using this, the change in the centrifugal force acting on the electron is

$$\Delta F_c = ev\Delta H, \tag{1.10}$$

which is balanced by the increase in the Lorentz force

$$\Delta F_L = ev\Delta B. \tag{1.11}$$

This indicates that the orbit of the electron precesses about the applied field with angular velocity

$$\omega_L = \frac{v}{r} = \frac{e}{2m}H. \tag{1.12}$$

This motion of the orbit is called *Larmor precession*. The magnetic moment produced by this motion is given by

$$\begin{aligned} \boldsymbol{\mu} &= -\left(\frac{e\Delta v}{2\pi r}\right)\pi r^2 \\ &= -\frac{e^2 r^2}{4m}H. \end{aligned} \tag{1.13}$$

As can be seen, the induced magnetization is opposite in direction to the magnetic field. This is called diamagnetism. Elememts like Cu, Ag, Au, Pb with no unpaired electrons demonstrate diamagnetism.

1.1.3 Paramagnetism

Paramagnetism appears only in elements with unpaired electrons. As in diamagnetism, the negative magnetic moment is induced even in paramagnetic materials. However, the alignment of the atomic moments with the magnetic field dominates, resulting in a positive magnetic moment. Paramagnetic materials exhibit susceptibility of the order of $\chi = 10^{-5} - 10^{-2}$.

If the atomic moment is assumed to be 1 Bohr magneton, then at a magnetic field of $H = 1 \times 10^6$ A/m, the magnetic energy is $\mu H \approx 1.2 \times 10^{-23}$ J. This is two orders of magnitude less than the thermal energy ($kT/2 = 2.1 \times 10^{-21}$ J) at room temperature. Therefore, a magnetic field of this magnitude can barely influence the atomic moments that get thermally agitated at such temperatures. Therefore, it takes enormous field to align the magnetic moments with the field. Lower the temperature, higher will be the susceptibility of paramagnetic materials. This is given by the Curie law:

$$\chi = \frac{N\mu^2}{3kT}, \tag{1.14}$$

which states that the susceptibility of paramagnetic materials is inversely proportional to the absolute temperature. The magnetization of paramagnetic materials can be quantitatively defined using *Langevin* function. For more details the readers are referred to [1].

1.1.4 Ferromagnetism

Ferromagnetism is characterized by a strong magnetic behavior. Susceptibility of ferromagnetic materials can be as high as $\chi = 1000$. The origin of such a strong magnetism is not only the strong atomic moment from the unpaired electrons but also the spontaneous magnetization produced due to the alignment of all atomic moments parallel to each other. Weiss [2] explained the mechanism of this spontaneous magnetization in 1907 by introducing an effective field called molecular field. Later in 1928 Heisenberg [3] proposed the exchange interaction energy between the atoms with spins S_i and S_j defined as

$$w_{ij} = -2JS_i \cdot S_j, \tag{1.15}$$

where J is the exchange integral, to be the source of the molecular field. This exchange interaction is a quantum mechanical effect. The exchange integral J determines if the lower energy state is spin parallel or antiparallel. If J is positive then spins are all aligned parallel to each other resulting in ferromagnetism. If J is negative then spins align antiparallel to each other resulting in antiferromagnetism. As with paramagnetic material, temperature plays an important role. The spontaneous magnetization occurs only below a critical temperature, called Curie temperature T_c. Beyond Curie temperature, the thermal energy agitates the atomic spins to the point where the atomic spins do not align parallel to each other anymore. In this temperature regime, ferromagnetic materials become paramagnetic.

The physical origins of the exchange interaction energy can be understood from Pauli's exclusion principle and Coulomb interaction. Suppose two atoms with

unpaired electrons are close to each other then if the spins of the two atoms are antiparallel, the electrons will share one molecular orbital. This increases the Coulomb energy. If this increase in the Coulomb energy is less than the energy minimization due to spin cancellation then the electrons maintain antiparallel spin. Such antiparallel alignment of spin is called antiferromagnetism. If it is the other way around, then the electrons maintain parallel spins and form separate molecular orbitals, according to Pauli's exclusion principle, thus decreasing the Coulomb energy. Such parallel alignment of spin is known as ferromagnetism.

The Exchange energy of an ensemble of atoms, like in a crystal, can be written [4] as

$$E_{ex} = A\left(\left(\frac{\partial \boldsymbol{\alpha}}{\partial x}\right)^2 + \left(\frac{\partial \boldsymbol{\alpha}}{\partial y}\right)^2 + \left(\frac{\partial \boldsymbol{\alpha}}{\partial z}\right)^2\right), \tag{1.16}$$

where A is the exchange stiffness constant and $\boldsymbol{\alpha}$ is the unit vector along the magnetization direction.

The exchange interaction leads to spontaneous magnetization but it does not dictate the direction in which the magnetization orients. So, the magnetization is free to orient along any direction in the crystal without changing the internal energy if no additional interaction exists. However in actual ferromagnetic materials, there exists an easy direction in which the magnetization likes to orient. Rotation of the magnetization away from this easy direction increases the internal energy of the system. Therefore rotation of the magnetization away from easy axes is only possible by applying a magnetic field. The energy that dictates the preference in magnetization orientation is called magnetic anisotropy. The anisotropy that

assigns an energy to different directions in the crystal is known as magnetocrystalline anisotropy and is given by

$$E_K = K_1 \left(\alpha_1^2\alpha_2^2 + \alpha_2^2\alpha_3^2 + \alpha_3^2\alpha_1^2\right) + K_2 \left(\alpha_1^2\alpha_2^2\alpha_3^2\right), \tag{1.17}$$

for materials with cubic crystal structure. Constants K_1 and K_2 are cubic anisotropy constants.

To understand how the magnetocrystalline anisotropy can be constructed from spin-pair energy, we should revisit equation (1.15), which is the expression for exchange energy and is independent of the crystal directions. Therefore, additional terms are added that are dependent on the orientation of the spins (or magnetization) with respect to the crystal axes. Interaction energy between two atomic spins can then be expressed as

$$w(\boldsymbol{\alpha}) = w_{ex} + l\left((\boldsymbol{\alpha}\cdot\boldsymbol{\beta})^2 - \frac{1}{3}\right) + q\left((\boldsymbol{\alpha}\cdot\boldsymbol{\beta})^4 - \frac{6}{7}(\boldsymbol{\alpha}\cdot\boldsymbol{\beta})^2 + \frac{3}{35}\right), \tag{1.18}$$

where the first term is the exchange energy that is independent of $\boldsymbol{\alpha}$ and the second term is dipole-dipole interaction term [1, 5].

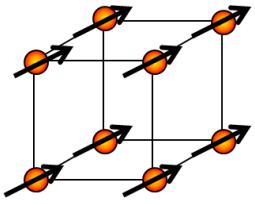

Figure 1.1: Ferromagnetic spins on a simple cubic lattice

For a cubic lattice as shown in figure 1.1, the magnetocrystalline anisotropy can be calculated by summing up all the spin pairs within the unit volume of the

crystal

$$E_K = \sum_i w_i, \tag{1.19}$$

where i is a spin pair. For simplicity, we consider here the interaction between the first nearest neighbors ignoring the interaction between distant pairs. Then expanding the above equation gives

$$E_K = N \sum_i l \left(\alpha_i^2 - \frac{1}{3} \right) + q \left(\alpha_i^4 - \frac{6}{7} \alpha_i^2 + \frac{3}{35} \right), \tag{1.20}$$

which can be simplified using the identity $\alpha_1^2 + \alpha_2^2 + \alpha_3^2 = 1$ to

$$E_K = -2Nq \left(\alpha_1^2 \alpha_2^2 + \alpha_2^2 \alpha_3^2 + \alpha_3^2 \alpha_1^2 \right) + \text{const.}, \tag{1.21}$$

where N is the number of atoms in a unit lattice. Comparing this with (1.17)

$$K_1 = -2Nq. \tag{1.22}$$

It should be noted here that we derived only the first term of the magnetocrystalline anisotropy as the interaction between distant pairs was ignored.

1.2 Magnetostriction

All ferromagnetic materials demonstrate magnetostriction - a change in shape due to a change in magnetization. It was first discovered in iron wires by Jame Joule in 1842 [6]. Magnetostriction arises due to the interaction between the atomic magnetic moments. If $\boldsymbol{\alpha}$ are the direction cosines of the magnetization and $\boldsymbol{\beta}$ are the direction cosines of the bond direction, then the interaction energy [1, 5] between two atomic moments (or two atoms) can be defined in terms of their interatomic

distance $\boldsymbol{r}$ as

$$w(\boldsymbol{r},\boldsymbol{\alpha}) = l(\boldsymbol{r})\left((\boldsymbol{\alpha}\cdot\boldsymbol{\beta})^2 - \frac{1}{3}\right) + q(\boldsymbol{r})\left((\boldsymbol{\alpha}\cdot\boldsymbol{\beta})^4 - \frac{6}{7}(\boldsymbol{\alpha}\cdot\boldsymbol{\beta})^2 + \frac{3}{35}\right). \tag{1.23}$$

Ignoring the higher order terms, the energy of the spin pair in an unstrained state can be written as

$$w(\boldsymbol{r},\boldsymbol{\alpha}) = l(\boldsymbol{r_0})\left((\boldsymbol{\alpha}\cdot\boldsymbol{\beta})^2 - \frac{1}{3}\right). \tag{1.24}$$

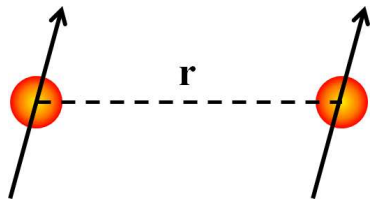

Figure 1.2: A spin pair with variable bond length $\boldsymbol{r}$. Arrows indicate direction of the spin

When the crystal is deformed by

$$\boldsymbol{\epsilon} = \left\{\begin{array}{c}\epsilon_{xx}\\ \epsilon_{yy}\\ \epsilon_{zz}\\ \epsilon_{xy}\\ \epsilon_{yz}\\ \epsilon_{zx}\end{array}\right\}, \tag{1.25}$$

the equilibrium bond length $\boldsymbol{r_0}$ changes to $\boldsymbol{r_0}(1+\boldsymbol{\epsilon})$. Calculating the change in the interaction energy Δw and summing it up for all the nearest neighbor pairs in a

unit volume of the lattice, one can get [1, 4]

$$E_{magel} = B_1 \left\{ \epsilon_{xx} \left(\alpha_1^2 - \frac{1}{3} \right) + \epsilon_{yy} \left(\alpha_2^2 - \frac{1}{3} \right) + \epsilon_{zz} \left(\alpha_3^2 - \frac{1}{3} \right) \right\}$$

$$+ B_2 \left(\epsilon_{xy}\alpha_1\alpha_2 + \epsilon_{yz}\alpha_2\alpha_3 + \epsilon_{zx}\alpha_3\alpha_1 \right) \tag{1.26}$$

$$= \mathbf{b}\boldsymbol{\epsilon}, \tag{1.27}$$

where

$$\mathbf{b} = \left\{ B_1 \left(\alpha_1^2 - \tfrac{1}{3}\right) \quad B_1 \left(\alpha_2^2 - \tfrac{1}{3}\right) \quad B_1 \left(\alpha_3^2 - \tfrac{1}{3}\right) \quad B_2\alpha_1\alpha_2 \quad B_2\alpha_2\alpha_3 \quad B_2\alpha_3\alpha_1. \right\} \tag{1.28}$$

This energy, expressed in terms of the magnetization direction of the atomic moments and the lattice strain, is called magnetoelastic energy. Constants B_1 and B_2 are called magnetomechanical coupling constants [7, 8] and can be calculated from the values of magnetostriction and elastic constants of a ferromagnetic material as will be seen later. The axis directions x,y, and z correspond to the $\langle 100 \rangle$ crystallographic directions of the material. Because of the magnetoelastic energy, the material strains when its magnetization is changed. Alternatively the magnetization also gets affected if the material is strained by external mechanical forces. This phenomenon was first discovered by Villari in 1865 and was since then called Villari effect [9].

To evaluate the expression for magnetostriction, the Gibbs free energy of the system is formulated as the Legendre transformation of the internal energy. Assuming isothermal and isentropic processes, the Gibbs free energy is reduced to the enthalpy of the system can be expressed as the sum of exchange energy E_{ex}, magnetocrystalline anisotropy energy E_K, magnetoelastic energy E_{magel}, elastic energy

E_{el}, magnetic work or Zeeman energy W_{mag}, and mechanical work W_{mech}

$$\mathcal{H} = E_{ex} + E_K + E_{magel} + E_{el} - W_{mag} - W_{mech}. \tag{1.29}$$

The expression for E_K was given in (1.17). The elastic energy can be written as

$$E_{el} = \frac{1}{2}\boldsymbol{\epsilon}^T \tilde{\mathbf{C}} \boldsymbol{\epsilon}, \tag{1.30}$$

where $\tilde{\mathbf{C}}$ is the stiffness matrix. For cubic materials, $\tilde{\mathbf{C}}$ is expressed using elastic constants c_{11}, c_{12}, and c_{44} as

$$\tilde{\mathbf{C}} = \begin{bmatrix} c_{11} & c_{12} & c_{12} & 0 & 0 & 0 \\ c_{12} & c_{11} & c_{12} & 0 & 0 & 0 \\ c_{12} & c_{12} & c_{11} & 0 & 0 & 0 \\ 0 & 0 & 0 & c_{44} & 0 & 0 \\ 0 & 0 & 0 & 0 & c_{44} & 0 \\ 0 & 0 & 0 & 0 & 0 & c_{44} \end{bmatrix}. \tag{1.31}$$

The expression for W_{mag} is given by

$$W_{mag} = \mu_0 \mathbf{M}^T \mathbf{H}, \tag{1.32}$$

while the expression for W_{mech} can be written as the product of an externally applied stress ($\boldsymbol{\sigma}$) given in equation (1.33) and the resulting strain ($\boldsymbol{\epsilon}$).

$$\boldsymbol{\sigma}^T = \begin{bmatrix} \sigma_{xx} & \sigma_{yy} & \sigma_{zz} & \sigma_{xy} & \sigma_{yz} & \sigma_{zx} \end{bmatrix}. \tag{1.33}$$

$$W_{mech} = \boldsymbol{\sigma}^T \boldsymbol{\epsilon} \tag{1.34}$$

Magnetization can be expressed as $\mathbf{M} = M_s \left[\alpha_1 \ \alpha_2 \ \alpha_3\right]^T$, where M_s is the saturation magnetization, which is a material property. Using this, the enthalpy of the system can be written as a function of α_i and $\boldsymbol{\epsilon}$. Therefore, the variables α_i and $\boldsymbol{\epsilon}$ can now be termed as the system's internal variables. Using equations (1.17), (1.32), (1.27), (1.30), and (1.34) the enthalpy can be expressed as

$$\begin{aligned}\mathcal{H}\left(\alpha_i, \boldsymbol{\epsilon}\right) = K_1 \left(\alpha_1^2\alpha_2^2 + \alpha_2^2\alpha_3^2 + \alpha_3^2\alpha_1^2\right) + K_2 \left(\alpha_1^2\alpha_2^2\alpha_3^2\right) \\ + \mathbf{b}\boldsymbol{\epsilon} + \frac{1}{2}\boldsymbol{\epsilon}^T\tilde{\mathbf{C}}\boldsymbol{\epsilon} - \mu_0\mathbf{M}^T\mathbf{H} - \boldsymbol{\sigma}^T\boldsymbol{\epsilon}.\end{aligned} \tag{1.35}$$

The equilibrium states of the system can be calculated by minimizing $\mathcal{H}$ with respect to its internal variables α_i and $\boldsymbol{\epsilon}$. It is assumed that $\mathcal{H}(\alpha_i, \boldsymbol{\epsilon})$ is a continuous function of α_i and $\boldsymbol{\epsilon}$ and has continuous second order partial derivatives.

Some of the earlier works[1, 4, 7, 8] that have derived the equilibrium strains did so under an assumption of a zero applied stress. The expression for the equilibrium strains assuming a constant 3-D stress was derived recently [10, 11], which will be presented here. The enthalpy of the system, which is defined in equation (1.35) with α_i and $\boldsymbol{\epsilon}$ as the internal variables, is minimized with respect to $\boldsymbol{\epsilon}$

$$\frac{\partial\mathcal{H}\left(\alpha_i, \boldsymbol{\epsilon}\right)}{\partial\boldsymbol{\epsilon}} = 0, \tag{1.36}$$

which gives

$$\mathbf{b}^T + \tilde{\mathbf{C}}\boldsymbol{\epsilon} - \boldsymbol{\sigma} = 0. \tag{1.37}$$

Solving for $\boldsymbol{\epsilon}$ yields

$$\boldsymbol{\epsilon}^* = \tilde{\mathbf{C}}^{-1}\boldsymbol{\sigma} - \tilde{\mathbf{C}}^{-1}\mathbf{b}^T = \boldsymbol{\epsilon}_{mech} + \boldsymbol{\lambda}. \tag{1.38}$$

Taking a second partial derivative with respect to $\boldsymbol{\epsilon}$ yields

$$\frac{\partial^2 \mathcal{H}\left(\alpha_i, \boldsymbol{\epsilon}\right)}{\partial \boldsymbol{\epsilon}^2} = \tilde{\mathbf{C}}, \tag{1.39}$$

which is a positive value and hence $\boldsymbol{\epsilon}^*$ corresponds to a relative minimum of $\mathcal{H}$. Therefore, $\boldsymbol{\epsilon}^*$ is the equilibrium strain.

The equilibrium strain derived earlier [1, 4, 7, 8] for zero stress included only the second part of the equation (1.38), which is the magnetostrictive $\boldsymbol{\lambda} = -\tilde{\mathbf{C}}^{-1}\mathbf{b}^T$ strain. For the non-zero stress condition, the equilibrium strain is a superposition of purely mechanical $\boldsymbol{\epsilon}_{mech} = \tilde{\mathbf{C}}^{-1}\boldsymbol{\sigma}$ and magnetostrictive strains.

Using equations (1.28) and (1.31), the magnetostrictive strain can be calculated as

$$\boldsymbol{\lambda} = \begin{Bmatrix} \frac{B_1}{c_{12}-c_{11}}\left(\alpha_1^2 - \frac{1}{3}\right) \\ \frac{B_1}{c_{12}-c_{11}}\left(\alpha_2^2 - \frac{1}{3}\right) \\ \frac{B_1}{c_{12}-c_{11}}\left(\alpha_3^2 - \frac{1}{3}\right) \\ -\frac{B_2}{c_{44}}\alpha_1\alpha_2 \\ -\frac{B_2}{c_{44}}\alpha_2\alpha_3 \\ -\frac{B_2}{c_{44}}\alpha_3\alpha_1 \end{Bmatrix}. \tag{1.40}$$

The elongation due to magnetostriction along any direction $(\gamma_1, \gamma_2, \gamma_3)$ can be evaluated using the expression

$$\begin{aligned} \frac{\delta l}{l} &= \lambda_{xx}\gamma_1^2 + \lambda_{yy}\gamma_2^2 + \lambda_{zz}\gamma_3^2 \\ &\quad + \lambda_{xy}\gamma_1\gamma_2 + \lambda_{yz}\gamma_2\gamma_3 + \lambda_{zx}\gamma_3\gamma_1, \end{aligned} \tag{1.41}$$

which becomes

$$\frac{\delta l}{l} = \frac{B_1}{c_{12} - c_{11}} \left(\gamma_1^2 \alpha_1^2 + \gamma_2^2 \alpha_2^2 + \gamma_3^2 \alpha_3^2 - \frac{1}{3} \right) - \frac{B_2}{c_{44}} \left(\gamma_1 \gamma_2 \alpha_1 \alpha_2 + \gamma_2 \gamma_3 \alpha_2 \alpha_3 + \gamma_3 \gamma_1 \alpha_3 \alpha_1 \right) \tag{1.42}$$

by substituting the expressions for λ_{ii} from equation (1.40).

The magnetostriction along the direction [100] occurs when the magnetization is along this direction. This can be calculated to be

$$\lambda_{100} = -\frac{2}{3} \frac{B_1}{c_{11} - c_{12}} \tag{1.43}$$

by using $\alpha_1 = \gamma_1 = 1$ and $\alpha_2 = \alpha_3 = \gamma_2 = \gamma_3 = 0$ in equation (1.42). Similarly, magnetostriction along [111] can be obtained to be

$$\lambda_{111} = -\frac{1}{3} \frac{B_2}{c_{44}} \tag{1.44}$$

by using $\alpha_i = \gamma_i = \frac{1}{\sqrt{3}}$ in equation (1.42).

Using equations (1.43) and (1.44), the magnetoelastic coupling constants can be expressed in terms of the magnetostriction constants and elastic constants as [1, 7]

$$B_1 = -\frac{3}{2} \lambda_{100} \left(c_{11} - c_{12} \right); \quad B_2 = -3 \lambda_{111} c_{44} \tag{1.45}$$

Substituting equation (1.45) in (1.40) and (1.42) gives

$$\boldsymbol{\lambda} = \begin{Bmatrix} \frac{3}{2} \lambda_{100} \left(\alpha_1^2 - \frac{1}{3} \right) \\ \frac{3}{2} \lambda_{100} \left(\alpha_2^2 - \frac{1}{3} \right) \\ \frac{3}{2} \lambda_{100} \left(\alpha_3^2 - \frac{1}{3} \right) \\ 3 \lambda_{111} \alpha_1 \alpha_2 \\ 3 \lambda_{111} \alpha_2 \alpha_3 \\ 3 \lambda_{111} \alpha_3 \alpha_1 \end{Bmatrix} \tag{1.46}$$

and

$$\frac{\delta l}{l} = \frac{3}{2}\lambda_{100}\left(\gamma_1^2\alpha_1^2 + \gamma_2^2\alpha_2^2 + \gamma_3^2\alpha_3^2 - \frac{1}{3}\right) + 3\lambda_{111}\left(\gamma_1\gamma_2\alpha_1\alpha_2 + \gamma_2\gamma_3\alpha_2\alpha_3 + \gamma_3\gamma_1\alpha_3\alpha_1\right) \tag{1.47}$$

respectively.

One can see that volume change due to the magnetostriction $\frac{\delta v}{v} = \lambda_{xx} + \lambda_{yy} + \lambda_{zz}$ is zero. This is the case because the higher order terms in equation (1.23) were ignored. The volume conserved magnetostriction is called Joule magnetostriction. All magnetostrictive materials, however, show some volume magnetostriction [7, 8, 12, 13] in addition to the Joule magnetostriction.

Substituting the equilibrium strains from equation (1.38) in equation (1.35) and simplifying, results in an additional anisotropy term with its anisotropy constant

$$\Delta K_1 = \frac{9}{4}\Big(\lambda_{100}^2(c_{11} - c_{12}) - 2\lambda_{111}^2 c_{44}\Big). \tag{1.48}$$

This anisotropy is called the magnetostriction induced anisotropy. Therefore, the effective magnetic anisotropy is the sum of magnetocrystalline anisotropy and magnetostriction induced anisotropy. As expected, if the magnetostriction is constrained then the magnetostriction induced anisotropy becomes zero. However, the constraint should be at length scales less than that of the exchange lengths [10]. This was experimentally verified by [14, 15].

1.3 Magnetic domains

As described in the previous section, the exchange energy results in a spontaneous magnetization of ferromagnetic materials. Because of this energy, the atomic spins are aligned parallel to each other. However, the net magnetization of the entire sample need not be magnetized to saturation. The material can split into domains with magnetization oriented in different directions. The reason behind this is: If the sample is magnetized in the same direction everywhere, the exchange energy is zero but as a result, the cost of magnetostatic energy (due to magnetic free poles on the surface) increases. Therefore, a balance is found between the exchange and magnetostatic energies. The material splits into magnetic domains. Within each domain the atomic spins are collinear but the direction is different in different domains. For example, if the material breaks into two domains as in figure 1.3b, the magnetostatic energy is halved compared to a single domain case in figure 1.3a. If the material breaks in to N domains then the magnetostatic energy reduces by $1/N$ times. However, breaking into domains costs exchange energy near the domain boundaries (domain walls) . Therefore, the material breaks into domains until an equilibrium is reached between the magnetostatic energy and magnetic domain wall energy. If the material has a cubic magnetocrystalline anisotropy or low magnetocrystalline anisotropy then closure domains can be formed resulting in zero magnetostatic energy as in figure 1.3d.

Weiss [2] proposed the existence of magnetic domains in ferromagnetic materials in 1907. Barkhausen [16] discovered in 1919 that the magnetization pro-

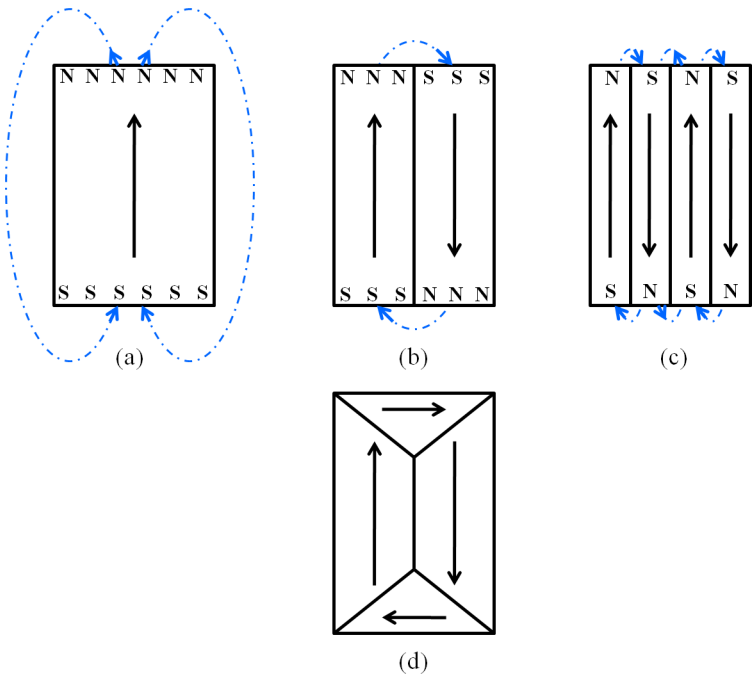

Figure 1.3: (a) Single domain with high magnetostatic energy, (b) forming two domains reduces the magnetostatic energy, (c) forming multiple domains reduces the magnetostatic energy further, (d) formation of closure domains results in zero magnetostatic energy

cess in ferromagnetic materials takes place in small discreet steps, which he called Barkhausen effect. It was thought that each step in the magnetization process corresponds to the flipping of a complete magnetic domain. Also, the magnetic domains were believed to be mesoscopic features.

Bitter [17] in 1931 made the first attempt to observe ferromagnetic domains under microscope using powder-pattern method. The observed domain patterns were maze patterns as shown in figure 1.4a, which were misinterpreted as the real domains. In 1934 Kaya [18] showed that the maze patterns were not real domains and are caused by stresses introduced during surface polishing. The true domain

structure, however, remained elusive. In 1949 Williams et al. [19] observed well-defined domain structures on a precisely cut, stress-free Fe-Si crystal as shown in figure 1.4b. Unlike maze domains the true domains are much larger in size and are

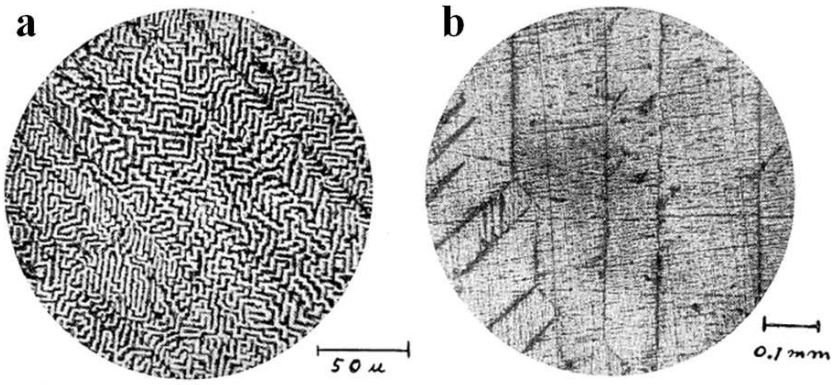

Figure 1.4: Bitter patterns in Fe-Si that is, (a) mechanically polished, (b) electrochemically polished or annealed [20].

more geometrical. Further discussion on magnetic domains is provided in Chapter 3.

1.4 Magnetostrictive materials

As discussed earlier, magnetostriction was discovered by Joule [6] in 1842 in Fe. Since then most ferromagnetic materials were discovered to demonstrate magnetostriction. Most common magnetostrictive materials include ferromagnetic materials like Fe, Ni, and Co. They have magnetostriction on the order of 10 $\mu\epsilon$ and did not have many practical applications. This, however, changed with the development of rare earth-Fe_2 alloy systems that have *giant* magnetostrictive properties. One such alloy is Terfenol-D, a Tb-Dy-Fe alloy that can generate a magnetostrictive

strain close to 2000 $\mu\epsilon$ [21–23]. Terfenol-D is being used commercially since then [24]. Although Terfenol-D exhibits giant magnetostriction, it suffers from poor tensile strength (∼30 MPa) and brittleness. As a result, its applications are limited to those involving only axial compressive forces.

Discovery of large magnetostriction in Fe–Ga alloys [25, 26] has spurred a new wave of research initiatives into magnetostrictive materials. These alloys are collectively known as Galfenol.

1.5 Iron-Gallium (Fe–Ga) alloys

For an excellent summary of the past research work on Fe–Ga, Supratik Datta's dissertation can be consulted [27]. Here only the research work pertinent to this dissertation is discussed.

Large magnetostriction was recently discovered in Fe–Ga alloys [25, 26]. It was found that like Fe-Al [28] alloys the magnetostriction significantly increases upon Ga addition to Fe. While peak magnetostriction of Fe-Al is ∼140 $\mu\epsilon$ [28], it is ∼400 $\mu\epsilon$ for Fe–Ga [26]. Such a large magnetostriction enhancement makes Fe–Ga a much more interesting alloy system. The magnetostrictive constants λ_{100} and λ_{111} of these alloys as a function of Ga at% are shown in figure 1.5. The magnetostriction of Fe–Ga alloys is an order of magnitude less than that of rare earth alloys like Tb-Dy-Fe but still large enough to be of practical use. In conjunction with their large magnetostriction, these alloys exhibit ductile-like behavior [29], high tensile strengths (∼ 400 MPa) [25, 30], low saturation fields (∼ 10 mT) [29, 31],

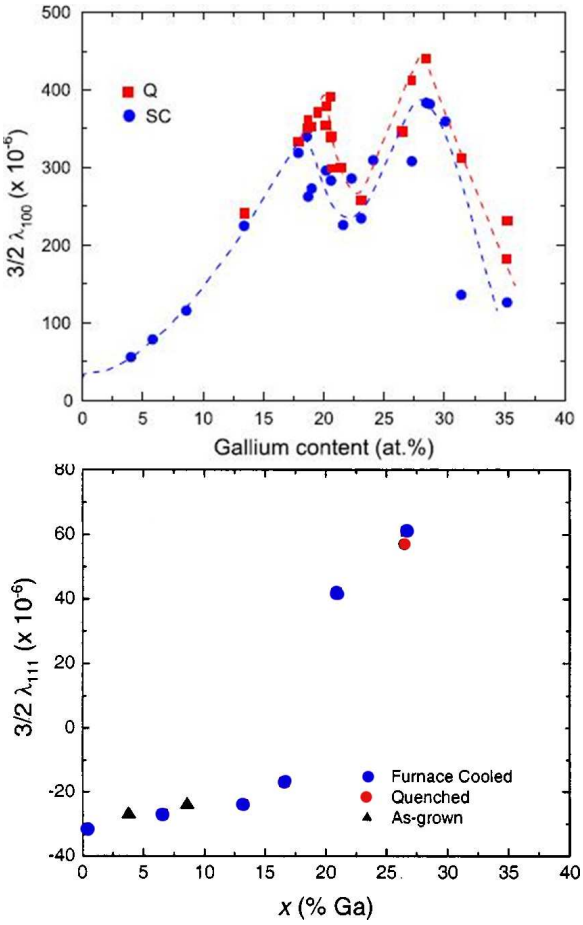

Figure 1.5: Magnetostrictive constants for Fe–Ga (single crystal) alloys for different at% Ga [26]. Two peaks in magnetostriction correspond to ∼20 at% Ga and ∼28 at% respectively.

low hysteresis [29]. Moreover, these alloys can be rolled [32, 33], machined [34], and welded [35] making it easy to manufacture these alloys into various shapes and sizes. Unlike Terfenol-D, these alloys can also be subjected to bending [27, 36–39] paving way to novel applications from macroscale [40–43] to nanoscale [37, 44–47].

Magnetostriction ($3/2\lambda_{100}$) of α-Fe increases monotonically from 36 $\mu\epsilon$ [7] to 300 $\mu\epsilon$ with a gradual addition of Ga concentration up to 17 at% Ga. Beyond this, the magnetostriction is thermal history dependent upto 25 at% Ga. While

quenching the alloy from a high temperature sustains the monotonic increase upto 20 at% Ga, slow-cooling decreases the magnetostriction beyond 17 at% Ga. Beyond 25 at%, the magnetostriction increases again with a second peak at 28 at% Ga.

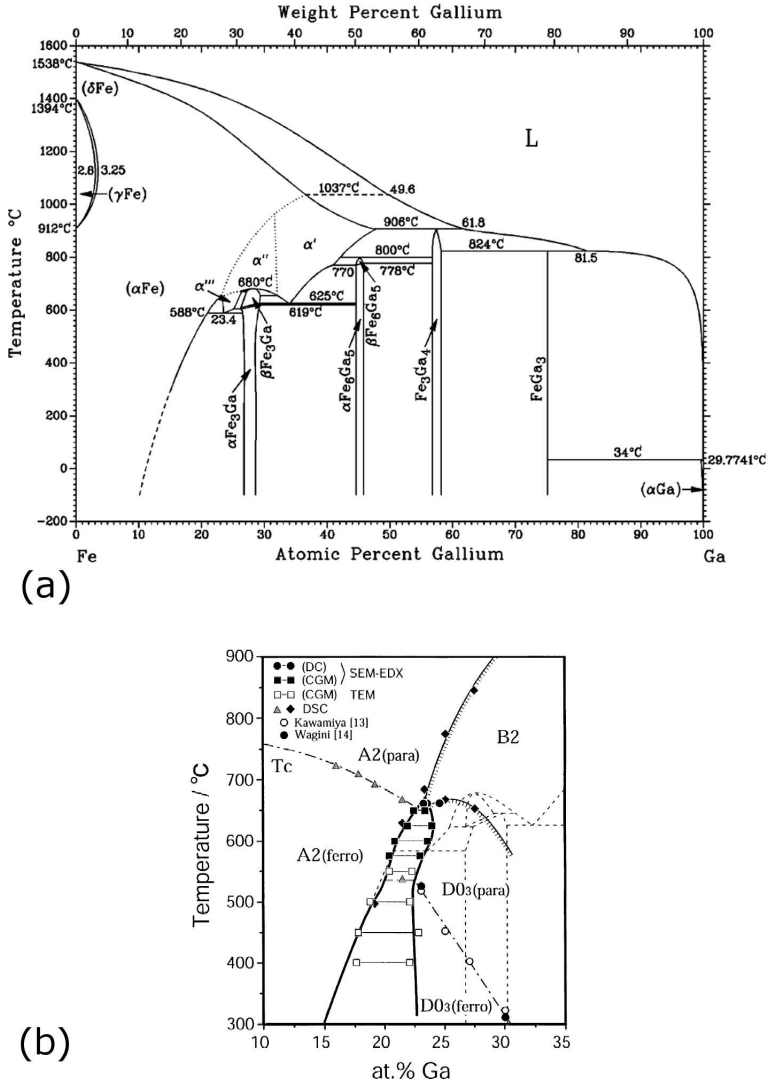

Figure 1.6: (a) Equilibrium phase diagram of Fe–Ga [48]. (b) Metastable phase diagram of Fe–Ga [49].

Figure 1.6a shows the equilibrium phase diagram [48]. At room temperature α-Fe has a body-centered cubic (BCC) or A2 crystal structure. A solid-solution of

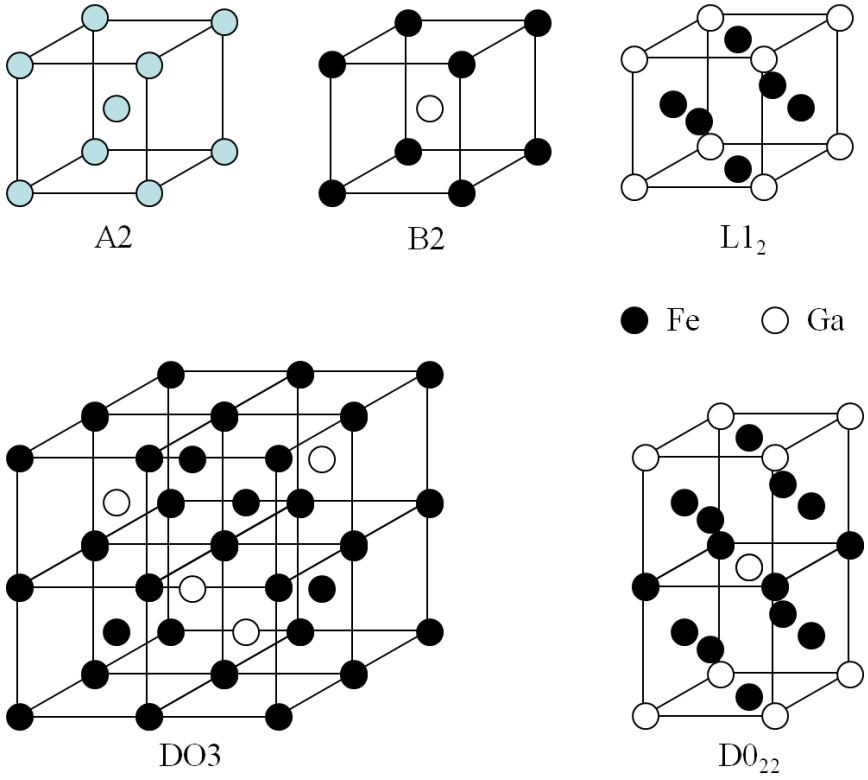

Figure 1.7: Structure of different phases in Fe–Ga

Fe and Ga forms upto 12 at% Ga, beyond which Fe–Ga alloy forms a mixture of two phases, A2 and $\alpha-Fe_3Ga$ ($L1_2$) upto 25 at%. At higher temperatures, phases like DO3, B2, $D0_{19}$ exist. The schematics showing the unit cells of these crystal structures are shown in figure 1.7.

The kinetics of equilibrium phase formations are extremely sluggish in Fe–Ga [50, 51]. For example, the formation of $D0_{19}$ and $L1_2$ phases can be easily avoided by normal cooling rates [49, 51, 52]. Therefore, the phase diagram at finite cooling rates is different from the equilibrium phase diagram. Ikeda et al. [49] evaluated the phase formation in Fe–Ga at finite cooling rates and developed the metastable phase diagram of Fe–Ga as shown in figure 1.6b. This metastable phase diagram

shows that when the alloys are cooled at nominal rates to room temperature then upto 15 at% Ga, Fe–Ga alloys make solid solutions with disordered BCC structure (A2). Beyond 15 at% Ga, DO3 begins to precipitate.

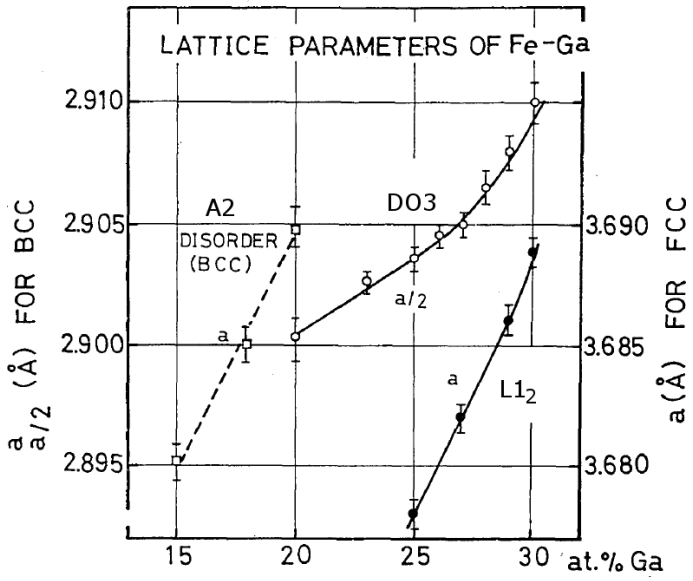

Figure 1.8: Lattice parameter of Fe–Ga [52]

Figure 1.8 shows the lattice parameter for A2, DO3, and $L1_2$ phases of Fe–Ga measured using X-ray diffraction [52]. It can be seen that the lattice parameter of all phases increase with the addition of Ga. It is interesting to note that at 20 at%, the lattice parameter of DO3 phase is less than that of A2.

The magnetic anisotropy as a function of Ga concentration was measured by Rafique et al. [53]. As shown in figure 1.9 the anisotropy contant K_1 decreases to almost zero as the first peak in magnetostriction is approached. Similarly the anisotropy constant K_2 also decreases in magnitude and becomes zero near the first peak. The elastic constants were measured by Wuttig et al. [54] and Clark et al.

[26] as shown in figure 1.10. While the tetragonal shear modulus $c' = (c_{11} - c_{12})/2$ linearly softens with increasing Ga at%, c_{44} remains more or less unchanged. Clark et al. [26] also show a linear increase in the magnetoelastic constant B_1 with the increase in Ga at% leading upto the first peak. Since the magnetostriction constant $\lambda_{100} = -B_1/3c'$ (see equation (1.45)), the dependence of magnetostriction on Ga at% leading to the first peak is quadratic. It is believed that the second peak is purely due to the softening of shear modulus [55].

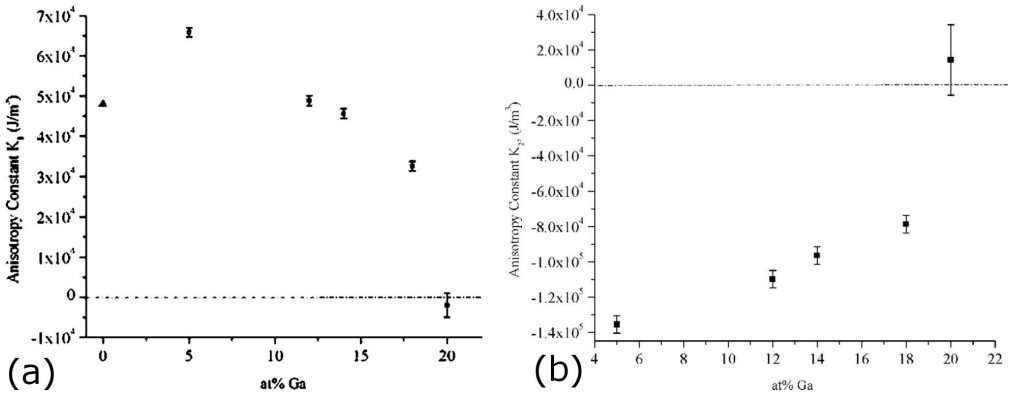

Figure 1.9: (a) Magnetic anisotropy constant K_1 and (b) Magnetic anisotropy constant K_2 as a function of Ga at% in Fe–Ga [53].

This large (more than tenfold) enhancement of magnetostriction in Fe–Ga is remarkable, especially since Ga is a nonmagnetic element. In addition to this the promising technological properties of Fe–Ga alloys stimulated intense studies focusing on elucidating the nature of the observed unusually large magnetostriction [50, 55–66]. Due to the complexity of the second magnetostriction peak, where multiple phase formations were reported [55], most of the research effort is focused on the first peak.

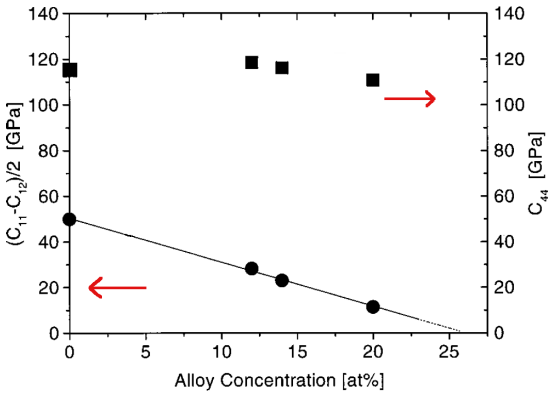

Figure 1.10: Shear elastic constants $c' = \frac{1}{2}(c_{11} - c_{12})$ and c_{44} as a function Ga at% [54]

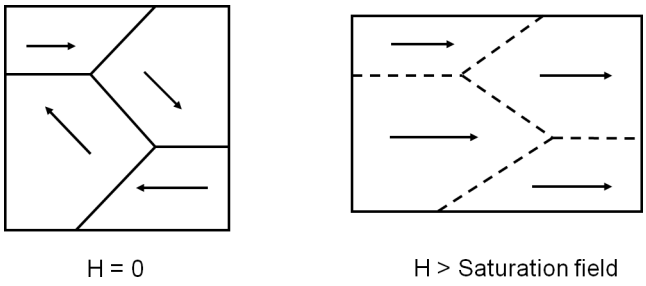

Figure 1.11: Mechanism of intrinsic magnetostriction. The magnetostriction arises within the atomic bond due to spin-orbit coupling.

Cullen et al. [56] proposed that the magnetostriction enhancement could be due to local ordering, possibly B2-like, within the disordered state. More recently, local Ga pairing was also proposed [58] to be the reason behind the decreased magnetocrystalline anisotropy (see figure 1.9) with increasing Ga composition. In this model, the magnetostriction is intrinsic to the material in a sense that the atomic bond undergoes deformation due to spin-orbit coupling. A competing idea proposed by Khachaturyan et al. [67, 68] theorizes the enhancement in the magnetostriction

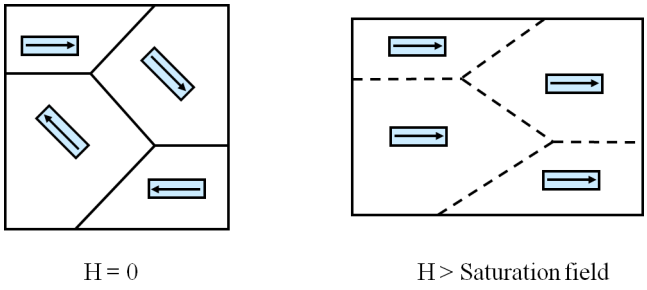

Figure 1.12: Mechanism of extrinsic magnetostriction. The magnetostriction arises due to the reorientation of tetragonal clusters in the presence of a magnetic field. The cluster shape itself is depicted to be tetragonal for illustrative purposes. The phase of the cluster is tetragonal and it can be in any shape.

to be due to tetragonal $D0_{22}$ heterogeneities. It was thought that these $D0_{22}$ heterogeneities are magnetically coupled to the matrix (A2) and the magnetostriction is a result of the heterogeneity reorientation. It was predicted that the heterogeneity results from the following series of transformations: (1) bcc $\rightarrow$ bcc$'$+ DO3 decomposition, (2) a diffusionless Bain strain transformation from DO3 to $D0_{22}$. The two competing ideas of magnetostriction in Fe–Ga are illustrated in figures 1.11 and 1.12.

Wu et al. [69, 70] showed through first principle calculations that B2-like local ordering of Ga atoms might play a crucial role in magnetostriction enhancement. Lograsso et al. [50] showed using X-ray diffraction that beyond 17 at% Ga, long range order sets in the slow-cooled samples (DO3 precipitation) and the magnetostriction goes down. Quenching the samples supresses the long range order and the high magnetostriction is sustained. It was also found that quenched samples have some short range order and it was postulated that this could be the

local ordering responsible for enhanced magnetostriction. However, the phase of this short range order could not be established owing to extremely weak anomalous reflections. Mössabauer studies [71] also found some short range order. Using Differential X-Ray Absorption Spectroscopy (DiffXAS) Pascarelli et al. [60] found that Fe-Fe bond within the vicinity of Ga-Ga pair shows an enhanced magnetostriction. However, their measured local strain of 390 $\mu\epsilon$ indicates a much lower macroscopic magnetostriction, which clearly does not agree with experimental values. X-ray synchrotron diffraction [55, 66] and X-ray diffraction [72] also showed the existence of short range ordering in quenched alloys near the first peak but their significance in magnetostriction enhancement could not be ascertained. However, Du et al. [66] found that in the quenched samples the short range order also has B2-like contributions and the average size of these clusters is 2-3 nm when the magnetostriction peaks. More recently, Zhang et al. [73] calculated the magnetostriction through first principles and showed different ordered structures for different compositions. It must be noted, however, that the first principle calculations by Wu et al. [69, 70] and Zhang et al. [73] may not be applicable to the real Fe–Ga alloys, which are disordered structures [74]. Khmelevska et al. [74] proposed that the magnetostriction in Fe–Ga could stem from a local symmetry effect. The magnetic disorder resulting from a local symmetry was thought to induce a chemical disorder.

Using High Resolution Transmission Electron Microscopy (HRTEM) Bhattacharyya et al. [59] showed the existence of heterogeneities. Through modeling, they claimed the clusters to be of $D0_{22}$-type. Their HRTEM images showed that the heterogeneities are spaced about 6 nm from each other. From magnetic domain

imaging, Bai et al. [57, 62] showed maze-like domain structure even after polishing the samples. They postulated such a domain structure to be a result of the tetragonal heterogeneity presence. More recently, Cao et al. [61] found short range ordering through neutron diffraction. They showed diffuse (100) peak that is slightly shifted towards lower q-values. They also show the (300) peak to split at 19 at% Ga concentration. They claim this to be the evidence for tetragonality and hence the short range order is $D0_{22}$ as theorized by the extrinsic model of magnetostriction.

1.6 Research objectives

An understanding of the origin of magnetostriction is clearly of high scientific and technological importance. Such an understanding will pave way to find better alloy systems with even higher magnetostriction while retaining or improving upon the good mechanical properties of Fe–Ga. However, even after years of research effort, discussed above, the origin of magnetostriction in Fe–Ga is still elusive.

One of the main shortcomings of previous research efforts is fragmentation. Due to the nature of phase mixture near the first peak that is very sensitive to composition and heat treatment, comparison study on disparate samples is often not reliable. Further, the short range order or heterogeneities were probed without applying any field. Studying their response to external magnetic and elastic fields could reveal their affect on the magnetostriction enhancement.

Therefore, the main objectives of this research is **to systematically conduct experiments on the same set of samples characterizing them at different**

length scales. To accomplish this, the following studies are conducted:

1. Characterize samples of different composition and heat treatments at macroscale, measuring their magnetostriction and reconstructing the state of the samples at remanence.

2. Study magnetic domains at remanence, under magnetic field, and under elastic field to see if the maze-like domain structure reported by Bai et al. [57, 62] gives any clues about the nature of the heterogeneities.

3. Study heterogeneities and their response to magnetic and elastic fields.

4. Identify the phase of these heterogeneities.

5. Compare all the experimental data measured at different length scales and understand the nature of heterogeneities and their affect on the magnetostriction enhancement.

To visualize heterogeneities and identify their phase, neutrons experiments were carried out. Neutrons, unlike X-rays or electrons, do not interact with the electron cloud because of their neutral charge and hence pass through bulk samples. This allows us to probe whole of samples without any sample preparation that may change the shape or size and make it difficult to compare with the macroscale characterization results. In addition, neutrons have magnetic spin ($s = \frac{1}{2}$), which makes them interact with the atomic magnetic moment, revealing precious magnetic information. Further, unlike electrons, neutrons do not get affected significantly by the applied magnetic fields, which makes it much easier to study the sample subjected to

magnetic or elastic fields. HRTEM images [59] showed that the heterogeneities were separated on average by about 6 nm. These length scales are within the regime of small-angle scattering. Therefore, small-angle neutron scattering was used to study the response of heterogeneities to magnetic and elastic fields. Neutron diffraction is used for phase identification.

Thesis organization

The sample set and their macroscopic characterization results form Chapter 2 of this dissertation. To image magnetic domains, magnetic force microscopy and Kerr microscopy were used. The description of these microscopic methods along with the results is provided in Chapter 3. Details about neutron small angle scattering and diffraction experiments along with the results are provided in Chapter 4. All the experimental results are summarized and conclusions are drawn in Chapter 5.

Chapter 2

Macroscale characterization

2.1 Overview

In this chapter, the magnetostriction of all the samples is carefully characterized with magnetic field applied along two of the in-plane easy-directions. From the magnetostriction measurements, the remanent states of the samples is estimated.

2.2 Sample specimens

All the samples were grown at the materials preparation center, AMES Lab [75]. While 15S, 18S, and 19Qe samples were cut from the ingots grown via the Bridgemann technique, 17S, 17Q, 20S, and 20Q samples were cut from the blocks grown via solid state annealing. All the samples with names ending with S are slow-cooled samples i.e., the samples were annealed at 1000 °C for 4 hours and then cooled down to room temperature at a rate of 10 °C/min. All the samples with names ending with Q are quenched samples i.e., the samples were annealed at 1000 °C for 4 hours and then water quenched to room temperature from 800 °C. The 19Qe sample was additionally electron irradiated at a flux of 3 MeV, 100 mA at 100 C for 100 min. This was done to enhance the defect concentration that is thought to aid the formation of nanoscale D022 tetragonal heterogeneities [67, 68]. All the

samples except the 15S are rectangular. The rectangular samples were cut such that their axes are collinear to the $\langle 1\,0\,0 \rangle$ crystallographic directions. The 15S sample was cut from the ingot at UMD. The orientation of the disk plane is already known from the orientation determination done by AMES labs. However, the orientation within the plane was not known. Since we know that for 15 at% Ga composition, $\langle 1\,0\,0 \rangle$ are the easy axes, a small magnetic field, below the saturation magnetic field, was applied along different directions within the plane and then the magnetization along that direction was measured using VSM. It can be seen from figure 2.1 that the maximum magnetization is along a direction 30 degrees anti-clockwise from the reference direction. Therefore, it was determined that this direction is the $[1\,0\,0]$. These results were further corroborated by measuring the orientation using Electron Back Scatter Detector (EBSD), which also showed the $[1\,0\,0]$ direction to be 30 degrees anti-clockwise from the reference direction.

Next, composition of all the samples was determined by Electron Dispersion Spectroscopy (EDS) at the UMD nanocenter. The composition was determined at more than 5 points on one of the surfaces and the average composition was determined. Table 2.1 shows the composition, standard deviation, heat treatment and dimensions of all the samples.

2.3 Magnetization

A vibrational sample magnetometer (VSM) was used to measure the magnetization of the samples. Samples were attached to a long rod that vibrates in the

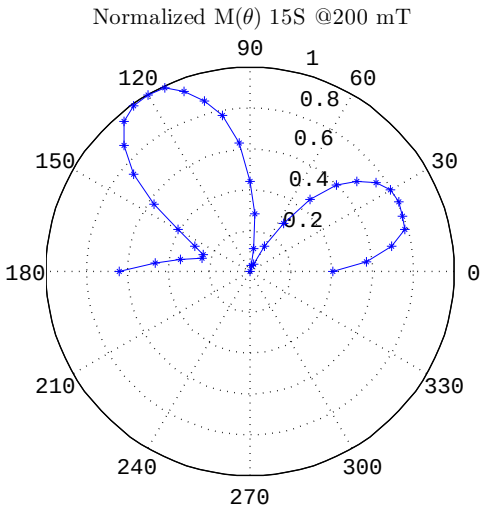

Figure 2.1: Magnetization of 15S vs. azimuthal angle

Table 2.1: Sample specimens

Sample	Avg Ga at%	Std deviation	Heat Treatment	Dimensions (mm^3)
15S	15.3	0.53	Slow cooled	$11\phi \times 1.2$
17S	17.5	NA	Slow cooled	$18.5 \times 14.5 \times 1.5$
17Q	17.3	0.43	Quenched	$20 \times 13 \times 1.3$
18S	18.1	0.56	Slow cooled	$12 \times 8.5 \times 1.8$
19Qe	19	0.53	Quenched	$25 \times 12 \times 0.5$
20S	19	0.6	Slow cooled	$18 \times 11 \times 0.7$
20Q	19.4	0.51	Quenched	$18 \times 11 \times 0.7$

presence of a magnetic field. The current induced in the coil due to the vibration of a magnetized sample gives a measure of the magnetization of the sample. For all

the measurements, a field ramp rate of 0.5 mT/s was used and the magnetization was measured point-by-point averaging over 10 seconds at each field point.

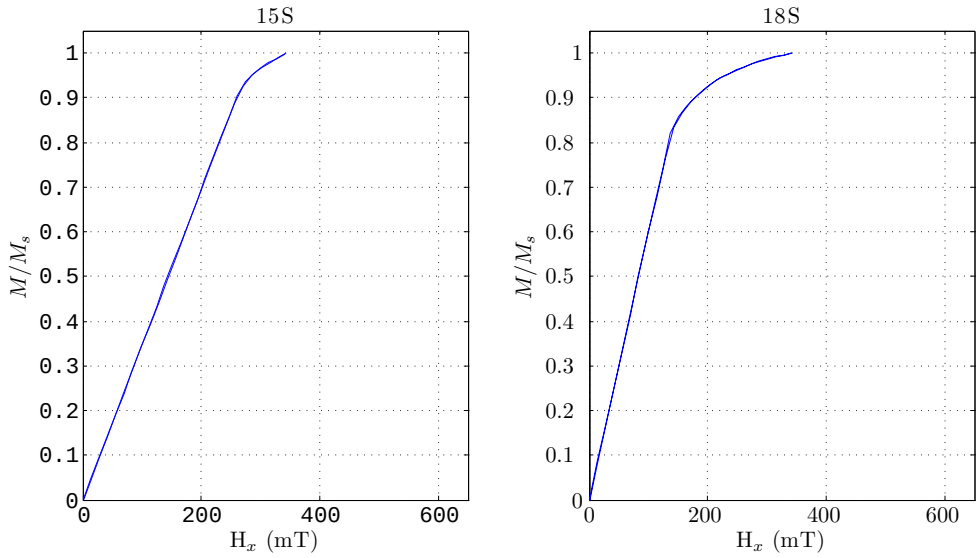

Figure 2.2: Magnetization of 15S (left) and 18S (right)

Figure 2.2 shows the magnetization of 15S (left) and 18S (right) samples. These two samples are the smallest in volume compared to the rest of the samples. However, they are still able to produce a large moment resulting in a high magnetic force. So, both the samples moved toward one of the magnetic poles at higher magnetic fields, bending the vibrating rod.

19Qe sample is larger than 15S or 18S samples. Therefore, to avoid any sample movement toward the poles, away from the saddle point, a smaller sample ($\phi = 3$ mm disk) was cut out from the ingot from which 19Qe was cut. It was ensured that the 3 mm disk was cut adjacent to the 19Qe so that there is minimal compositional variation between the two. Figure 2.3 (left) shows the magnetization of this 3 mm

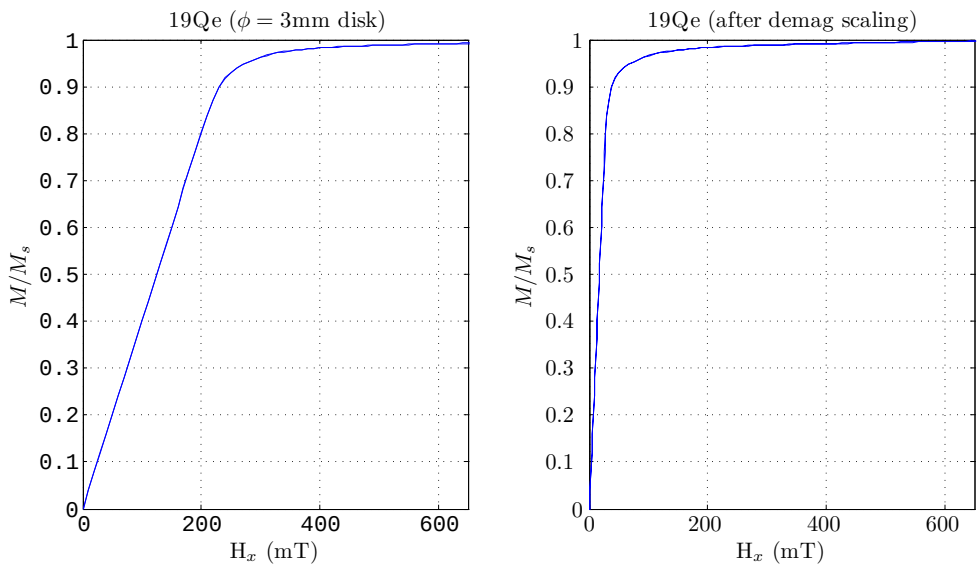

Figure 2.3: Magnetization of 19Qe

sample. Since this 3 mm sample is dimensionally different from the 19Qe, they each have different demagnetization factors. Therefore a FEM model was used to estimate the demagnetization field of both the samples. The demagnetization factor along $\boldsymbol{hatx}$ was calculated to be 0.1455 for the 3 mm disk and 0.0157 for the 19Qe. In figure 2.3 (right), the magnetization of the 3 mm sample is scaled using the demagnetization factors of 3 mm and 19Qe samples to estimate the magnetization of the 19Qe sample. It can be seen that the magnetostriction of the 19Qe in figure 2.9 and the estimated magnetization of the 19Qe in figure 2.3 (right) saturate at more or less the same magnetic field.

From M-H curves of 15S, 18S, and 19Qe samples, it can be seen that the hysteresis in these samples is almost negligible. For example, the coercivity of the 19Qe was 0.2 mT and the remanent magnetization was $\sim$ 5 mT. So, Fe–Ga is

magnetically very soft.

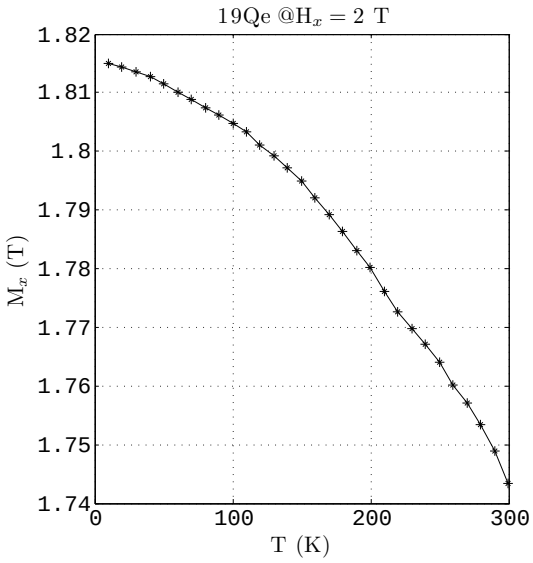

Figure 2.4: Magnetization vs Temperature @$H_x = 2$ T for 19Qe

Another 2 mm disk was cut from the 19Qe sample and the magnetization of this sample was measured from room temperature to 10 K using a SQUID. Figure 2.4 shows the magnetization vs. temperature. As expected [1, 4], the magnetization increases as the temperature decreases.

2.4 Magnetostriction

2.4.1 Experimental procedure

A coordinate system was chosen such that the x-, y-, and z axes correspond to [1 0 0], [0 1 0], and [0 0 1] of the samples respectively. An electromagnet was used to apply magnetic field up to 0.8 T. A bidirectional resistive strain gage rosette

was used to measure strain along x- and y-directions. The field was ramped up from ~ 0.1 mT (remanent field) to 650 mT and then down to ~ 0.1 mT at a rate of $\sim \pm 10$ mT/s. Data was acquired using National Instruments DAQ board and LabView software.

Throughout this dissertation, λ_j^i means magnetostrictive strain along direction $\hat{\mathbf{j}}$ due to the magnetic field along direction $\hat{\mathbf{i}}$. If $\hat{\mathbf{i}}$ and $\hat{\mathbf{j}}$ are easy axes then λ_i^i represents $\lambda \parallel H$ and $\lambda_{j\neq i}^i$ represents $\lambda \perp H$.

2.4.2 Remanent state calculation

From the magnetostriction measurements the magnetization distribution at remanence can be estimated. If a, b, and c are the fractions of magnetic moments oriented along $\hat{\mathbf{x}}$, $\hat{\mathbf{y}}$, and $\hat{\mathbf{z}}$ respectively, then $a+b+c = 1$ and $a, b, c \geq 0$. In a perfectly demagnetized sample, $a = b = c = 1/3$. Assuming volume magnetostriction $\lambda_v = 3v\lambda$ for simplicity, the in-plane magnetostrictions can be defined in terms of the initial magnetic moment distribution as following:

$$\lambda_x^x = b\lambda + c\lambda + v\lambda$$

$$\lambda_y^x = -b\lambda + v\lambda$$

$$\lambda_y^y = a\lambda + c\lambda + v\lambda$$

$$\lambda_x^y = -a\lambda + v\lambda.$$

From the above equations,

$$\lambda = \lambda_x^x - \lambda_x^y = \lambda_y^y - \lambda_y^x.$$

Therefore, λ is taken as $((\lambda_x^x - \lambda_x^y) + (\lambda_y^y - \lambda_y^x))/2$.

Reducing the above equations such that they are linearly independent gives:

$$b + c + v = p = \lambda_x^x/\lambda = \lambda_x^y/\lambda + 1 \tag{2.1a}$$

$$-b + v = q = \lambda_y^x/\lambda = \lambda_y^y/\lambda - 1 \tag{2.1b}$$

$$a + b + c = 1, \tag{2.1c}$$

where p and q are calculated as $p = (\lambda_x^x/\lambda + \lambda_x^y/\lambda + 1)/2$ and $q = (\lambda_y^x/\lambda + \lambda_y^y/\lambda - 1)/2$. At least one more independent measurement is necessary to obtain a unique solution. In the absence of such a measurement a range of solutions can be obtained as follows

$$\max\{0, (p-1), q\} \leq v \leq (p+q)/2. \tag{2.2}$$

Choosing a given value of v from equation (2.2),

$$a = 1 - p + v \tag{2.3a}$$

$$b = v - q \tag{2.3b}$$

$$c = p + q - 2v. \tag{2.3c}$$

2.4.3 Results and Discussion

Figures 2.9 - 2.11 show the magnetostriction data for all the samples obtained using an automated LabVIEW data acquisition program.

In a perfectly demagnetized sample and in the absence of any residual stress, λ_x^x and λ_y^y are always $2/3\lambda$, meaning the remanent states $a = b = c = 1/3$. However, this is not observed in all the samples. Since the hysteresis in the magnetostriction

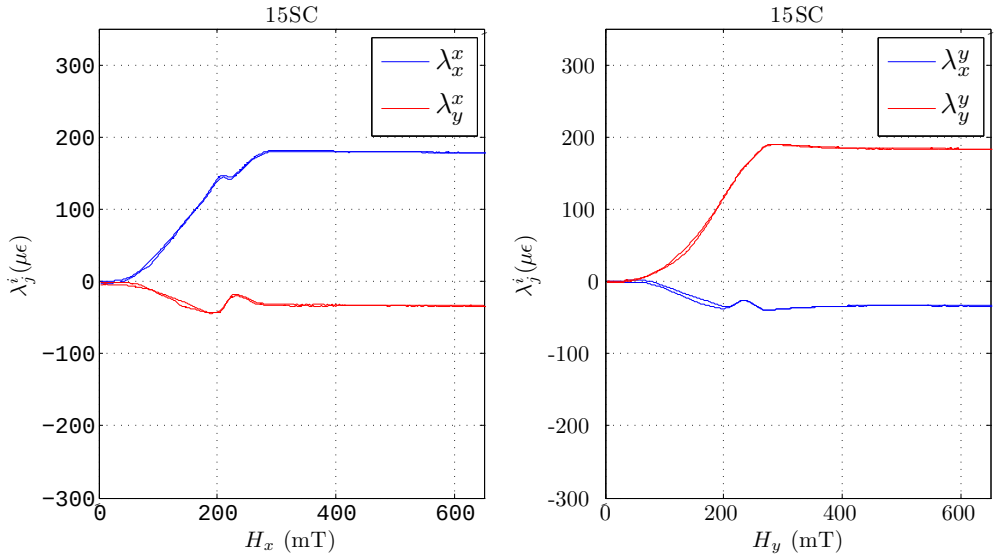

Figure 2.5: Magnetostriction of 15S under H applied along $\hat{\boldsymbol{x}}$ (left) and $\hat{\boldsymbol{y}}$ (right)

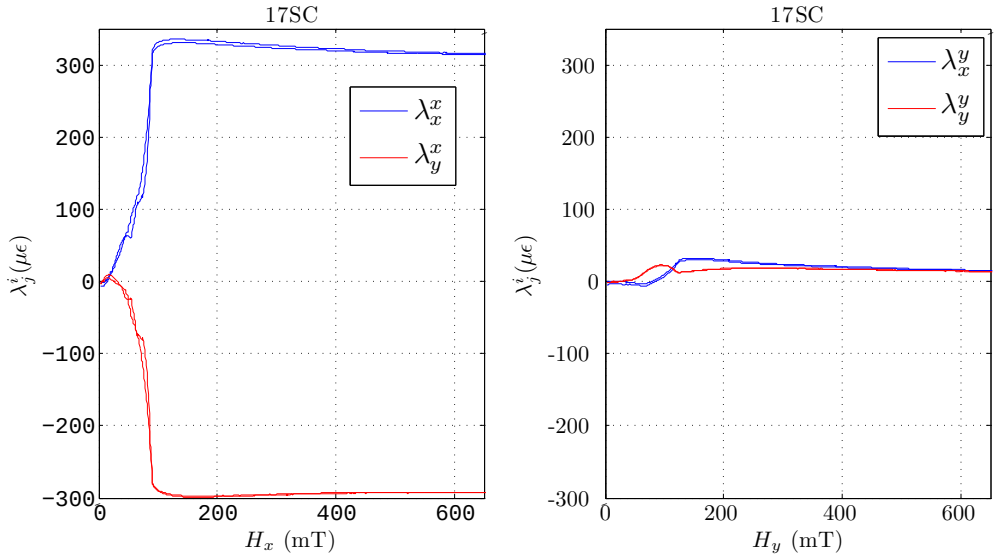

Figure 2.6: Magnetostriction of 17S under H applied along $\hat{\boldsymbol{x}}$ (left) and $\hat{\boldsymbol{y}}$ (right)

data is almost negligible, the deviation can be attributed to some anisotropy, either due to shape or the presence of a residual stress.

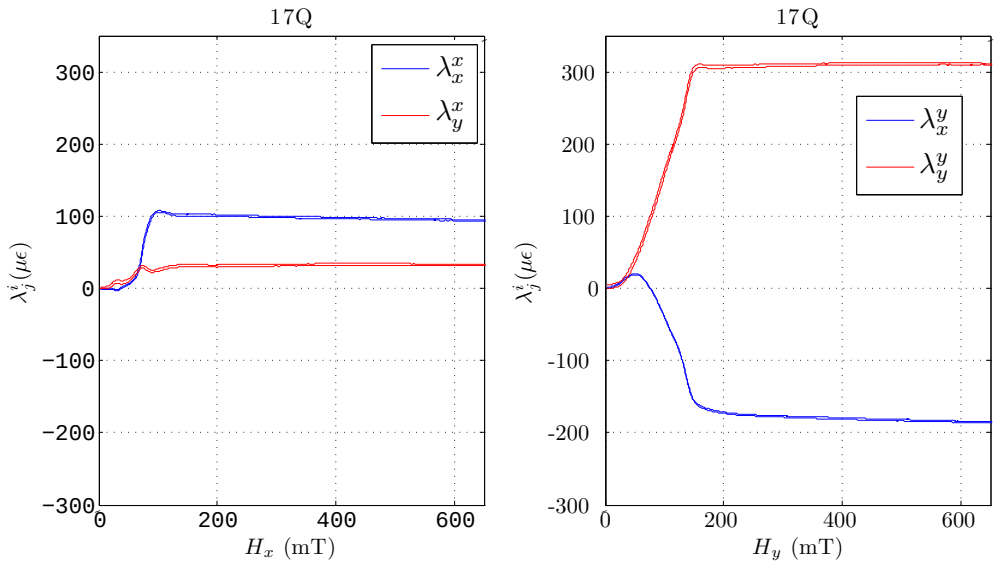

Figure 2.7: Magnetostriction of 17Q under H applied along $\hat{\boldsymbol{x}}$ (left) and $\hat{\boldsymbol{y}}$ (right)

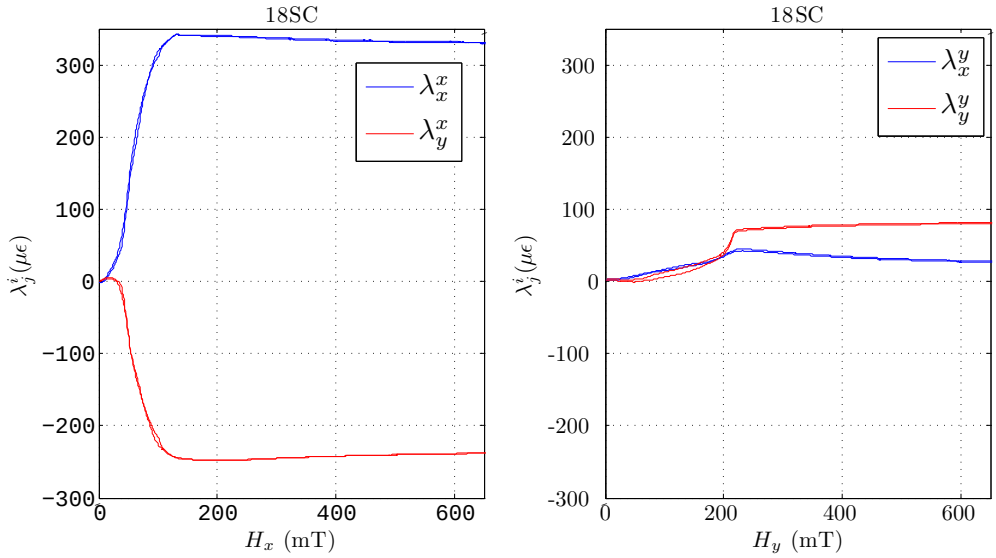

Figure 2.8: Magnetostriction of 18S under H applied along $\hat{\boldsymbol{x}}$ (left) and $\hat{\boldsymbol{y}}$ (right)

Of at most interest is sample 17S that shows 100% magnetization oriented along $\pm\hat{\boldsymbol{y}}$ at remanence. This is extraordinary because attempts have been made

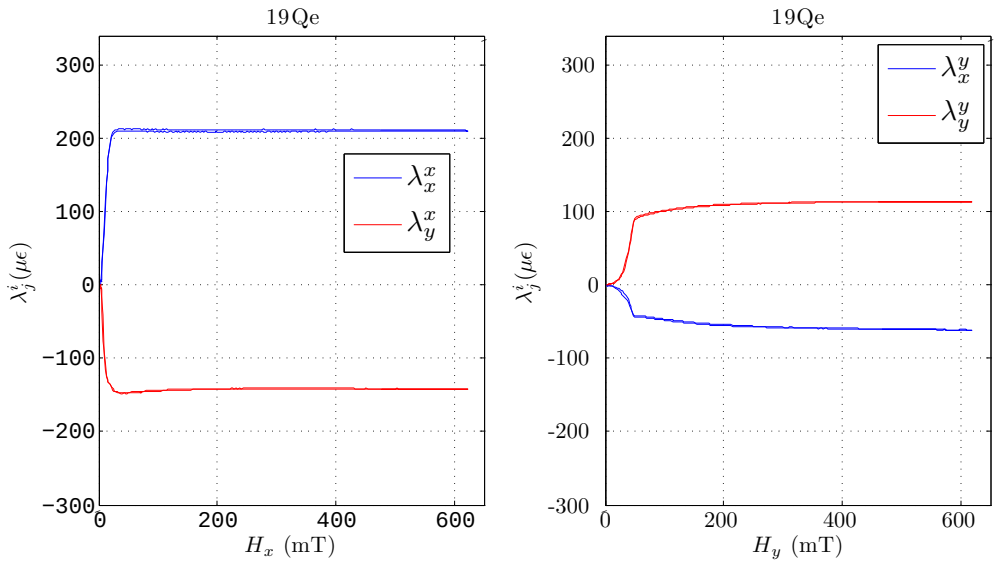

Figure 2.9: Magnetostriction of 19Qe under H applied along $\hat{\boldsymbol{x}}$ (left) and $\hat{\boldsymbol{y}}$ (right)

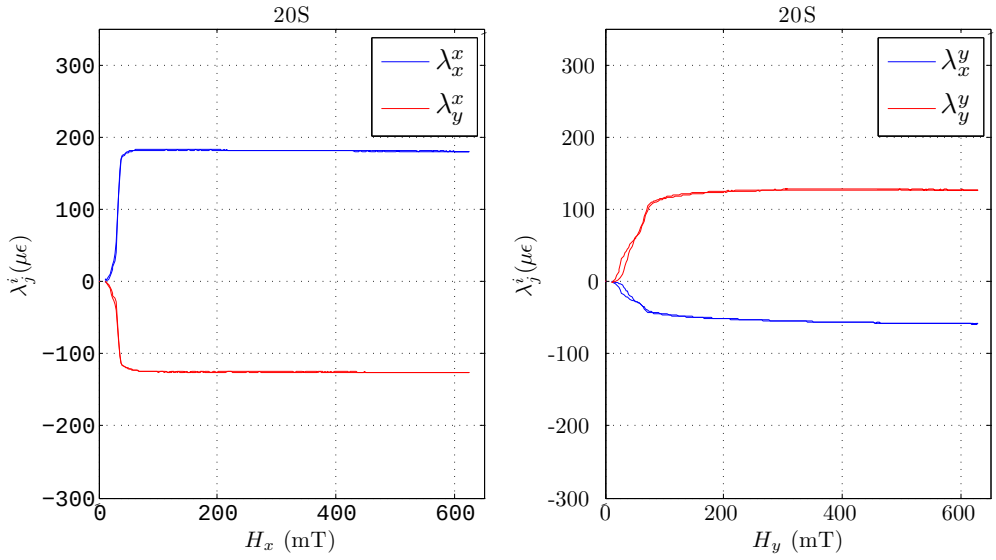

Figure 2.10: Magnetostriction of 20S under H applied along $\hat{\boldsymbol{x}}$ (left) and $\hat{\boldsymbol{y}}$ (right)

to induce an anisotropy in Fe–Ga either by magnetic field annealing [76] or stress annealing [77, 78] but such an anisotropy has not previously been observed in an

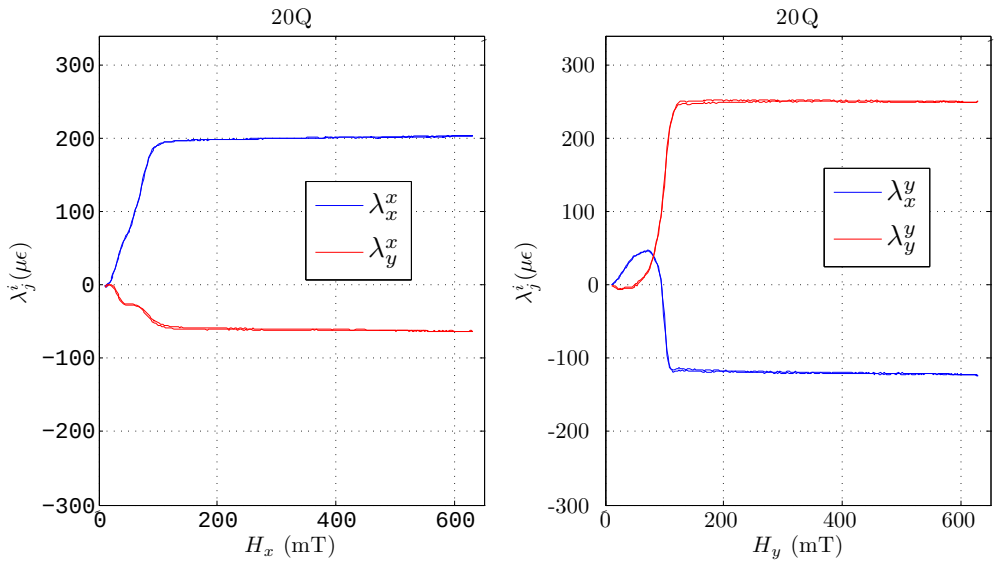

Figure 2.11: Magnetostriction of 20Q under H applied along $\hat{\boldsymbol{x}}$ (left) and $\hat{\boldsymbol{y}}$ (right)

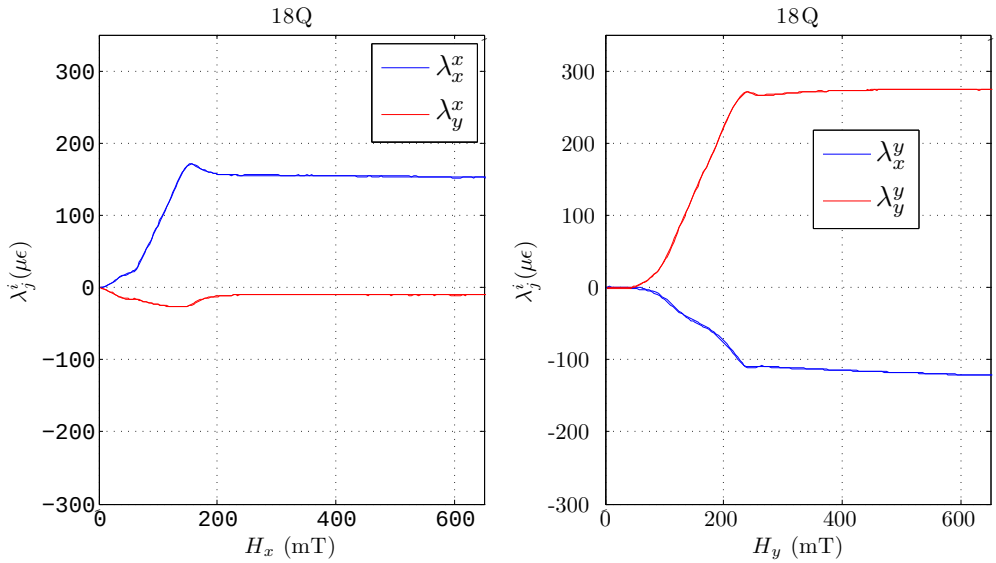

Figure 2.12: Magnetostriction of 18Q under H applied along $\hat{\boldsymbol{x}}$ (left) and $\hat{\boldsymbol{y}}$ (right)

as-grown sample, i.e. one that has not undergone processes designed to selectively develop such an anisotropy. The reason for this is unclear. It is thought that the

DC heating coil used for annealing this sample might have caused the magnetic field annealing effects. However, it could not be reproduced. In that sense, this sample is quite unique. It is important to note that such an anisotropy at remanence is shown not only by 17S but also by other samples, especially 17Q, 18S, and 20S.

In order to see if re-annealing the sample can remove the anisotropy and "reset" the sample, 18S was annealed at 1000 °C for four hours and then water quenched from 800 °C to room temperature. Figure 2.12 shows the magnetostriction measurement after re-annealing 18S sample. Calculating the remanent states now show $a \in [0.46\ 0.71]$, $b \in [0.03\ 0.29]$, and $c \in [0\ 0.51]$. The anisotropy that is still present can be explained to be due to the shape of the sample. The magnetostatic energy or the shape anisotropy also has a profound influence on the remanent states.

The values for λ_x^x, λ_y^x, λ_x^y, λ_y^y, and λ are given in table 2.2. Using equations (2.3a) - (2.3c), contribution of the volume magnetostriction to the linear magnetostriction, $v\lambda$ and the remanent states a, b, c are listed in table 2.3.

2.5 Summary

The macroscopic characterization of all the samples was performed. This is essential because every sample is unique in its own way. The remanent state of the sample perhaps depends on many parameters and it is very difficult to produce two samples that are identical in every aspects. Therefore, characterizing every sample - composition, magnetostriction, magnetization - is very important. These results form a basis for the analysis of measurements in Chapters 3 and 4.

Table 2.2: Magnetostriction at $H = 800$ mT

Sample	λ_x^x	λ_y^x	λ_y^y	λ_x^y	λ
15S	177 ± 1	-35 ± 1	181 ± 1	-35 ± 1	215 ± 2
17S	312 ± 1	-295 ± 1	12 ± 1	12 ± 1	303 ± 2
17Q	92 ± 1	31 ± 1	310 ± 1	-189 ± 1	280 ± 2
18S	331 ± 1	-237 ± 1	83 ± 1	25 ± 1	312 ± 2
18Q	150 ± 1	-11 ± 1	274 ± 1	-125 ± 1	280 ± 2
19Qe	212 ± 1	-143 ± 1	115 ± 1	-62 ± 1	266 ± 2
20S	183 ± 1	-127 ± 1	128 ± 1	-59 ± 1	248 ± 2
20Q	203 ± 1	-63 ± 1	249 ± 1	-119 ± 1	317 ± 2

Table 2.3: Remanent states

Sample	$v\lambda^*(\mu\epsilon)$	a^*	b^*	c^*
15S	[0 72]	[0.17 0.50]	[0.16 0.5]	[0 0.67]
17S	[10 10]	[0 0]	[1 1]	[0 0]
17Q	[30 61]	[0.78 0.89]	[0 0.11]	[0 0.22]
18S	[21 50]	[0 0.1]	[0.81 0.9]	[0 0.19]
18Q	[0 72]	[0.46 0.71]	[0.03 0.29]	[0 0.51]
19Qe	[0 31]	[0.22 0.33]	[0.55 0.67]	[0 0.23]
20S	[0 31]	[0.25 0.38]	[0.5 0.62]	[0 0.25]
20Q	[0 67]	[0.37 0.58]	[0.21 0.42]	[0 0.43]

* [min max]

Chapter 3

Magnetic domains

3.1 Overview

In this chapter, magnetic domain imaging using magnetic force microscopy (MFM) and Kerr microscopy is discussed. Domains were imaged both at remanence as well as under externally applied magnetic and elastic fields. In section 3.2, a background is given highlighting the expected domain patterns in these alloys and discussing the domain imaging published in the literature. In subsequent sections, the results from magnetic domain studies at remanence, under magnetic field, and under elastic field are provided.

3.2 Background

In cubic materials with $K_1 > 0$ ($\langle 100 \rangle$ are the easy axes), such as Fe, Fe-Si, or Fe-Al, there are two kinds of magnetic domain walls: 180° walls separating two domains for e.g. [100]/[$\bar{1}$00] domains with magnetization anti-parallel to each other, and 90° walls separating two domains for e.g. [100]/[010] whose magnetizations are at right angles. In cubic materials with $K_1 < 0$ ($\langle 111 \rangle$ are the easy axes), there are three kinds of magnetic domain walls: 180°, 109°, and 71°. It is common to classify all domain walls other than 180° walls as 90° walls [1]. If one considers a

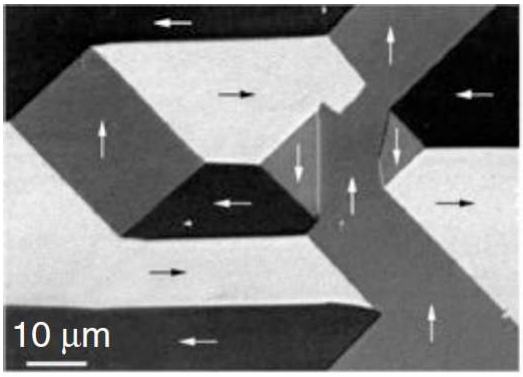

Figure 3.1: Magnetic domains on (001) Fe-3 at% Si showing 180° separating [100]/[$\bar{1}$00]-type domains and 90° domain walls separating [100]/[010]-type domains. Taken from [79].

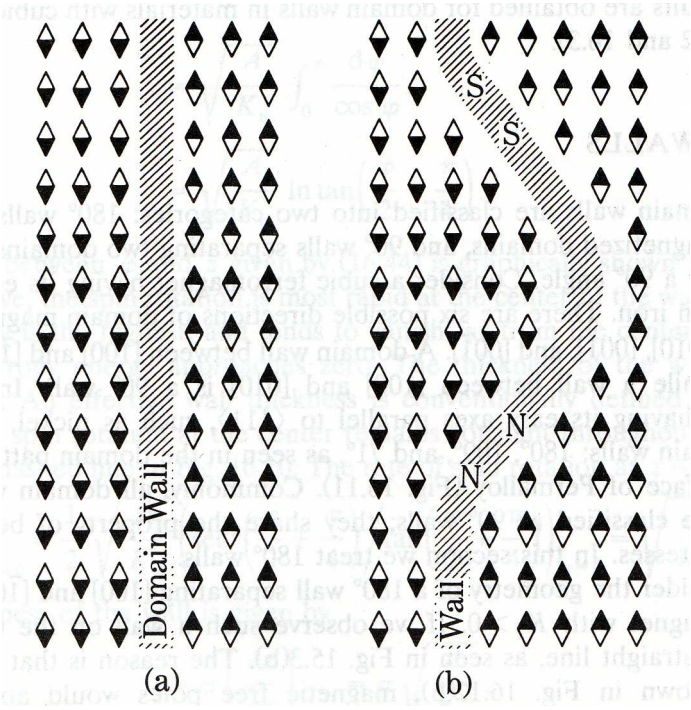

Figure 3.2: (a) Straight 180° domain wall leads to minimal magnetostatic energy (b) 180° domain wall that is not straight costs magnetostatic energy [1].

180° wall in a cubic material with $K_1 > 0$ separating [100] and [$\bar{1}$00] domains on a (001) surface, figure 3.2 shows why these domain walls are straight. If the wall is curved as in figure 3.2b, magnetic free poles would appear along the curved portion of the wall, giving rise to a demagnetizing field opposite to the magnetization of the domains. To reduce the magnetostatic energy arising out of a curved wall, the 180° wall straightens as in figure 3.2a. When a 180° wall is viewed from a

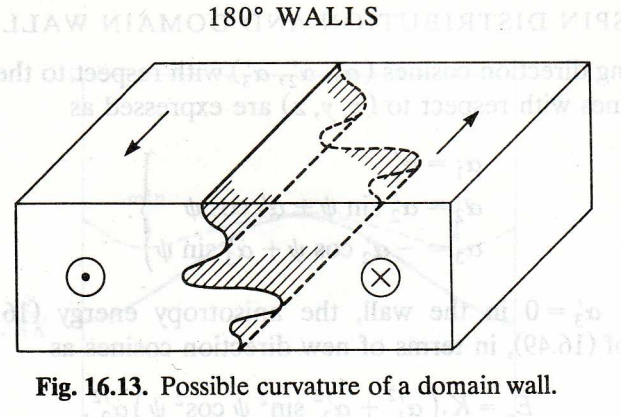

Fig. 16.13. Possible curvature of a domain wall.

Figure 3.3: Possible curvature of a 180° domain wall in a material with uniaxial anisotropy [1].

direction parallel to the domain magnetization, the wall may be curved as shown in figure 3.3. This is possible because the curvature does not result in any magnetic free poles. The curvature, however, increases the total surface area of the domain wall thus increasing the wall energy. Therefore, such curved domain walls form only when the additional energy can be sustained. Possible reasons for sustaining curvature in the domain walls include the presence of inclusions or voids, irregular distribution of internal residual stresses, and the dependence of the wall energy on the crystallographic directions. One such example is the maze domain structure in

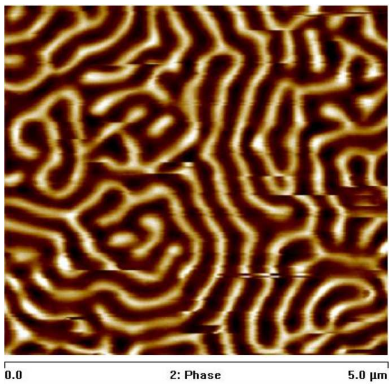

Figure 3.4: Maze domain structure with curved domain walls in polycrystalline Ni thin film with out-of-plane anisotropy [80].

polycrystalline Ni thin film with out-of-plane anisotropy, shown in figure 3.4. The curved domain walls are 180° walls separating domains with magnetization aligned out-of- and into- plane.

Figure 3.5: *Fir tree* magnetic domain pattern in (100) Fe-Al that is slightly mis-oriented [81].

Also, a slight misorientation of the crystal plane relative to the surface being observed can change the magnetic domain pattern [79]. For example, figure 3.5 shows the magnetic domain pattern on a (100) surface of Fe-Al [81] that is slightly

mis-oriented. This domain pattern is called *fir tree* pattern that forms near a 180° domain wall. There are several such domain patterns that can form on the mis-oriented surfaces. For more details, refer to [79].

3.2.1 Magnetic Force Microscopy (MFM)

Magnetic Force Microscopy or MFM is a scanning technique to image spatial variation of magnetic forces on a sample's surface. Under appropriate conditions, this allows magnetic domain imaging. A cantilever with tip coated with ferromagnetic material, typically Co/Cr, is used under close proximity to the surface intended for the investigation. There are two interaction forces between the tip and the surface - van der Waals force and magnetic force. Typically, van der Waals forces dominate as the tip gets closer (< 50 nm usually) to the sample giving topographic information. Increasing the distance from the sample surface weakens the van der Waals interaction and beyond a critical distance (above 50 nm) magnetic forces dominate. Therefore, MFM scanning mode is also sometimes called the "lift height" method. The topographic profile of the surface is first measured by scanning the tip at close proximity and then in the second pass, the magnetic information is recorded by lifting the tip a certain height above the surface.

The magnetic information can be extracted in a static mode or dynamic mode. In static mode, the tip displacement due to magnetic forces is measured. A more sensitive method utilizes the dynamic properties of the tip [82]. In this method, the

cantilever is oscillated (by a piezoelectric bimorph) near its resonant frequency

$$\omega_0 = \sqrt{\frac{k}{m}}. \tag{3.1}$$

When the tip comes under the influence of a force, F, then the vertical component of the force gradient, $\partial F/\partial z$ is detected by the microscope. Under this approximation, the cantilever can be considered to behave, under the influence of the tip-sample interaction force, as if it had a modified spring constant

$$k_F = k - \frac{\partial F}{\partial z}. \tag{3.2}$$

This change in the spring constant of the cantilever modifies its resonant frequency to

$$\omega = \omega_0 \sqrt{1 - \frac{1}{c}\frac{\partial F}{\partial z}}. \tag{3.3}$$

Assuming $\partial F/\partial z \ll k$, the shift in resonant frequency can be given by

$$\Delta\omega \approx -\frac{1}{2c}\frac{\partial F}{\partial z}. \tag{3.4}$$

A change in the resonant frequency changes the tip's oscillation amplitude as well as the phase shift, which can be measured. In this dissertation, the phase shifts are used to image the magnetic domains.

MFM offers a very high magnetic spatial resolution $\sim$ 30 nm [82]. However, it is a scanning technique and hence it is inherently slow. As the scanning area increases, the scanning time increases as well. Moreover, the maximum area that is possible to scan is $\sim$ 100 μm. Therefore, MFM is suitable to image thin films, nanoparticles, nanowires, and bulk materials in which domain sizes are typically less than 100 μm.

3.2.2 Kerr microscopy

3.2.2.1 Magneto-Optic Kerr effect

Kerr effect [83], named after John Kerr, is one of the several magneto-optical effects [79]. When a plane-polarized light is reflected off of a magnetized surface, the polarization rotates by an angle known as Kerr angle. It can be phenomenologically described by

$$\boldsymbol{D} = \epsilon(\boldsymbol{E} + iQ_K \boldsymbol{m} \times \boldsymbol{E}), \tag{3.5}$$

where $\boldsymbol{\epsilon}$ is the dielectric constant, Q_K is a material parameter that describes the strength of the Kerr effect. The vector $\boldsymbol{D}$ can be interpreted as secondary light amplitude being generated by the magneto-optical interaction of the electrical vector $\boldsymbol{E}$ of the illuminating plane light wave with the magnetization vector $\boldsymbol{m}$ of the sample.

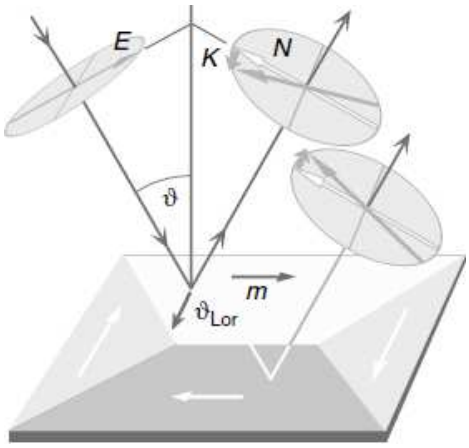

Figure 3.6: Illustration of the elementary magneto-optical interaction for the longitudinal Kerr effect. The sample with in-plane magnetization is illuminated using light that is polarized parallel to the plane of incidence. Taken from [79].

When the light wave is incident on the magnetic sample, electrons are set in vibration motion. The Lorentz force ($\boldsymbol{m} \times \boldsymbol{E}$) on the electrons results in the Lorentz movement, ϑ_{Lor}. If this Lorentz movement is projected onto the plane perpendicular to the direction of propagation of the reflected light, the magneto-optical amplitude or Kerr amplitude $\boldsymbol{K}$ is obtained. This Kerr amplitude is polarized perpendicular to the regular reflected amplitude $\boldsymbol{N}$ that is polarized in the same plane as the incident light. The interference of $\boldsymbol{K}$ and $\boldsymbol{N}$ results in the rotation of the polarization vector by $\Phi_K = |\boldsymbol{K}|/|\boldsymbol{N}|$, which, by using an analyzer, leads to the domain contrast.

There are different configurations of Kerr microscopy based on different geometries that result in being sensitive to different directions of magnetizations. All these geometries can be derived from the knowledge of the Lorentz movement. An appropriate direction of the incident light needs to be selected for a given magnetization direction to produce a Lorentz movement leading to a measurable Kerr rotation. Kerr rotation is proportional to the magnetization component parallel to the reflected beam of light. When the polarizer is set to either parallel or orthogonal to the incidence plane and $\vartheta \neq 0$, the configuration is called *longitudinal* Kerr effect (figure 3.6). In such configuration, the Kerr amplitude is proportional to the sine of the angle of incidence, $\sin(\vartheta)$. Therefore, if the magnetization lies within the surface as in figure 3.6, the maximum Kerr amplitude is obtained if the plane of incidence is parallel to the direction of magnetization and the Kerr amplitude disappears for perpendicular incidence. Hence, longitudinal Kerr effect with oblique incidence is used to image such domains. Perpendicular incidence ($\vartheta = 0$), also known as *polar* Kerr effect, can be used to image domains that are magnetized perpendicular to the

sample surface.

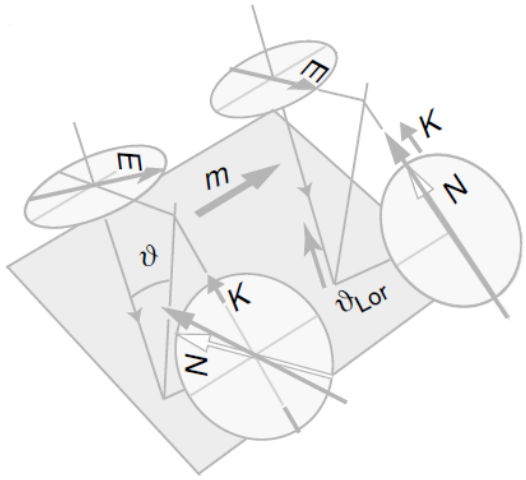

Figure 3.7: Illustration of the elementary magneto-optical interaction for the transverse Kerr effect. The sample with in-plane magnetization is illuminated using light that is polarized at 45° to the plane of incidence. Taken from [79].

In *transverse* Kerr effect, as shown in figure 3.7, the in-plane magnetization is normal to the plane of incidence. Light with $\boldsymbol{E}$ parallel to this plane generates a Kerr amplitude but it is in the same direction as $\boldsymbol{N}$, the normally reflected beam. This only generates an amplitude variation and no rotation. If the polarization of the incident light is at 45° to the plane of incidence, then the component of $\boldsymbol{E}$ perpendicular to the incidence plane is not affected and the component parallel to the incidence plane is modulated in its amplitude upon reflection. By superposition, this results in the rotation of the polarization leading to the in-plane magnetization sensitivity.

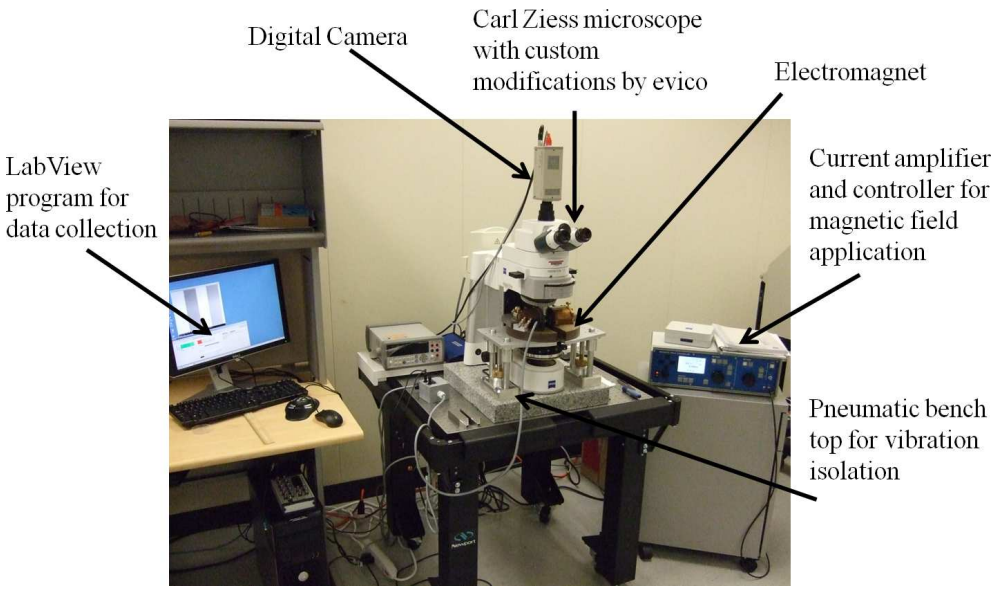

Figure 3.8: Kerr microscope setup

3.2.2.2 Wide-field Kerr microscopy

Wide-field Kerr microscopy is most versatile technique for magnetic domain visualization, especially because it is real-time, non-invasive, and high contrast method. Figure 3.8 shows the wide-field Kerr microscope that has been assembled by Evico Magnetics GmbH. Optical illumination is used and the microscope has a field of view from several mm down to μm using objective lenses from 5× to 100×. A rotatable electromagnet is capable of applying magnetic fields in-plane up to 1 T. A CCD camera is used to obtain digital images.

Typically, the Kerr amplitude $\boldsymbol{K}$ is much smaller compared to the regular reflected amplitude $\boldsymbol{N}$. Because of this, the contrast of the domains is weak (figure 3.9a). The image obtained has both magnetic and topographic information. Since the Kerr amplitude is weaker, topographic information dominates. Therefore, a

domain-free image containing only topographic information is used as background and is subtracted from the image to enhance the contrast. The background image can be obtained either saturating the sample under a magnetic field or applying an alternating field and taking several averages. By subtracting thus obtained background image, the contrast can be immensely enhanced as in figure 3.9b.

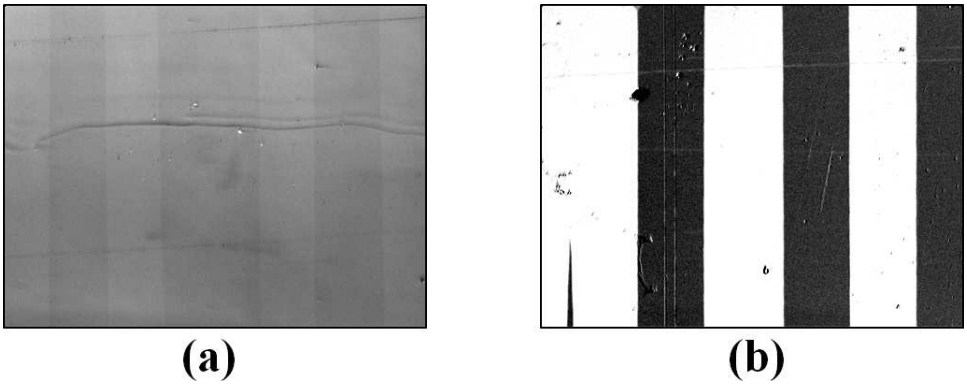

Figure 3.9: Subtracting the background enhances the contrast

Further, degree of magnetization of a sample can be estimated from its domain images. For example, figure 3.10 shows the histogram of a domain image. The four gray levels in the image represent four different domains. These four gray levels can be found in the histogram image. The intensity peaks of two medium gray levels merge into a single peak. By integrating the area under each peak, one can estimate the area of the corresponding magnetic domain. This way, it is possible to estimate the degree of magnetization of the sample.

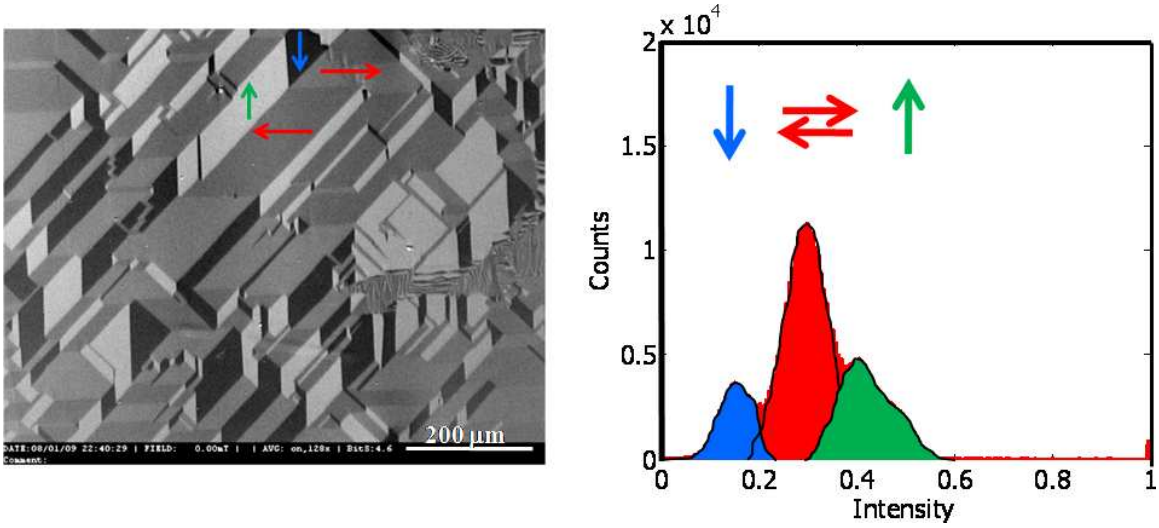

Figure 3.10: A magnetic domain image (left) with four kinds of domains and its histogram (right) showing peaks corresponding to the domains

3.2.3 Expected domain structure in Fe–Ga

The equilibrium magnetic domain state of magnetostrictive materials is determined by the balance of magnetocrystalline anisotropy, stress-induced anisotropy, exchange, magnetostatic, magnetostrictive self-, and Zeeman energies. As discussed in section 1.3, magnetic domains are primarily formed to reduce the magnetostatic energy, but the domain character depends on the quality factor $Q = K/K_d$ [79], where K is the first-order constant of any kind of anisotropy and $K_d = 0.5\mu_0 M_s^2$ is the stray field energy coefficient with M_s being the saturation magnetization. If $Q \ll 1$, the stray field energy dominates resulting in in-plane domain patterns that minimize stray fields, even at the expense of anisotropy energy. If $Q > 1$ a domain structure forms to minimize the anisotropy energy even if that leads to stray fields [79]. Details of the domain patterns also depend on the sample shape (film or bulk

material), stress state, and most importantly in case of bulk specimens, on the surface orientation. If a surface contains easy anisotropy directions, simple domains will develop. However, with increasing surface-misorientation, the patterns become increasingly complex (supplementary and branched domains are then observed for details see [79]).

In terms of magnetic microstructure, Fe–Ga alloys belong to the class of iron-like materials, i.e. cubic materials with positive magnetocrystalline anisotropy in which the $\langle 100 \rangle$ crystallographic directions are magnetically favored. In alloys containing less than 20 at% Ga, $0 < K_1 < 65\ kJ/m^3$ [53] and $M_s > 1.6$ T [84] resulting in $Q < 0.06 \ll 1$. One therefore expects domains like in iron, which are of flux-closing character with regular 180°- and 90° domain walls [85, 86] as shown in figure 3.1. The higher magnetostriction of Fe–Ga, however, will increasingly support the formation of elastically compatible domains to reduce the magnetostrictive self energy, and will render the material more sensitive to lower mechanical stresses when compared to pure iron. On a (001)-surface of Fe–Ga, one would expect to observe domains that are magnetized along the four surface-parallel easy directions [100], $[\bar{1}00]$, [010] and $[0\bar{1}0]$ like Fe-Si in figure 3.1. The structure can be either "basic" domains separated by 180° and 90° walls, or closure domains of underlying $[001]/[00\bar{1}]$ basic domains if the $[001]/[00\bar{1}]$-axes should be favored by mechanical stress.

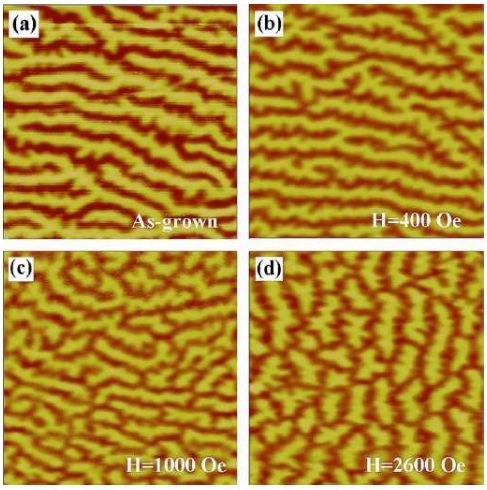

Figure 3.11: MFM images of Fe-19 at. %Ga upon applying a step-increased field normal to the sample surface, (a) as-grown state, (b) H = 400 Oe, (c) H = 1000 Oe, and (d) H = 2600 Oe. [62]

3.2.4 Literature review

Prior domain studies [57, 62, 87, 88] revealed highly complex and heterogeneous domains in Fe–Ga alloys. Often, these domains are of a maze-character that is typical for magnetic films with out-of-plane anisotropy [79]. Based on their maze-like MFM images (see fig. 3.11), Bai et al. [57] stated that the domain size in bulk Fe–Ga single crystals decreased and became increasingly irregular with increasing Ga content. Typical domain widths for x = 20 were reported to be less than 0.4 μm with domain lengths less than 2 μm. They hypothesized that the increasing nonuniformity of the domains is due to the D03-like precipitates in the A2 matrix. This observation was cited in support of theoretical predictions regarding magnetostriction enhancement in Fe–Ga alloys [67, 68]. Zhou et al. [87] studied the domain structures of polycrystalline $Fe_{81}Ga_{19}$ alloys using MFM with differ-

ent degrees of undercooling. They reported domain structures with maze-like and other complicated patterns that seem to have little correlation with the grain size or orientation. Song et al. [88] studied a polycrystalline $Fe_{81}Ga_{19}$ alloy subjected to compressive and grinding stresses, using scanning electron acoustic microscopy (SEAM) and MFM. They reported stripe-like main domain structures using SEAM with subdomains of dendrite morphology using MFM. They did, however, detect some evidence of 90° and 180° domain walls. Xing et al. [55] employed Lorentz microscopy on thinned specimens, which revealed no relation between the magnetic domains and the underlying microstructure as postulated by Bai et al. [57]. The magnetic domains showed straight 90° and 180° domain walls for $x = 10$ and irregular domain walls for $x = 20$ and 31. In contrast, the MFM study of [57] showed a complex domain structure for $x = 12$, 20, and 25. In more recent work [62], Bai et al. imaged complex domain patterns and showed that the out-of-plane anisotropy leading to the maze-like complex domains increases with increasing Ga concentration. It was noted that the domain irregularities under an applied magnetic field did not fit conventional domain growth or magnetization rotation mechanisms [79] and the unconventional magnetization rotation mechanism was explained to be due to the presence of heterogeneities in the A2 matrix.

As discussed in chapter 1, Fe-Al alloys show a similar magnetostriction enhancement as Fe–Ga alloys [28]. It is thought that the mechanism of this enhancement could be similar in these two alloy systems [56]. The magnetic domain structure in Fe-Al alloys, however, showed the expected domain patterns [81]. Figure 1.4 in chapter 1 shows the magnetic domains in Fe-Si imaged using Bitter pattern

technique. Chikazumi et al. [20] showed the stringent surface finish requirements for domain visualization in Fe-Si. Kaya [18], Williams et al. [19] and Chikazumi et al. [20] showed that the mazelike domain patterns (see fig. 1.4a) are due to mechanical polishing and when the sample is either annealed after mechanical polish or electrochemically polished, then the real domains (see fig. 1.4b) can be imaged. Such surface requirements not only affect Fe-Si but any mechanically soft bulk specimens [79]. It is important for the surface to be well polished and free of scratches and stress that might influence the domain structure. Mechanical polishing is known to induce a thick, glass-like or amorphous layer with large stress known as Beilby layer [89]. The stress-induced anisotropy on the damaged surface overwhelms the stray-field energy resulting in fine out-of-plane magnetized maze domain structures, which are not representative of the "true" domain structures hidden underneath [20]. Hua et al. [90] showed that a strong surface anisotropy can induce dense stripe domains in bulk materials, akin to those observed in Fe–Ga. Moreover, the similarity in the maze domain structure due to surface stresses in Fe-Si [20] with the Fe–Ga domain structure reported in [57, 87] necessitates a re-evaluation of the Fe–Ga domain structure.

Domain patterns under stress were observed in Fe-Si alloys [91] but such a study was not conducted on Fe–Ga. So, in this chapter, magnetic domains of Fe–Ga were studied not only under magnetic fields but also elastic fields.

3.3 Experimental procedure

For the magnetic domain study, 19Qe, 17S, and 17Q samples were used. MFM and Kerr micrscopes are used to image the magnetic domains. A high moment (HM-MESP) Co/Cr coated tip magnetized perpendicular to the surface was used in the tapping mode^{TM}. A lift height of 50 nm was used to obtain the magnetic force gradient images. For the wide field Kerr microscope, longitudinal mode (longitudinal Kerr effect) at oblique incidence with either longitudinal ($\pm\hat{\boldsymbol{y}}$) or transverse ($\pm\hat{\boldsymbol{x}}$) sensitivity [79] was used. When the longitudinal sensitivity is used, the [010]/[0$\bar{1}$0] or $\pm\hat{\boldsymbol{y}}$ domains appear bright and dark while the [100]/[$\bar{1}$00] or $\pm\hat{\boldsymbol{x}}$ domains appear gray. Similarly, when the transverse sensitivity is used, the $\pm\hat{\boldsymbol{x}}$ domains appear bright and dark while the $\pm\hat{\boldsymbol{y}}$ domains appear gray. The samples were held in place by means of double-sided tape.

3.4 Magnetic domains at remanence

In this section, the magnetic domain structure in the 17S, 17Q, and 19Qe samples at remanence is imaged using magnetic force and Kerr microscopy.

3.4.1 Conventional polishing

The surface coplanar with (001) for each of the three samples was mechanically polished using increasingly finer polishing media. First, the samples were polished using SiC sheets starting from 400 grit down to 1200 grit size and subsequently alumina suspension was used down to 0.3μm. The samples were then etched with

10 % Nital solution for 30 seconds. This polishing procedure is similar to that described in [57, 87]. After polishing all the samples, the magnetic domain structure was imaged under zero magnetic field. Figure 3.12a shows the Kerr image obtained in the longitudinal mode, which does not reveal any domain structure. Switching to the polar mode reveals the domain pattern similar to the maze pattern in Ni thin films with out-of-plane anisotropy. The magnetization of these domains is aligned indeed out-of- and into- the plane since their contrast was maximum in the polar mode and they became invisible in the longitudinal mode (see section 3.2.2.2).

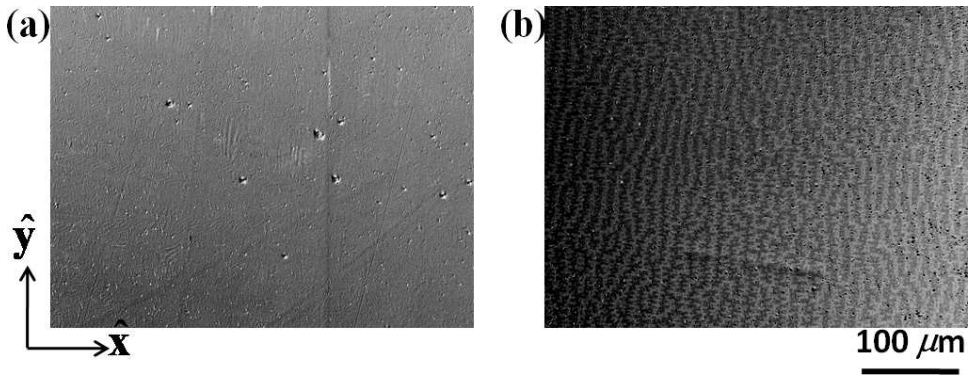

Figure 3.12: Kerr image of (001) surface of 17S in (a) longitudinal mode and (b) polar mode.

Figure 3.13 shows the magnetic domain structure of 17S as imaged by MFM. The bright and dark areas indicate domains with magnetization out-of or into the surface. This corroborates the magnetic domain structure as imaged by the Kerr microscope in figure 3.12.

Figure 3.14 shows the magnetic domain structures of 17Q and 19Qe as imaged by MFM. It can be seen that in all three samples, 17S, 17Q, and 19Qe, the magneti-

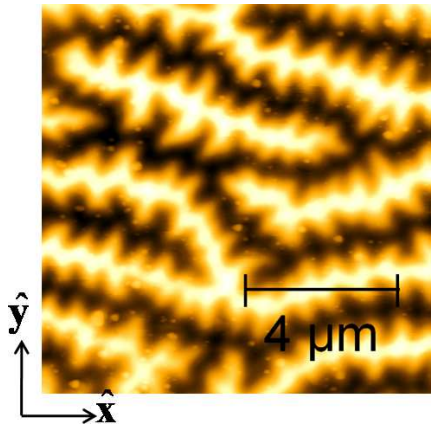

Figure 3.13: MFM image of (001) surface of 17S, showing maze pattern with out-of-plane magnetization.

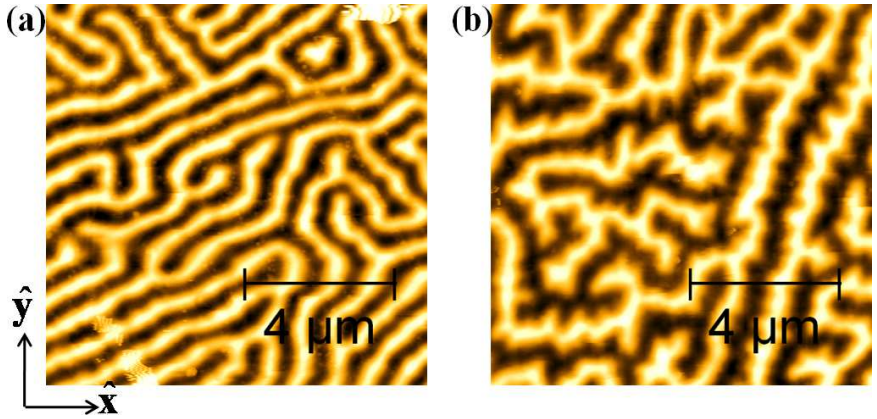

Figure 3.14: MFM image of (001) surface of (a) 17Q and (b) 19Qe, showing maze pattern with out-of-plane magnetization.

zation of the domains is oriented out-of- and into the imaged plane. These patterns are similar to the maze domain patterns reported by [57, 87, 88]. Contrary to the reported correlation between the domain size and the sample composition [57], it was found that domain patterns vary in size and structure within the same sample.

As described in section 3.2, an out-of-plane anisotropy is necessary to overcome

the magnetostatic energy to form out-of-plane magnetized domains. That is, the quality factor must be $Q > 1$. Also, for the domain walls to curve in a single crystal sample, there must be inclusions or voids, or there must be an internal stress distribution [1]. The hypothesis of Bai et al. [57] that the maze patterns are a result of $D0_{22}$ precipitates agrees with both the inclusion and internal stress distribution reasons. A $D0_{22}$ precipitate (inclusion) will lead to local stresses near the $D0_{22}$ and matrix (A2 phase) boundary. However, it is also possible that these domain patterns are limited to the surface and the stress distribution could be as a result of surface damage due to conventional polishing. It was demonstrated by Kaya [18], Williams et al. [19] and Chikazumi et al. [20] (see figure 1.4) that maze patterns in Fe-Si are not representative of the "true" domain structure and are limited to the damaged surface. The "true" domain structure, consisting of wide in-plane domains with straight 90° and 180° domain walls (on a [1 0 0]-surface) was rather revealed after electro-polishing the samples surface or annealing the sample at high temperature to allow the damaged layer to re-crystallize. Therefore, to verify whether the maze domain patterns imaged in Fe–Ga are due to the surface damage or $D0_{22}$ inclusions, the surfaces were polished further to carefully remove the damage layer without introducing anymore damage.

3.4.2 Additional silica gel polishing

Etching the samples in 10% Nital at 70 °C for 4 minutes or more revealed the expected domain structure in 19Qe as shown in figure 3.15. However, the sur-

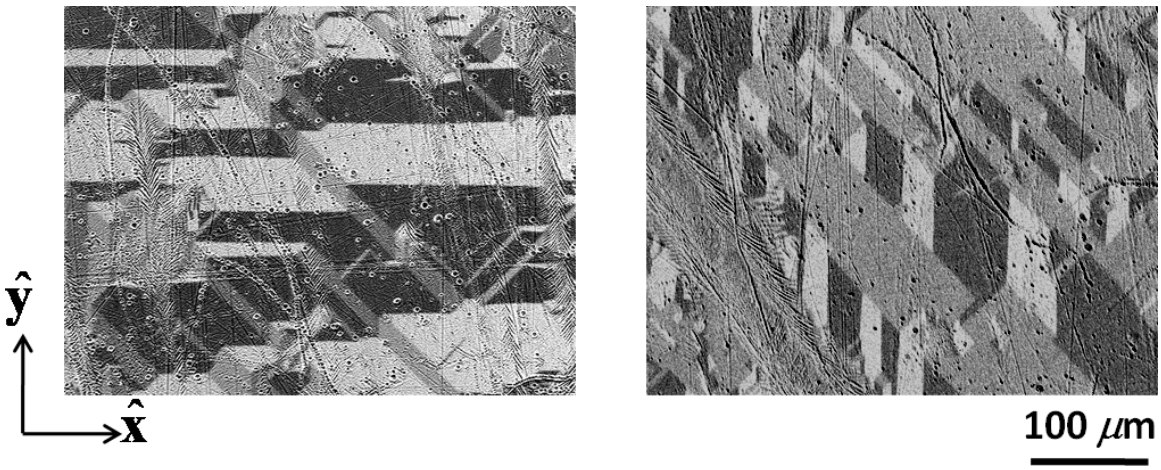

Figure 3.15: Etching in Nital for more than 4 minutes

face finish degraded significantly with the formation of pits and otherwise invisible scratches becoming much more pronounced due to the Nital etching. In other samples, the surface condition degraded so badly with the formation of pits that no Kerr contrast from the magnetic domains could be observed.

A relatively simple technique to remove the damaged layer that utilizes an additional polishing step using colloidal amorphous silica was described by Hoffmann et al. [92].

It is believed that alumina, a hard material, introduces a dense network of deep scratches that result in a high surface stress. Silica gel contains amorphous SiO_2 particles with mean size about 60 nm, which are much softer in comparison to the metals. Polishing with silica gel gradually removes the "mountains" without introducing new scratches thus allowing the disturbed surface layer to gradually thin down (see figures 3.16b, 3.16c, 3.16d).

Applying this technique, all the samples were additionally polished using com-

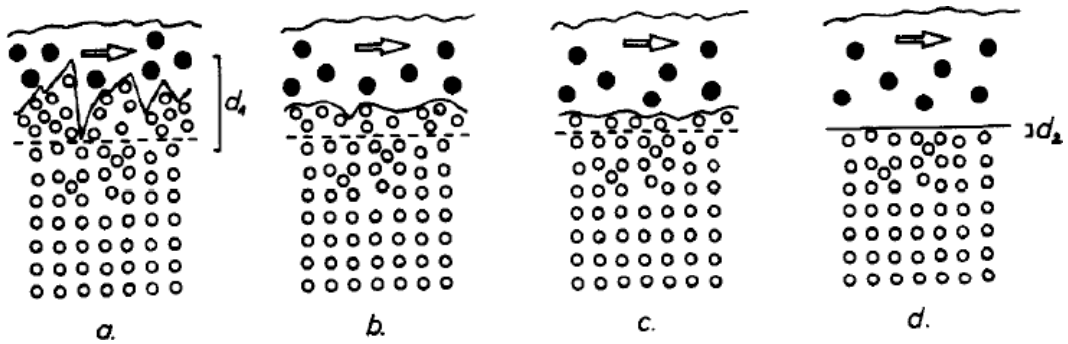

Figure 3.16: (a) Highly stressed surface layer with effective thickness d_1 after polishing with alumina powder. (b,c) Reduction of the stressed layer thickness with silica gel polishing. (d) Extremely smooth surface with stressed layer thickness $d_2 \ll d_1$. Taken from [92]

mercially available 0.06 μm silica suspension. Figure 3.17 shows the domain structure evolution of 17S with the silica gel polishing time. It took 75 minutes to get rid of the damaged surface layer in this sample. In general, it took 1 - 3 hours of silica polishing to remove the damaged layer.

The typical domain size in these samples is much larger than the maximum scan size of the MFM. Since contrast is obtained only near domain walls, most of the MFM (see fig 3.18) scans do not show any magnetic features. As a result, it takes multiple iterations of positioning a sample for a scan before a domain wall can be imaged using MFM. Figure 3.19 shows the MFM images of 17S, 17Q, and 19Qe samples obtained after silica gel polishing. Contrast exists only near the domain walls, which indicates that the magnetization of all the domains is oriented within the (001) plane. Both the expected 90° and 180° domain walls can be seen.

Typical Kerr domain images are shown in Figure 3.20. These images show four different gray scales indicating four different domain phases each of them magnetized

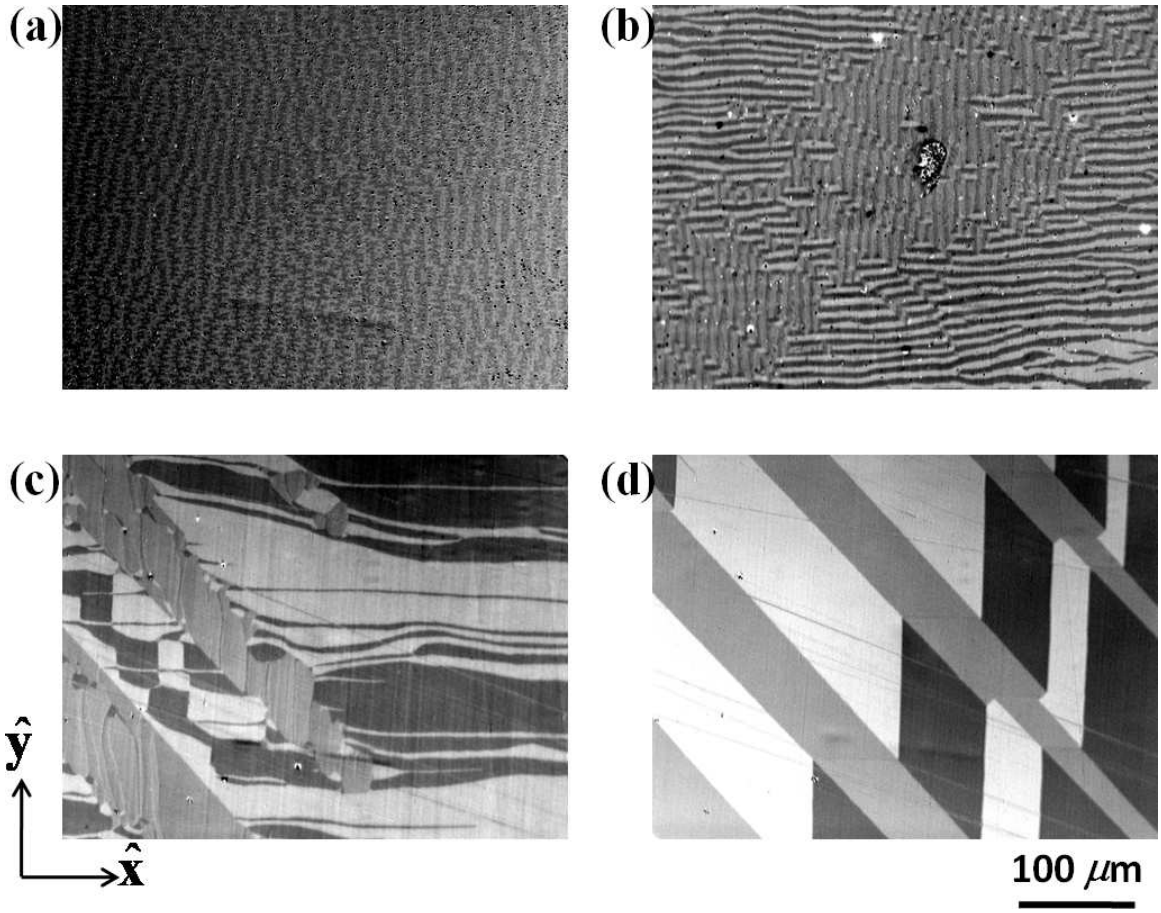

Figure 3.17: Domain structure of 17S as a function of silica gel polishing time (a) t = 0, (b) t = 20 min, (c) t = 50 min, (d) 75 min.

along one of the four ⟨100⟩ directions within the (001) plane. The domains thus imaged show the same characteristics as observed by MFM. Since each Kerr image covers more than four times the area of the maximum MFM scan, the difference in the Kerr and MFM images can be solely attributed to different scales. Further, the difference between the Kerr and MFM images of sample 19Qe additionally stems from different areas of the sample that were imaged.

Figure 3.21 shows a high magnification MFM scans of 19Qe sample showing

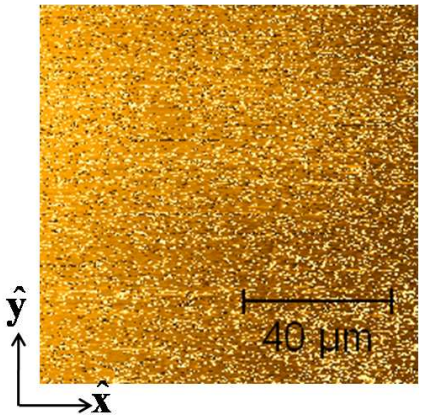

Figure 3.18: No domain structure visible in 17S with MFM even at the maximum scan size

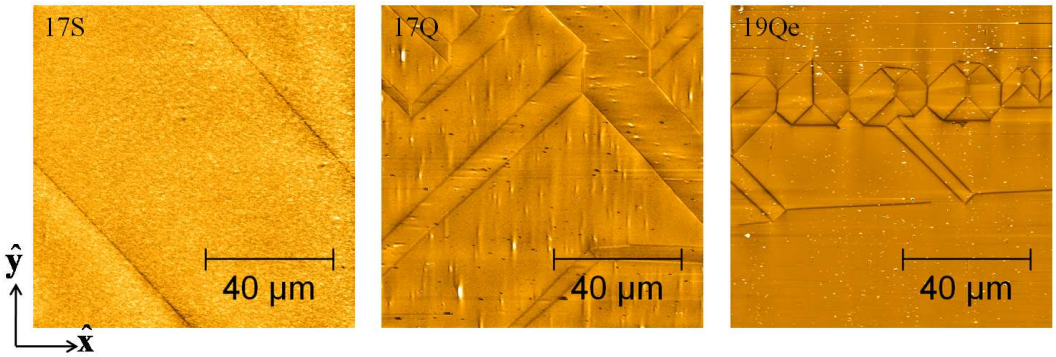

Figure 3.19: MFM images after additional polishing with colloidal silica.

the meeting point of two 90° domain walls and one 180° domain wall. The high magnification image shows no evidence for any subdomain structure reported by Song et al. [88].

Figure 3.22 shows that domain splitting can occur near areas of stress concentration such as scratches. The domain walls that form as a result are usually not straight. They can curve or form an angle as shown in the figure. The high stress

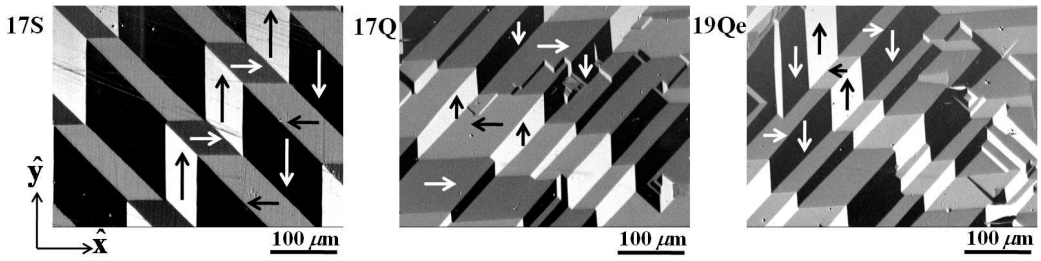

Figure 3.20: Typical Kerr images after additional polishing with colloidal silica. The domains show 90° and 180° domain walls with domains oriented along [100], [$\bar{1}$00], [010] and [0$\bar{1}$0].

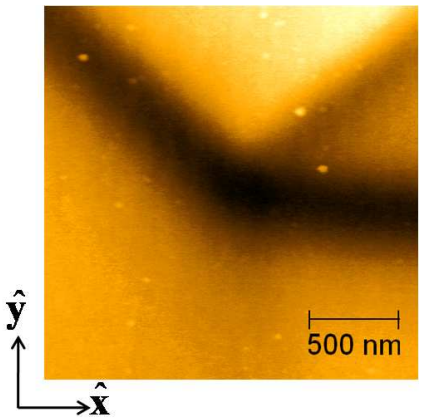

Figure 3.21: High magnification MFM scan of 19Qe showing 90° and 180° domain walls

concentration within a scratch results in maze-like domain patterns as shown in the inset of figure 3.22.

3.4.3 Discussion

The maze-like domain patterns with out-of-plane magnetization were observed in conventionally polished Fe–Ga samples. Such domains typically appear when

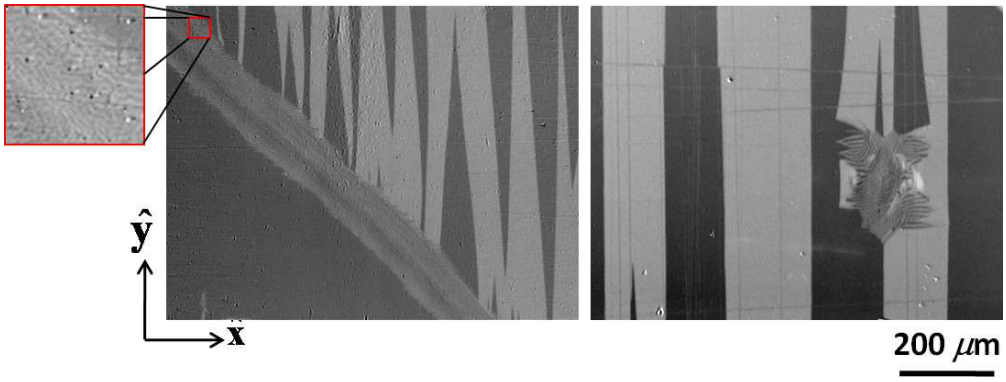

Figure 3.22: Domain splitting near areas of stress concentration in 17Q (left) and 17S (right). Inset shows a magnified view of the maze domain structure within the scratch.

$Q = K/K_d > 1$. Choosing $K = K_1$ for $Fe_{100-x}Ga_x$ ($x \leq 20$), $Q \ll 1$. Therefore, a sufficiently strong perpendicular anisotropy, K_u, must be present so that the total anisotropy $K = K_1 + K_u$ is strong enough to obtain $Q > 1$. Bai et al. attributed K_u to the presence of heterogeneities responsible for the enhancement of the magnetostriction. However, the present study clearly demonstrates that the need to invoke an additional uniaxial anisotropy arises from the polishing-induced surface damage. If one assumes that the damaged surface layer is still single-crystalline, the additional anisotropy K_u could reflect the surface stress-induced anisotropy. It would then follow that the maze-like domains appear readily in Fe–Ga because of the alloy's high magnetostriction. The stress-induced anisotropy scales linearly with magnetostriction. Hence, even smaller surface stresses due to mechanical polishing result in a high stress-induced anisotropy when compared to α-Fe. The Fe–Ga alloys, therefore, require even more stringent surface treatments than known from pure iron or Fe-Si alloys.

The key for true domain visualization in bulk Fe–Ga alloys is to remove the damaged surface layer of the conventionally polished surface without further inducing any significant surface stress. Removing the top layer after conventional polishing by etching in 10% Nital at 70 °C for more than 4 minutes revealed the expected domain structure. However, the surface finish degraded significantly with the formation of pits and otherwise invisible scratches becoming much more pronounced due to the Nital etching. Additional amorphous silica suspension polishing as the last step was found to be sufficient to remove the top surface layer without introducing new scratches or anisotropies. Following this step, the unperturbed domain structures of the samples were revealed. These patterns were similar to those expected with the magnetization oriented along the four possible $\langle 1\,0\,0 \rangle$ directions within the (001) plane and with straight 90° and 180° domain walls. Further, the domains were typically larger than 100 μm, which is the maximum scan length of an MFM. The longitudinal Kerr images show much larger domains and provide contrast to identify the four possible orientations of the magnetization of the domains. Therefore, one can conclude that the previously reported domain patterns for Fe–Ga bulk material are due to the surface conditions and do not represent the true domain structure.

3.5 Magnetic domains under magnetic and elastic fields

Now that the real magnetic domains could be imaged, studies measuring the magnetic domains response to magnetic and elastic fields are conducted. In this

section, the response of magnetic domains in 19Qe, 17S, and 17Q to the applied magnetic fields is provided first followed by the magnetic domains response in 19Qe and 17S to the applied elastic fields.

3.5.1 Experimental setup

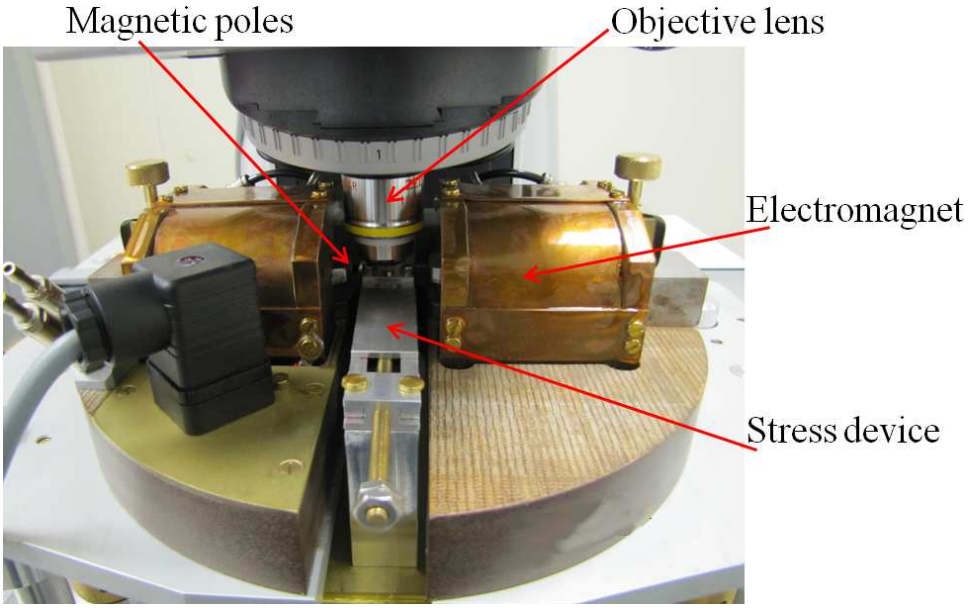

Figure 3.23: An electromagnet that can be rotated was used to apply magnetic field along $\pm\hat{\boldsymbol{x}}$ or $\pm\hat{\boldsymbol{y}}$. Due to space constraints between the poles of the electromagnet, stress could be applied only along $\pm\hat{\boldsymbol{y}}$.

The samples were held in place by means of double-sided tape. An electromagnet as shown in 3.23 was used to apply a magnetic field along the $\pm\hat{\boldsymbol{x}}$ or $\pm\hat{\boldsymbol{y}}$ direction. The remanent stray field from the electromagnet at the sample position was 1 mT. Due to the space constraints as shown in figure 3.23, elastic field was applied only along $\hat{\boldsymbol{y}}$ direction, by tightening the screw of a custom built device (see figure 3.24). In-situ strain measurement was made along the $\pm\hat{\boldsymbol{y}}$ direction using a

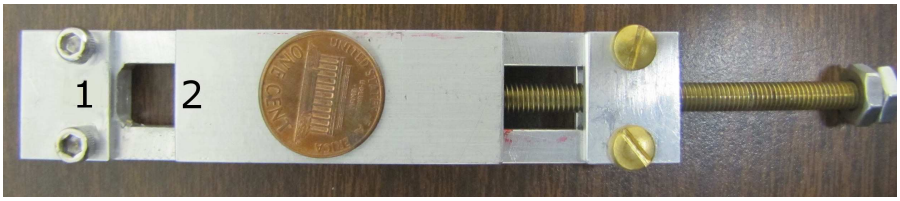

Figure 3.24: Device built from high strength aluminum to apply compressive stresses. Samples are squeezed between 1 and 2 by manually turning the screw.

resistive strain gage bonded on the backside of the sample. Under an externally applied elastic field, the measured strain along $\pm\hat{\boldsymbol{y}}$ includes both elastic and magnetoelastic strains because of which calculation of stress values was not possible. Therefore, the elastic field was quantified in terms of the measured strain. The magnetostriction measurements were corroborated with the ex-situ measurements obtained with bidirectional rosette strain gages from chapter 2.

3.5.2 Domains under magnetic field

Figure 3.25 shows the magnetic domain structure in 19Qe with increasing magnetic field applied along the $\hat{\boldsymbol{x}}$ direction. Longitudinal mode with transverse sensitivity of the microscope was selected to obtain these images. The images show all four types of domains with magnetization oriented along the easy axes: $\hat{\boldsymbol{x}}$, $-\hat{\boldsymbol{x}}$, $\hat{\boldsymbol{y}}$, $-\hat{\boldsymbol{y}}$, within the (0 0 1) plane. With $H \parallel \hat{\boldsymbol{x}}$, $\pm\hat{\boldsymbol{x}}$ domains grow by domain wall motion and eventually engulf the whole sample beyond ~ 30 mT. The magnetostriction measurements, both λ_x^x and λ_y^x, are shown in figure 3.25. As expected, λ_x^x is positive and λ_y^x is negative. Both the magnetic domain structure and the magnetostriction

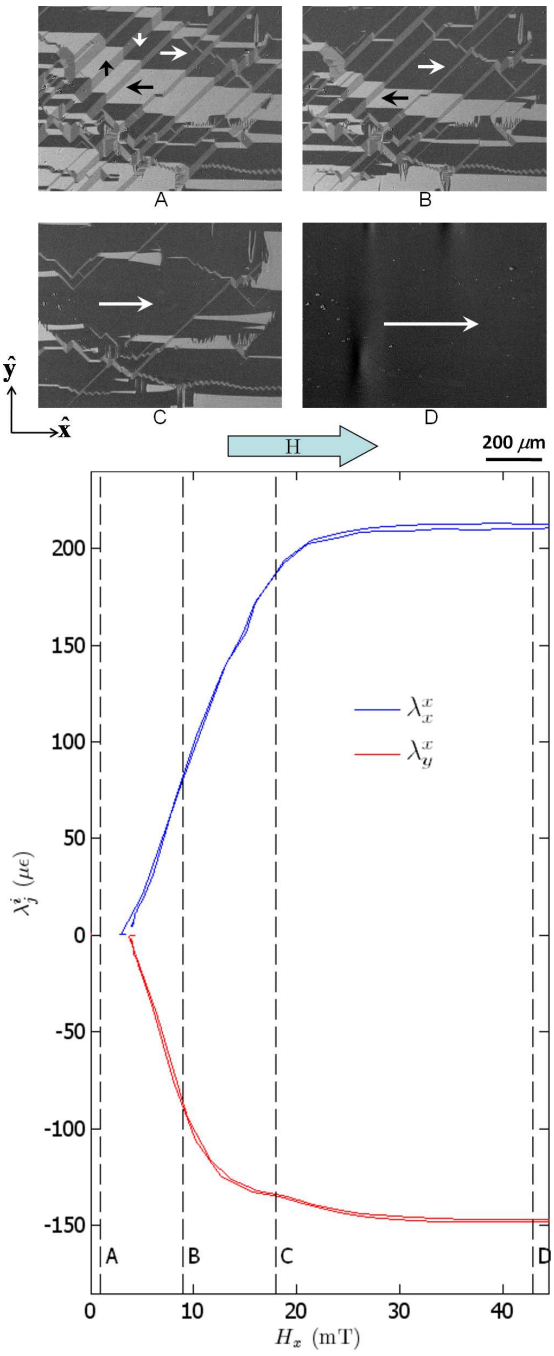

Figure 3.25: Magnetic domain structure evolution in 19Qe with magnetic field applied along $\hat{\boldsymbol{x}}$

saturate at around the same magnetic field $\sim$ 40 mT. Figure 3.26 shows the local magnetization calculated by integrating the area covered by $\hat{\boldsymbol{x}}$ (black) domains

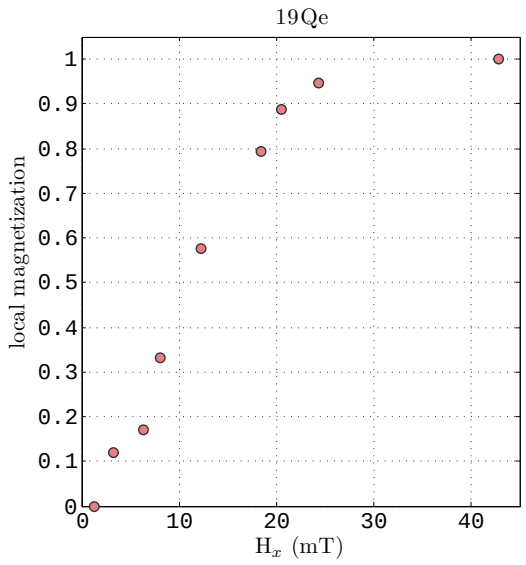

Figure 3.26: Magnetization measure in 19Qe from Kerr microscope with magnetic field applied along $\hat{\boldsymbol{x}}$

from the Kerr images. Thus calculated local magnetization also saturates at about the same field as the magnetostriction. This also agrees with the magnetization measurement of 19Qe in figure 2.3.

Evolution of the magnetic domain structure of 17S with magnetic field applied along $-\hat{\boldsymbol{x}}$ is shown in figure 3.27. Splitting of the domains, visible in the domain images at < 52 mT, are due to the scratch marks on the imaged surface that might have formed during the last stage of polishing. The Kerr contrast clearly shows that all the domains at zero magnetic field were of $\pm\hat{\boldsymbol{y}}$ type, possibly due to the superposition of some uniaxial anisotropy onto the cubic anisotropy. At a magnetic field of $\sim$52 mT this uniaxial anisotropy is overcome and the $-\hat{\boldsymbol{x}}$ domains begin to nucleate. Beyond this magnetic field, the $-\hat{\boldsymbol{x}}$ domains grow by domain wall motion eventually engulfing the material at > 100 mT. As expected, the magnetostriction

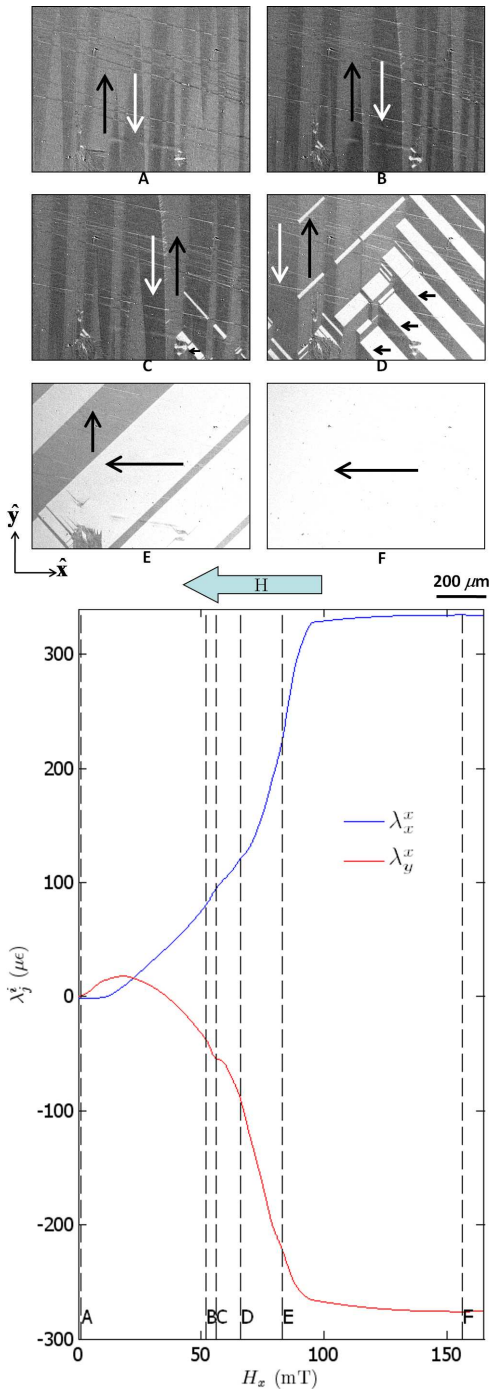

Figure 3.27: Magnetic domain structure evolution in 17S with magnetic field applied along $-\hat{\boldsymbol{x}}$

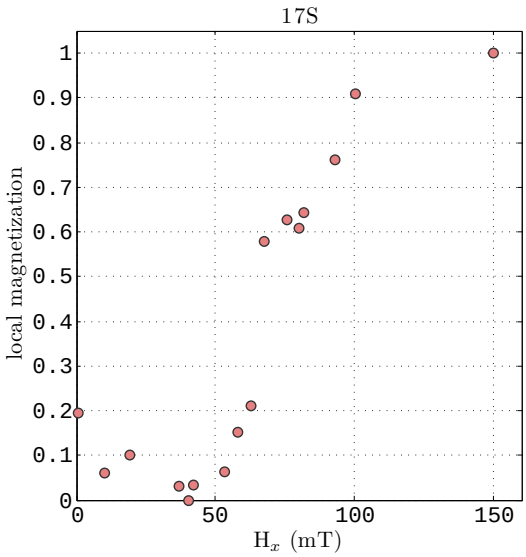

Figure 3.28: Magnetization measure in 17S from Kerr microscope with magnetic field applied along $\hat{\boldsymbol{x}}$

measurement is consistent with the magnetic domain evolution, both saturating at ~ 100 mT. Figure 3.28 shows the local magnetization curve measured by integrating the area covered by $-\hat{\boldsymbol{x}}$ (white) domains from the Kerr images. Thus calculated local magnetization also saturates at about the same field as the magnetostriction. Therefore, it appears that these surface domains are same as the bulk domains. Also, the formation of large $-\hat{\boldsymbol{x}}$ domains under field indicate that the domain walls go through the thickness of the sample. If the domains are limited to the surface then much smaller $-\hat{\boldsymbol{x}}$ with many more domain walls are expected. More on this is elaborated later when discussing 17Q domain images.

To verify whether the domains are truly the bulk domains, the backside surface of the sample was also polished. Figures 3.29 and 3.30 show the magnetic domain images and the local magnetization calculation from the domain images for the

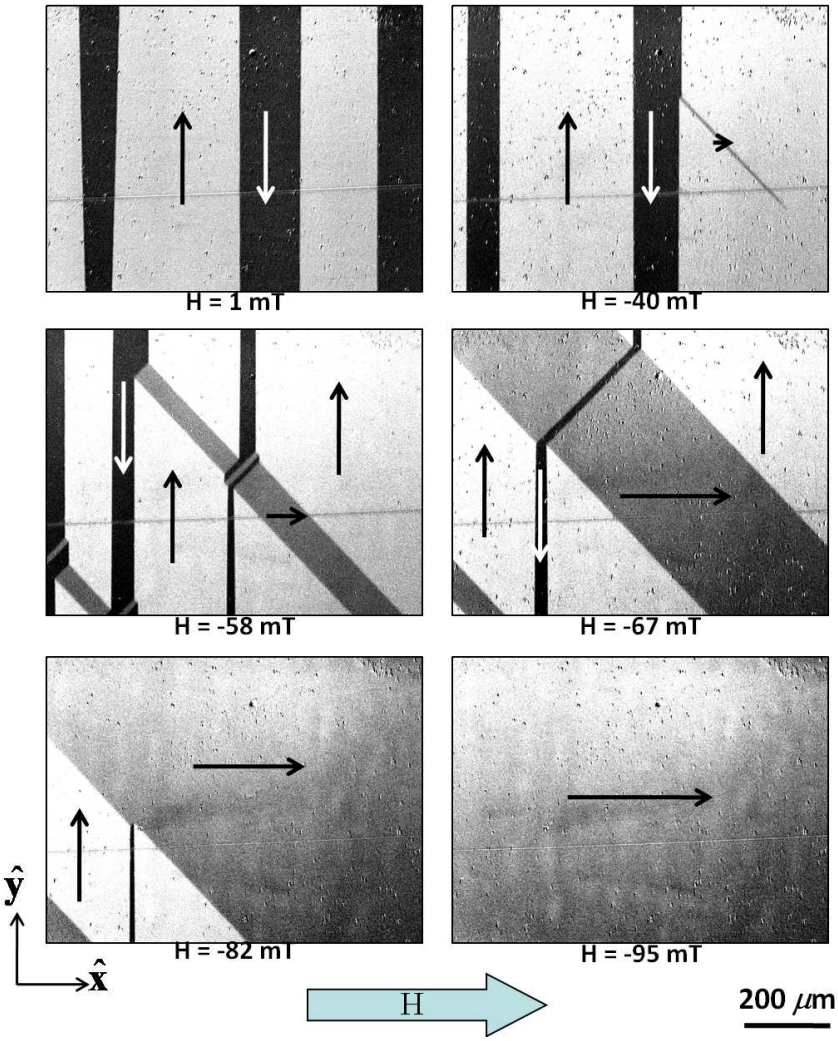

Figure 3.29: Magnetic domain structure evolution in 17S (backside) with magnetic field applied along $-\hat{\boldsymbol{x}}$

backside surface of the 17S sample. The domain structure at remanence and the domain structure evolution with field is similar on both the surfaces. This shows that the domains on both the surfaces are same as the bulk domains. Further, it can be said that the additional uniaxial anisotropy is present through out the sample. This is also consistent with the remanent states estimated for this sample in table 2.3.

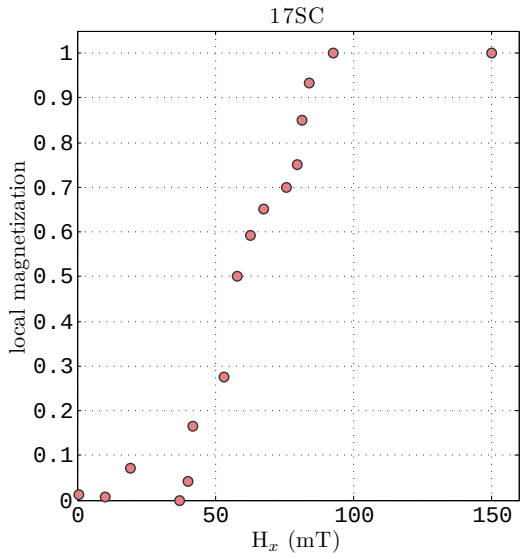

Figure 3.30: Magnetization measure in 17S (backside) from Kerr microscope with magnetic field applied along $\hat{\boldsymbol{x}}$

Figure 3.31 shows the evolution of the magnetic domain structure in 17Q under a magnetic field applied along $-\hat{\boldsymbol{x}}$. Longitudinal sensitivity was used to obtain these images. Similar to 17S, the magnetization in this sample is oriented along $\pm\hat{\boldsymbol{y}}$ at zero magnetic field i.e., there appears to be a uniaxial anisotropy favoring the $\pm\hat{\boldsymbol{y}}$ directions. At $\sim$ 50 mT the uniaxial anisotropy is overcome and the $-\hat{\boldsymbol{x}}$ domains begin to nucleate. Figure 3.32 shows the local magnetization calculated by integrating the area covered by the $-\hat{\boldsymbol{x}}$ (gray) domains. The local magnetization saturates at $\sim$70 mT. One key difference from the 17S sample is that beyond the critical magnetic field ($\sim$50 mT) required to overcome the uniaxial anisotropy, the $-\hat{\boldsymbol{x}}$ (gray) domains are much smaller in size and there are many more 90° domain walls. If these domain walls go through the thickness of the sample, the energy required to form such a large number of domain walls is high. Further, if these

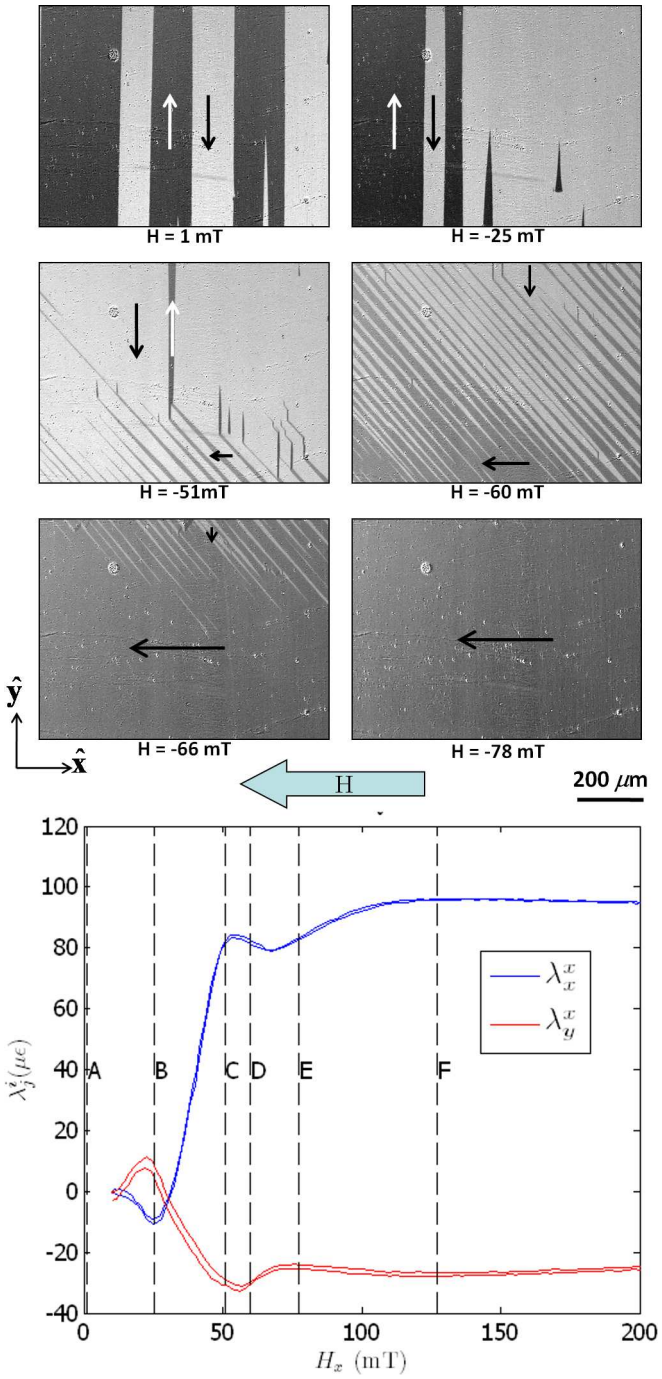

Figure 3.31: Magnetic domain structure evolution in 17Q with magnetic field applied along $-\hat{\boldsymbol{x}}$

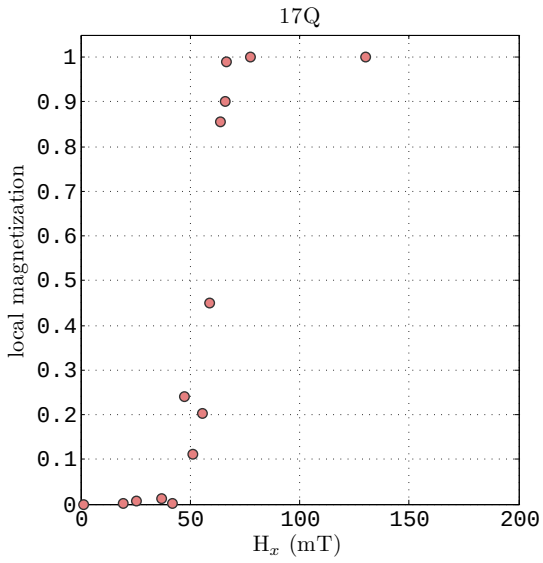

Figure 3.32: Magnetization measure in 17Q from Kerr microscope with magnetic field applied along $\hat{\boldsymbol{x}}$

are the bulk domains then the magnetostriction λ_x^x should be close to λ (280 $\mu\epsilon$). However, λ_x^x was measured to be much lower (92 $\mu\epsilon$). Therefore, it is probable that these domains are limited to this front surface and are not the bulk domains.

The sample was polished on the back side and the domain structure was measured. Figure 3.33 shows the magnetic domain evolution with increasing magnetic field. It can be observed that the stripe domain structure on the back side is similar to the front side but the remanent domains are of $\pm\hat{\boldsymbol{x}}$-type instead of $\pm\hat{\boldsymbol{y}}$-type. The magnetostriction measurement on this side shows λ_y^y to be more than λ (due to the additional volume magnetostriction component). This agrees with the expected value. Further, the local magnetization calculated by integrating the $-\hat{\boldsymbol{y}}$ domains, shown in figure 3.34, also agrees with the magnetostriction data. The formation of large number of 90° domain walls indicates that the domain walls may not be going

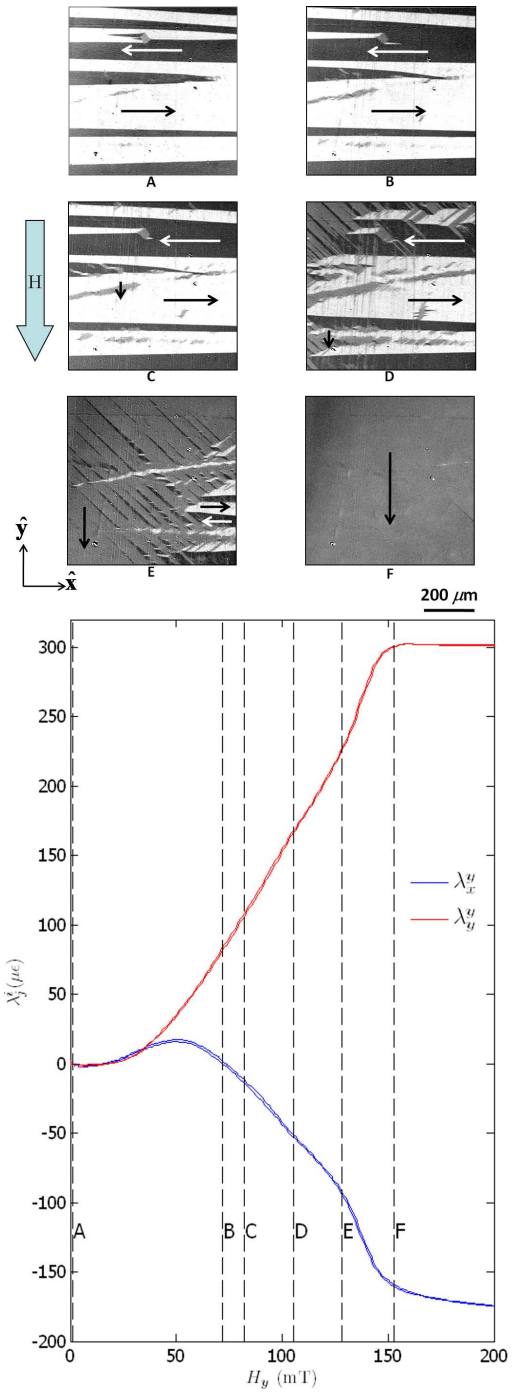

Figure 3.33: Magnetic domain structure evolution in 17Q (back side) with magnetic field applied along $-\hat{\boldsymbol{y}}$

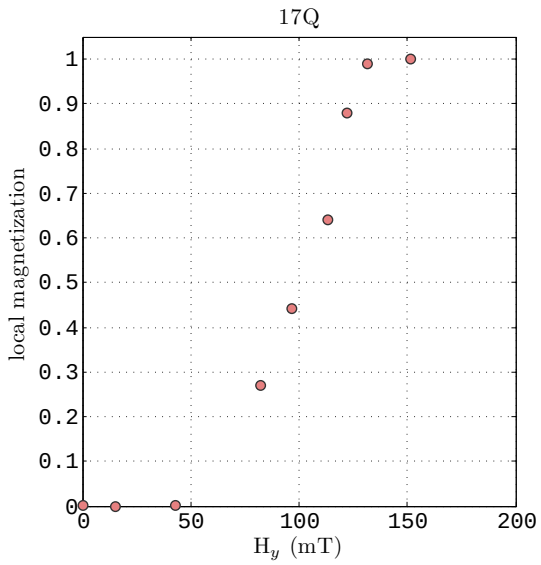

Figure 3.34: Magnetization measure in 17Q (backside) from Kerr microscope with magnetic field applied along $\hat{\boldsymbol{x}}$

through the thickness of the sample. Since $|\lambda_x^y|$ is less than $|\lambda_y^y|$ the bulk domain structure is expected to have $\pm\hat{\boldsymbol{z}}$-type domains and thus different from the domain structures imaged on either side of the sample. Therefore, unlike 17S, the domains imaged in 17Q do not represent the bulk domains.

3.5.3 Domains under elastic field

Figure 3.35 shows the magnetic domains in 19Qe under a compressive elastic field applied along $\hat{\boldsymbol{y}}$. The images show that the $\pm\hat{\boldsymbol{x}}$ magnetic domains grow by domain wall motion and eventually form two large domains separated by a 180° domain wall at $\sim -1500\,\mu\epsilon$. This is expected because the compressive elastic field results in a stress-induced anisotropy along $\pm\hat{\boldsymbol{y}}$ thus favoring magnetization to orient along $\pm\hat{\boldsymbol{x}}$ or $\pm\hat{\boldsymbol{z}}$. On the (001) surface, the magnetostatic energy precludes $\pm\hat{\boldsymbol{z}}$

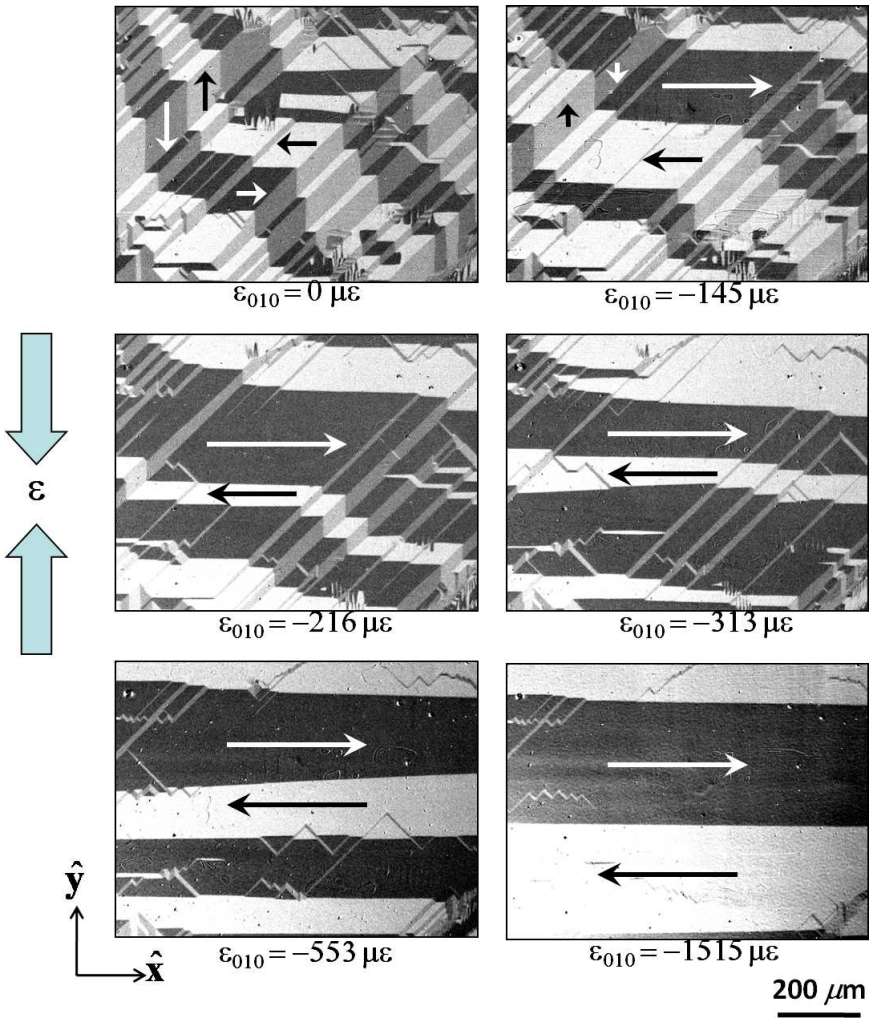

Figure 3.35: Magnetic domain structure evolution in 19Qe with compressive elastic field applied along $\hat{\boldsymbol{y}}$

domains and hence, only $\pm\hat{\boldsymbol{x}}$ are favored.

Next, the magnetic domain evolution in 17S under elastic field is shown in figure 3.36. Similar to the magnetic field case, it took a compressive elastic field of $\sim -600\,\mu\epsilon$ to overcome the uniaxial anisotropy present in this sample. Appearance of domain walls that are not straight is possibly due to the scratch marks. Beyond $-600\,\mu\epsilon$, $\pm\hat{\boldsymbol{x}}$ domains grow at the expense of $\pm\hat{\boldsymbol{y}}$ domains. As can be seen, at

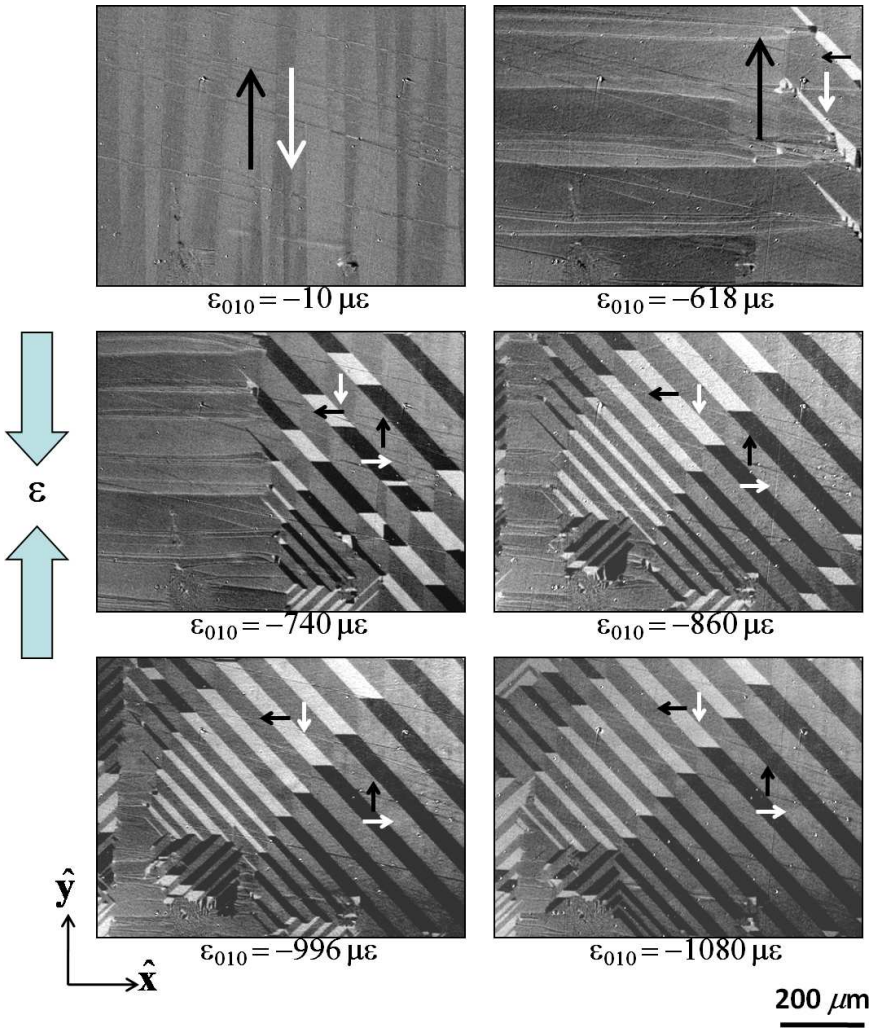

Figure 3.36: Magnetic domain structure evolution in 17S with compressive elastic field applied along $\hat{\boldsymbol{y}}$

the maximum elastic field applied ($\sim -1100\,\mu\epsilon$), the sample still has $\pm\hat{\boldsymbol{y}}$ domains. Higher elastic fields could not be applied due to the limitation of the maximum force that can be applied using the elastic field setup. One cannot rule out the possibility that the bulk domain structure consists predominantly $\pm\hat{\boldsymbol{z}}$ domains and the domain structure imaged at the maximum elastic field is limited to the surface.

In figure 3.37, the maximum possible compressive elastic field ($\epsilon_0 = -1140\,\mu\epsilon \parallel$

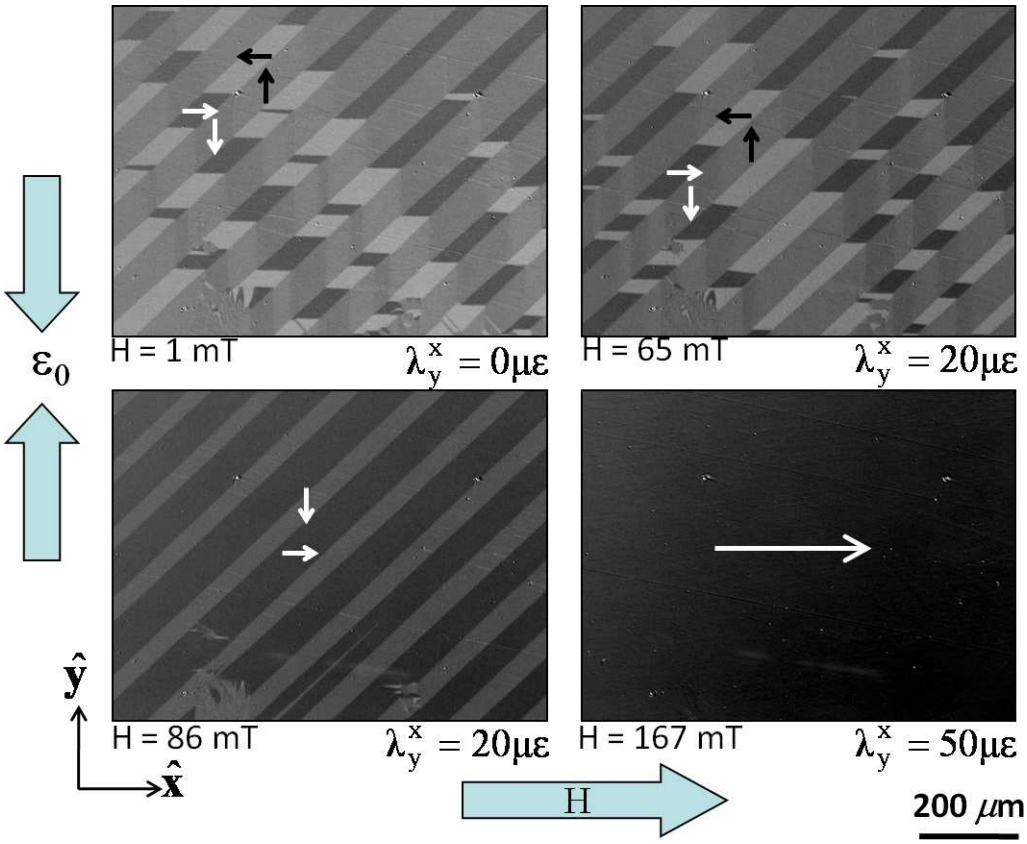

Figure 3.37: Magnetic domain structure evolution in 17S with an elastic pre-strain $\epsilon_0 = -1140\,\mu\epsilon \parallel \hat{\boldsymbol{y}}$ and magnetic field applied along $\hat{\boldsymbol{x}}$

$\hat{\boldsymbol{y}}$) was applied and then a magnetic field was superimposed. The strain gage indicator was zeroed and λ_y^x was measured. The $\pm\hat{\boldsymbol{y}}$ domains still present at zero magnetic field could either be because the sample is not elastically saturated or because the bulk domain structure (after elastic saturation) consists of $\pm\hat{\boldsymbol{z}}$ domains. Applying a magnetic field along $\hat{\boldsymbol{x}}$ makes the $\hat{\boldsymbol{x}}$ domains grow. The $+\hat{\boldsymbol{x}}$ domains initially grow at the expense of the $-\hat{\boldsymbol{x}}$ domains and then the $\pm\hat{\boldsymbol{y}}$ and $\pm\hat{\boldsymbol{z}}$ domains, eventually covering the entire sample at > 100 mT. The in-situ magnetostriction measurements λ_y^x are shown below the domain images in figure 3.37. Contrary to the expectation,

λ_y^x was positive. Therefore, the strain measured could be dominated by the volume magnetostriction component. Further, since the Joule magnetostriction component is possibly insignificant, one can deduce that the bulk domain structure after elastic saturation consists of predominantly $\pm\hat{\boldsymbol{z}}$ domains.

3.6 Discussion and conclusions

In this chapter, the domain structures of 19Qe, 17S, and 17Q samples were imaged. The maze-like domain patterns with out-of-plane magnetization were observed in conventionally polished Fe–Ga samples as previously reported by [57, 62, 87, 88]. It was shown that such irregular maze-like domain patterns for Fe–Ga bulk materials result from improper polishing. Such domains typically appear when quality factor $Q = K/K_d > 1$. As described in section 3.4.3, choosing $K = K_1$ for $Fe_{100-x}Ga_x$ ($x \leq 20$), $Q \ll 1$. Therefore, unless a sufficiently strong perpendicular anisotropy, K_u, is present such that the total anisotropy $K = K_1 + K_u$ is strong enough to obtain $Q > 1$, maze-like domain patterns should not form. Bai et al. attributed the additional uniaxial anisotropy, K_u, to the presence of heterogeneities that were claimed to be responsible for the enhancement of the magnetostriction [59, 61]. However, the present study clearly demonstrates that the need to invoke an additional uniaxial anisotropy arises from the polishing-induced surface damage. If the damaged surface layer is still single-crystalline, the additional anisotropy K_u could be attributed to the surface stress-induced anisotropy. It would then follow that the maze-like domains appear readily in Fe–Ga because of the alloy's high magnetostric-

tion. Since the stress-induced anisotropy scales linearly with magnetostriction, even smaller surface stresses due to mechanical polishing result in a high stress-induced anisotropy when compared to α-Fe, Fe-Si, or Fe-Al . Therefor, Fe–Ga alloys require even more stringent surface treatments than known from pure iron, Fe-Si, or Fe-Al alloys.

After properly polishing the samples and imaging the true domain structures, the influences of externally applied magnetic and of elastic fields on the domains were studied. The magnetic domain evolution was compared with the magnetostriction data. The local magnetization estimated from the magnetic domain images was also compared. In 19Qe and 17S samples under magnetic field, the domain images, local magnetization, and the magnetostriction were consistent. Imaging the magnetic domains on the bottom side of the 17S sample revealed identical stripe domain structure. This agrees with the remanent state of the sample estimated from the magnetostriction data in chapter 2. In 17Q sample, the remanent domain structure was a stripe structure that does not agree with the remanent state estimate. Imaging the domain structure on the bottom side of this sample revealed stripe domains with magnetization flipped 90° compared to the top side. When magnetic field was applied perpendicular to the magnetization of the domains (on either side) much smaller domains (compared to the 17S sample) with magnetization parallel to the field formed with a large number of domain walls. It is energetically expensive to form such a large number of domain walls should these domain walls penetrate through the thickness of the sample. Hence, the domains imaged on either side of the sample must be limited to the surface and perhaps do not go through the bulk of

the sample as in 17S. Further, the difference in saturation magnetic fields of 17Q in figures 3.32 and 3.34 is simply because the field was applied in different directions. The difference can be attributed to different demagnetization factors along the two directions.

Under elastic field, both 19Qe and 17S samples behaved as per the expectations. The magnetization rotates perpendicular to the direction of compressive elastic field applied. This happens via domain growth through domain wall motion in 19Qe. In 17S it happens via domain nucleation and then the domain growth through domain wall motion. After elastic saturation, two kinds of domains remain separated by 180° domain walls formed in 19Qe sample. At the maximum elastic field applied to the 17S, there were still four types of domains. This could mean that elastic saturation was not reached. However, when a magnetic field was superimposed a positive magnetostriction was measured perpendicular to the magnetic field. This happens when the Joule magnetostriction is dominated by the volume magnetostriction component. This indicates that perhaps the sample was elastically saturated with magnetization oriented along the thickness of the sample and the domains imaged are limited only to the surface without permeating through the sample. Elastic field could not be applied to 17Q because the sample's edges were not smoothed. Due to this the sample's edges could not be in complete contact with the elastic field apparatus leading to non-uniform elastic fields.

In conclusion, it was shown that insufficient polishing causes residual stresses that induce a perpendicular surface anisotropy resulting in maze-like surface domains, hiding the real domains. Due to increased magnetostriction, Fe–Ga alloys

are perhaps more susceptible to the formation of surface stress-induced domain patterns. It was demonstrated that an additional polishing step using colloidal silica sufficed to remove the damaged surface layer. The "true" domains as imaged by both MFM and Kerr microscopies show large in-plane domains with sharp 90° and 180° domain walls, as expected for soft-magnetic materials that are cubic with positive anisotropy energy. From these results, the conclusions of previous works that the presence of heterogeneities in Fe–Ga engenders irregular maze-like domain patterns [57, 62] or that a dendritic subdomain structure exists within the regular domains of Fe–Ga [88] cannot be upheld. From the domain images under magnetic field, the magnetic domains, local magnetization, and magnetostriction were observed to be strongly connected. From the elastic field experiments, it was observed that the magnetic domains respond to the elastic fields as expected. In summary, there was no evidence of any unusual behavior in Fe–Ga alloys. In all the three samples studied, the magnetic domains and magnetostriction seem to be closely connected with each other. Further, there is no evidence of any heterogeneity related irregularities from the magnetic domain images.

Chapter 4

Neutron Scattering

4.1 Overview

In this chapter, neutron scattering experiments are detailed. First some background on neutrons and neutron scattering is provided. In the next section, interaction of neutrons with nuclei, resulting in nuclear scattering is explained followed by a section detailing the magnetic scattering due to the interaction of neutron with atomic spins. Thereafter, neutron diffraction from single crystals is introduced. In subsequent sections, setup for various experiments conducted followed by the results are provided.

4.2 Background

The neutron is one of the several subatomic particles. Unlike electrons or protons, the neutron has no charge. It has a mass of 1.675×10^{-27} Kg [93], and a magnetic moment of -9.649×10^{-27} JT^{-1} [93]. Like all subatomic particles, the neutron displays the wave/particle duality i.e., it can be both a particle and a wave at the same time. As such the neutrons display a variety of wave behaviors like reflection, refraction, diffraction etc.

When a beam of neutrons is incident on a sample of thickness ζ, it leads to 1)

a transmitted beam, 2) coherent scattering, 3) incoherent scattering, 4) absorption, and 5) multiple coherent scattering. Therefore, the total scattering cross section can be expressed as

$$\sigma_T = \sigma_{coh} + \sigma_{incoh} + \sigma_{abs}. \tag{4.1}$$

Coherent scattering involves correlations between the positions of an atom and hence it contains structural and magnetic information of a sample. Incoherent scattering involves correlations between the position of an atom at time zero and the position of the same atom at time t. Thus, there is no interference of scattered waves from different nuclei. Thus, incoherent scattering often leads to a flat background, independent of the scattering angle. For a brief overview of neutron scattering the readers are referred to [94] and for a detailed overview, the readers are referred to [93]. In this chapter, we limit our discussion to the coherent elastic scattering.

The neutron scattering has two components: *nuclear scattering*, due to the interaction of the neutrons with the nucleus of the atoms, and *magnetic scattering*, due to the interaction of the magnetic spin of neutrons with the magnetic moment (or unpaired electrons).

4.2.1 Nuclear Scattering

In elastic scattering, the scattering neutron changes only its direction i.e., only the momentum is transfered and not the energy. So, if the wave vector of the incident neutron is $\boldsymbol{k}$ and the scattered neutron is $\boldsymbol{k_s}$ then $|\boldsymbol{k}| = |\boldsymbol{k_s}|$. Compared to the wavelength of the neutrons ($\sim 10^{-10}$ m), the range of the nuclear forces (10^{-14}

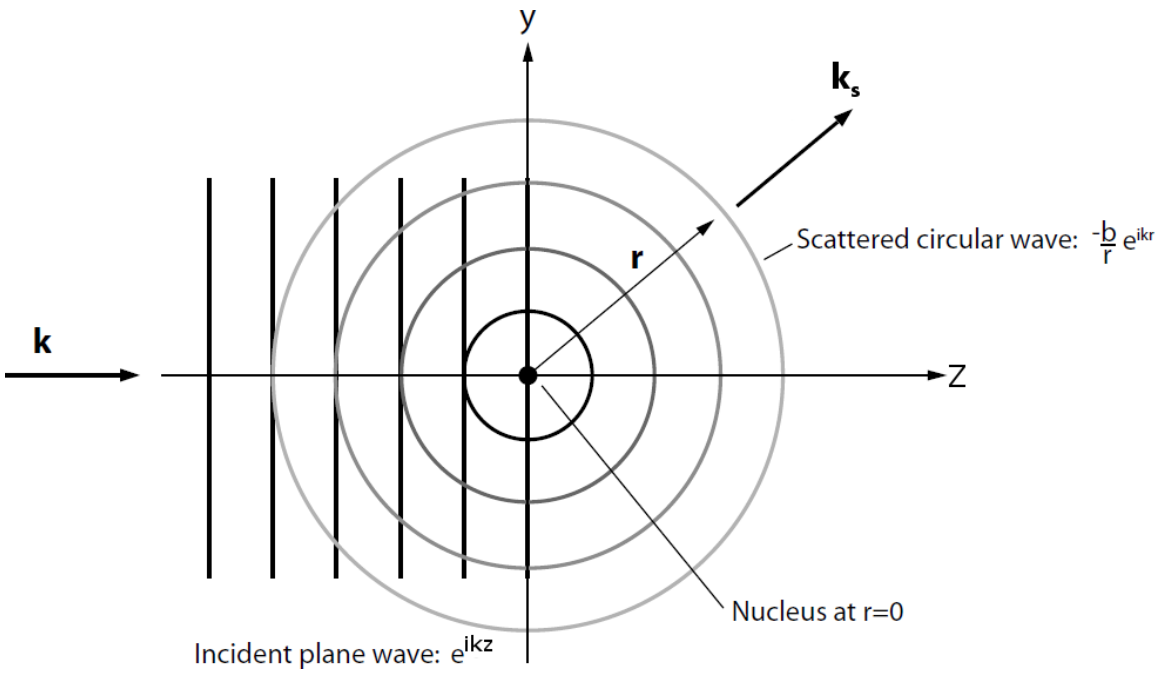

Figure 4.1: Schematic showing the elastic scattering of the neutron from a fixed nucleus. Taken from [94]

to 10^{-15} m) that cause the scattering is much shorter. Thus, the nucleus essentially acts as a point scatterer leading to a scattering wave that is spherically symmetric.

By assuming the origin to be at the position of the nucleus, and the incident neutron's wave vector $\boldsymbol{k}$ to be along the z-axis of the coordinate system (see figure 4.1), the wave function of the incident neutrons can be represented by

$$\psi_i = e^{ikz}. \tag{4.2}$$

Since the scattered wave is spherically symmetric, the wavefunction of the scattered neutrons at a point $\boldsymbol{r}$ can be written as

$$\psi_s = -\frac{b}{r}e^{ikr}, \tag{4.3}$$

where b is the nuclear scattering length representing the interaction of the neutron

with the nucleus. An effective interaction potential ($V(\boldsymbol{r})$), called Fermi pseudopotential, is described. For a single nucleus, this potential is related to the scattering length as $V(\boldsymbol{r}) = b_j\delta(\boldsymbol{r} - \boldsymbol{r}_j)$, where δ is the Dirac delta function. For an assembly of nuclei, the potential $V(\boldsymbol{r})$ can be written in terms of the scattering length as

$$V(\boldsymbol{r}) = \sum_j b_j\delta(\boldsymbol{r} - \boldsymbol{r}_j). \tag{4.4}$$

The negative sign in equation (4.3) is arbitrary and corresponds to a positive value of b for a repulsive interaction potential. The scattering length is a complex number and varies rapidly with the energy of the neutron. The imaginary part of the scattering length corresponds to absorption. Nuclei of ^{103}Rh, ^{113}Cd, ^{157}Gd, and ^{176}Lu, which have a large imaginary part, strongly absorb neutrons. Since the majority of the nuclei have a small imaginary part and do not significantly absorb neutrons, their scattering lengths can be treated as real quantities.

For a three-dimensional assembly of nuclei, the resulting scattered wave can be written as the sum of the scattered vectors from all the nuclei

$$\psi_s = -\sum_j \left(\frac{b_j}{r}\right) e^{i\boldsymbol{q}\cdot\boldsymbol{r}}, \tag{4.5}$$

where $\boldsymbol{q} = \boldsymbol{k} - \boldsymbol{k_s}$ is the scattering vector with $\boldsymbol{k}$ and $\boldsymbol{k_s}$ being the wave vectors of the incident and scattered neutrons respectively.

4.2.1.1 Scattering Cross Section

Scattering cross-section is a measure of the *effective* area of the nucleus that scatters the neutrons. It is the quantity that is actually measured in a scattering

experiment. If a beam of neutrons of a given energy E is incident on a scattering system (see figure 4.2), a neutron counter can be set up that counts the neutrons scattered into the solid angle $d\Omega$ along the direction θ, ϕ. The differential cross-section can then be defined as

$$\frac{d\sigma}{d\Omega} = \frac{\text{number of neutrons scattered per second into } d\Omega}{\Phi d\Omega}, \tag{4.6}$$

where Φ is the flux of the incident neutrons. The total scattering cross-section is the number of neutrons scattered in all directions and is given by

$$\sigma_{tot} = \int_{alldirections} \left(\frac{d\sigma}{d\Omega}\right) d\Omega. \tag{4.7}$$

Experimentally these cross-sections are typically quoted per atom or per molecule and thus the expressions above are divided by the number of atoms or molecules in the scattering system.

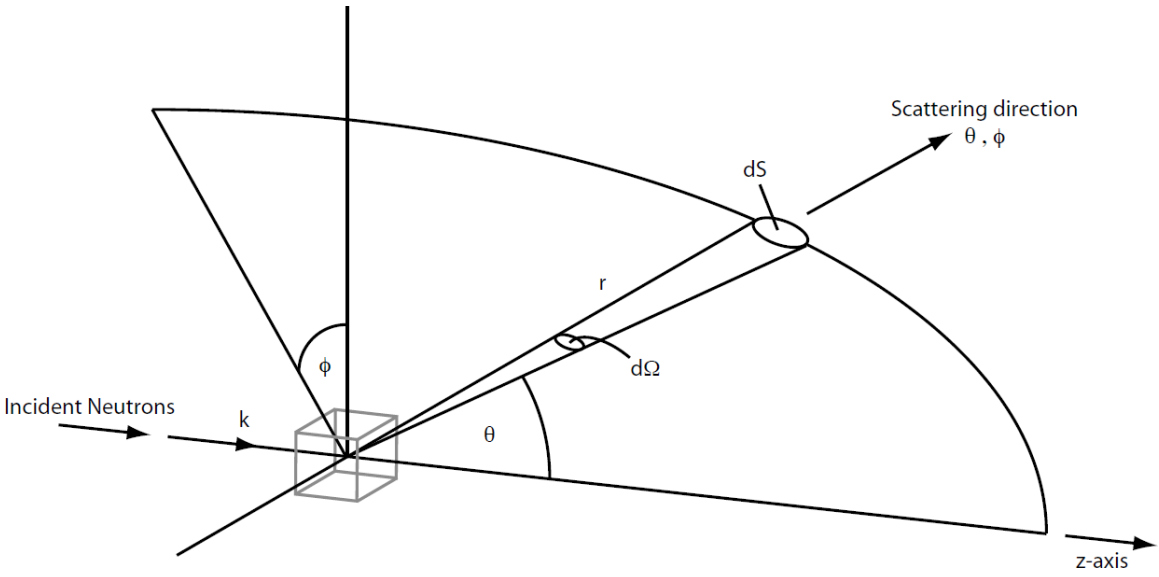

Figure 4.2: Geometry of a scattering experiment [93]

Using the above expressions, the cross-section $d\sigma/d\Omega$ can be calculated. If the velocity of the neutrons is denoted as v then the number of scattered neutrons passing through an area dS per second is

$$v dS|\psi_s|^2 = v\frac{dS}{r^2}\left|\sum_j^N b_j e^{i\boldsymbol{q}\cdot\boldsymbol{r}}\right|^2 = v\left|\sum_j^N b_j e^{i\boldsymbol{q}\cdot\boldsymbol{r}}\right|^2 d\Omega. \tag{4.8}$$

The flux of incident neutrons is

$$\Phi = v|\psi_i|^2 = v. \tag{4.9}$$

From the definition of the scattering cross-section in equation (4.6),

$$\frac{d\sigma}{d\Omega}(\boldsymbol{q}) = \frac{1}{N}\frac{v\left|\sum_j^N b_j e^{i\boldsymbol{q}\cdot\boldsymbol{r}}\right|^2 d\Omega}{\Phi d\Omega} = \frac{1}{N}\left|\sum_j^N b_j e^{i\boldsymbol{q}\cdot\boldsymbol{r}}\right|^2. \tag{4.10}$$

The scattering cross-section can also be expressed in terms of the interaction potential $V(\boldsymbol{r})$ as

$$\frac{d\sigma}{d\Omega}(\boldsymbol{q}) = \frac{1}{\nu}\left|\int_\nu V(\boldsymbol{r})e^{i\boldsymbol{q}\cdot\boldsymbol{r}}dr\right|^2, \tag{4.11}$$

where ν is volume of the scattering system.

4.2.2 Magnetic Scattering

Equation (4.4) defines the potential for the interaction of the neutron with the nucleus, which yields the nuclear scattering cross-section equation in (4.11). Similary, we must derive the potential $V_M(\boldsymbol{r})$ defining the magnetic interaction between the neutron and unparied electrons.

The magnetic dipole moment of the neutron can be defined as

$$\boldsymbol{\mu}_n = -\gamma\mu_N\boldsymbol{\sigma}, \tag{4.12}$$

where

$$\mu_N = \frac{e\hbar}{2m_p} \tag{4.13}$$

is the nuclear magneton. m_p is the mass of the proton and e its charge. γ is a positive constant known as gyromagnetic operator and its value is $\gamma = 1.913$. $\boldsymbol{\sigma}$ is the Pauli spin operator for the neutron and is represented by a 2×2 matrix [93].

Similarly, the magnetic dipole moment of the electron can be defined as

$$\boldsymbol{\mu}_e = -2\mu_B \boldsymbol{s}, \tag{4.14}$$

where

$$\mu_B = \frac{e\hbar}{2m_e} \tag{4.15}$$

is the Bohr magneton. m_e is the mass of the electron. $\boldsymbol{s}$ is the spin angular momentum operator for the electrons. Its values are $\pm\frac{1}{2}$.

The magnetic field due to the magnetic dipole moment of the electron at a point $\boldsymbol{R}$ from it can be expressed as

$$\boldsymbol{B}_S = \nabla \times \left(\frac{\mu_0}{4\pi} \frac{\boldsymbol{\mu_e} \times \hat{\boldsymbol{R}}}{R^2} \right), \tag{4.16}$$

where $\hat{\boldsymbol{R}}$ is a unit vector parallel to $\boldsymbol{R}$. Using Biot-Savart law that states the magnetic field at a point $\boldsymbol{R}$ due to a current element $I\,dl$, the magnetic field due to the momentum of the electron can be obtained as

$$\boldsymbol{B}_L = \frac{\mu_0}{4\pi} I \frac{d\boldsymbol{l} \times \hat{\boldsymbol{R}}}{R^2}, \tag{4.17}$$

where the current element for the moving electron with momentum $\boldsymbol{p}$ is

$$I\,d\boldsymbol{l} = -\frac{e}{m_e}\boldsymbol{p} = -\frac{2\mu_B}{\hbar}\boldsymbol{p}. \tag{4.18}$$

The total magnetic field due to an electron is therefore

$$\boldsymbol{B} = \boldsymbol{B}_S + \boldsymbol{B}_L = \frac{\mu_0}{4\pi}\left\{\nabla \times \left(\frac{\boldsymbol{\mu}_e \times \hat{\boldsymbol{R}}}{R^2}\right) - \frac{2\mu_B}{\hbar}\frac{\boldsymbol{p} \times \hat{\boldsymbol{R}}}{R^2}\right\} \tag{4.19}$$

The magnetic interaction potential of the neutron with dipole moment $\boldsymbol{\mu}_n$ due to this magnetic field ($\boldsymbol{B}$) is

$$V_M(\boldsymbol{R}) = -\boldsymbol{\mu}_n \cdot \boldsymbol{B} = -\gamma\mu_N^2\mu_B\sigma \cdot \left\{\nabla \times \left(\frac{\boldsymbol{s} \times \hat{\boldsymbol{R}}}{R^2}\right) + \frac{1}{\hbar}\frac{\boldsymbol{p} \times \hat{\boldsymbol{R}}}{R^2}\right\}. \tag{4.20}$$

The first term in this equation

$$\boldsymbol{W}_S = \nabla \times \left(\frac{\boldsymbol{s} \times \hat{\boldsymbol{R}}}{R^2}\right) \tag{4.21}$$

is the potential arising from the spin of the electron and the second term

$$\boldsymbol{W}_L = \frac{1}{\hbar}\frac{\boldsymbol{p} \times \hat{\boldsymbol{R}}}{R^2} \tag{4.22}$$

is the potential arising from the orbital motion of the electron.

Using $V_M(\boldsymbol{R})$ instead of $V(\boldsymbol{r})$ in equation (4.11), the magnetic scattering cross-section is

$$\frac{d\sigma}{d\Omega}(\boldsymbol{q}) = \frac{1}{\nu}\left|\int V_M(\boldsymbol{R})e^{i\boldsymbol{q}\cdot\boldsymbol{r}}dr\right|^2. \tag{4.23}$$

If we consider the spin contribution of the ith electron with spin $\boldsymbol{s}_i$ and position vector $\boldsymbol{r}_i$ then

$$\int \boldsymbol{W}_{Si}(\boldsymbol{R})e^{i\boldsymbol{q}\cdot\boldsymbol{r}}dr = \int \nabla \times \left(\frac{\boldsymbol{s}_i \times \hat{\boldsymbol{R}}}{R^2}\right)e^{i\boldsymbol{q}\cdot\boldsymbol{r}}dr. \tag{4.24}$$

Using the mathematical result (refer to [93] for derivation)

$$\nabla \times \left(\frac{\boldsymbol{s} \times \hat{\boldsymbol{R}}}{R^2}\right) = \frac{1}{2\pi^2}\int \hat{\boldsymbol{k}} \times (\boldsymbol{s} \times \hat{\boldsymbol{k}})e^{i\boldsymbol{k}\cdot\boldsymbol{R}}\,d\boldsymbol{k} \tag{4.25}$$

and that $\boldsymbol{r} = \boldsymbol{r}_i + \boldsymbol{R}$,

$$\int \boldsymbol{W}_{Si}(\boldsymbol{R}) e^{i\boldsymbol{q}\cdot\boldsymbol{r}} dr = \frac{1}{2\pi^2} e^{i\boldsymbol{q}\cdot\boldsymbol{r}_i} \int \hat{\boldsymbol{k}} \times (\boldsymbol{s}_i \times \hat{\boldsymbol{k}}) e^{i(\boldsymbol{q}+\boldsymbol{k})\cdot\boldsymbol{R}} d\boldsymbol{k}\, d\boldsymbol{R}. \tag{4.26}$$

Since

$$\int e^{i(\boldsymbol{q}+\boldsymbol{k})\cdot\boldsymbol{R}} d\boldsymbol{R} = (2\pi)^3 \delta(\boldsymbol{q}+\boldsymbol{k}), \tag{4.27}$$

the spin contribution to the magnetic cross section can be expressed as

$$\int \boldsymbol{W}_{Si}(\boldsymbol{R}) e^{i\boldsymbol{q}\cdot\boldsymbol{r}} dr = 4\pi e^{i\boldsymbol{q}\cdot\boldsymbol{r}_i} \left\{ \hat{\boldsymbol{q}} \times (\boldsymbol{s}_i \times \hat{\boldsymbol{q}}) \right\}. \tag{4.28}$$

Next we consider the orbital contribution of the ith electron with momentum $\boldsymbol{p}_i$ at position $\boldsymbol{r}_i$ to simplify

$$\int \boldsymbol{W}_{Li}(\boldsymbol{R}) e^{i\boldsymbol{q}\cdot\boldsymbol{r}} dr = \frac{1}{\hbar} \int \frac{\boldsymbol{p} \times \hat{\boldsymbol{R}}}{R^2} e^{i\boldsymbol{q}\cdot\boldsymbol{r}} dr. \tag{4.29}$$

Again using $\boldsymbol{r} = \boldsymbol{r}_i + \boldsymbol{R}$ and the mathematical result [93]

$$\int \frac{\hat{\boldsymbol{R}}}{R^2} e^{i\boldsymbol{q}\cdot\boldsymbol{r}} dr = 4\pi i \frac{\hat{\boldsymbol{q}}}{q}, \tag{4.30}$$

equation (4.29) can be simplified to

$$\int \boldsymbol{W}_{Li}(\boldsymbol{R}) e^{i\boldsymbol{q}\cdot\boldsymbol{r}} dr = \frac{4\pi i}{\hbar q} e^{i\boldsymbol{q}\cdot\boldsymbol{r}_i} (\boldsymbol{p}_i \times \hat{\boldsymbol{q}}). \tag{4.31}$$

Substituting equations (4.28) and (4.31) in equation (4.23)and simplifying,

$$\frac{d\sigma}{d\Omega}(\boldsymbol{q}) = -\frac{\gamma r_0}{\nu} \left| \boldsymbol{\sigma} \cdot \boldsymbol{Q}_\perp \right|^2, \tag{4.32}$$

where

$$\boldsymbol{Q}_\perp = \int \left\{ \hat{\boldsymbol{q}} \times (\boldsymbol{s} \times \hat{\boldsymbol{q}}) + \frac{i}{\hbar q} (\boldsymbol{p} \times \hat{\boldsymbol{q}}) \right\} e^{i\boldsymbol{q}\cdot\boldsymbol{r}} dr. \tag{4.33}$$

The operator $\boldsymbol{Q}_\perp$, known as Halpern-Johnson vector [95], is related to the total magnetization $\boldsymbol{M}$ (sum of the magnetic moment due to spin and orbital motion) of the scattering system as follows

$$\boldsymbol{Q}_\perp = -\frac{1}{2\mu_B}\left\{\hat{\boldsymbol{q}} \times (\boldsymbol{M}(\boldsymbol{q}) \times \hat{\boldsymbol{q}})\right\}, \tag{4.34}$$

where $\boldsymbol{M}(\boldsymbol{q})$ is the Fourier transform of $\boldsymbol{M}(\boldsymbol{r})$. $\boldsymbol{M}_\perp$ can be defined as $\boldsymbol{M}_\perp = \hat{\boldsymbol{q}} \times (\boldsymbol{M}(\boldsymbol{q}) \times \hat{\boldsymbol{q}})$ and can be simplified to

$$\boldsymbol{M}_\perp = \boldsymbol{M}(\boldsymbol{q}) - (\boldsymbol{M}(\boldsymbol{q}) \cdot \hat{\boldsymbol{q}})\, \hat{\boldsymbol{q}}. \tag{4.35}$$

This indicates that only the component of magnetization perpendicular to the scattering vector is effective in scattering the neutrons.

Using this,

$$\frac{d\sigma}{d\Omega}(\boldsymbol{q}) = \frac{1}{\nu}\left(\gamma r_0\right)^2 \left|\boldsymbol{\sigma} \cdot \boldsymbol{Q}_\perp\right|^2. \tag{4.36}$$

The operator $\boldsymbol{\sigma}$ depends only on the spin coordinates of the neutron and the operator $\boldsymbol{Q}_\perp$ depends only on the coordinates (both space and spin) of the electron. And they both are independent of each other.

Equation (4.36) can alternatively be expressed using bracket notation [93] as

$$\frac{d\sigma}{d\Omega}(\boldsymbol{q}) = \frac{1}{\nu}\left(\gamma r_0\right)^2 \sum_{\sigma\sigma_s} p_\sigma \left|\langle\sigma_s|\boldsymbol{\sigma} \cdot \boldsymbol{Q}_\perp|\sigma\rangle\right|^2, \tag{4.37}$$

where p_σ is the probability that the neutron is initially in the state σ. It describes the polarization of the incident beam. The neutron has spin $\frac{1}{2}$ and so has two spin states which are denoted by $+$ and $-$. These may be regarded as corresponding 'spin up' and 'spin down' relative to a specified axis (x axis). The bracket notation

indicates the probability of an incident neutron with spin state σ to get scattered to have a spin state σ_s.

4.2.2.1 Unpolarized Neutrons

For unpolarized incident neutrons,

$$p_u = p_v = \frac{1}{2}. \tag{4.38}$$

Simplifying equation (4.37) (for details refer to [93]) and using equation (4.34) we can get

$$\frac{d\sigma}{d\Omega}(\boldsymbol{q}) = \frac{1}{\nu}\left(\frac{\gamma r_0}{2\mu_B}\right)^2 |\boldsymbol{M}_\perp|^2 . \tag{4.39}$$

The total scattering cross-section is the sum of nuclear and magnetic cross-sections. Therefore the total scattering cross-section is

$$\frac{d\Sigma}{d\Omega}(\boldsymbol{q}) = \frac{1}{\nu}\left(\frac{\gamma r_0}{2\mu_B}\right)^2 \left(A^2 + |\boldsymbol{M}_\perp|^2\right), \tag{4.40}$$

where

$$A = V(\boldsymbol{q})\left(\frac{2\mu_B}{\gamma r_0}\right)^2, \tag{4.41}$$

$V(\boldsymbol{q})$ is the Fourier transform of the neutron-nuclear interaction potential $V(\boldsymbol{r})$ defined in equation (4.4).

Let the incident neutrons are along z axis. Then the scattering vector lies in the $y-x$ plane and can be expressed in terms of the azimuthal angle θ (x axis as

the reference) as $\hat{\boldsymbol{q}} = (\cos\theta, \sin\theta, 0)$. If the components of $\boldsymbol{M}_\perp$ are (X, Y, Z) then

$$\boldsymbol{M}_\perp = \begin{pmatrix} X\sin^2\theta - Y\sin\theta\cos\theta \\ Y\cos^2\theta - X\sin\theta\cos\theta \\ Z \end{pmatrix}. \tag{4.42}$$

Therefore, equation (4.39) can be expanded to

$$\frac{d\Sigma}{d\Omega}(\boldsymbol{q}) = \frac{1}{\nu}\left(\frac{\gamma r_0}{2\mu_B}\right)^2 \left(A^2 + Z^2 + X^2\sin^2\theta + Y^2\cos^2\theta - 2XY\sin\theta\cos\theta\right). \tag{4.43}$$

4.2.2.2 Polarized Neutrons

Equation (4.37) can be rewritten using equation (4.34) as

$$\frac{d\Sigma}{d\Omega}(\boldsymbol{q}) = \frac{1}{\nu}\left(\frac{\gamma r_0}{2\mu_B}\right)^2 \sum_{\sigma\sigma_s} p_\sigma \left|\langle\sigma_s|\boldsymbol{\sigma}\cdot\boldsymbol{M}_\perp|\sigma\rangle\right|^2. \tag{4.44}$$

Polarized neutrons give rise to four cross-sections, which can be called *spin-state* cross-sections and they are:

$$+\to+, \quad -\to-, \quad +\to-, \quad -\to-. \tag{4.45}$$

Of these, cross-sections corresponding to $+\to+$ and $-\to-$ are called *non-spin-flip* cross-sections and $+\to-$ and $-\to+$ are called *spin-flip* cross-sections.

The total scattering cross-section, including nuclear and magnetic cross-sections can then be defined as

$$\frac{d\Sigma}{d\Omega}(\boldsymbol{q}) = \frac{1}{\nu}\left(\frac{\gamma r_0}{2\mu_B}\right)^2 \sum_{\sigma\sigma_s} p_\sigma \left|\langle\sigma_s|A - \boldsymbol{\sigma}\cdot\boldsymbol{M}_\perp|\sigma\rangle\right|^2. \tag{4.46}$$

Now, let an operator be defined such that

$$U^{\sigma_s\sigma} = \langle\sigma_s|A - \boldsymbol{\sigma}\cdot\boldsymbol{M}_\perp|\sigma\rangle, \tag{4.47}$$

then (refer to [93, 96] for derivation), assuming the direction of polarization to be along $\boldsymbol{hatx}$,

$$\begin{aligned} U^{++} &= A - M_{\perp x}, \\ U^{--} &= A + M_{\perp x}, \\ U^{+-} &= -(M_{\perp z} + iM_{\perp y}), \\ U^{+-} &= -(M_{\perp z} - iM_{\perp y}). \end{aligned} \tag{4.48}$$

Therefore, the non-spin-flip scattering cross-section is

$$\begin{aligned} \frac{d\Sigma^{\pm\pm}}{d\Omega}(\boldsymbol{q}) =& \frac{1}{\nu}\left(\frac{\gamma r_0}{2\mu_B}\right)^2 |A \mp M_{\perp x}|^2 \\ =& \frac{1}{\nu}\left(\frac{\gamma r_0}{2\mu_B}\right)^2 \Big(A^2 + X^2 \sin^4\theta + Y^2 \sin^2\theta\cos^2\theta - 2XY \sin^3\theta\cos\theta \\ & \mp 2AX \sin^2\theta \pm 2AY \sin\theta\cos\theta\Big) \end{aligned} \tag{4.49}$$

and the spin-flip scattering cross-section is

$$\begin{aligned} \frac{d\Sigma^{\pm\mp}}{d\Omega}(\boldsymbol{q}) =& \frac{1}{\nu}\left(\frac{\gamma r_0}{2\mu_B}\right)^2 |M_{\perp z} \pm iM_{\perp y}|^2 \\ =& \frac{1}{\nu}\left(\frac{\gamma r_0}{2\mu_B}\right)^2 \Big(Z^2 + X^2 \sin^2\theta\cos^2\theta + Y^2 \cos^4\theta - 2XY \cos^3\theta\sin\theta\Big). \end{aligned} \tag{4.50}$$

It can be seen that as expected the sum of all spin-state cross-sections equals twice the cross-section for unpolarized neutrons in equation (4.43).

4.2.3 Small-Angle Neutron Scattering

So far the discussion was focused on atomic scales dealing with atomic nuclei. However, for small-angle neutron scattering, length scales much larger than the

atomic dimensions are important. The neutron wavelength, λ , and scattering angle, θ_s , determine the scattering length scale. The relationships

$$|q| = \frac{4\pi}{\lambda} \sin(\theta_s) \approx \frac{4\pi\theta_s}{\lambda}, \tag{4.51}$$

and

$$d = \frac{2\pi}{|q|} \approx \frac{\lambda}{2\theta_s} \tag{4.52}$$

show that for small θ_s (or small-angle), d is much larger. Further, through the use of cold (i.e. long wavelength) neutrons and tight beam collimation, the SANS instruments are able to probe structure on a length scale, d, ranging from 1 nm to nearly 10,000 nm. Therefore, it is easier to think in terms of material properties rather than the atomic properties. As a result, scattering length density (SLD) is important than the scattering length itself.

The nuclear scattering length density (SLD) of a phase can be calculated as

$$\rho(r) = \frac{\sum_i^N b_i \delta(r - R_i)}{\nu}, \tag{4.53}$$

where b_i is the scattering length of the ith atom in the unit cell and ν is the volume of the unit cell.

Magnetic SLD can be calculated using

$$\rho_m = \frac{1}{\nu} \frac{\gamma r_0}{2\mu_B} M = CM, \tag{4.54}$$

where $C = 2.9109 \times 10^{-5}/4\pi$ Å^{-2}T^{-1} [97] and M is the magnetization of the phase in T.

4.2.3.1 Contrast

For simplicity, considering nuclear scattering alone, the macroscopic cross-section can be expressed as

$$\frac{d\Sigma}{d\Omega}(\boldsymbol{q}) = \frac{1}{\nu}\left|\int_{\nu}\rho(\boldsymbol{r})e^{i\boldsymbol{q}\cdot\boldsymbol{r}}dr\right|^2. \tag{4.55}$$

This shows us that small angle scattering arises due to the inhomogeneities in scattering length density $\rho(\boldsymbol{r})$.

Now, let us consider a scattering system that has two phases with scattering length densities to be ρ_1 and ρ_2 respectively and volumes ν_1 and ν_2 respectively. Using equation (4.55) and breaking the total volume into two sub volumes

$$\frac{d\Sigma}{d\Omega}(\boldsymbol{q}) = \frac{1}{\nu}\left|\int_{\nu_1}\rho_1 e^{i\boldsymbol{q}\cdot\boldsymbol{r}}dr_1 + \int_{\nu_2}\rho_2 e^{i\boldsymbol{q}\cdot\boldsymbol{r}}dr_2\right|^2 \tag{4.56}$$

gives

$$\frac{d\Sigma}{d\Omega}(\boldsymbol{q}) = \frac{1}{\nu}(\rho_1-\rho_2)^2\left|\int_{\nu_1} e^{i\boldsymbol{q}\cdot\boldsymbol{r}}dr_1\right|^2. \tag{4.57}$$

Therefore the scattering cross-section is proportional to the square of the difference in scattering length densities. The integral term describes the spatial arrangement of the material (and hence the phases). It can be seen that experimentally only the term $(\rho_1-\rho_2)^2$ can be determined and it is not possible to determine if $\rho_1 > \rho_2$ or otherwise.

As described in the introduction, Fe–Ga alloys may have one or more of the following phases - A2, DO3, $D0_{22}$, $L1_2$, or B2. The scattering length of Fe and Ga are 9.45 fm and 7.228 fm [98] respectively. The DO3, $D0_{22}$, $L1_2$ phases have 25% Ga and 75% Fe and B2 has 50% Ga and 50% Fe. Table 4.1 shows the nuclear

and magnetic SLDs calculated for different phases in Fe–Ga. As discussed earlier,

Table 4.1: Scattering Length Densities (SLDs)

Phase	Nuclear SLD ($Å^{-2}$)	†Magnetic SLD ($Å^{-2}$)
‡A2	7.4×10^{-6}	4.0×10^{-6}
DO3	7.3×10^{-6}	3.2×10^{-6}
*$D0_{22}$	7.3×10^{-6}	3.2×10^{-6}
*$L1_2$	7.3×10^{-6}	3.2×10^{-6}
*B_2	6.9×10^{-6}	$< 3.2 \times 10^{-6}$

‡ Assuming $Fe_{81}Ga_{19}$ and $M = 1.74$ T (measured in Chapter 2).

* Assuming $\nu = \nu_{A2}$

† M values taken from [99]

a contrast in neutron scattering results due to the difference in the SLDs of matrix and heterogeneity. It can be seen from table 4.1 that the nuclear SLDs of A2, DO3, $D0_{22}$, and $L1_2$ are very similar. Therefore, a very weak nuclear contrast is expected even if there are any heterogeneities of different phase existing in these alloys. The presence of such heterogeneities can still be detected as they are expected to provide a good magnetic contrast.

4.2.4 Neutron Diffraction by Crystals

The summation in equation (4.10) extends to all the nuclei in the sample. In a crystal, the nuclei are arranged in a repetitive structure called a lattice. Assuming a cubic structure and the lattice parameter to be a, a lattice vector $\boldsymbol{a}$ can be defined as $\boldsymbol{a} = a(n_1\hat{\boldsymbol{i}} + n_2\hat{\boldsymbol{j}} + n_3\hat{\boldsymbol{k}})$. The position of any nucleus ($\boldsymbol{r}$) can then be defined in terms of the position of the nucleus in the unit cell ($\boldsymbol{r}_l$) as $\boldsymbol{r} = \boldsymbol{r}_l + \boldsymbol{a}$. Using this, equation (4.10) can be re-written as

$$\frac{d\sigma}{d\Omega}(\boldsymbol{q}) \propto \left| \sum_j^N \sum_l b_l e^{i\boldsymbol{q}\cdot(\boldsymbol{r}_l+\boldsymbol{a})} \right|^2 \tag{4.58}$$

$$\propto \left| S(\boldsymbol{q}) \sum_j e^{i\boldsymbol{q}\cdot\boldsymbol{a}} \right|^2 . \tag{4.59}$$

where $S(\boldsymbol{q})$ is called the unit-cell structure factor. Index l in the summation for $S(\boldsymbol{q})$ covers for all the nuclei within a unit cell of the lattice. Using (for derivation refer to [93])

$$\sum_j e^{i\boldsymbol{q}\cdot\boldsymbol{a}} = \frac{(2\pi)^3}{\nu_0} \sum_\tau \delta(\boldsymbol{q} - \boldsymbol{\tau}), \tag{4.60}$$

where ν_0 is the volume of the unit cell, one can write

$$\frac{d\sigma}{d\Omega}(\boldsymbol{q}) \propto \left| S(\boldsymbol{q}) \sum_\tau \delta(\boldsymbol{q} - \boldsymbol{\tau}) \right|^2 . \tag{4.61}$$

where $\boldsymbol{\tau}$ is the reciprocal lattice vector. For cubic materials, $\boldsymbol{\tau} = 2\pi/a(h\hat{\boldsymbol{i}} + k\hat{\boldsymbol{j}} + l\hat{\boldsymbol{k}})$. Hence,

$$S_{hkl} = \sum_l b_l e^{i2\pi(hn_1+kn_2+ln_3)} \tag{4.62}$$

and the scattering cross-section is the square of the structure factor and is visible only when $\boldsymbol{q} = \boldsymbol{\tau}$. Therefore,

$$\left(\frac{d\sigma}{d\Omega}\right)_{hkl} \propto |S_{hkl}|^2 , \tag{4.63}$$

which indicates that the structure factor S_{hkl} determines which of the reciprocal lattice points will be visible.

4.2.5 Optimal thickness

One important question is how much thick the sample should be to obtain an optimal intensity of the scattered neutron beam. As discussed before, the incident neutrons on a scattering system lead to 1) transmitted neutrons 2) coherently scattered neutrons 3) incoherently scattered neutrons, and 4) absorbed neutrons. The sum of all these four cross-sections is the total cross-section Σ_T (see equation (4.1). If ζ is the sample thickness then the expression for the transmission is

$$T = \frac{I}{I_0} = \exp\left(-\Sigma_T \zeta\right) \tag{4.64}$$

and the expression for the scattered intensity is

$$I_s \propto \zeta T \left(\frac{d\Sigma_{coh}}{d\Omega}\right) \propto \zeta \exp\left(-\Sigma_T \zeta\right) \left(\frac{d\Sigma_{coh}}{d\Omega}\right), \tag{4.65}$$

where I is the intensity of the transmitted neutrons, I_0 is that of the incident neutrons, I_s is that of the coherently scattered neutrons.

When $\sigma_T \approx \sigma_{coh}$, i.e., when $\sigma_{incoh} + \sigma_{abs}$ is negligible, then there may be a problem of multiple scattering. To mitigate this, the thickness of the sample ζ is choosen such that the transmission $T \geq 90\%$. When $\sigma_{coh} \ll \sigma_T \approx \sigma_{incoh} + \sigma_{abs}$ then

the multiple scattering problem is no longer present. In such case, the scattered intensity I_s is maximized. Since

$$I_s \propto \zeta \exp\left(-\Sigma_T \zeta\right) \left(\frac{d\Sigma_{coh}}{d\Omega}\right) \approx \zeta \exp\left(-\Sigma_T \zeta\right), \tag{4.66}$$

the maximum occurs when $\zeta = 1/\Sigma_T$ that results in $T = 1/e = 37\%$.

4.3 Setup

4.3.1 Small-Angle Neutron Scattering (SANS)

Small-Angle Neutron Scattering (SANS) probes structure in materials on the nanometer (10^{-9} m) to micrometer (10^{-6} m) scale. SANS is widely used to study polymers [100]. A contrast is produced due to a difference in the magnetization of the sample at different length scales. The NG3 and NG7 30m SANS instruments [101] at NIST Center for Neutron Research (NCNR) were used in this study. The schematic of the instrument is shown in figure 4.3 and the characteristics of the instruments is listed in table 4.2

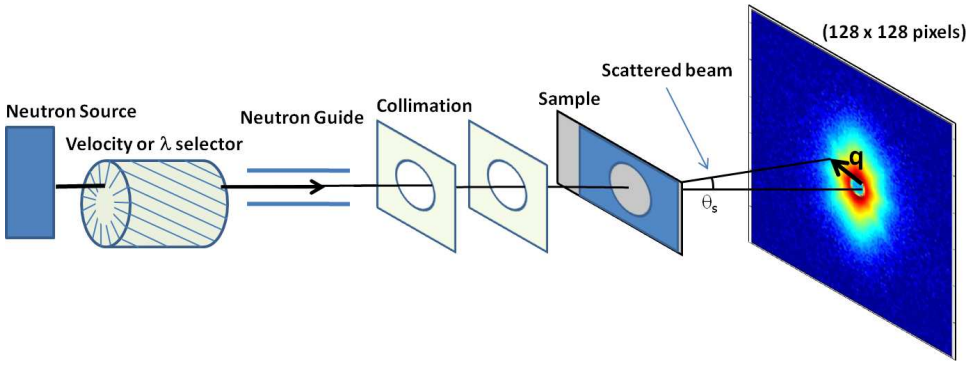

Figure 4.3: Schematic of Small-Angle Neutron Scattering (SANS)

Table 4.2: 30m NG3SANS Characteristics [102]

Source:	Neutron guide 6×6 cm^2
Monochromator:	Mechanical velocity selector with variable speed and pitch
Wavelength (λ):	5 Å to 20 Å
λ spread:	$\Delta\lambda/\lambda = 10\%$ to 30% (FWHM)
Collimation:	Circular pin hole / lenses
Q-range:	0.001 to 0.6 Å^{-1}
Size regime:	10 Å to 6000 Å
Detector:	64×64 cm^2 He-3 position sensitive area detector proportional counter with (0.5 cm^2 resolution) i.e., 128×128 pixels
Magnetic field:	0 - 1.6 T at sample position

Since the scattering vector

$$q \approx \frac{4\pi\theta_s}{\lambda}, \tag{4.67}$$

the q-resolution function is

$$\left(\frac{\Delta q}{q}\right)^2 = \left(\frac{\Delta\theta_s}{\theta_s}\right)^2 + \left(\frac{\Delta\lambda}{\lambda}\right)^2. \tag{4.68}$$

Therefore at lower q's $\Delta\theta_s/\theta_s$ dominates and at higher q's $\Delta\lambda/\lambda$ dominates. To achieve a low $\Delta\theta/\theta$ the neutron beam needs to be collimated. Either pin-hole collimators (as shown in figure 4.3) or focusing lenses [101] are used for this purpose.

A tight wavelength spread $\Delta\lambda/\lambda$ cuts down the available intensity. So, a tight wavelength spread is employed if one is particularly interested in higher q's.

The 128×128 pixels on the detector count the neutrons. Scattering from the sample is not the only contributor to the detector counts. Scattering from sample holder, scattering from the air, and stray neutrons and electronic noise also contributes to the detector counts. Scattering from the holder and air together is called scattering from cell. Stray neutrons and electronic noise contribution is called blocked beam as it will be present even when the beam is switched off. Therefore, the intensity from the scattering experiment can be written as

$$I_{scat} = C_0 T_{sample+cell} \left(\left(\frac{d\Sigma}{d\Omega} \right)_{sample} + \left(\frac{d\Sigma}{d\Omega} \right)_{empty} \right) + I_{Blockedbeam}, \tag{4.69}$$

where $C_0 = A\zeta\phi\Delta\Omega\epsilon t$, A is the sample area and ϵ is the detector efficiency. Hence apart from the scattering and transmission measurements, empty cell, blocked beam, and detector sensitivity measurements are also necessary. Empty cell measurement is repeating the scattering experiment without the sample but leaving the sample holder and rest of the equipment as is. Blocked beam measurement is measuring the detector counts with the beam completely blocked. These give

$$I_{empty} = C_0 T_{cell} \left(\frac{d\Sigma}{d\Omega} \right)_{empty} + I_{Blockedbeam}, \tag{4.70}$$

and

$$I_{bkd} = I_{Blockedbeam}, \tag{4.71}$$

Using the transmission measurements $T_{sample+cell}$ and T_{cell}, the corrected in-

tensity can be calculated as

$$I_{cor} = (I_{scat} - I_{bkd}) - \left(\frac{T_{Sample+cell}}{T_{cell}}\right)(I_{empty} - I_{bkd}). \tag{4.72}$$

The corrected data is then calibrated with the detector sensitivity measurement

$$I_{cal} = \frac{I_{cor}}{\text{Normalized detector sensitivity}}. \tag{4.73}$$

4.3.2 Ultra Small-Angle Neutron Scattering (USANS)

BT5 perfect crystal USANS instrument [103] at NCNR in Gaithersburg, MD was also used in this study to probe the sample at even lower q's - down to 1×10^{-5} Å^{-1}. BT5 is perfect crystal diffractomer (PCD) based instrument. Channel-cut silicon (220) crystals are used as monochromator and analyzer. The perfect crystals provide high angular resolution and the multiple reflections sharpen the beam profile, improving the signal-to-noise ratio. BT5 has a signal-to-noise ration of 10^5 at a scattering vector $q = 0.0005$ Å^{-1}

Similar to the Small-Angle Neutron Scattering, the neutron transmission should be $T > 90\%$ to avoid multiple scattering problem. In USANS, transmission T is

$$T = \frac{I_0 - I_{SAS}}{I_0}, \tag{4.74}$$

where I_0 is the intensity on the Bragg peak of the perfect crystal, i.e., at $|q| = 0$ and I_{SAS} is the intensity of the small angle scattering i.e., for $|q| \neq 0$. It simply means that the scattered beam intensity should be less than 10% of the transmitted beam for it not to be resulting from multiple scattering.

Figure 4.5 shows the schematic of the q-space probed by USANS. USANS is only sensitive to the momentum vector along horizontal direction ($\hat{\boldsymbol{x}}$). The narrow

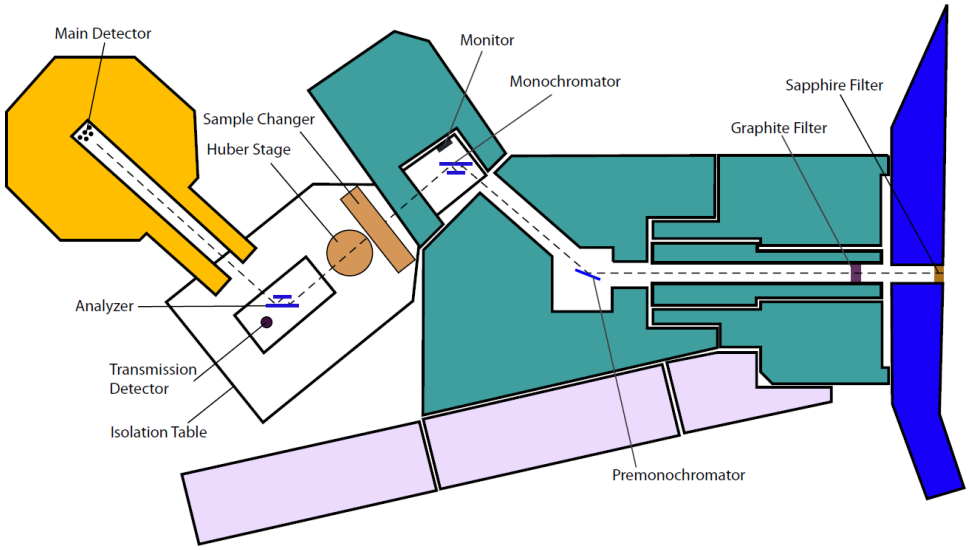

Figure 4.4: Schematic of Ultra Small-Angle Neutron Scattering (USANS) [104]

slit in the figure represents the q-space measured by the analyzer at a given tilt angle. By tilting the analyzer, q_x (or q_h) can be measured at a step size of 2×10^{-5} Å^{-1}. The vertical q-space measured is always 0.117 Å^{-1}. Therefore, USANS data is one-dimensional.

4.3.3 Single Crystal Neutron Diffraction

The single crystal neutron diffractometer, TriCS at Paul Scherrer Institut in Villigen, Switzerland was used for the diffraction studies. This instrument uses thermal neutrons of wavelength 1.18 - 2.32 Å with a resolution of 0.5%. The flux at the sample is up to 1×10^6 n/cm^2/sec. At $\lambda = 1.18$ Å, maximum q that can be reached is 8.98 Å^{-1}. Therefore for Fe–Ga, $\sqrt{h^2 + k^2 + l^2} \leq 4$ can be probed.

The instrument needs to be calibrated to move from the crystal coordinate

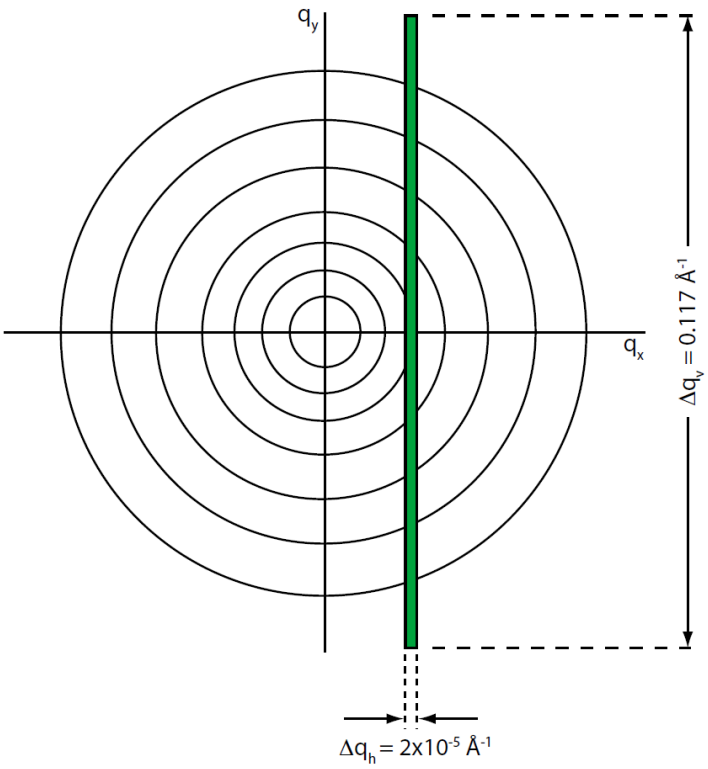

Figure 4.5: Circles represent iso-intensity contours from isotropic small angle scattering. The Narrow slit represents the scattered region collected by the BT5 analyzer. [105]

system to the instrument coordinate system and back. This is done using a UB matrix [107]. To find the UB matrix that transforms the desired crystal reciprocal coordinates to the equivalent instrument setting angles, two known Bragg peaks are used. Once the UB matrix is evaluated, the instrument setting angles can be calculated and appropriately changed to reach a desired point in the sample's reciprocal space.

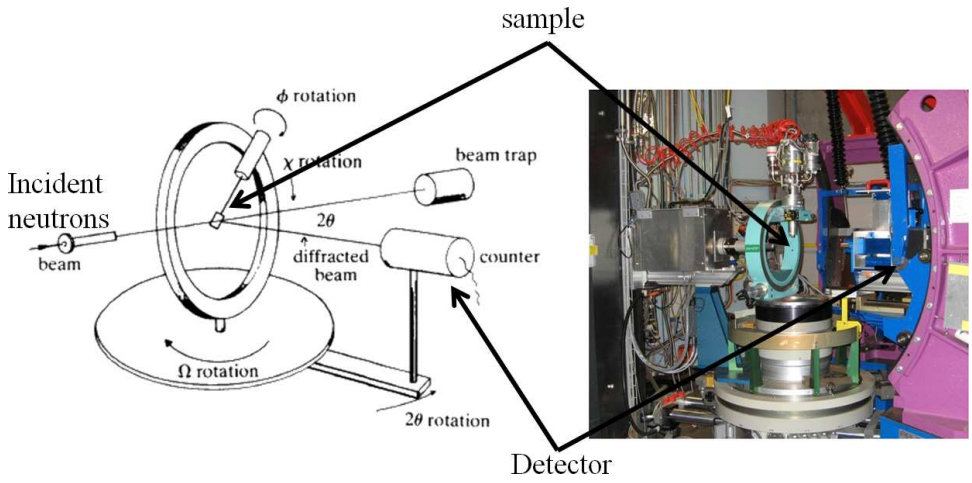

Figure 4.6: Schematic of triple axes single crystal neutron diffractometer (left). TriCS intrument at Paul Scherrer Institut, Switzerland (right) [106]

4.4 Unpolarized SANS

In this section, SANS results using unpolarized neutrons are detailed. Samples 19Qe, 18S, 18Q, 17S, 17Q, 15S, 20S, and 20Q were used for the SANS experiments under magnetic field. For SANS experiments under elastic field, 19Qe sample was used. SANS experiments were conducted in two or three different configurations of the instrument so as to cover the desired q range. The samples were placed such that their long axes, labeled $\hat{\boldsymbol{x}}$ or [100] are along the horizontal direction, parallel to the horizontal axis of the detector and the $\hat{\boldsymbol{z}}$ axis of the sample (thickness) is parallel to the neutron beam direction. $|q|$ values between $0.001 \leq |q| \leq 0.02$ Å^{-1} are labeled as *lowq* and $|q| \geq 0.02$ as *highq*. A beamstop was used to cover the transmitted beam while measuring the scattering and removed while measuring the transmission. A circular aperture of diameter 9.5 mm was placed in front of the

sample. As described in the introduction, TEM results [59] show the separation between two heterogeneities is about 6 nm. When the sample is saturated, the main source of magnetic inhomogeneity should be from the heterogeneities. Therefore, it is expected that the scattering will occur at these length scales i.e., at highq. When the sample is not saturated then the magnetic inhomogeneity can be even at higher lengths scales or lowq due to the presence of domains and domain walls. Therefore, lowq scattering is expected to be present only under magnetic fields below saturation. All the data shown here were reduced using SANS reduction software developed by NCNR [108]. In the next sections, magnetic field experiments are detailed followed by elastic field experiments.

4.4.1 Under magnetic field

Magnetic field experiments using unpolarized neutrons were conducted on 19Qe, 18S, 18Q, 17S, 17Q, 15S, 20S, and 20Q samples. Magnetic fields as high as 1.6 T were applied along $\hat{\boldsymbol{x}}$ using a conventional electromagnet.

Transmission measurements showed that for sample 19Qe, $T \approx 95\%$. Therefore, the scattering from this sample should not have any noticeable effect from multiple scattering.

Figure 4.7 shows the SANS lowq images of 19Qe subjected to a magnetic field along $\hat{\boldsymbol{x}}$. The dark circle in the center is the beamstop. Streaks running along 0, 90, and ± 45 degrees to the $\hat{\boldsymbol{x}}$ axis or along $\langle 100 \rangle$ and $\langle 110 \rangle$ crystallographic directions of the sample can be seen. These streaks result from the scattering of the neutrons

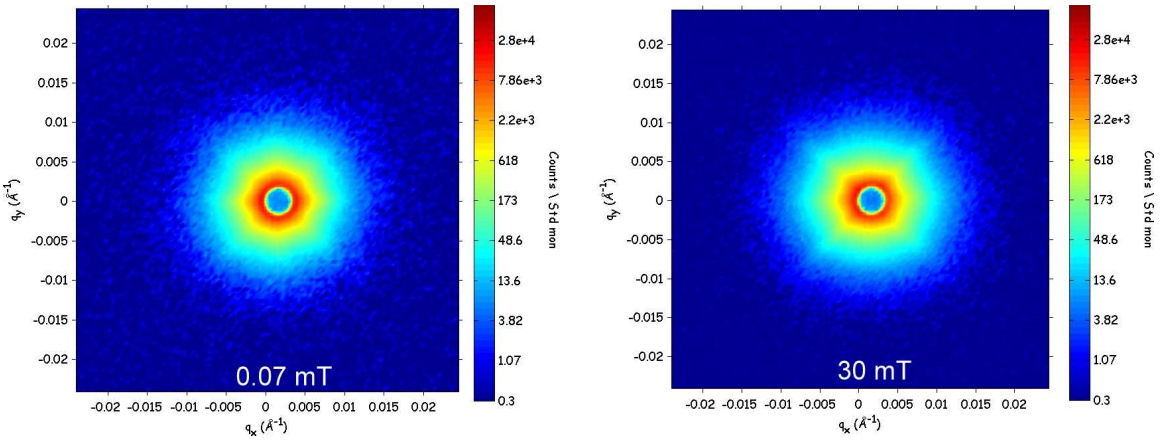

Figure 4.7: 19Qe SANS lowq images for $H_x = 0.07$ mT and 30 mT. Streaks along 0, 90, and ±45 degrees to the $\hat{\boldsymbol{x}}$ are due to the 90° and 180° domains walls

from the domain walls. It was shown in Chapter 3 that the 180° domain walls run along the ⟨100⟩ crystallographic directions and 90° domain walls run along the ⟨110⟩ crystallographic directions. Therefore, neutrons scattering from these 90° and 180° domain walls lead to streaks along 0, 90, and ±45 directions in the scattering plane.

Although hysteresis is negligible in Fe–Ga, a high magnetic field (∼1.3 T), much larger than the saturation field was applied to the sample along $-\hat{\boldsymbol{x}}$ and then the field was lowered to remanence. After pre-treating the sample to a high negative field, the lowq SANS experiment was repeated with increasing magnetic fields along $\pm\hat{\boldsymbol{x}}$. The resulting lowq SANS images are shown in figure 4.8. The scattering at lowq now looks slightly anisotropic. This is possibly due to the formation of $\pm\hat{\boldsymbol{x}}$ domains when the sample was pre-treated with high magnetic field. As discussed in section 4.2.2 and equation (4.34), only the component of magnetization perpendicular to the scattering vector leads to neutron scattering. Therefore, due to the high number of

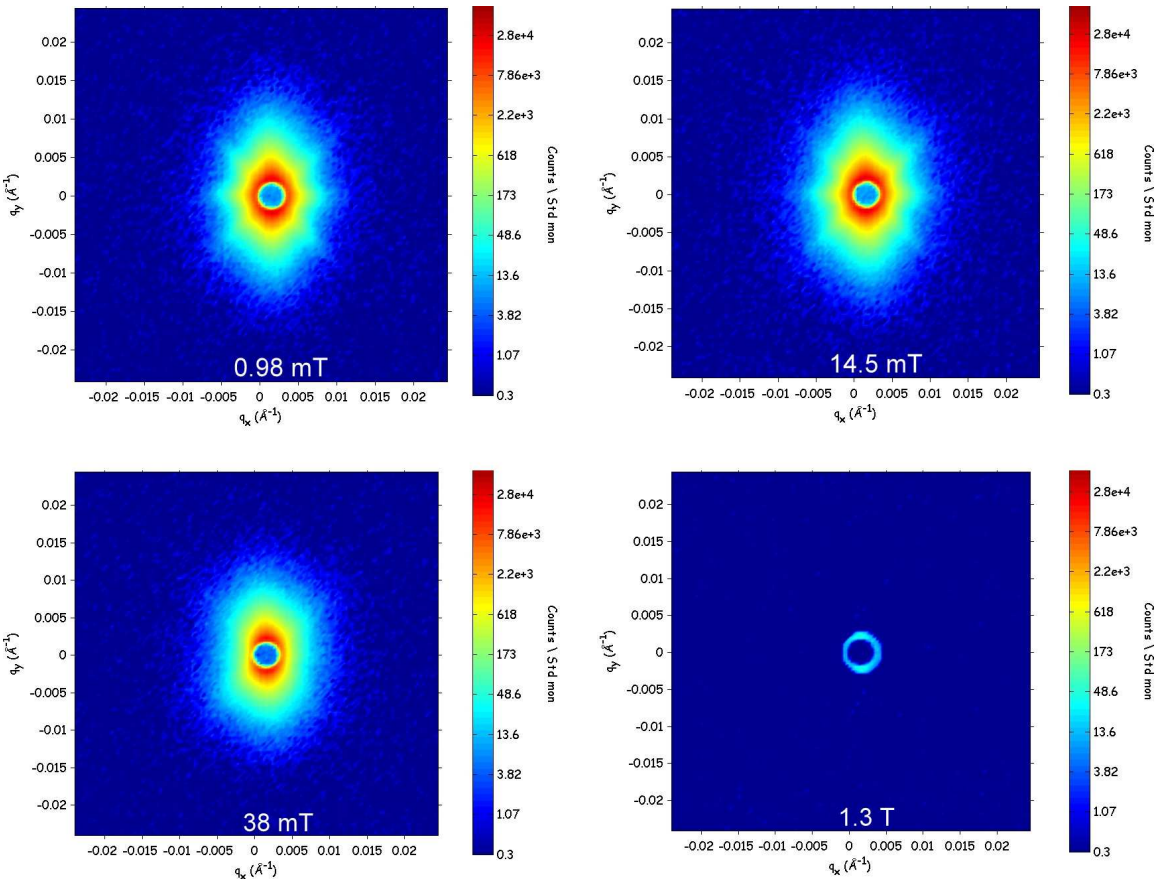

Figure 4.8: 19Qe SANS lowq images under magnetic field after pre-treating the sample with $H = -1.3$ T. Streaks along 0, 90, and ± 45 degrees to the $\hat{\boldsymbol{x}}$ are due to the 90° and 180° domains walls

$\pm\hat{\boldsymbol{x}}$ domains than $\pm\hat{\boldsymbol{y}}$ domains, the scattering will be more along the $\pm\hat{\boldsymbol{y}}$ directions, leading to an anisotropy. Further lower q SANS images were also obtained, which are shown in figure 4.9. When the results in figure 4.9 were obtained the sample was in finely polished state for the domain observation reported in chapter 3. The presence of streaks, more clearly visible in figure 4.9, along 0, 90, and ± 45 directions is, again, due to the 90° and 180° domain walls. It can be seen that as magnetic field is increased, the scattering decreases and finally disappears at a high field. This

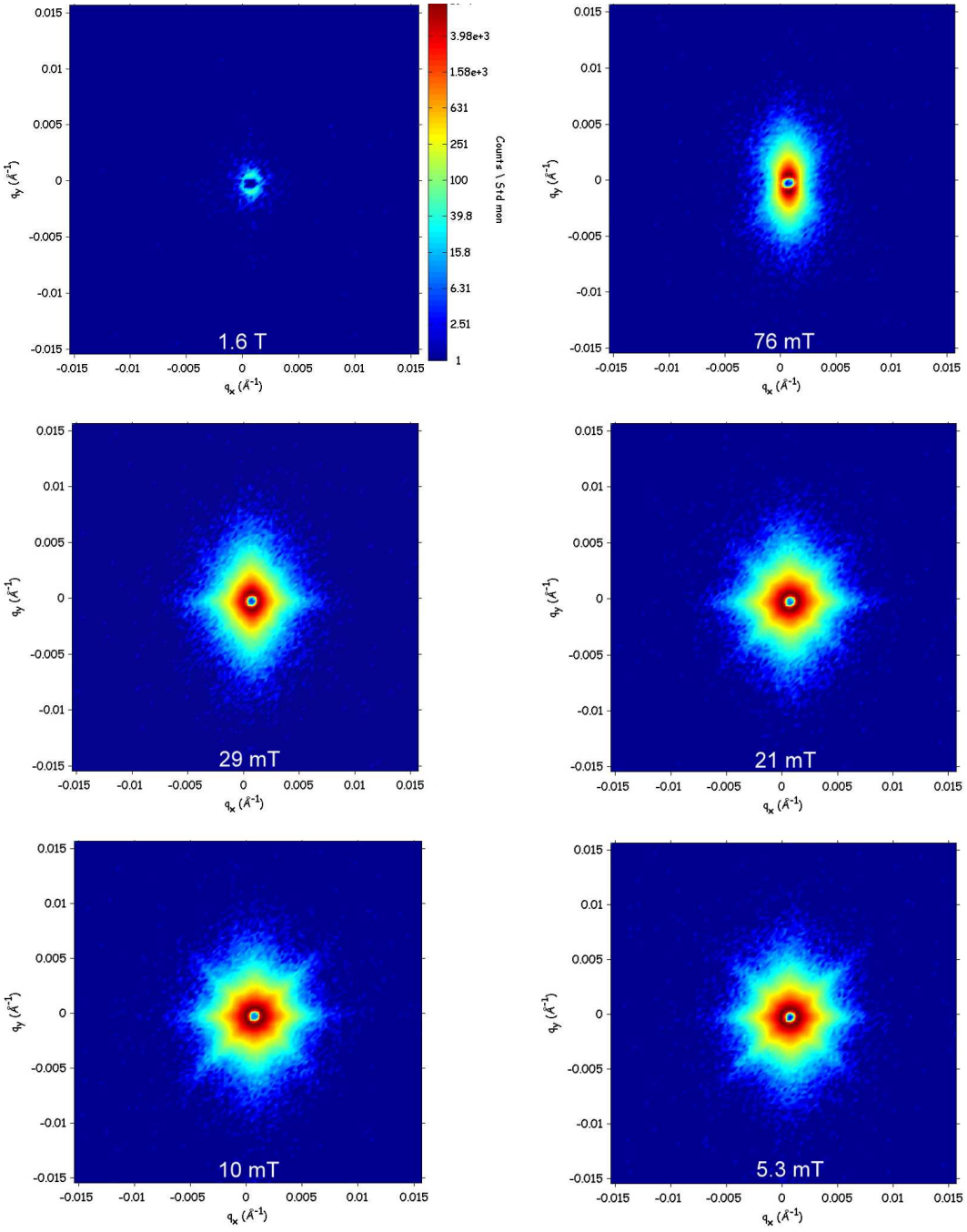

Figure 4.9: 19Qe SANS lowq (lower) images. In addition the top surface of the sample was finely polished such that magnetic domains are visible. Streaks along 0, 90, and ± 45 degrees to the $\hat{\boldsymbol{x}}$ are more clearly visible.

is consistent with the thought that the lowq scattering stems from the magnetic domains and domain walls. As the magnetic field is increased, the magnetic domain walls and number of domains decrease and eventually disappear. Therefore, in a way, the lowq scattering reflects the sample's state of magnetization.

Figure 4.10 shows the SANS images at highq, which show strong anisotropy in scattering. The scattering is predominantly along $\hat{\boldsymbol{x}}$ at remanence, which rotates under the magnetic field and eventually is oriented along $\hat{\boldsymbol{y}}$ after saturation. The scattering after saturation shows a clear sine-squared dependence on the azimuthal angle indicating the presence of heterogeneities with distinct magnetization from that of the host matrix.

Figure 4.11 shows SANS images for higher q values. To cover these q values, the detector was moved such that a larger reciprocal space (and hence higher q values) can be covered from the center ($q = 0$). These images show that there is no significant small-angle scattering higher than the q values covered in figure 4.10.

Figure 4.12 shows the averaged intensity for different $|q|$ values. On the left side is the intensity averaged in the 30 degree sector along horizontal ($\hat{\boldsymbol{x}}$) direction and on the right side is the intensity averaged in the 30 degree sector along vertical ($\hat{\boldsymbol{y}}$) direction. It can be seen that for lowq (i.e., for $q < 0.02$ Å^{-1}) the scattering intensity decreases with increasing magnetic field both along the horizontal and vertical sectors, as is expected if lowq represents magnetic domain wall scattering. In the highq range, the intensity decreases along the horizontal direction and increases along the vertical direction with increasing magnetic field. This shows that the net scattering intensity (sum along all directions) in this q range is field independent.

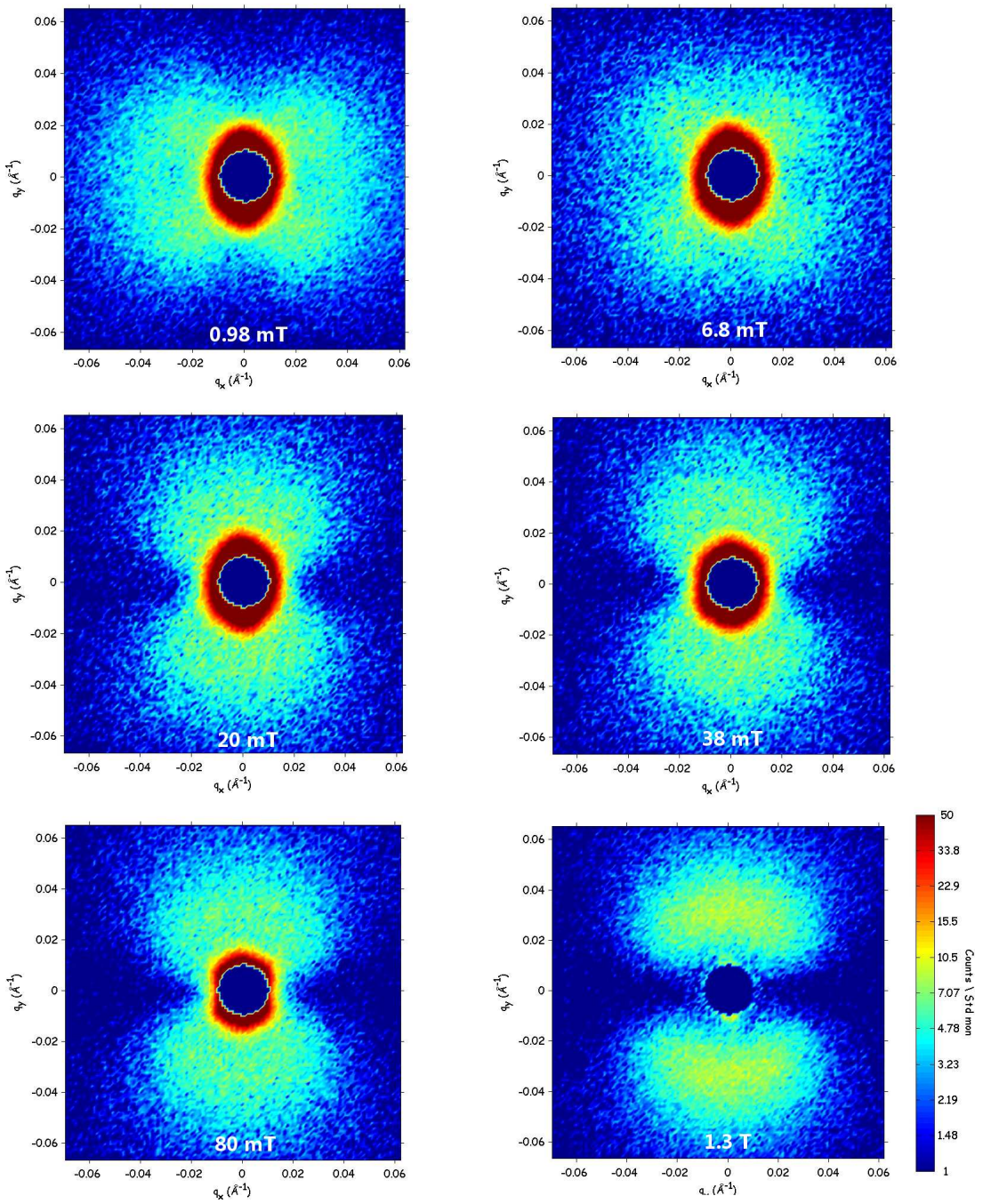

Figure 4.10: 19Qe SANS highq images under magnetic field after pretreating the sample with $H = -1.3$ T. Strong anisotropy in the scattering suggests presence of heterogeneities

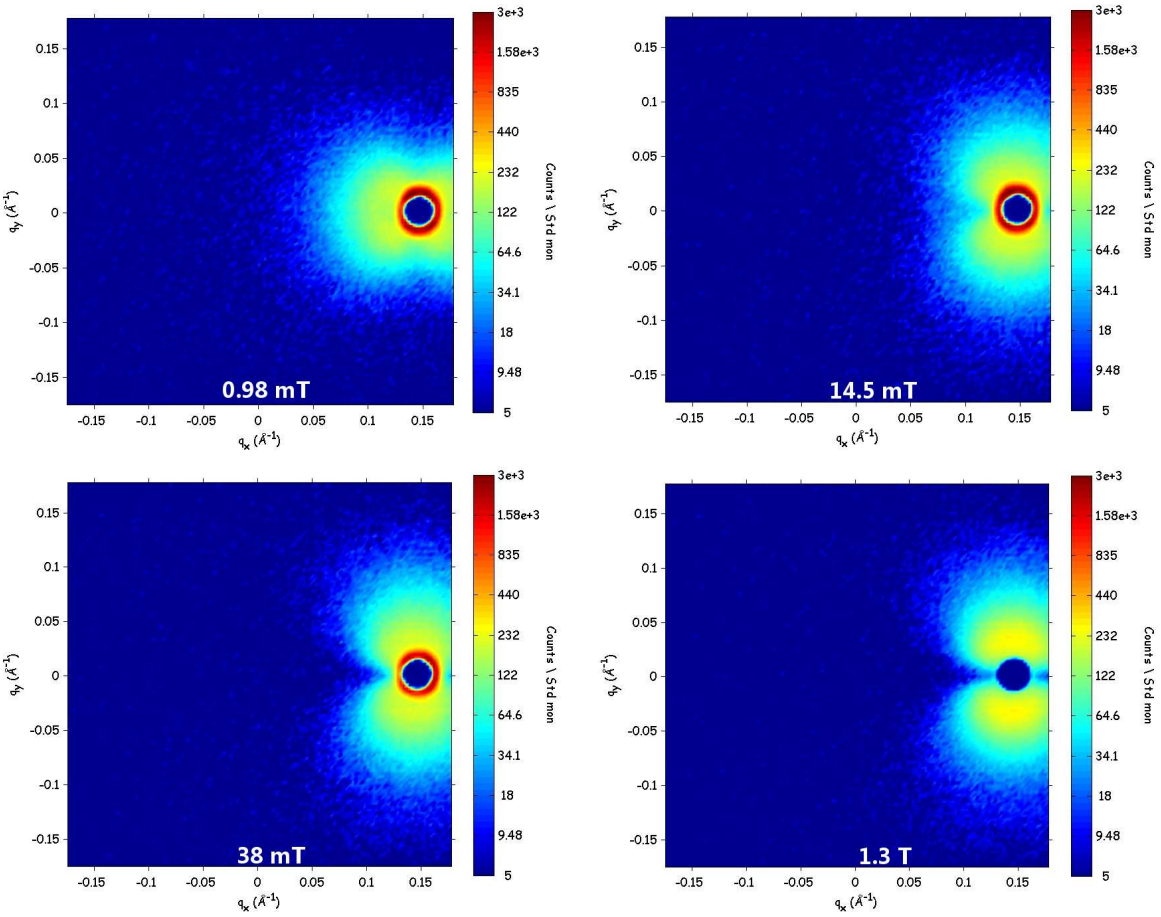

Figure 4.11: 19Qe SANS highq (higher) images under magnetic field after pre-treating the sample with $H = -1.3$ T. Detector was moved to cover even higher q values.

Also, the scattering persists even after saturation. This is possible only if the scattering sites leading to the scattering in this q range have the magnitude of their magnetization distinct from that of the matrix. Further a peak at $q \approx 0.04$ Å^{-1} indicates an average separation between the scattering sites to be ~ 15 nm.

When the magnetization is saturated along $\hat{\boldsymbol{x}}$ the Fourier components of the magnetization along $\hat{\boldsymbol{y}}$ and $\hat{\boldsymbol{z}}$ directions will be zero. Substituting $Y = 0$ and $Z = 0$

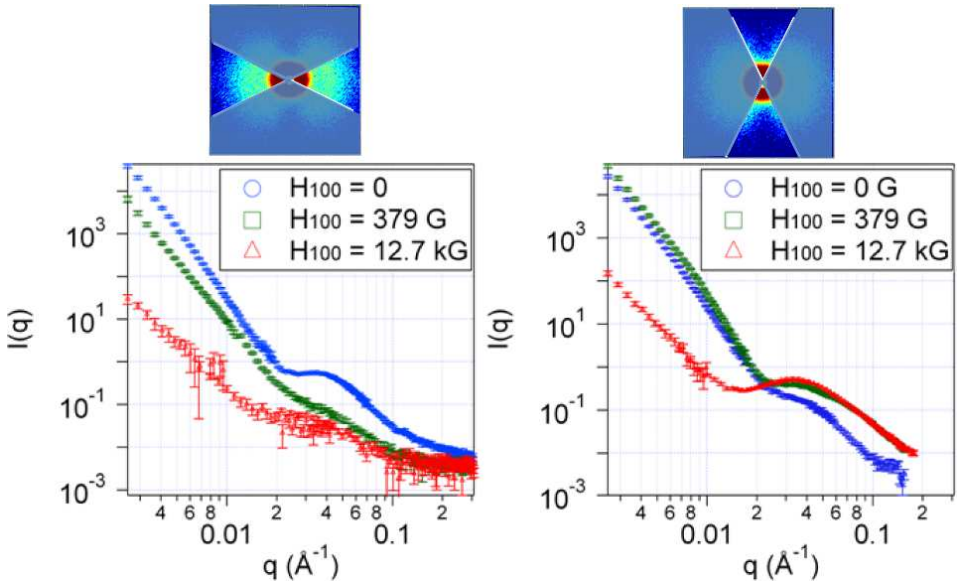

Figure 4.12: 19Qe SANS I vs. q averaged along a 30 degree horizontal sector (left) and a 30 degree vertical sector (right)

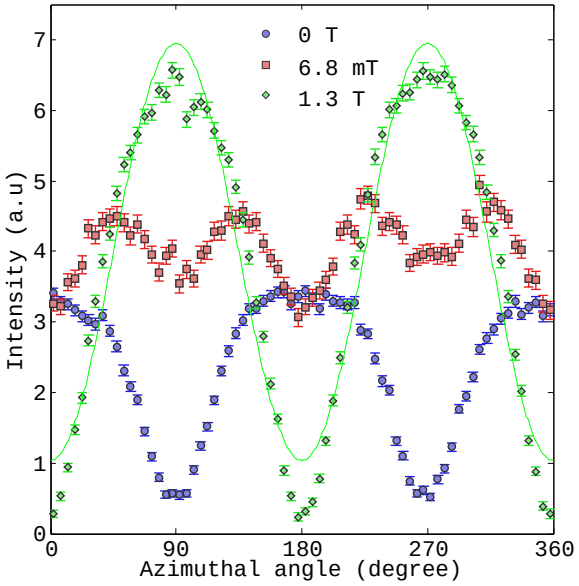

Figure 4.13: Azimuthal angle θ dependence of the SANS intensity averaged over $0.021 \leq |q| \leq 0.057$ Å^{-1} for 19Qe

in equation (4.43), the intensity for unpolarized neutrons can be written as

$$I(\boldsymbol{q}) = A^2 + X^2(q)\sin^2\theta. \tag{4.75}$$

The intensity after saturation in figure 4.13 clearly has $\sin^2\theta$ dependence. From equation (4.43), it is expected that at remanence, if the sample is in a perfectly demagnetized state, the scattering should be isotropic i.e., there should not be any θ dependence. However, it can be seen that the anisotropy exists at remanence. This indicates a pre-strained remanent state in the sample, which agrees with the remanent state calculation (showing 64-76% magnetization oriented along $\pm\hat{\boldsymbol{y}}$) for this sample in table 2.3. Almost negligble scattering along $\hat{\boldsymbol{x}}$ shows that the nuclear contribution A^2 to scattering intensity is neglible, as expected. The four-fold anisotropy at $H = 6.8$ mT cannot be readily explained with equation (4.43). It may be a result of complex magnetization variation near the heterogeneity/matrix boundary. Such a pattern has been observed in the past [109] and micromagnetic simulation was offered as a likely avenue to understand this phenomenon. In this dissertation, no attempt has been made to understand this any further.

Next, 18S sample was studied. Transmission measurements on this sample showed $T \approx 88\%$. Since it is less than 90%, there might be a small effect from the multiple scattering.

Figure 4.14 shows the lowq SANS intensity for the 18S sample. Again, the streaks formed due to the domain wall scattering are clearly visible. The streak along 45-degrees becomes intense at $H = 40$ mT. From the remanent state calculation in table 2.3, it was found that the sample has a strong anisotropy at remanence. If

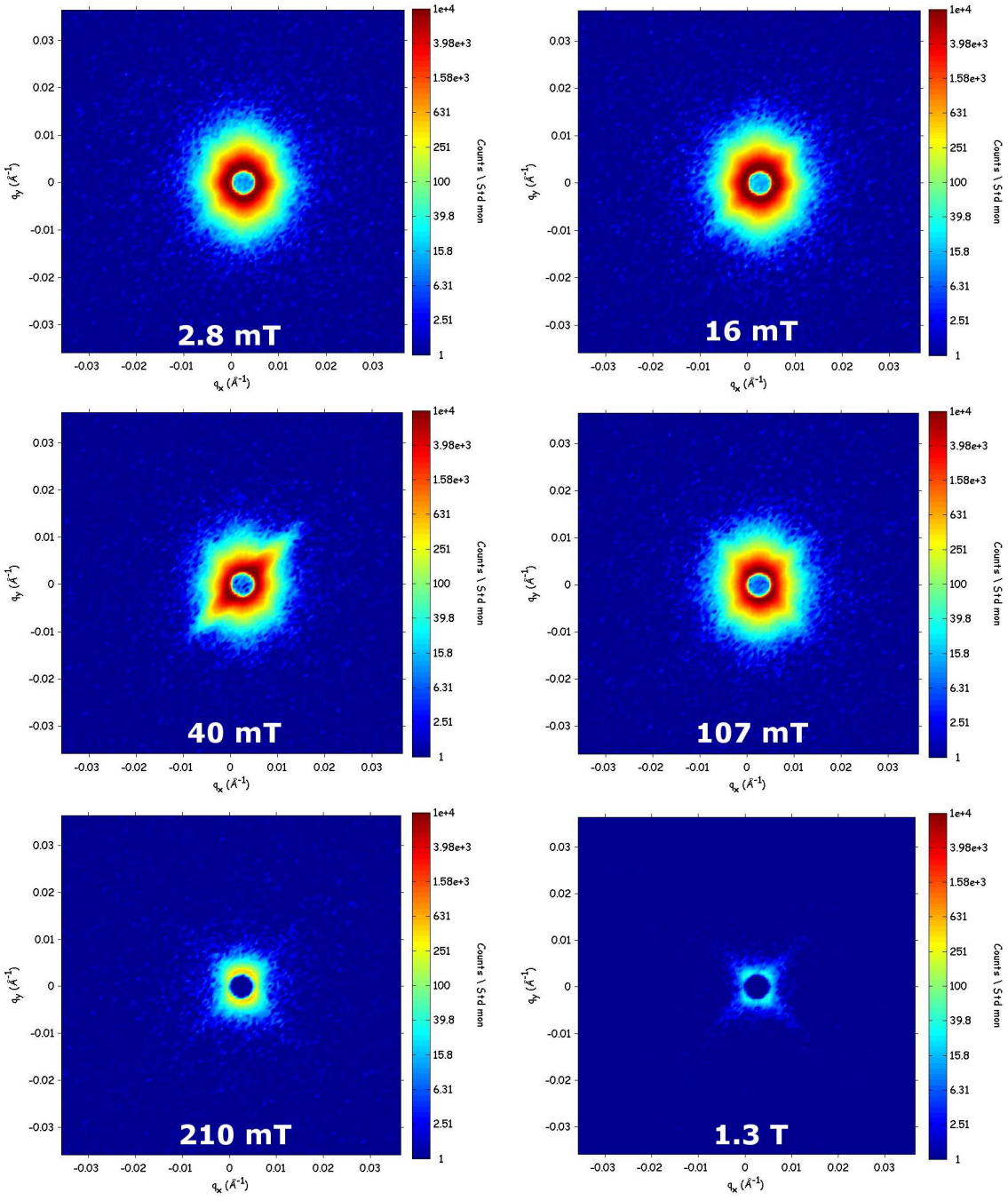

Figure 4.14: 18SLowQ

the domains are all oriented in one direction at remanence, as in 17S sample (see figure 3.29), at a critical field perpendicular to the direction of the magnetization

of the domains at remanence, 90° domain walls form. This increase in the 90° domain walls could be the reason for the intense 45-degree streak. Unfortunately, domain study was not conducted on this sample to verify this explanation. After saturation, the scattering intensity is much reduced. However, there is still some scattering, especially along the ±45-degrees. As the sample is saturated, it is likely that this scattering is nuclear in origin - perhaps from crystalline imperfections. Nonetheless, the overall character of the lowq scattering is similar to that of the 19Qe sample.

Highq SANS images of 18S sample in figure 4.15 show no significant scattering as the 19Qe did. On careful inspection, however, some anisotropy is visible in the scattering image at $H = 1.3$ T. This is more pronounced in the azimuthal plot shown in figure 4.16. This plot also shows that similar to 19Qe sample, there is an anisotropy even at remanence. This indicates that the 18S sample is also in a pre-strained remanent state. It was estimated, in table 2.3, that in the remanent state, 18S is predominantly (81-90%) magnetized along $\pm\hat{\boldsymbol{y}}$. The higher remanent state scattering along $\pm\hat{\boldsymbol{x}}$ (0 degrees) is in agreement with the remanent state calculation.

In figure 4.17, merging lowq and highq data for 18S sample is shown. The difficulty in aligning the lowq and highq data is possibly due to the multiple scattering effect. It could also be due to the changing instrument resolution between the two instrument configurations used to obtain lowq and highq data. Since the transmission through 18S was measured to be 88%, multiple scattering effect is inevitable. However, the misalignement problem was limited to lower magnetic fields. At a higher magnetic field, the sample becomes more homogeneous due to the reduction

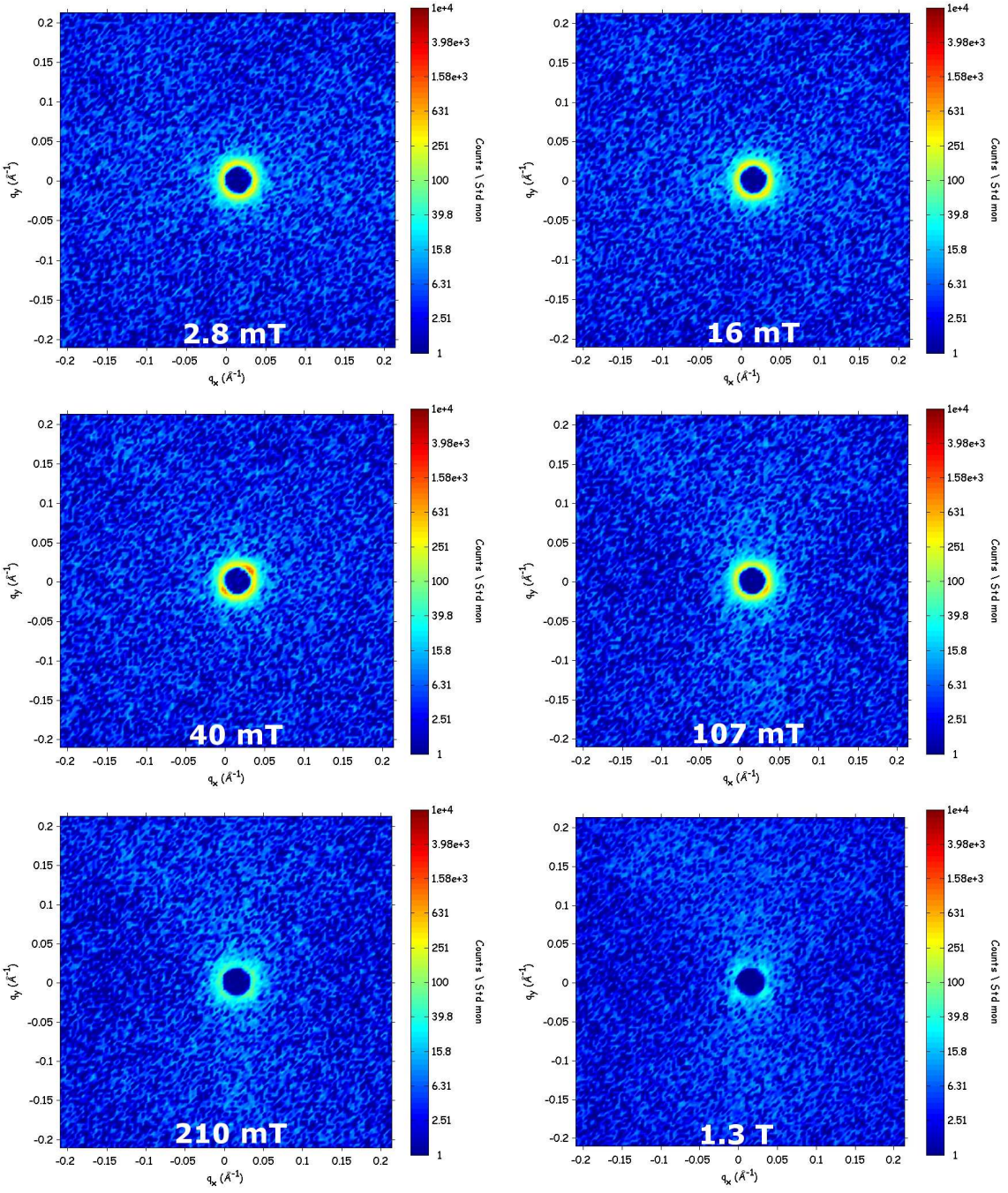

Figure 4.15: SANS highq images of 18S subjected to magnetic field. Very weak anisotropy can be discerned from the scattering image at $H = 1.3$ T.

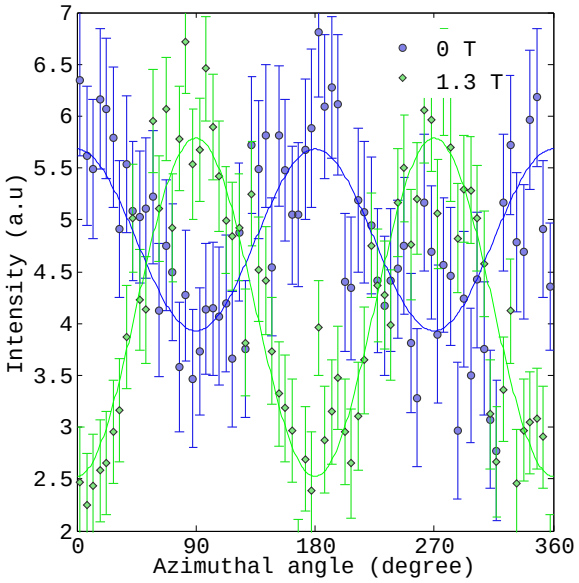

Figure 4.16: Azimuthal angle θ dependence of the SANS intensity averaged over $0.039 \leq |q| \leq 0.15$ Å^{-1} for 18S

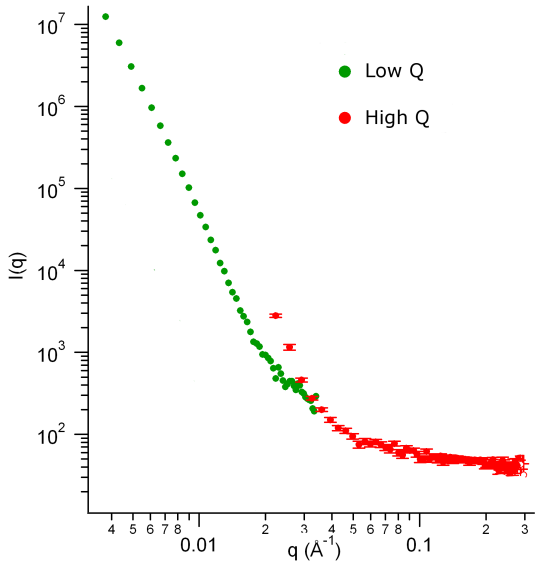

Figure 4.17: Merging lowq and highq data in 18S sample. The misalignment of the intensity curves is possibly due to the multiple scattering effect

of domain and domain walls possibly leading to a reduced multiple scattering effect.

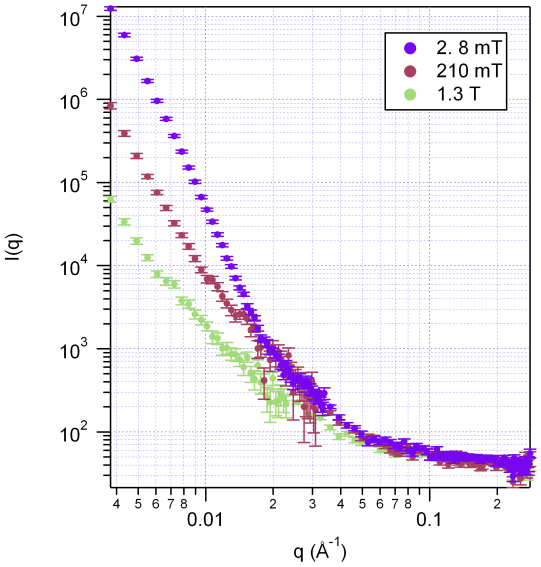

Figure 4.18: 18S SANS I vs. $|q|$ circularly averaged in all directions. No peak is perceptible.

In figure 4.18, circularly averaged (in all directions) intensity for 18S is plotted. Non-overlapping points in $H = 2.8$ mT curve were deleted. The intensity at lower q values decreases with increasing magnetic field as expected. There seems to be no apparent peak as in the 19Qe sample. However, the azimuthal plot in figure 4.16 clearly shows a sine squared dependence indicating the presence of heterogeneities. The lack of peak indicates that the heterogeneities are dilute and there is no average separation between them as in the 19Qe case.

Next, the 18S sample was heat treated for four hours at 1000 °C and then water quenched to room temperature. Measurement of magnetostriction showed a decrease in the maximum magnetostriction by 32 $\mu\epsilon$. Quenching was expected to boost the magnetostriction of the slow-cooled sample. However, the decrease could

be attributed to a possible loss of Ga. Composition analysis was not performed on this sample after the heat-treatment. In view of the reduced magnetostriction, this sample was treated as completely new sample and no comparative study between different heat treatments was conducted. Transmission measurements showed $T \approx$ 85%. Therefore, multiple scattering is expected to affect the measurements.

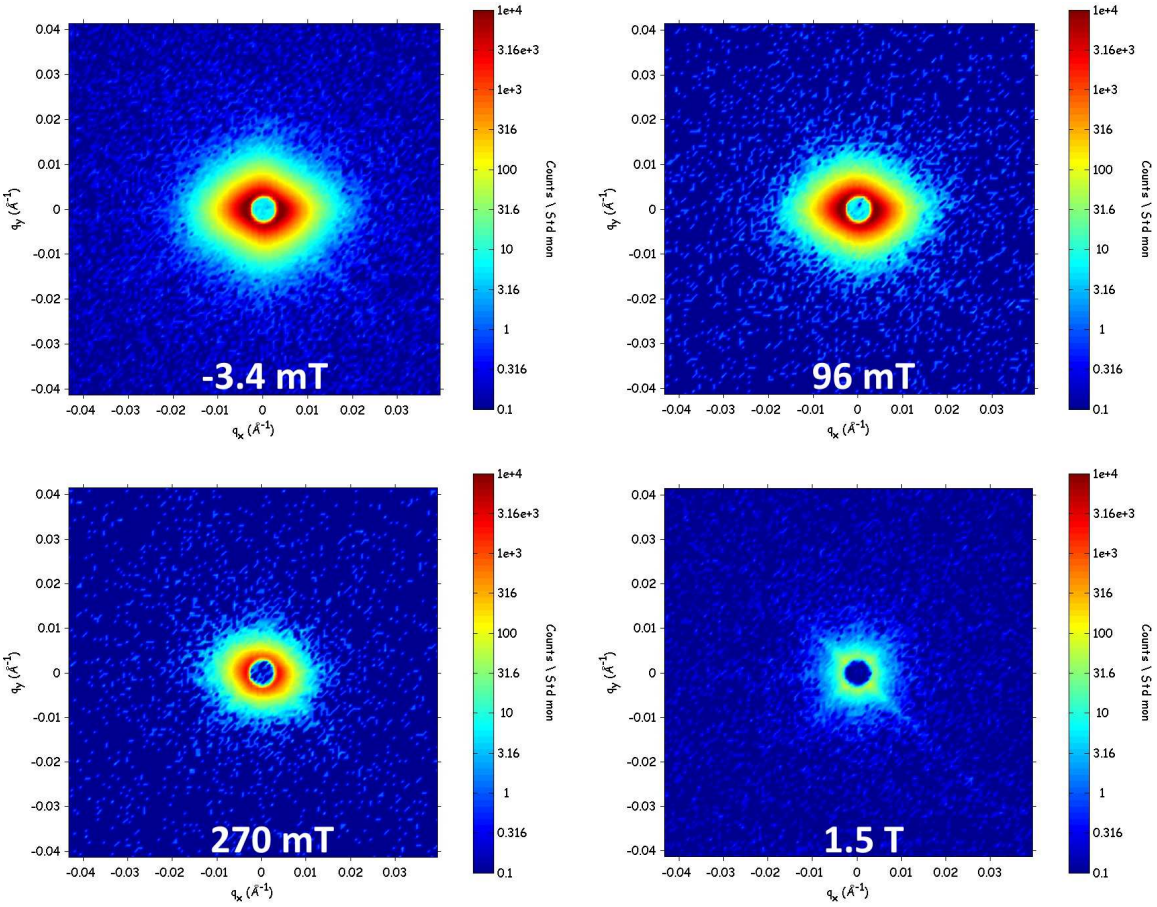

Figure 4.19: SANS lowq images of 18Q under magnetic field

Figure 4.19 shows lowq SANS images of 18Q. As expected from the domain wall and domain scattering, the scattering decreases with increasing magnetic field. Residual scattering at high magnetic field beyond saturation indicates nuclear scat-

tering possibly from crystalline imperfections.

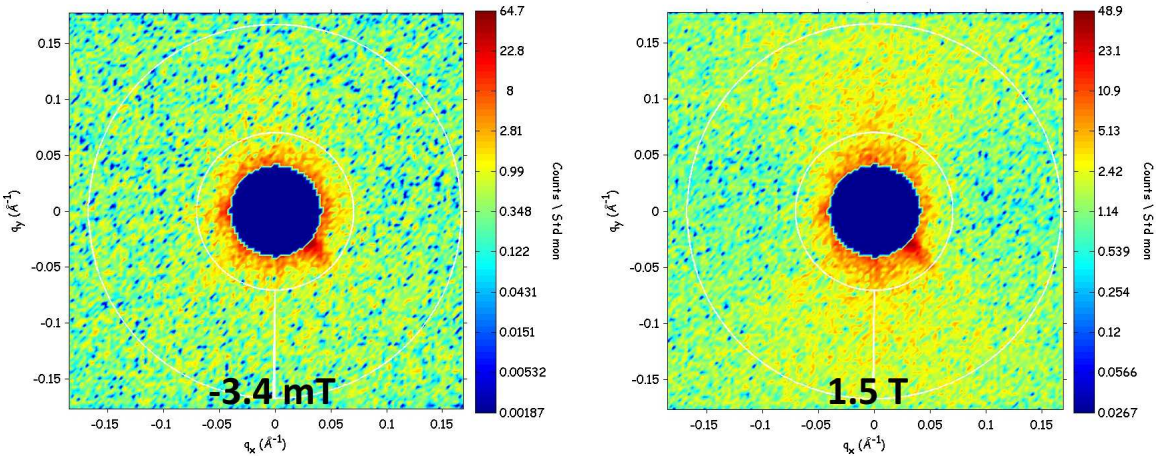

Figure 4.20: SANS highq images of 18Q under magnetic field

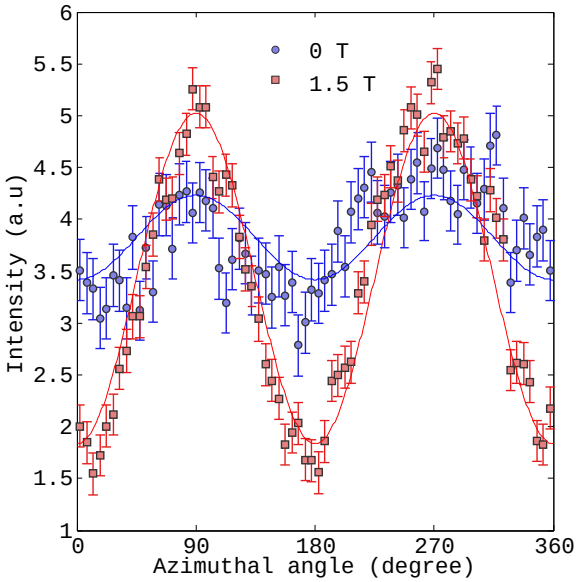

Figure 4.21: Azimuthal angle θ dependence of the SANS intensity averaged over $0.039 \leq |q| \leq 0.15$ Å^{-1} for 18Q

Highq SANS images for 18Q sample are shown in figure 4.20. Clearly, there is an anisotropy at $H = 1.5$ T. This can also be understood from the azimuthal

angle plot in figure 4.21. There is some anisotropy at remanence but this is in the same direction as when the sample is saturated. It was estimated in chapter 2 that 18Q sample has 46-71% magnetization oriented along $\pm\hat{\boldsymbol{x}}$ and only 3-29% magnetization oriented along $\pm\hat{\boldsymbol{y}}$. This is in quite a good agreement with the anisotropy measurements in figure 4.21.

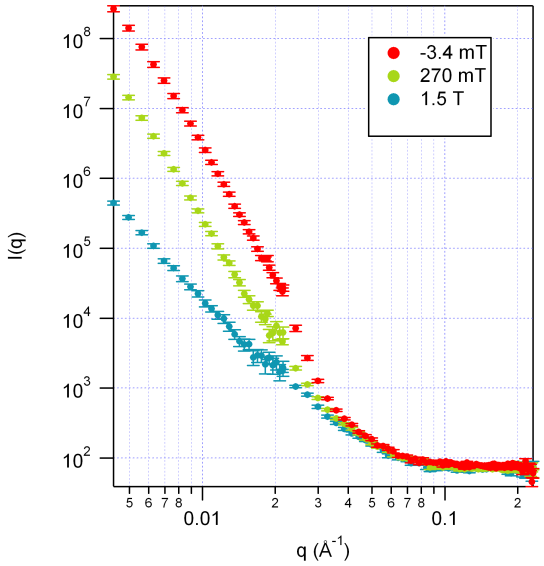

Figure 4.22: 18Q SANS I vs. $|q|$ circularly averaged in all directions. No peak is perceptible.

Figure 4.22 shows SANS intensity of 18Q averaged in all directions. Similar to 18S, there is no perceivable peak in the intensity curves. The lowq intensities decrease with increasing magnetic field as is expected. The lack of prominent peak is indicative of dilute heterogeneities that lead to the anisotropy in scattering shown in figure 4.21.

Transmission measurements on 15S sample showed $T \approx 81\%$. Therefore, multiple scattering is expected to affect the measurements in this sample as it did in

18S and 18Q.

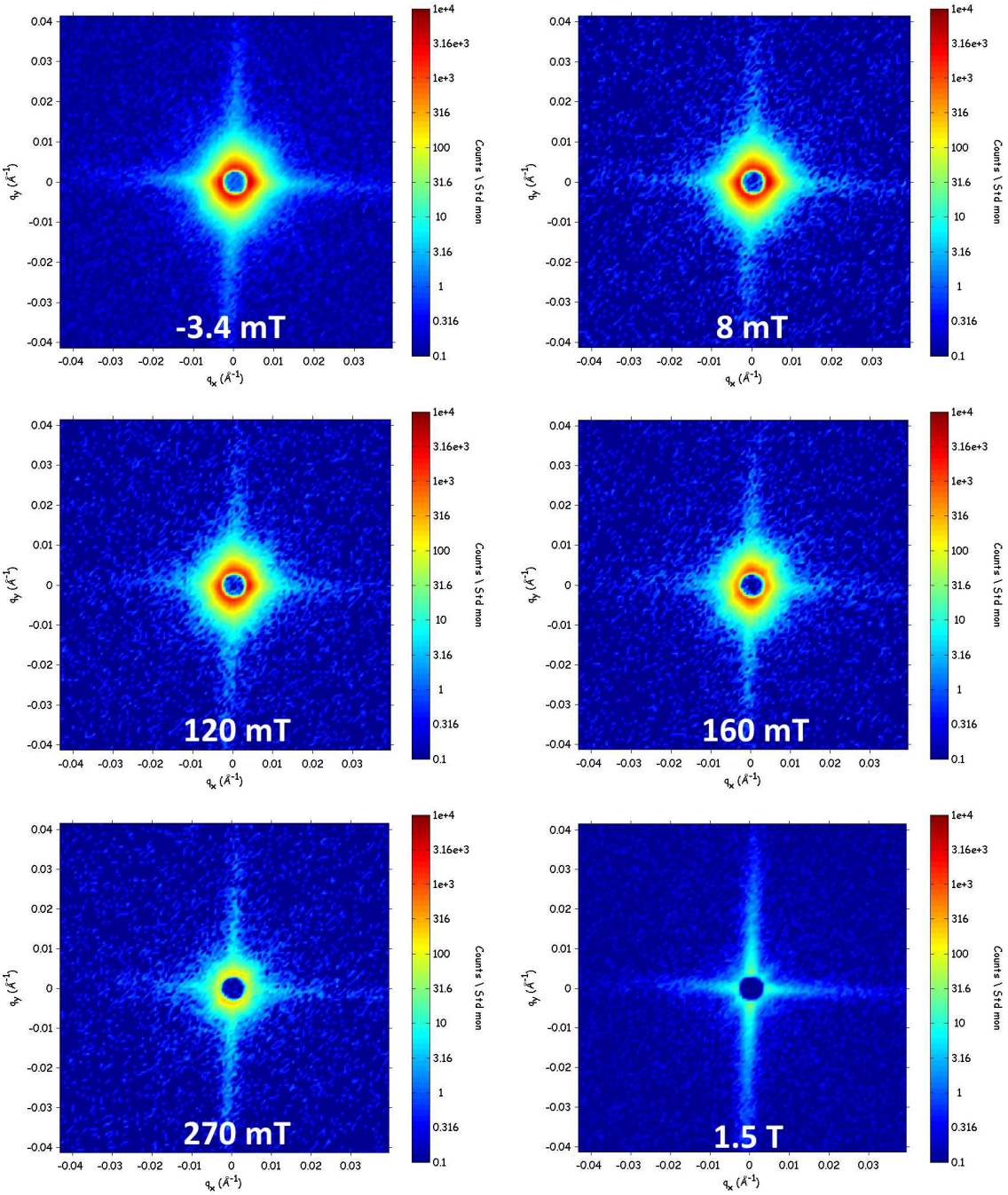

Figure 4.23: SANS lowq images of 15S under magnetic field. Scattering at $H = 1.5$ T indicates nuclear scattering due to crystalline imperfections

Figure 4.23 shows the SANS lowq images of 15S sample. Strong scattering

even after saturation indicates its nuclear origins. This scattering could be from crystalline imperfections as in 18S and 18Q samples. It is of interest to note that the nuclear scattering is predominantly along $\hat{\boldsymbol{x}}$ and $\hat{\boldsymbol{y}}$ directions or along $\langle 100 \rangle$ in 15S whereas it was along ± 45 degrees to $\hat{\boldsymbol{x}}/\hat{\boldsymbol{y}}$ directions or $\langle 110 \rangle$ in 18S and 18Q sample.

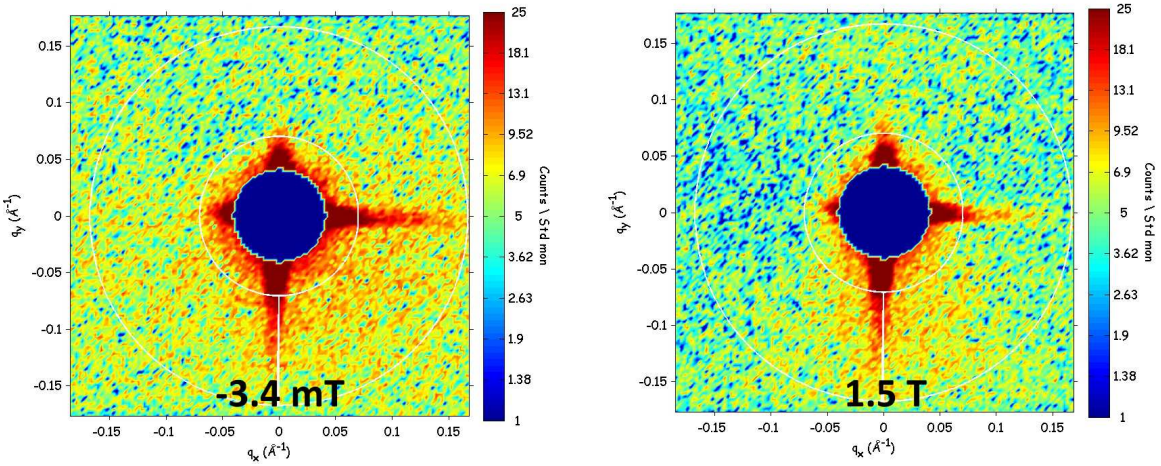

Figure 4.24: SANS highq images of 15S under magnetic field

Figure 4.24 shows highq SANS images for 15S sample. The streaks along $\hat{\boldsymbol{x}}/\hat{\boldsymbol{y}}$ due to nuclear scattering extend to the high q range. This obscures any anisotropy present due to magnetic scattering in the azimuthal angle plots shown in figure 4.25. Since the nuclear scattering is field independent, this problem can be solved by subtracting the lower magnetic field scattering image from the scattering image at saturation field. Figure 4.26 shows the azimuthal angle dependence of the intensity obtained from subtracting $H = -3.4$ mT image from $H = 1.5$ T image. Clearly, there is an anisotropy that is sine squared dependent on the azimuthal angle. This

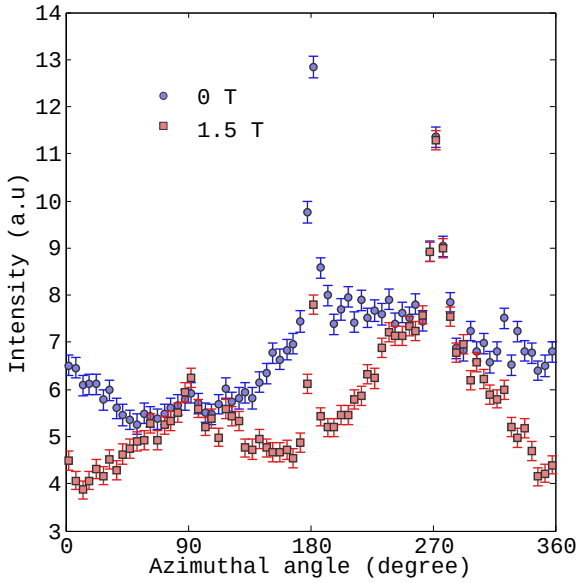

Figure 4.25: Azimuthal angle θ dependence of the SANS intensity averaged over $0.041 \leq |q| \leq 0.17$ Å^{-1} for 15S. Strong nuclear scattering leads to deviation from the sine squared dependence.

shows that the heterogeneities are present in 15S sample as well.

Figure 4.27 shows the circularly averaged I vs. q curves for increasing magnetic fields. Similar to the samples discussed before, the lowq intensity decreases with field. And similar to 18S and 18Q, there is no peak in the intensity. Therefore, the heterogeneites responsible for scattering intensity to be sine squared dependent on azimuthal angle at saturation fields, are dilute.

Next the 17S sample was studied. Transmission measurements on this sample showed $T \approx 82.2\%$. Therefore, as in 18S, 18Q, 15S, multiple scattering likely has an effect on the measurements.

Figure 4.28 shows the lowq SANS images for the 17S sample. A high magnetic field was applied and the scattering was measured by decreasing the field to

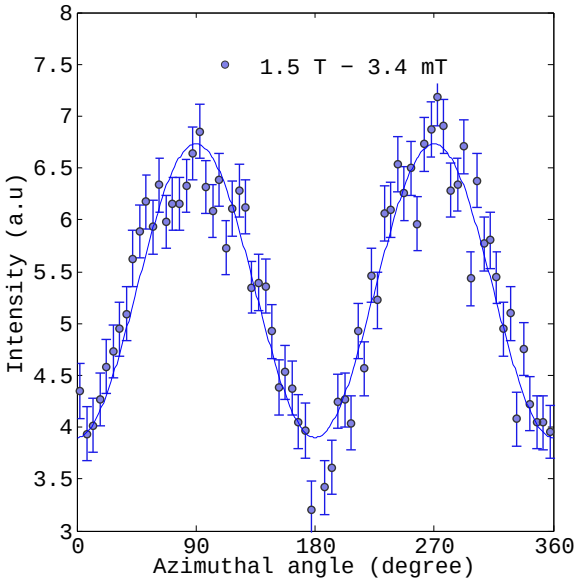

Figure 4.26: Azimuthal angle θ dependence of the SANS intensity averaged over $0.041 \leq |q| \leq 0.17$ Å^{-1} for 15S. Nuclear scattering, which is field independent was removed by subtracting $H = -3.4$ mT scattering image from $H = 1.5$ T image.

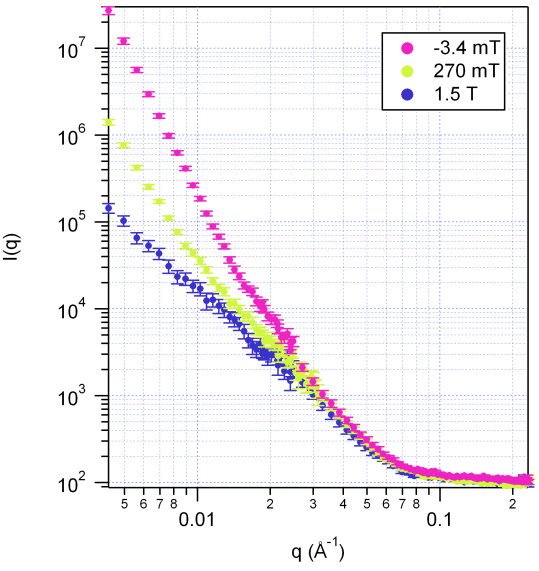

Figure 4.27: 15S SANS I vs. $|q|$, circularly averaged in all directions.

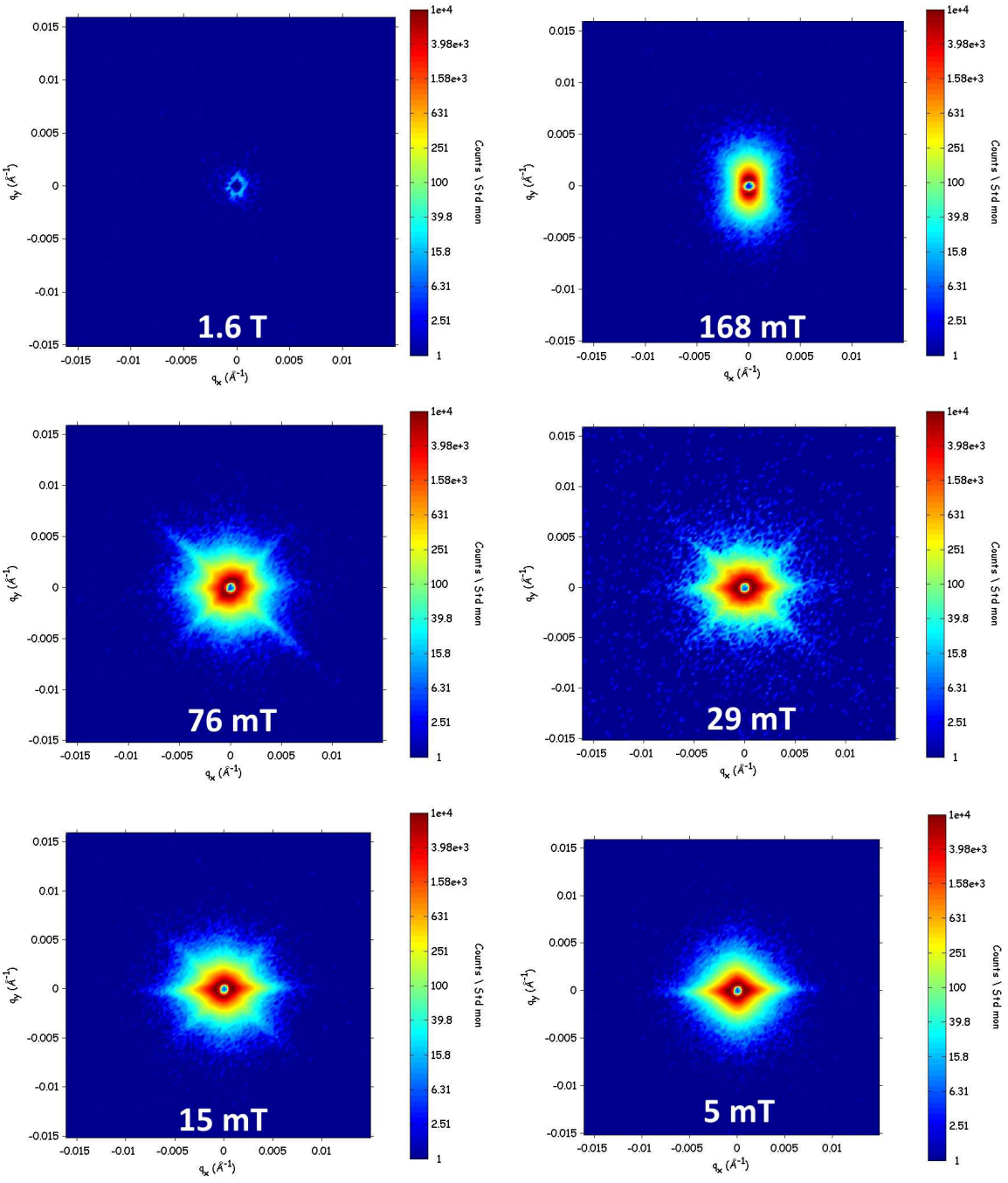

Figure 4.28: SANS lowq images of 17S under magnetic field.

remanence. Before applying a high magnetic field, the scattering was measured with the sample in its remanent state and it matches with the remanent state scatter-

ing image shown in the figure 4.28. It can be observed that streaks along 0, 90, and ±45 degrees are visible only at the intermediate fields. At remanence, only the streak along 0 degrees or along $\hat{\boldsymbol{x}}$ is visible. The domain structure images of this sample (see figures 3.29 and 3.27) show domain walls running along $\pm\hat{\boldsymbol{y}}$. Such domain walls will lead to streaks along $\pm\hat{\boldsymbol{x}}$ in the reciprocal space, which agrees well with the measured scattering profile. As magnetic field is increased along $\hat{\boldsymbol{x}}$, 90° domain walls start to form as can be seen in figures 3.29 and 3.27. These lead to the formation of ±45 degree streaks. It can also be observed that a 90-degree streak along $\pm\hat{\boldsymbol{y}}$ is absent at all magnetic fields. This is because given the domain structure in this sample at remanence, 180° domain walls along $\pm\hat{\boldsymbol{x}}$ will not form when a magnetic field is applied along $\hat{\boldsymbol{x}}$. Figures 3.29 and 3.27 also do not show any 180° domain walls oriented along $\pm\hat{\boldsymbol{x}}$.

Figure 4.29 shows highq scattering images for 17S sample. Upon careful inspection, an anisotropy can be seen in the scattering at high magnetic fields. Similar anisotropy but in perpendicular direction can also be found in the scattering image at remanence. Figure 4.30 shows the azimuthal angle dependence of the scattering intensity. It is more clear from this plot that there is a strong anisotropy at remanence that flips its orientation upon applying a field beyond saturation. The nature of the intensity dependence on the azimuthal angle is sine squared. Therefore, the heterogeneities are present even in this sample.

Figure 4.31 shows the circularly averaged I vs. q curves for 17S sample under increasing magnetic fields. The lowq intensity decreases with field as is expected and as shown to happen in other samples. And similar to 18S, 18Q, and 15S, there

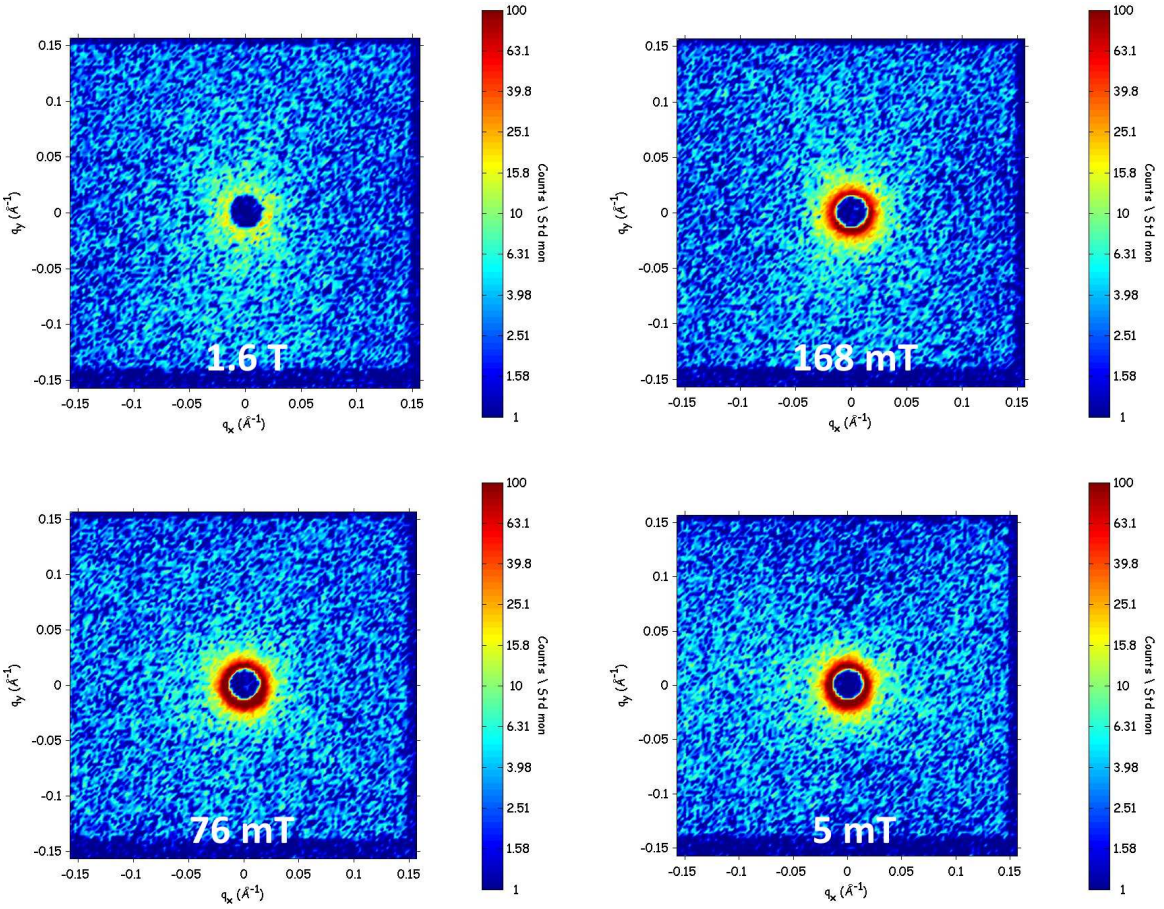

Figure 4.29: SANS highq images of 17S under magnetic field.

is no peak in the intensity. Therefore, the heterogeneites responsible for scattering anisotropy at saturation fields, are dilute.

Next 17Q sample was studied. Transmission measurements showed $T \approx$ 81.3%. Therefore, as it was for 18S, 18Q, 15S, and 17S, the multiple scattering is expected to have some effect on the measurements.

Figure 4.32 shows lowq SANS images for 17Q sample. As in the case of 17S, a high magnetic field was applied and the scattering was measured by decreasing the field to remanence. Before applying a high magnetic field, the scattering was

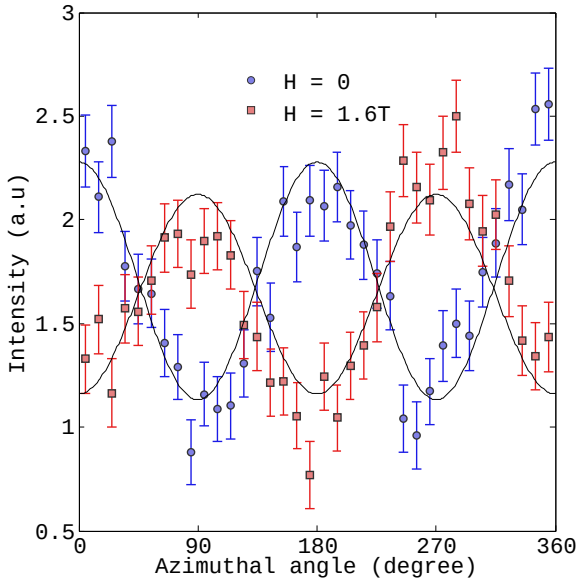

Figure 4.30: Azimuthal angle θ dependence of the SANS intensity averaged over $0.045 \leq |q| \leq 0.14$ Å^{-1} for 17S.

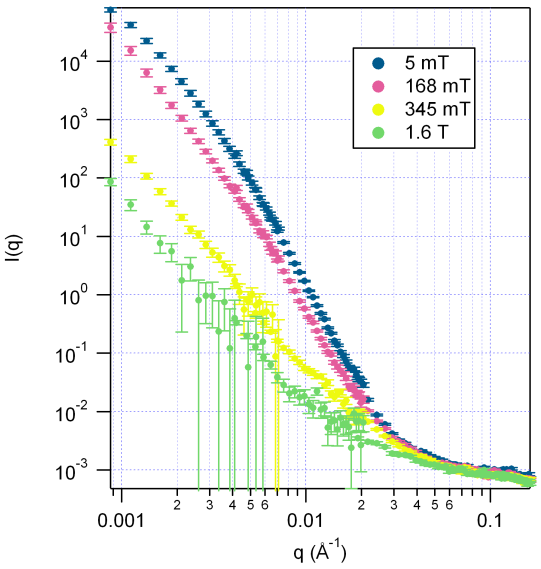

Figure 4.31: 17S SANS I vs. $|q|$, circularly averaged in all directions.

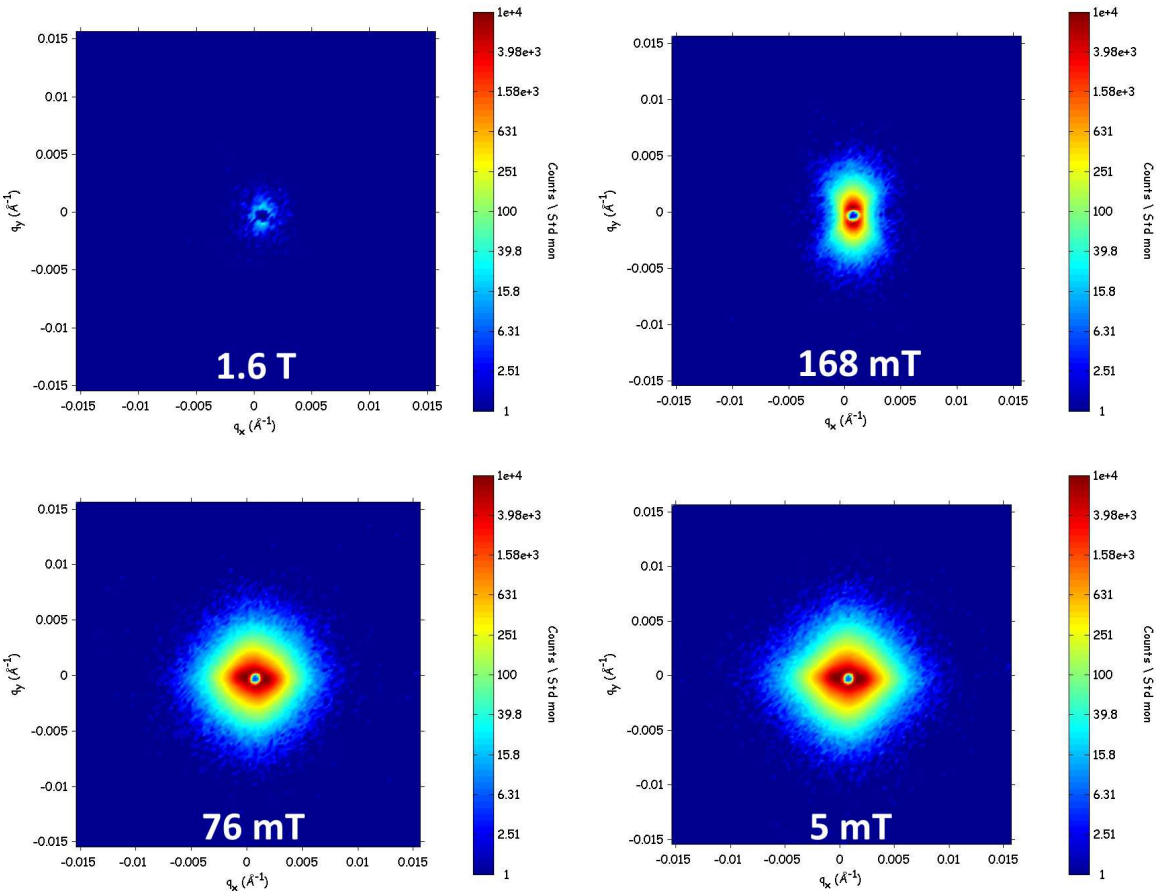

Figure 4.32: SANS lowq images of 17Q under magnetic field.

measured with the sample in its remanent state and it matches with the remanent state scattering image shown in the figure 4.32. The absence of streaks due to the domain wall scattering is quite evident from these images. The remanent state calculation for this sample in table 2.3 shows that 78-89% of the magnetization is oriented along $\pm\hat{\boldsymbol{x}}$. It also shows that 0-22% of it is oriented along $\pm\hat{\boldsymbol{z}}$. Since the scattering due to the domain walls running out-of-plane (along the $\pm\hat{\boldsymbol{z}}$ direction) is independent of the azimuthal angle, it can obfuscate the streaks arising from the in-plane domain walls.

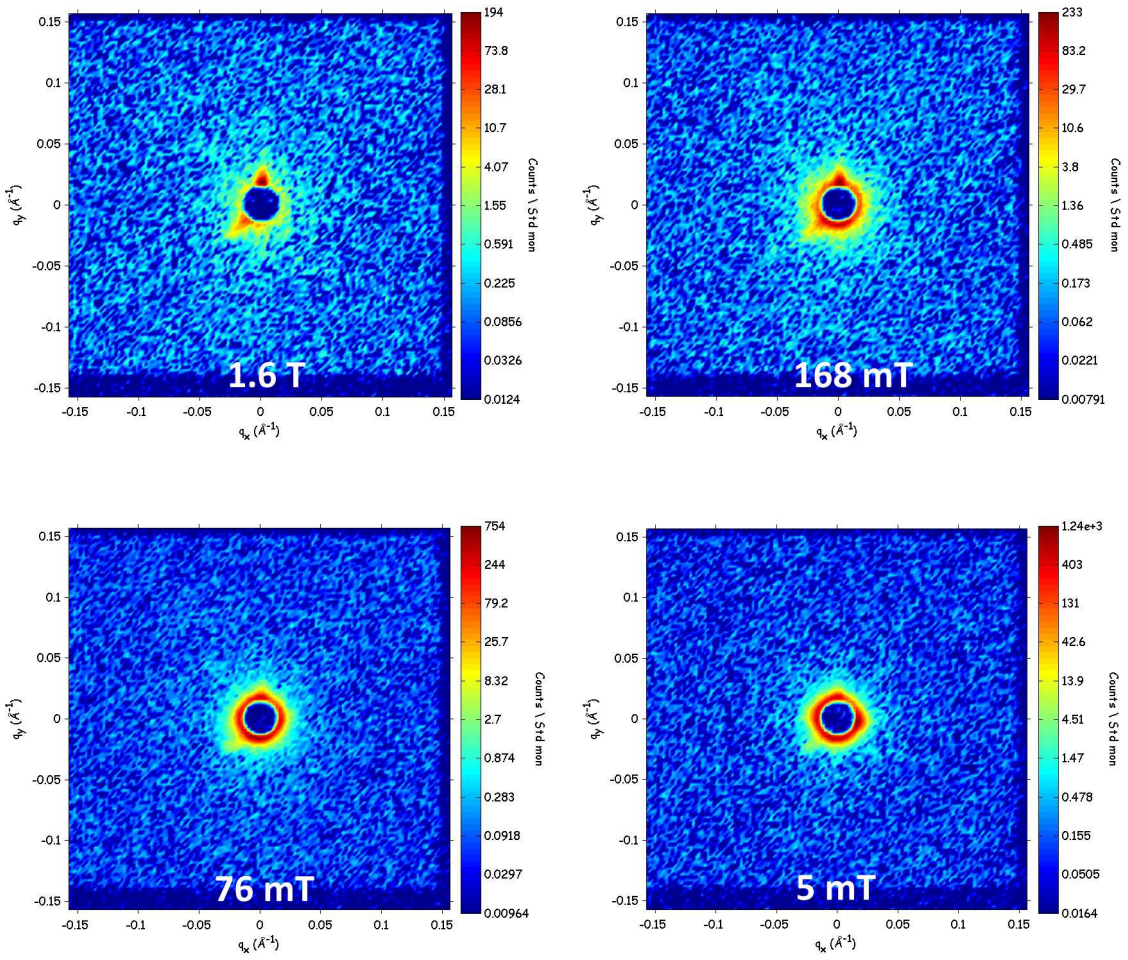

Figure 4.33: SANS highq images of 17Q under magnetic field.

Figure 4.33 shows the SANS highq images for 17Q. There is some scattering even at high fields, which could be of nuclear origin. However, this seems to be limited to lower q values in the highq range. A clear anisotropy is not perceivable from the images directly. However, from the azimuthal plots in figure 4.34, the anisotropy in scattering is prominently visible. The intensity dependence on azimuthal angle at $H = 1.6$ T is sine squared. Further, it can be observed that there is an anisotropy already present at remanence in the same direction as $H = 1.6$ T. As discussed

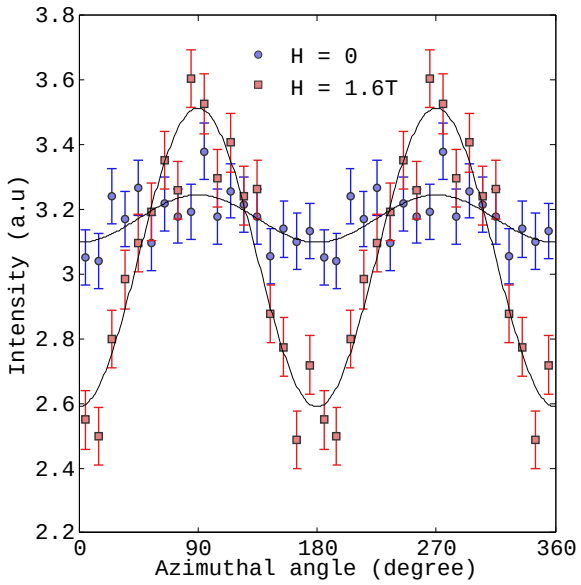

Figure 4.34: Azimuthal angle θ dependence of the SANS intensity averaged over $0.045 \leq |q| \leq 0.14$ Å^{-1} for 17Q.

earlier, the results in table 2.3 show that the remanent state of 17Q has 78-89% of the magnetization oriented along $\pm\hat{\boldsymbol{x}}$. Therefore it is expected that the scattering has an anisotropy along $\pm\hat{\boldsymbol{y}}$ at remanence, which agrees well with the measurement in figure 4.34.

Figure 4.35 shows the circularly averaged I vs. q plots for 17Q sample under different magnetic fields. The tapering of the intensity at lower q values for low magnetic fields is likely due to the extinction of the neutron beam because of multiple scattering.

The next sample studied was 20S. Transmission measurements on this sample showed $T \approx 89\%$. Therefore, multiple scattering is expected to have some contribution to the scattering images but it should not be significant.

Figure 4.36 shows lowq scattering images of 20S under magnetic field. From

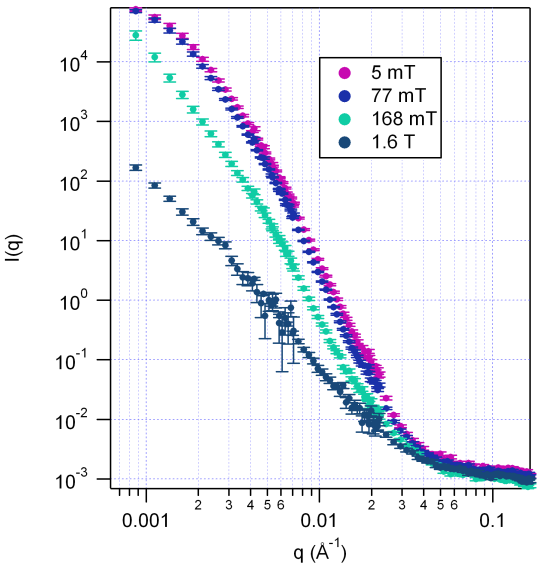

Figure 4.35: 17Q SANS I vs. $|q|$, circularly averaged in all directions.

the images at lower magnetic fields it can be observed that streaks along ±45 degrees are more prominent than at 0 and 180 degrees. This indicates that there are more 90° than 180° domain walls in the sample for lower fields. This is possible only when the magnetization is equi-distributed along $\hat{\boldsymbol{x}}$ and $\hat{\boldsymbol{y}}$. This agrees with the remanent state calculation in table 2.3, which shows that 25-38% of the magnetic moments are oriented along $\pm\hat{\boldsymbol{x}}$ and 50-62% to be oriented along $\hat{\boldsymbol{y}}$.

Highq SANS images are shown in figure 4.37. The anisotropy in scattering is strikingly clear unlike the highq scattering in 18S, 18Q, 15S, 17S, and 17Q samples. The four-fold symmetry seen in 19Qe is also remarkably clear from the scattering images themselves. It can be seen that at $H = 1.6$ T the scattering is mostly along $\hat{\boldsymbol{y}}$ and also seems to have a sine-squared dependence on the azimuthal angle. This indicates the presence of heterogeneities. As the magnetic field is lowered the two-

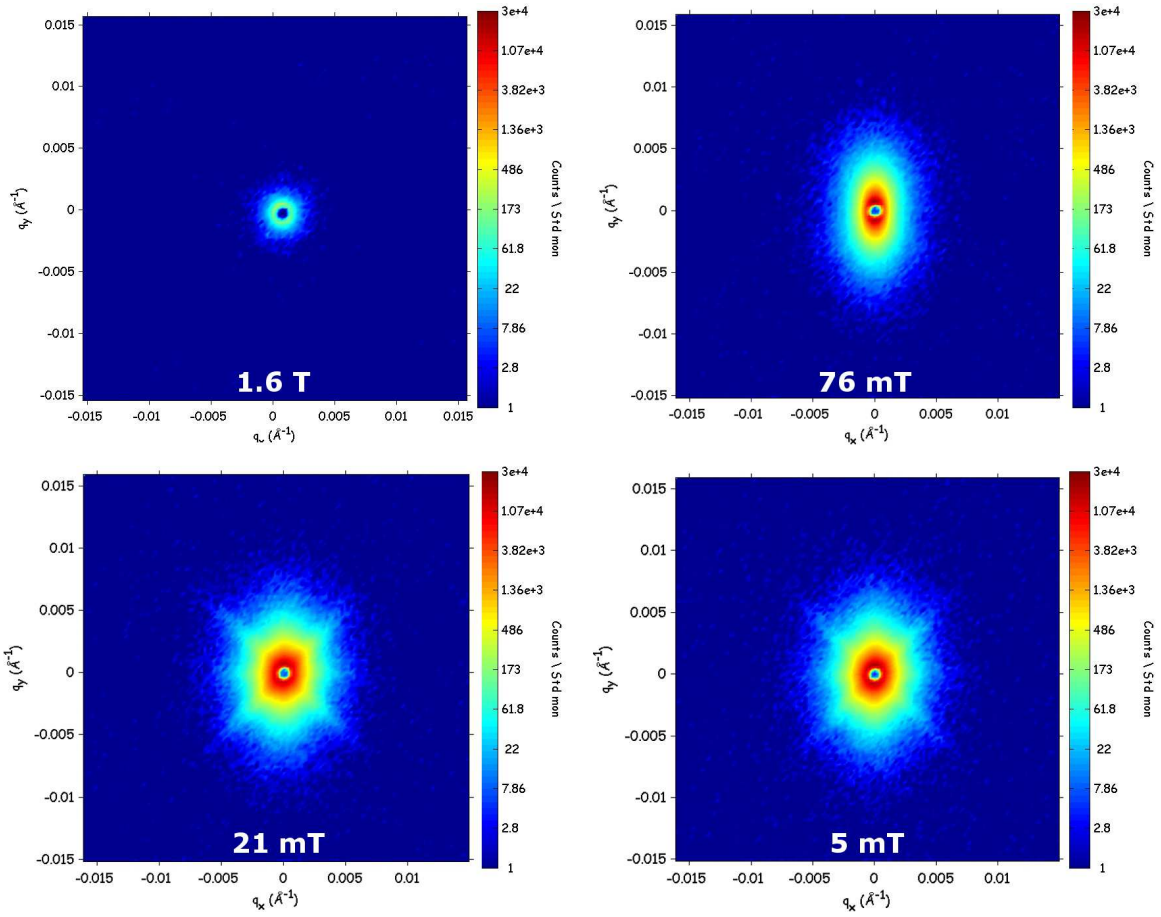

Figure 4.36: 20S lowq SANS images under decreasing magnetic field

fold symmetry becomes four-fold. As explained in the case of 19Qe, with equally distributed magnetic moments, which appears to be the case in 20S, an isotropic scattering is expected at remanence. The four-fold symmetry seen here could be related to subtle magnetic distribution near the heterogeneity/matrix interface.

Figure 4.38 shows the azimuthal angle dependence of the intensity for 20S. As expected from the highq scattering images in figure 4.37, at remanence the intensity has a $\sin^2\theta\cos^2\theta$ dependence, which can not be explained from the theory presented in the introduction. At fields beyond saturation, however, the dependence is clearly

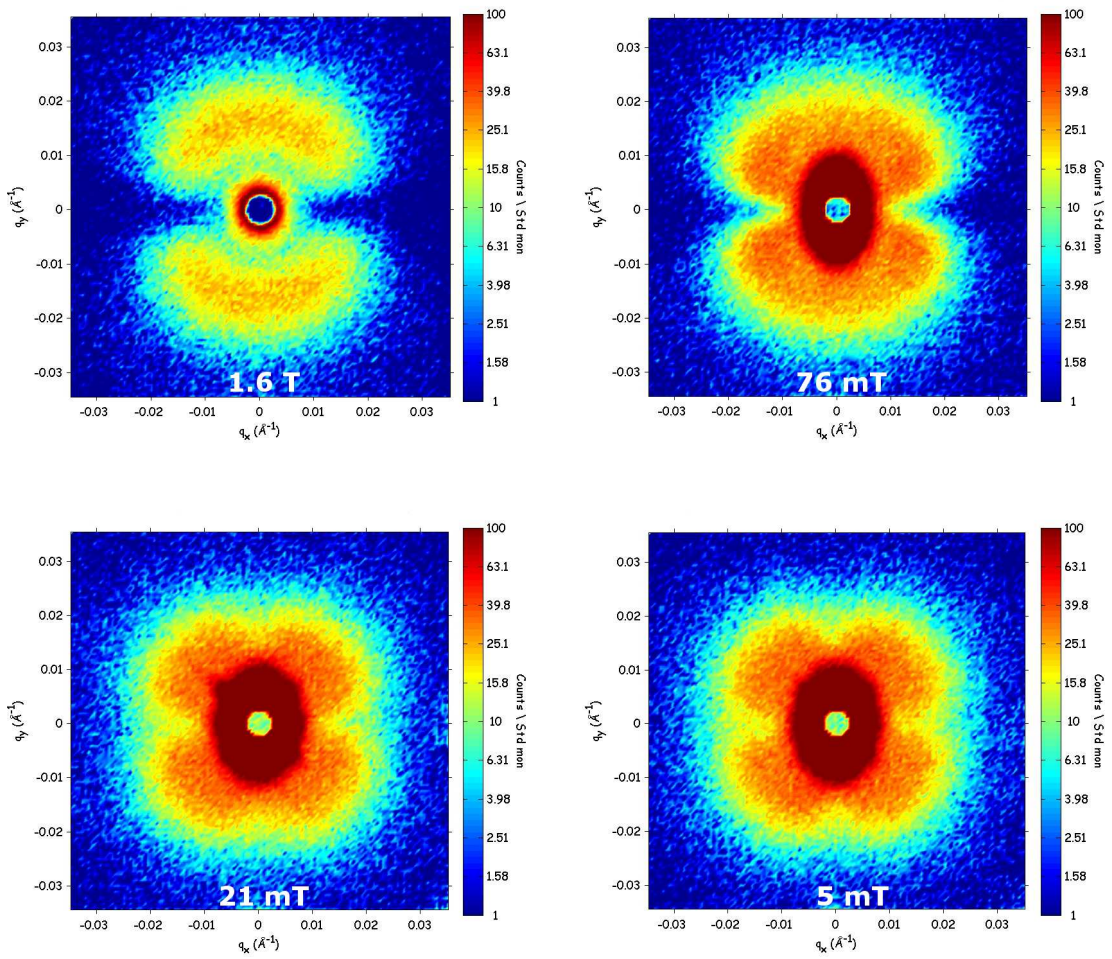

Figure 4.37: 20S highq SANS images under decreasing magnetic field

$\sin^2\theta$.

Figure 4.39 shows circularly averaged scattering intensity. A peak corresponding to $q \approx 0.018$ Å^{-1} can be seen in the intensity. This corresponds to a $d-$spacing of ∼35 nm. Therefore, the scattering sites or the heterogeneities responsible for the highq scattering are spaced, on average, 35 nm apart. As the peak exists at the border of lowq and highq scattering, there is also an effect of domain wall scattering near the peak. Therefore, when the magnetic field is increased, the intensity of the

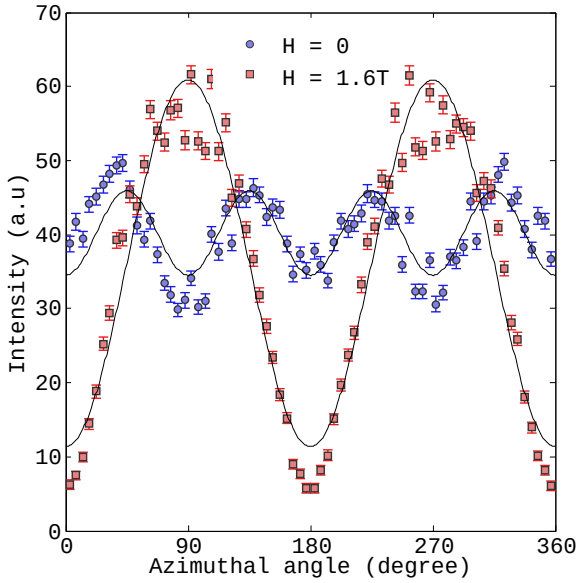

Figure 4.38: Azimuthal angle θ dependence of the SANS intensity averaged over $0.029 \leq |q| \leq 0.14$ Å^{-1} for 20S.

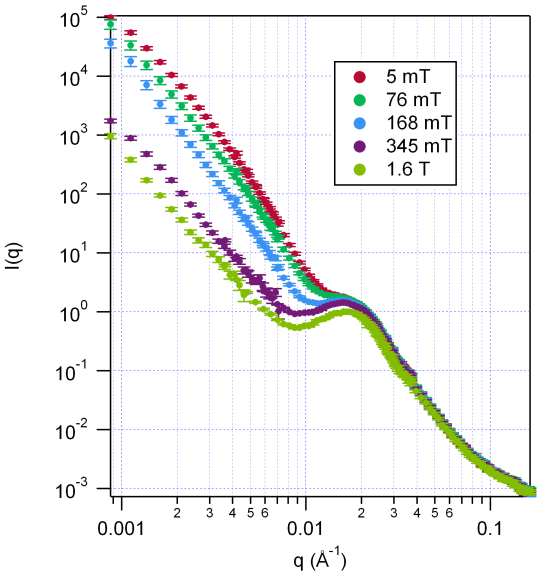

Figure 4.39: 20S SANS I vs. $|q|$, circularly averaged in all directions.

peak reduces because of the reduced domain wall scattering. The scattering in this sample is very similar to 19Qe sample than any other samples looked at in this study.

Next, the 20Q sample was studied. Transmission measurements on this sample showed $T \approx 92\%$. As $T > 90\%$, the multiple scattering effect is expected to be minimal.

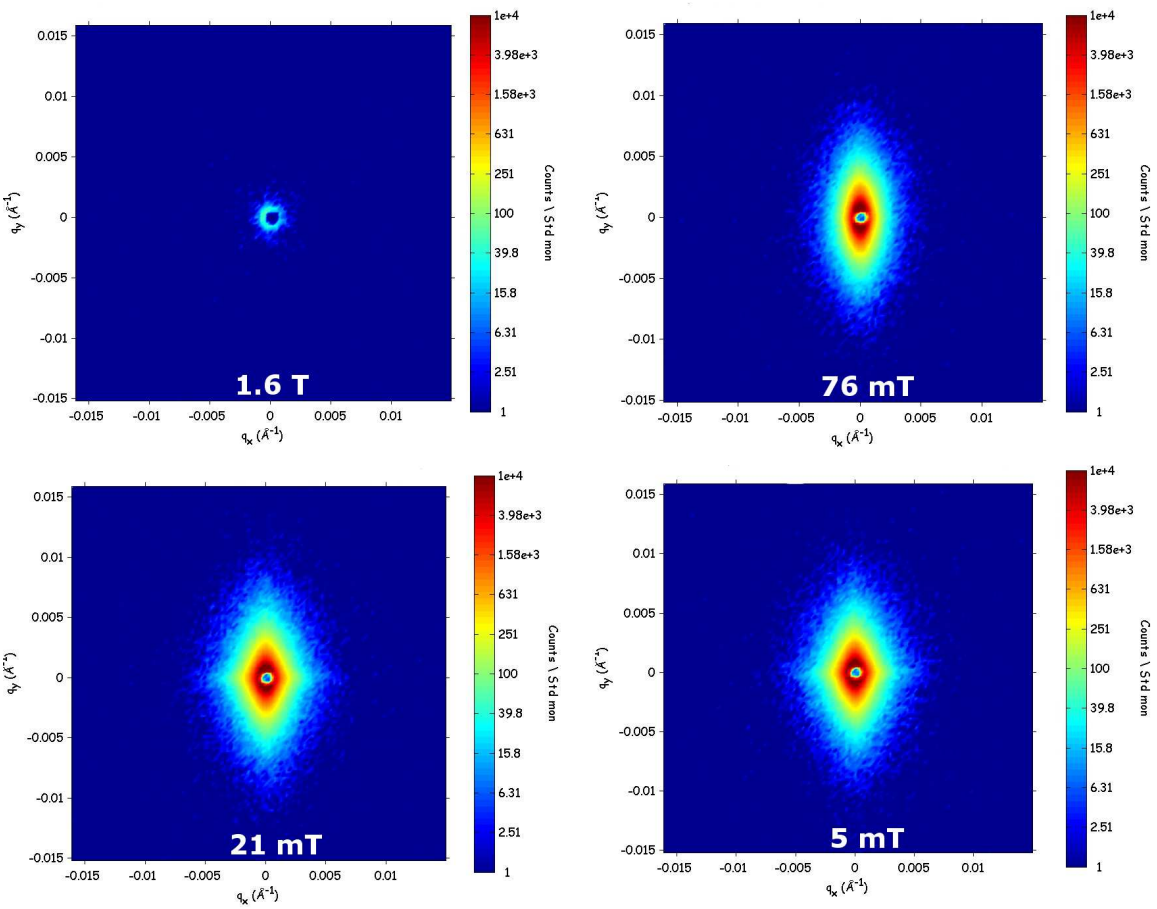

Figure 4.40: 20Q lowq SANS images under decreasing magnetic field

Lowq SANS images for 20Q under decreasing magnetic field are shown in figure 4.40. It can be observed that the streaks representing 90° domain walls are absent

for all magnetic fields. This could be because of the remanent state of the sample. Also, if the magnetization is aligned along the thickness ($\pm\hat{\boldsymbol{z}}$) of the sample, then the isotropic scattering resulting from such domain walls can obscure the streaks. The estimation of the remanent states of this sample from table 2.3 shows that 0-43% of the magnetic moments could be oriented along $\pm\hat{\boldsymbol{z}}$. Magnetic domain images could have been useful but such a study could not be conducted on this sample.

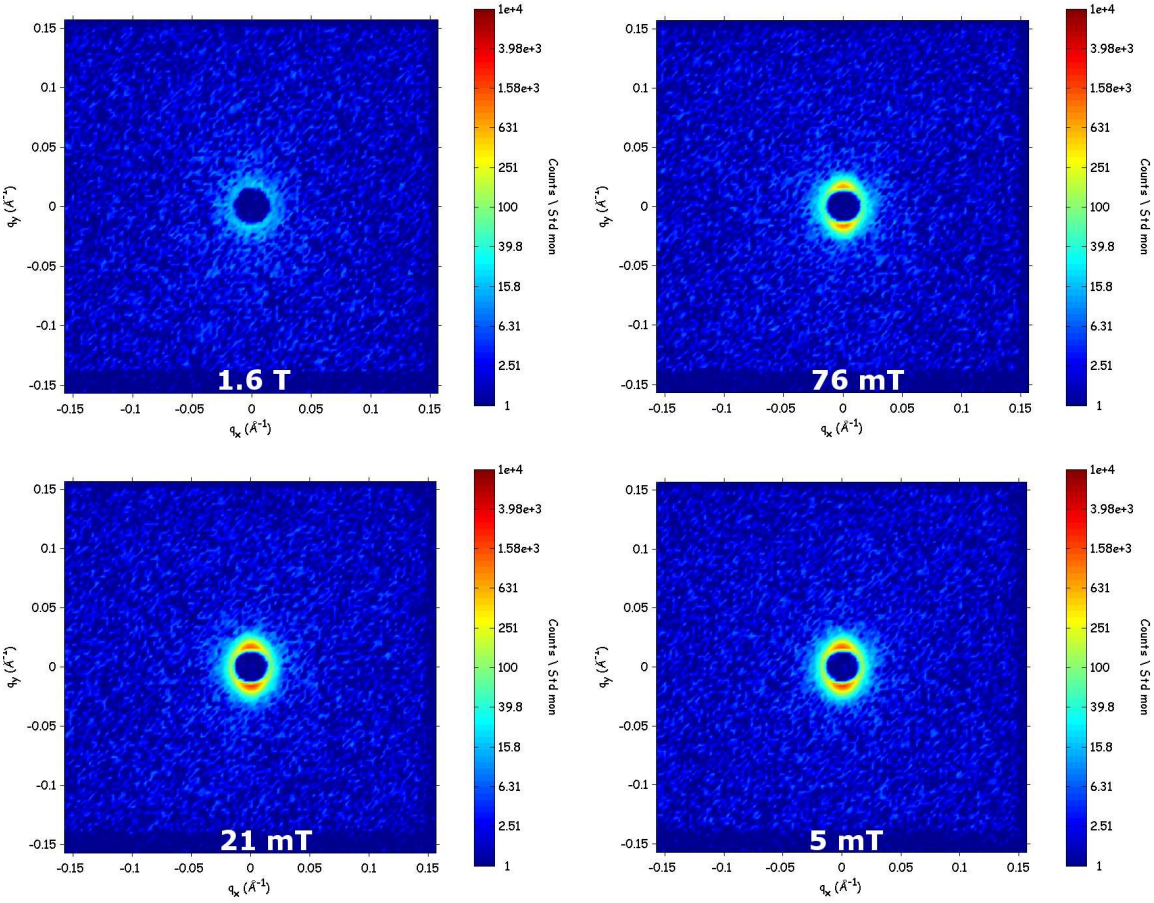

Figure 4.41: 20Q highq SANS images under decreasing magnetic field

Figure 4.41 shows highq SANS images for 20Q sample. The scattering at this q range was expected to be anisotropic as seen in 19Qe and 20S. However, the

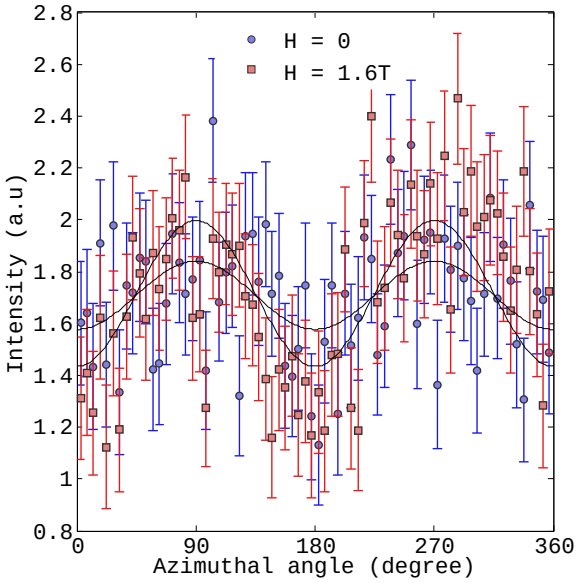

Figure 4.42: Azimuthal angle θ dependence of the SANS intensity averaged over $0.029 \leq |q| \leq 0.14$ Å^{-1} for 20Q.

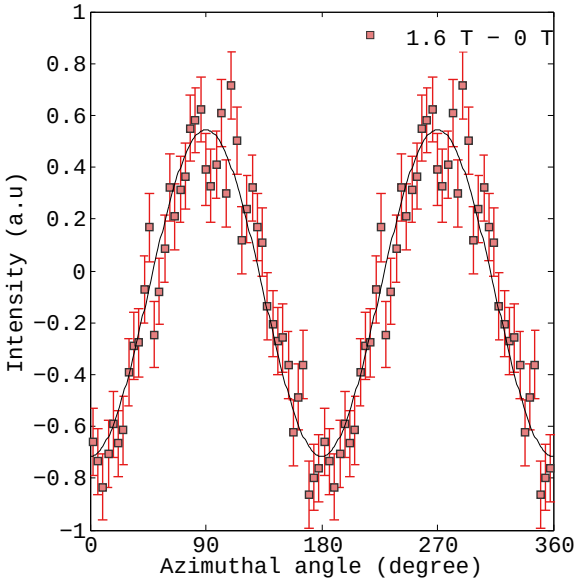

Figure 4.43: Azimuthal angle θ dependence of the SANS intensity of 20Q. Intensity at remanence was subtracted from the intensity at $H = 1.6$ T and averaged over $0.029 \leq |q| \leq 0.14$ Å^{-1}.

anisotropy in scattering seems imperceptible from the scattering images. Contrary to the expectation, the scattering in 20Q is closer in nature to 15S, 17S, 18Q, 17S, and 17Q rather than 19Qe or 20S. Plotting the azimuthal angle dependence of the scattering in figure 4.42 shows anisotropy. However statistics were barely sufficient to distinguish the anisotropy. It must be noted that the counting time for 19Qe, 20S, and 20Q is same. Plotting the scattering dependence on the azimuthal angle by subtracting the intensity at remanence from that at $H = 1.6$ T shows the anisotropy more clearly (see figure 4.43).

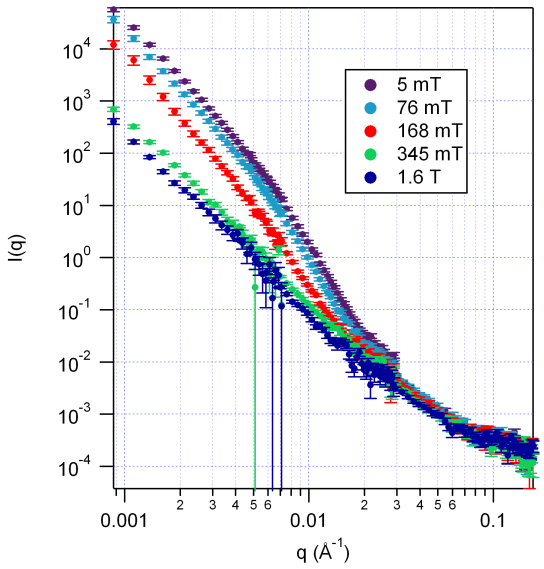

Figure 4.44: 20Q SANS I vs. $|q|$, circularly averaged in all directions.

Figure 4.44 shows circularly averaged intensity of 20Q. The intensity curves are more similar to the rest of the samples rather than 19Qe or 20S sample. There is no peak corresponding to the average separation of the heterogeneities. The lowq scattering decreases with increasing magnetic field as expected. The lack of peak in

the intensity curves and a very weak scattering anisotropy shows that the heterogeneities are much less in volume in 20Q compared to any other sample studied.

Table 4.3: Summary of unpolarized SANS results under magnetic field

Sample	Anisotropy at H > 1.3 T	Anisotropy at remanence	Avg heterogeneity separation
15S	Weak	NA	random
17S	Weak	Twofold along $\pm\hat{\boldsymbol{x}}$	random
17Q	Weak	negligible	random
18S	Weak	Twofold along $\pm\hat{\boldsymbol{x}}$	random
18Q	Weak	negligible	random
19Qe	Strong	Twofold along $\pm\hat{\boldsymbol{x}}$	15 nm
20S	Strong	Fourfold along $\pm 45^\circ$	34 nm
20Q	Weak	negligible	random

Results from unpolarized SANS experiments are summarized in table 4.3. Peaks in SANS intensity curves were observed only for 19Qe and 20S samples. The anisotropy in the intensity was also strong in the same samples. At remanence, the anisotropy in the SANS intensity was present in all the samples. For 15S sample, the anisotropy was obscured by the nuclear scattering.

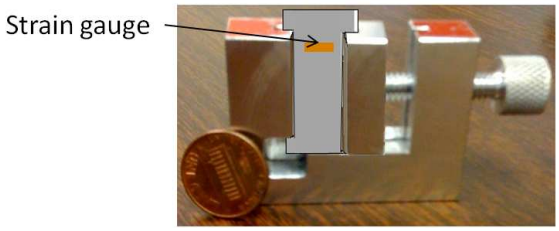

Figure 4.45: Device used to apply compressive elastic load to the sample. A resistive strain gage bonded to the sample was used to quantify the applied load

4.4.2 Under elastic field

SANS experiments as described in the previous section were repeated on 19Qe sample. For these experiments, 19Qe was subjected to an elastic field. A compressive load was applied along $\hat{\boldsymbol{y}}$ using a device shown in figure 4.45. For applying a load, the sample was compressed by manually turning the nob and compressing the sample between a fixed and a movable high strength aluminum plates. A resistive strain gage bonded to the sample, as shown in figure 4.45, was used to quantify the load that was applied to sample.

Figure 4.46 shows lowq SANS images of 19Qe under elastic field. When the elastic field is increased, there appears to be some change in the lowq scattering in that it becomes more symmetrical for intermediate elastic fields. However, even at the maximum elastic load that could be applied, the scattering is still present unlike the magnetic field case. When the sample is subjected to a compressive elastic field along $\hat{\boldsymbol{y}}$, the magnetization is expected to re-orient perpendicular to the compressive elastic field direction i.e., along $\pm\hat{\boldsymbol{x}}$ or $\pm\hat{\boldsymbol{z}}$. From domain studies in chapter 3 and

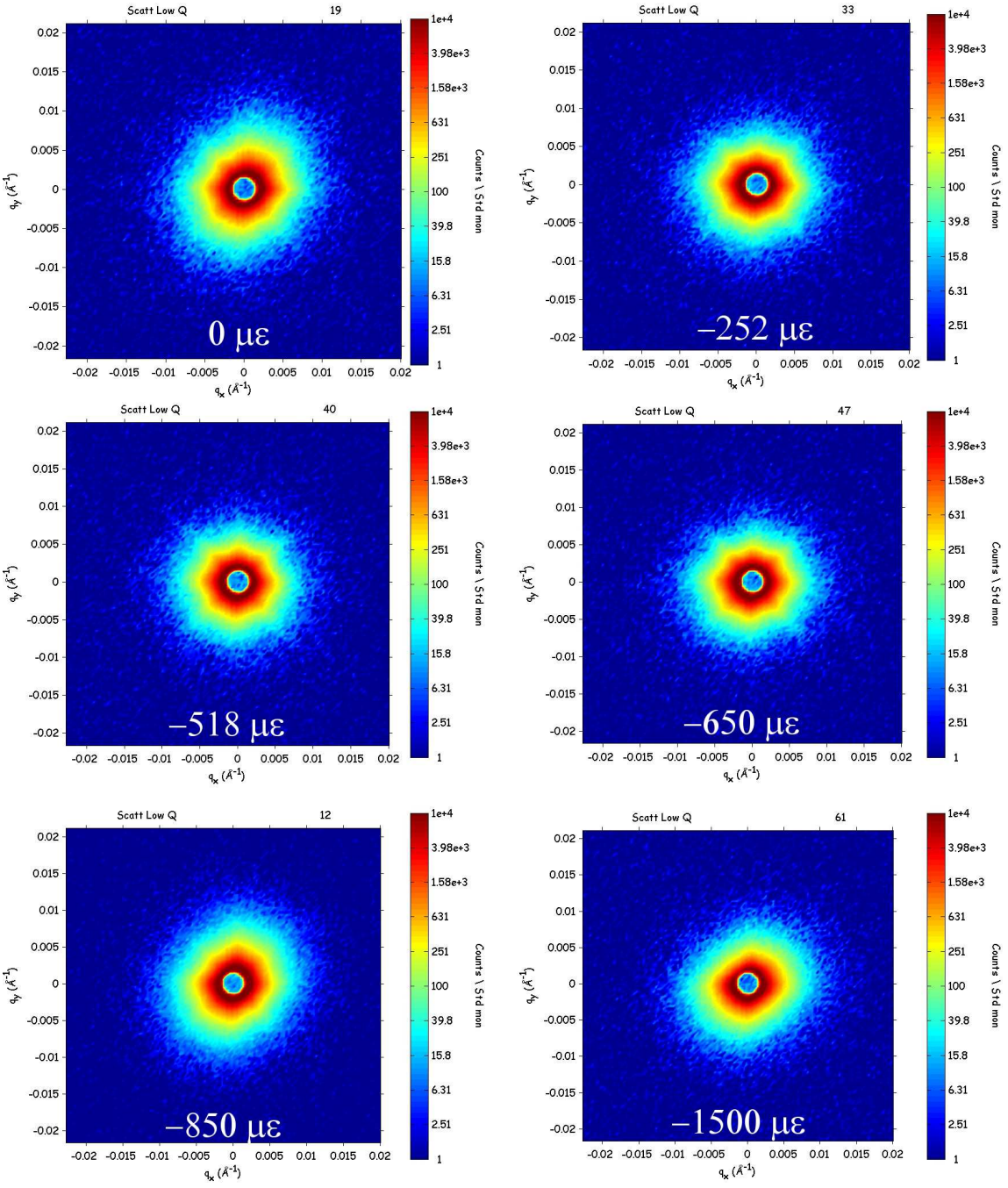

Figure 4.46: 19Qe lowq SANS images under elastic field

figure 3.35, it can be seen that $\pm\hat{\boldsymbol{x}}$ domains with 180° domain walls running along $\hat{\boldsymbol{x}}$ form up on application of a compressive stress on 19Qe. Therefore a streak along

$\hat{\boldsymbol{x}}$ is expected in the lowq SANS image. However, there was no significant change seen in the lowq scattering.

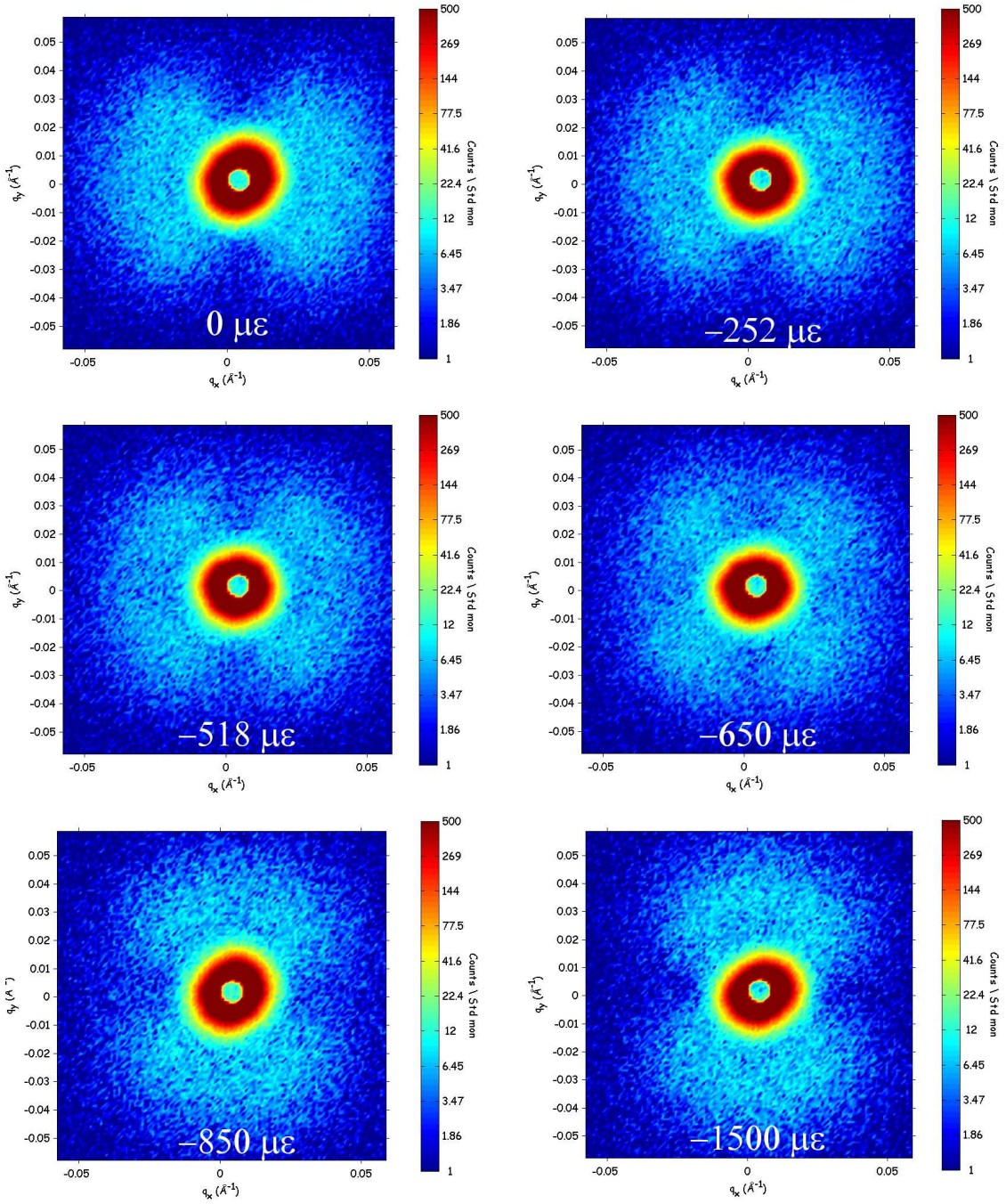

Figure 4.47: 19Qe highq SANS images under elastic field

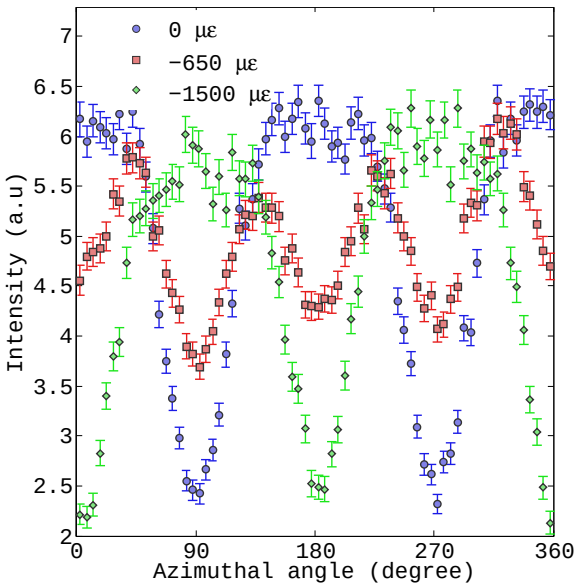

Figure 4.48: Azimuthal angle θ dependence of the SANS intensity averaged over $0.02 \leq |q| \leq 0.051$ Å^{-1} for 19Qe under elastic field

SANS highq scattering images of 19Qe are shown in figure 4.47 for increasing elastic fields. At remanence, the scattering has a two-fold symmetry, as observed previously in figure 4.11. This indicates, as discussed before, that the magnetization of the heterogeneities responsible for scattering is oriented along $\pm\hat{\boldsymbol{y}}$. Upon applying a compressive elastic field along $\pm\hat{\boldsymbol{y}}$, the magnetization is expected to reorient either along $\pm\hat{\boldsymbol{x}}$ or along $\pm\hat{\boldsymbol{z}}$. It can be seen from the images that under elastic field the scattering eventually reorients itself to align along $\pm\hat{\boldsymbol{y}}$ i.e., the magnetization of the heterogeneities reoriented along $\pm\hat{\boldsymbol{x}}$. The response of the magnetization of the heterogeneities is in accordance with the magnetic domains as imaged by Kerr microscopy in chapter 2, figure 3.35. However, the magnetic domain wall scattering in figure 4.46 is not in agreement. At intermediate elastic fields, the scattering shows a four-fold symmetry similar to the magnetic field case. This, as explained

before, could be due to the distribution of magnetization at the heterogeneity/matrix interface. Intensity dependence on the azimuthal angle plotted in figure 4.48 shows the anisotropy changing from two-fold along $\pm\hat{\boldsymbol{x}}$ to four-fold and to two-fold along $\pm\hat{\boldsymbol{y}}$ clearly.

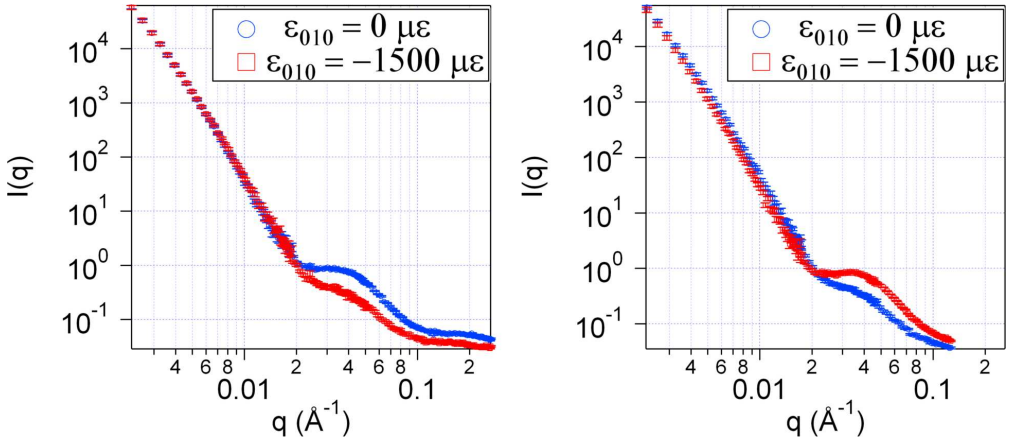

Figure 4.49: SANS I vs. $|q|$ of 19Qe under increasing compressive elastic field along $\hat{\boldsymbol{y}}$, averaged along a 30 degree horizontal sector (left) and a 30 degree vertical sector (right).

Circularly averaged intensity of 19Qe under elastic field is shown in figure 4.49. As observed in the lowq and highq SANS images in figures 4.46 and 4.47, there is a minimal change in the lowq scattering with applied compressive elastic fields. Whereas, the highq scattering clearly reduced along the horizontal sector and increases along the vertical sector. These results show that while highq scattering for magnetic and elastic fields are similar, lowq scattering seems to differ.

4.5 Polarized SANS

As described in section 4.2.2.2, polarized neutrons give rise to four cross-sections - two of them are non-spin-flip while the other two are spin-flip. From the expressions derived for non-spin-flip and spin-flip scattering in equations (4.49) and (4.50), it can be seen that while non-spin-flip scattering has a nuclear contribution superimposed on the magnetic contribution, spin-flip scattering has magnetic contribution alone. This offers a very good opportunity to separate the nuclear component from the magnetic component, that could lead to gaining valuable information about the nature of the heterogeneities. The neutron beam is polarized using Fe/Si transmission polarizer and the scattered neutrons were analyzed using a cell of nuclear spin polarized ^{3}He. Using such a setup, all four cross-section were measured. The sample placement was similar to the unpolarized neutron experiments.

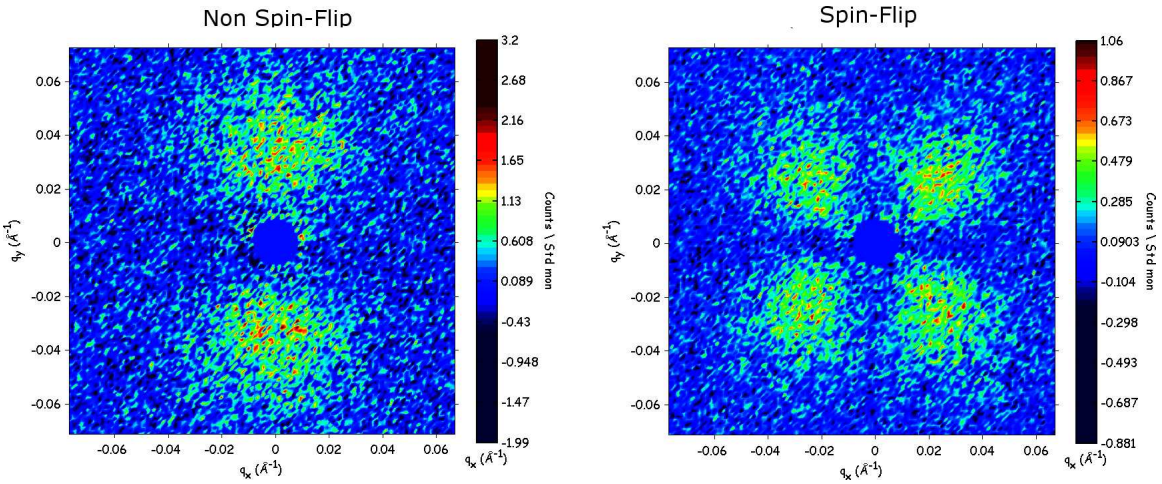

Figure 4.50: 19Qe non-spin-flip scattering (left) and spin-flip scattering (right) images at $H = 1.3$ T

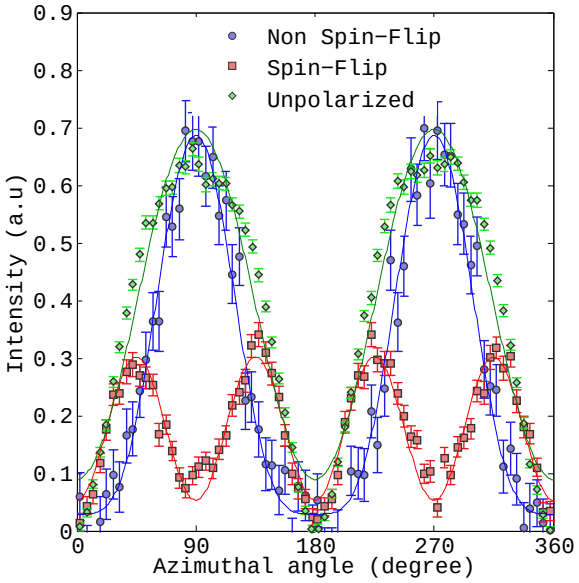

Figure 4.51: Azimuthal angle dependence of non-spin-flip and spin-flip scattering in comparison to scattering of unpolarized neutrons for 19Qe at $H = 1.3$ T. Intensity was averaged for $0.02 \leq q \leq 0.057$ Å^{-1}.

Figure 4.50 shows the scattering images obtained from the polarized neutrons at $H = 1.3$ T. On the left is the scattering image from non-spin-flip scattering and on the right is the image from spin-flip scattering. In figure 4.51, the azimuthal angle dependence of the non-spin-flip and spin-flip scattering are plotted. It can be seen that the non-spin-flip scattering has a clear $\sin^4\theta$ dependence and spin-flip scattering has a clear $\sin^2\theta\cos^2\theta$ dependence as is expected from the expressions in equations (4.49) and (4.50). It can also be seen that the scattering is predominantly magnetic and nuclear contribution appears to be negligible, as expected.

The polarization of the neutron beam that passes through the sample, should directly give the magnetization measurement of the sample. If $F = I^+/I^-$ is the flipping ratio, where I^+ is the intensity of the transmitted neutrons with parallel

spin and I^- is the intensity of the transmitted neutrons with antiparallel spin, then polarization P can be defined as

$$P = \frac{F-1}{F+1}. \tag{4.76}$$

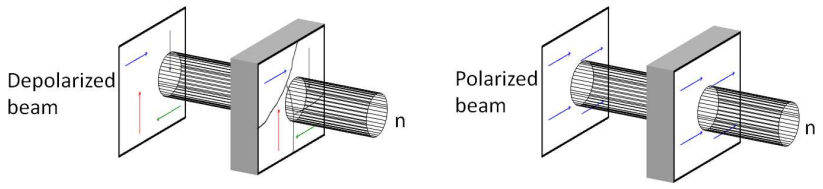

Figure 4.52: Schematic of depolarized neutron beam due to the presence of magnetic domains and polarized neutron beam at saturation.

As shown in figure 4.52, when multiple magnetic domains are present the neutrons passing through the sample get depolarized. When the sample is in a single magnetic state, beyond magnetic saturation, the neutrons get completely polarized. Therefore, polarization of the neutrons give a direct measure of the magnetization of the sample.

Figure 4.53 shows the neutron polarization measurement for 19Qe with increasing magnetic field. From these measurements the sample seems to saturate between 100 - 200 mT. However, the magnetization measurement using VSM in figure 2.3 and using Kerr microscopy in figure 3.26 both show the saturation to take place around 30 mT.

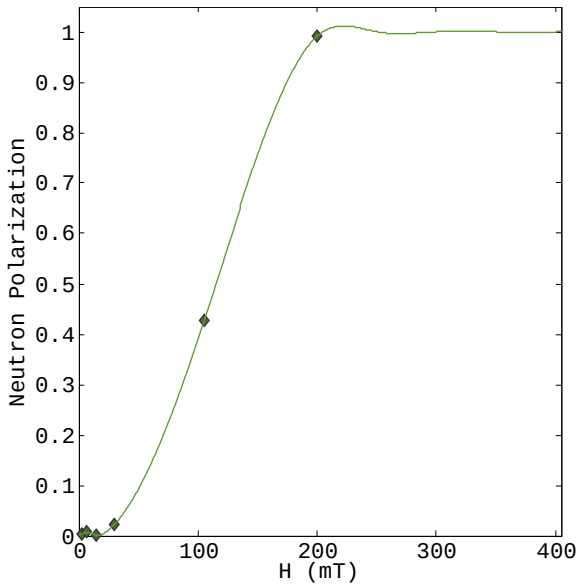

Figure 4.53: Neutron polarization with increasing magnetic field for 19Qe.

4.6 Ultra Small-Angle Neutron Scattering

In this section, the results from Ultra Small-Angle Neutron Scattering (USANS) experiments conducted on 19Qe, 20S, 17S, 17Q samples are presented. USANS allows the samples to be probed at q-values much lower than that possible with SANS - as low as 3×10^{-5} Å^{-1}. This allows one to probe away from the length scales where heterogeneities may effect the domain wall scattering. With $q = 3 \times 10^{-5}$ Å^{-1}, a sample can be probed at length scales as large as 20 μm. It should be noted that these length scales are still lower than the domain sizes (see chapter 3). Therefore, the scattering is still expected to occur due to the domain walls.

For the USANS experiments, samples were placed such that their long axis was parallel to the horizontal direction ($\hat{\boldsymbol{x}}$) of the instrument. In other words, the q values probed by USANS correspond to the SANS q_x values averaged over all q_y.

As in the SANS experiments, magnetic field was applied along $\hat{\boldsymbol{x}}$ with the help of a conventional electromagnet capable of applying fields up to 1.2 T.

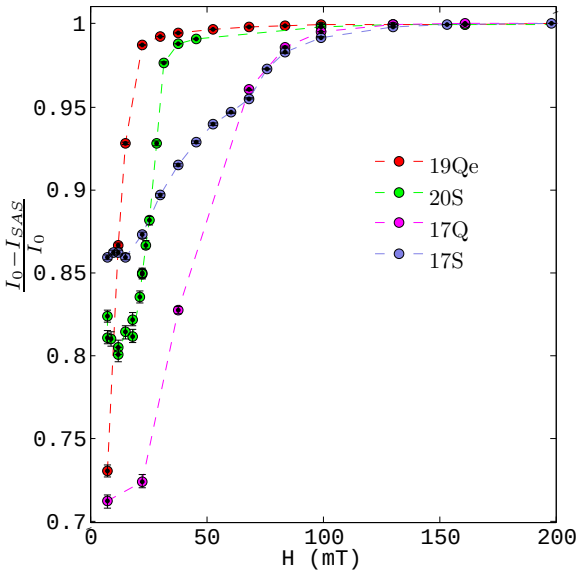

Figure 4.54: USANS transmission measurements for 19Qe, 20S, 17Q, and 17S. I_{SAS} was measured at $q = 1.7 \times 10^{-4}$ Å^{-1}.

As discussed in the introduction for USANS, multiple scattering effects can be minimized if the transmission

$$T = \frac{I_0 - I_{SAS}}{I_0} \tag{4.77}$$

is greather than 90%. Here I_0 is the intensity at $q = 0$ i.e., intensity at the bragg peak of the perfect crystal. I_{SAS} is the intensity of the small angle scattering, for some $q \neq 0$. For the transmission experiments, I_{SAS} was measured at $q = 1.7 \times 10^{-4}$ Å^{-1}.

Figure 4.54 shows the transmission measurements for 19Qe, 20S, 17Q, and 17S. At remanence, the tranmission of all the samples is less than 90%. With

increasing magnetic field, however, the tranmission also increases. As the density of domain walls is reduced with magnetic field, the scattering probability also goes down, increasing the tranmission. Therefore, USANS intensity was measured for only those magnetic fields for which $T \geq 90\%$ such that multiple scattering can be safely ignored.

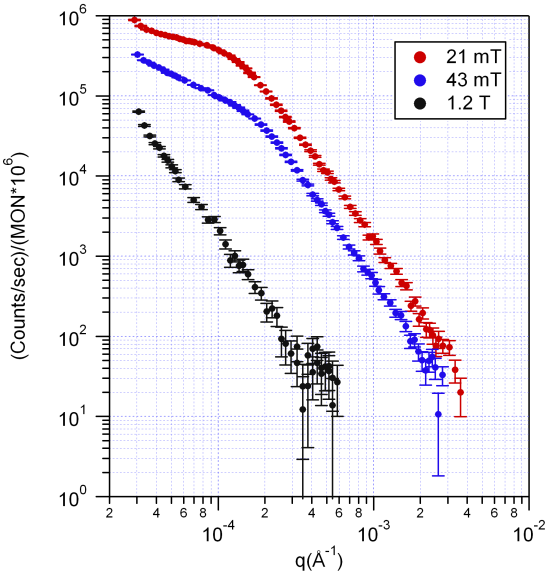

Figure 4.55: 19Qe USANS intensity curves for increasing magnetic fields

Figure 4.55 shows the USANS intensity for 19Qe sample under increasing magnetic field. At $H = 21$ mT, there appears to be a broad peak at $q \approx 1 \times 10^{-4}$ Å^{-1}, which shifts to $q \approx 2 \times 10^{-4}$ Å^{-1} at $H = 43$ mT, and disappears completely at $H = 1.2$ T. The scattering across all q-values decreases with increasing magnetic field, consistent with the expectation. However, there is still significant scattering even at $H = 1.2$ T. If the source of the scattering is magnetic and from the domain walls, it is expected to completely go away when a magnetic field as high as $H = 1.2$

T is applied, which is way beyond the saturation magnetic field ($\sim$ 30 mT) of this sample.

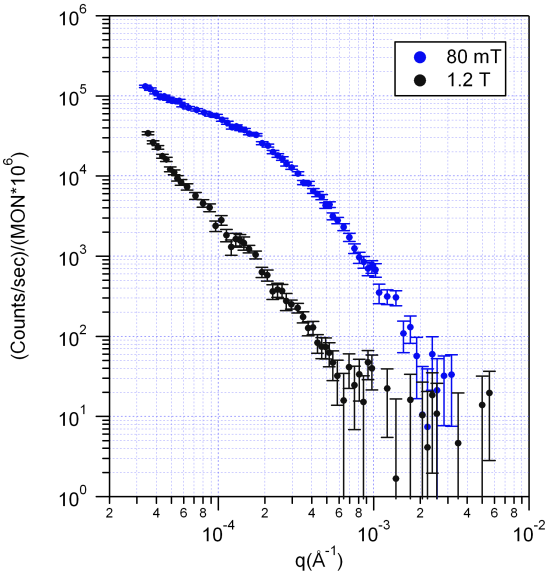

Figure 4.56: 20S USANS intensity curves for increasing magnetic fields

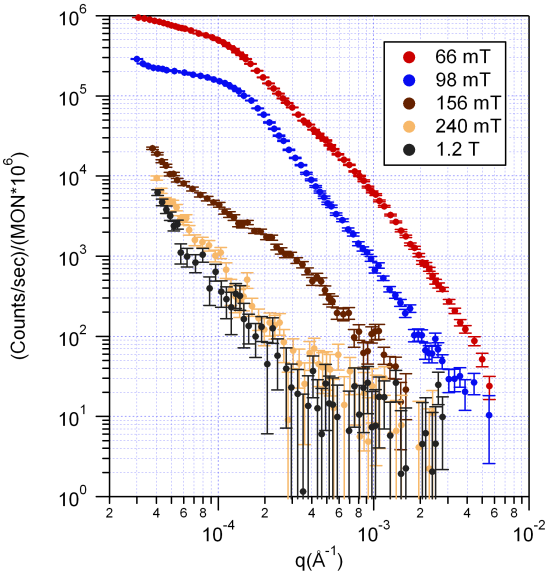

Figure 4.57: 17Q USANS intensity curves for increasing magnetic fields

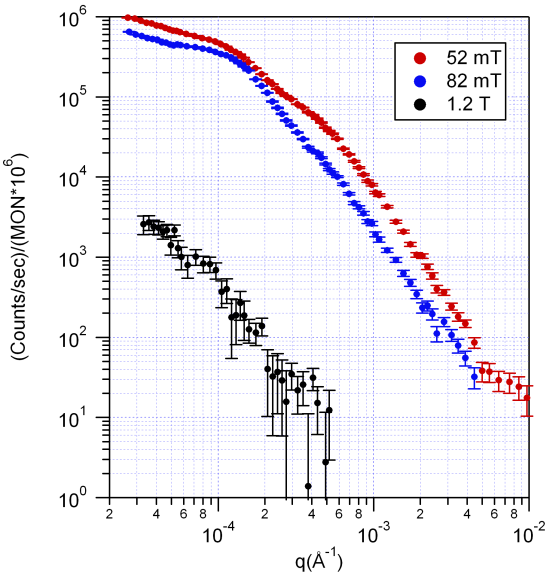

Figure 4.58: 17S USANS intensity curves for increasing magnetic fields

Similarly, USANS intensity under increasing magnetic field is shown in figures 4.56, 4.57, and 4.58 for 20S, 17Q, and 17S respectively. A broad peak at $q \approx 1 \times 10^{-4}$ that shifts towards higher q-values, eventually disappearing can be seen to exist in all the three samples. Further, the scattering does not completely go away even at $H = 1.2$ T. This is contrary to the expectation but seems to be a characteristic of all the samples studied.

Next, the USANS experiments were conducted to study the effect of sample's surface conditions on the scattering results. All the USANS results shown above are either for unpolished samples or one of the surfaces polished. Samples 19Qe, 17Q, and 17S were those with one side polished whereas 20S was unpolished. Since the neutrons pass through the sample, if there were any effect of the surface conditions on the scattering, both the surfaces must be polished. Therefore, for the next study,

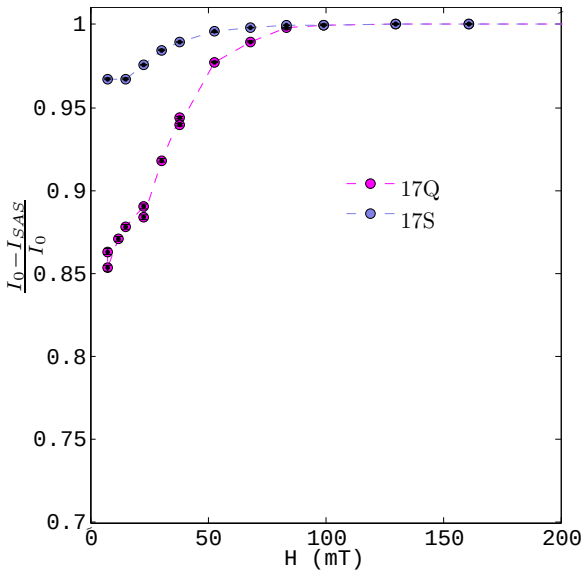

Figure 4.59: USANS transmission measurements of 17Q and 17S after they polishing them both sides. I_{SAS} was measured at $q = 1.7 \times 10^{-4}$ Å^{-1}.

17Q and 17S were finely polished on other side as well, as described in chapter 3, such that true domains were visible. Now, 17Q and 17S were finely polished on either side.

The transmission experiments were repeated on 17Q and 17S after polishing them on both sides. The results are shown in figure 4.59. Compared to the transmission measurements before polishing both sides in figure 4.54 the transmission has improved significantly. At remanence, the transmission of 17Q has improved from 71% to 85% while the transmission of 17S has improved from 85% to 97%. This already shows that surface conditions of the sample has a significant effect on USANS.

Figures 4.60 and 4.61 show the USANS intensity of 17Q and 17S respectively

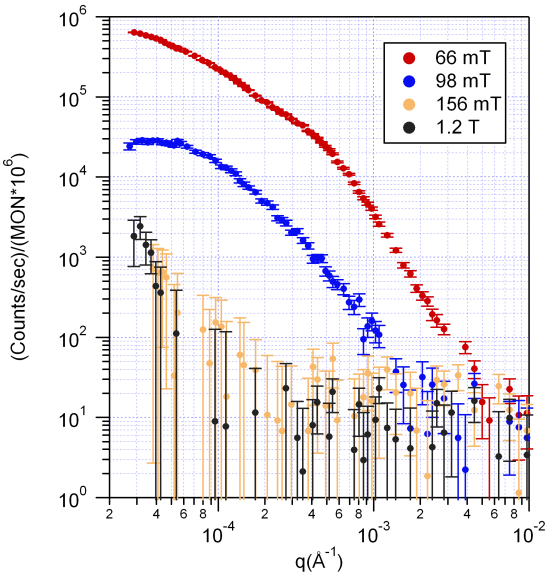

Figure 4.60: 17Q USANS intensity curves for increasing magnetic fields after top and bottom surfaces were polished

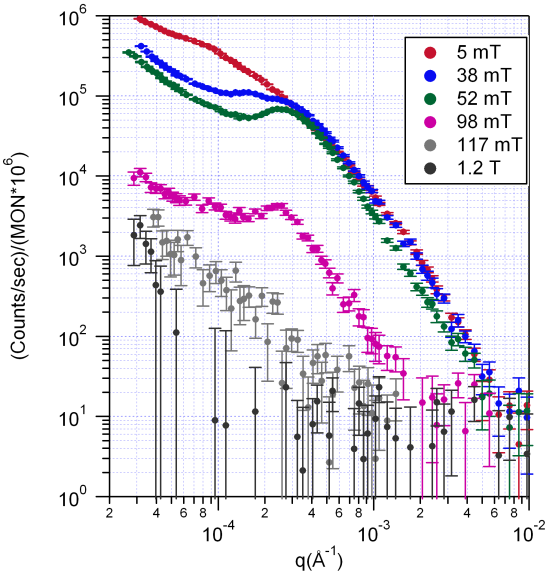

Figure 4.61: 17S USANS intensity curves for increasing magnetic fields after top and bottom surfaces were polished

after they have been polished on both sides. The scattering intensity at $H = 1.2$ T drastically came down compared to the same before they were polished (see figures 4.57, and 4.58) on both sides. Therefore, it seems that the high field scattering before they were polished on both sides could be from the surface crystalline imperfections.

4.7 Neutron Diffraction

Fe–Ga are cubic alloys with lattice parameter $a \approx 2.9$ Å[52]. The phase in which Fe–Ga exists below 18 at% Ga is A2 [55]. A2 phase has disordered bcc structure as shown in figure 1.7. The primitive unit cell of this bcc phase is the one which contains atoms at (0,0,0) and (1/2,1/2,1/2). Using equation (4.62), structure factor of the A2 phase for $Fe_{1-x}Ga_x$ can be calculated as

$$\begin{aligned} S_{hkl} &= b_{av}e^{i2\pi(0)} + b_{av}e^{i\pi(h+k+l)} \\ &= b_{av}\left(1 + e^{i\pi(h+k+l)}\right) \end{aligned} \tag{4.78}$$

where $b_{av} = (b_{Fe}(1-x) + b_{Ga}(x))$ and $b_{Fe} = 9.45$ fm and $b_{Ga} = 7.288$ fm [98] are the neutron scattering lengths of Fe and Ga respectively. For *odd* $h+k+l$, $S_{hkl} = 0$. As a result, any reciprocal lattice point where $h+k+l$ is odd will be invisible i.e., reciprocal lattice point (200) will be visible but (100) will be invisible. Calculating the structure factor similarly for other plausible phases - DO3, $D0_{22}$, B2, $L1_2$ - indicates that both (200) and (100) reciprocal lattice points will be visible for these phases. Further, the (1/2 1/2 1/2) reciprocal lattice point (a superlattice reflection) will be visible only for DO3 and $D0_{22}$ and not for A2, B2 and $L1_2$.

Figure 4.62 shows the rocking curves for the (200) reciprocal lattice point of all

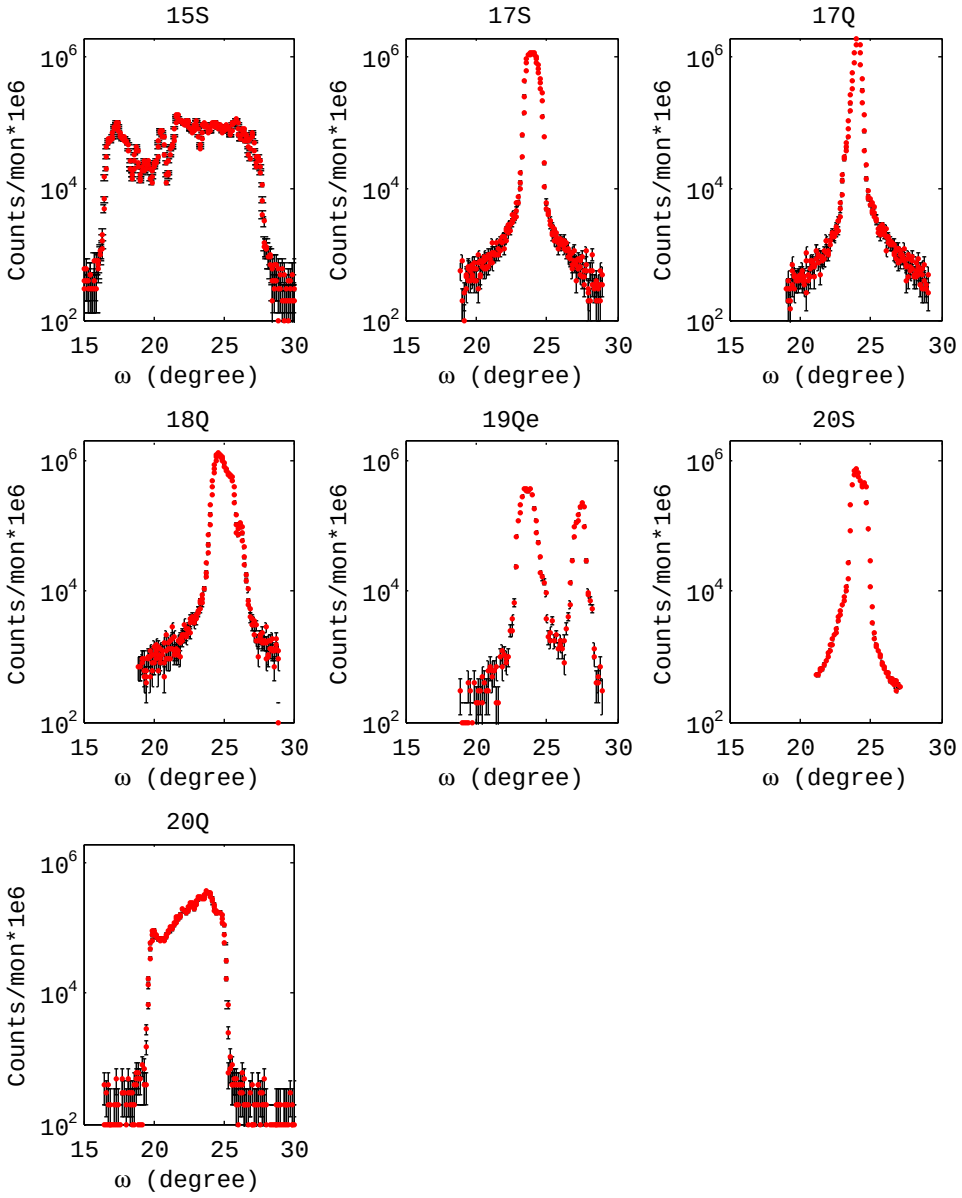

Figure 4.62: Rocking curves for (200) reciprocal point. Multiple peaks were observed in all the samples that show the samples were not perfect crystals but contain more than one crystal that are slightly misoriented.

the samples. Multiple peaks in the rocking curve show that none of the samples is a perfect single crystal. Rather, the samples contain more than one crystallite that are slightly mis-oriented. With so many peaks, the peak with the highest intensity was selected to define the UB matrix.

Table 4.4: lattice parameter

Sample	15S	17S	17Q	18Q	19Qe	20S	20Q
a (Å)	2.9025	2.9026	2.9030	2.9061	2.9059	2.9010	2.9090

Assuming $a = 2.9$ Å, the (200) reciprocal point should be at $2\theta \approx 48°$. Measuring 2θ scans allowed to calculate the lattice parameter for the samples. The values thus calculated are listed in table 4.4. These values are slightly higher for lower at% Ga compared with the lattice parameter measurements by Kawamiya et al. [52] but the trend is in good agreement. The decrease of the lattice parameter for slow-cooled 20S compared to 20Q is also in good agreement.

Since the {200} reciprocal points are visible for all the phases, the (200) and (002) reciprocal points were used to calculate the UB matrix [107], which helps in transforming the reciprocal space coordinates into the instrument angles. After calculating the UB matrix, the sample's reciprocal space was probed.

Figure 4.63 shows the [h00] reciprocal line scans for all the samples. The Gaussian fits to the peaks after subtracting the background and normalizing to the (200) peak intensity are shown in figure 4.64. 19Qe and 20S samples show very sharp peak. This indicates the presence of one or more of the ordered phases. 17Q

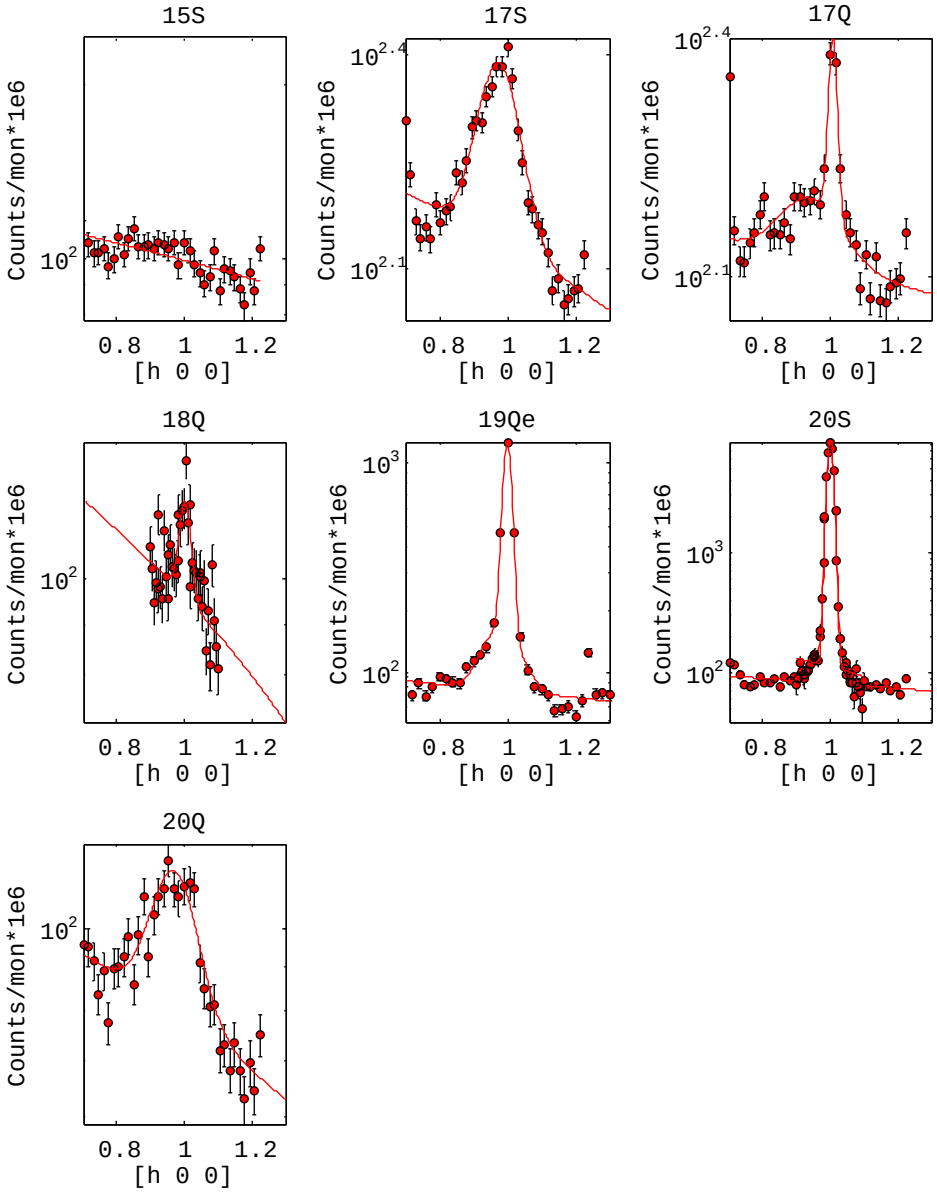

Figure 4.63: (h00) reciprocal line scans. 19Qe and 20S show sharp (100) peaks. 17S, 17Q, 18Q, 20Q show weak or diffuse (100) peaks. 15S shows no peak at all.

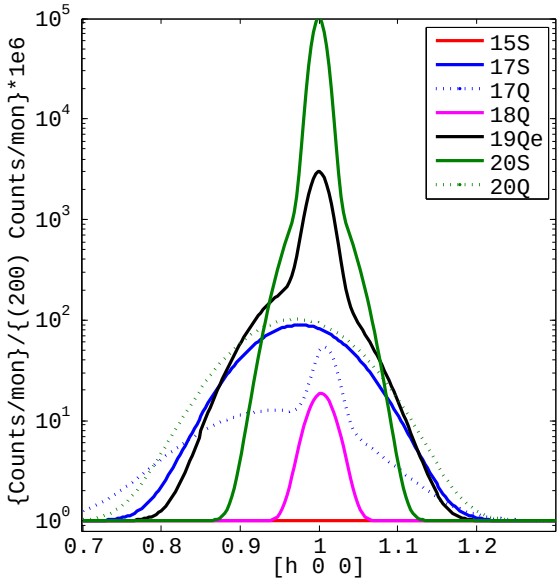

Figure 4.64: Gaussian fits to the (100) peaks with background subtracted and normalized to the (200) peak intensity. 19Qe and 20S show sharp + diffuse (100) peaks, 17Q shows weak + diffuse (100) peak, 18Q shows weak (100) peak, 17S and 20Q show diffuse (100) peaks and 15S shows no (100) peak.

and 18Q samples show weak (100) peaks indicating that the ordered phase exists in these samples but has much lower volume fraction. All the samples except 18Q show diffuse peak at (100), possibly due to size-effect of the ordered phase precipitates. The [h00] line scan was not long enough to capture the diffuse peak in 18Q so its presence can not be ruled out. 17S and 20Q samples do not show either sharp peak at (100). Rather, the peaks are weak and diffuse. 15S sample does not show any peak at (100) at all, indicating the lack of any significant presence of ordered phases.

Therefore, an ordered phase is present in all the samples except 15S. In order to identify which of the ordered phases are present, one must look at the (1/2 1/2 1/2) reciprocal point. As discussed earlier, this point is visible only for DO3 and $D0_{22}$.

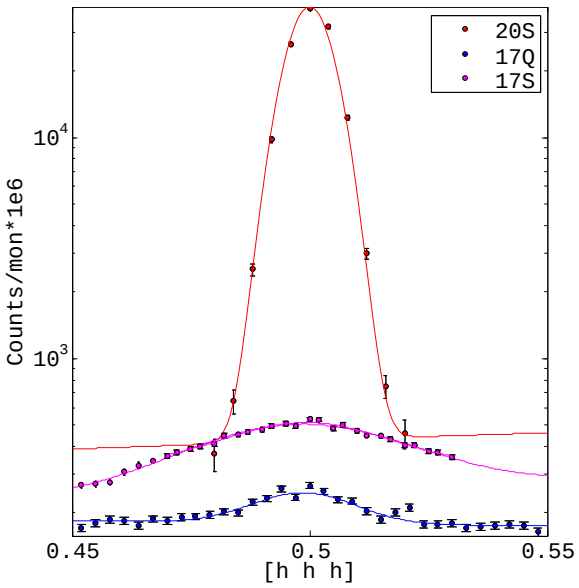

Figure 4.65: (hhh) reciprocal line scans. 20S shows sharp (1/2 1/2 1/2) peak. 17Q shows weak (1/2 1/2 1/2) peak. 17S shows a diffuse (1/2 1/2 1/2) peak.

Figure 4.65 shows the (hhh) reciprocal line scans for 17S, 17Q, and 20S samples. Figure 4.66 shows the Gaussian fits to the (1/2 1/2 1/2) peaks with background subtracted and normalized to the (200) peak intensity. For all of them the (1/2 1/2 1/2) reciprocal point is visible. 20S shows a sharp peak, 17Q shows a weak peak and 17S shows a broad diffuse peak. Since the (1/2 1/2 1/2) point is visible, the precipitated phase in these samples could be either DO3 or $D0_{22}$.

4.8 Discussion and conclusions

Results from Small-Angle Neutron Scattering (SANS) using unpolarized and polarized neutrons, with applied magnetic and elastic fields were shown in sections 4.4 and 4.5. Neutrons scatter only when there is a inhomogeneity in the sample

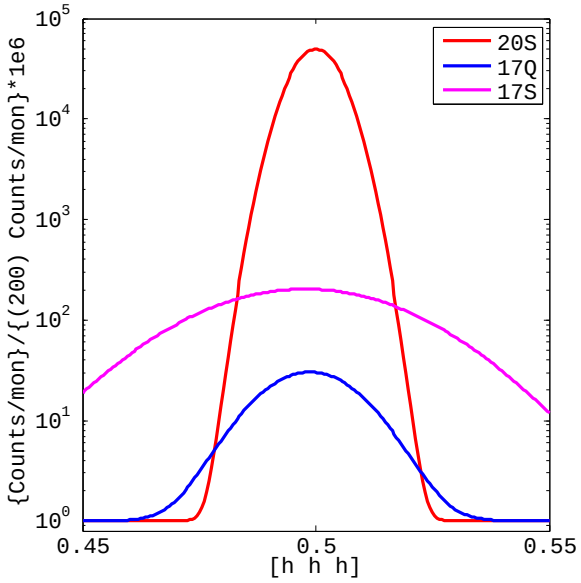

Figure 4.66: Gaussian fits to the (1/2 1/2 1/2) peaks with background subtracted and normalized to the (200) peak intensity. 20S shows sharp (1/2 1/2 1/2) peak. 17Q shows weak (1/2 1/2 1/2) peak. 17S shows a diffuse (1/2 1/2 1/2) peak.

leading to a significant contrast. This inhomogeneity could be structural, chemical, or magnetic. At lower magnetic fields, the presence of magnetic domains can also be viewed as a kind of inhomogeneity. Unpolarized SANS results in section 4.4 showed both kinds of magnetic inhomogeneities present in the sample - magnetic domain walls in the lowq regime and magnetic heterogeneities in the highq regime. Because lowq scattering is chased away by applying magnetic fields beyond saturation, it can be said with full confidence that it indeed represents magnetic domain wall scattering. The highq scattering on the other hand persists even after applying saturation fields. Further, highq scattering shows $\sin^2\theta$ dependence on the azimuthal angle indicating that the scattering sources at these length scales (heterogeneties) have a distinct magnetization than the matrix in which they are embedded.

In order to understand if the heterogeneities are the source of magnetostriction in Fe–Ga alloys, the scattering changes at highq and lowq representing heterogeneities and domain walls respectively is compared with the bulk magnetostriction measured for these samples from chapter 2. Since SANS intensity $I \propto |\boldsymbol{M}_{\perp}|^2$, square root of I was compared to the magnetostriction. All the measurements were scaled to fit between 0 and 1 for easy comparison.

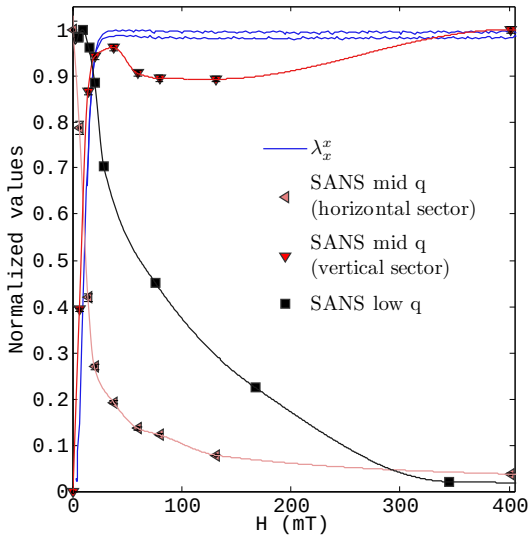

Figure 4.67: 19Qe lowq, highq SANS comparison with magnetostriction. Highq SANS was averaged along 30° sectors between $0.025 < q < 0.05$ Å^{-1}. Lowq SANS was circularly averaged between $0.0069 < q < 0.0195$ Å^{-1}.

For all samples, lowq scattering decreased with increasing magnetic fields (see figures 4.67 - 4.74). This is consistent with the thought that the lowq scattering occurs due to the presence of domain walls. The highq scattering clearly shows that it re-orients under magnetic field. The highq scattering along the horizontal ($\hat{\boldsymbol{x}}$) sector decreases while along the vertical ($\hat{\boldsymbol{y}}$) sector increases with increasing

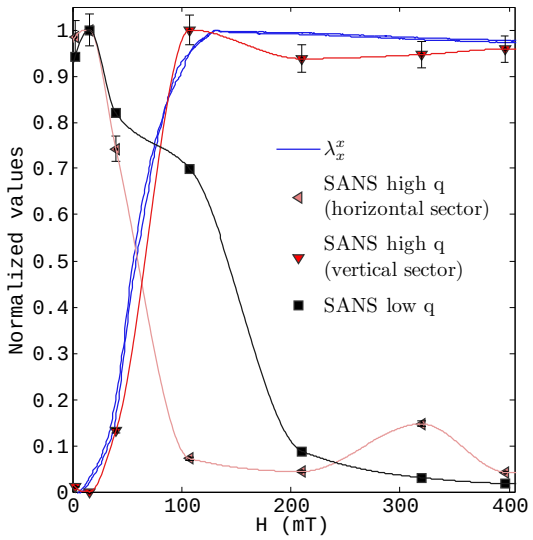

Figure 4.68: 18S lowq, highq SANS comparison with magnetostriction. Highq SANS was averaged along 30° sectors between $0.039 < q < 0.15$ Å^{-1}. Lowq SANS was circularly averaged between $0.0049 < q < 0.023$ Å^{-1}.

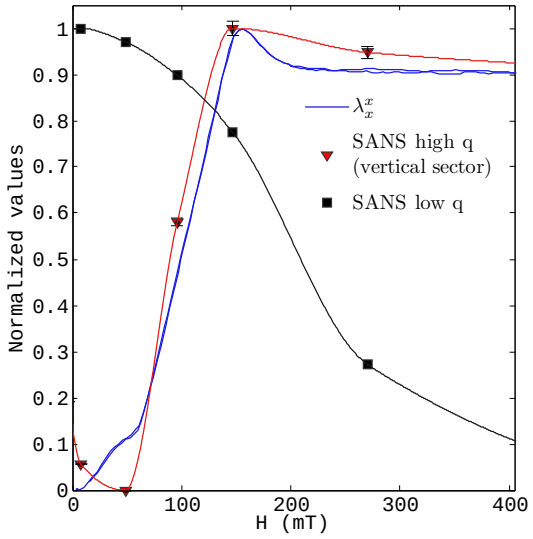

Figure 4.69: 18Q lowq, highq SANS comparison with magnetostriction. Highq SANS was averaged along 30° sectors between $0.041 < q < 0.17$ Å^{-1}. Lowq SANS was circularly averaged between $0.006 < q < 0.039$ Å^{-1}.

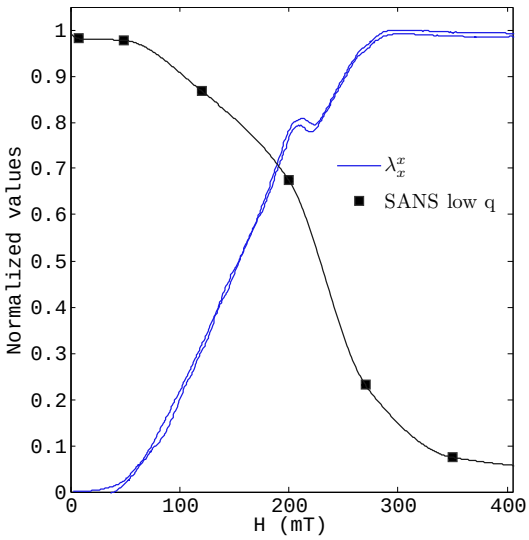

Figure 4.70: 15S lowq, highq SANS comparison with magnetostriction. Lowq SANS was circularly averaged between $0.0056 < q < 0.04$ Å^{-1}. Highq SANS was dominated by nuclear scattering from crystalline imperfections

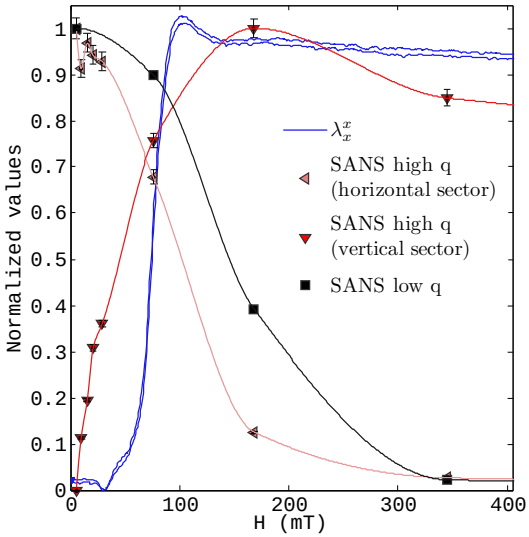

Figure 4.71: 17Q lowq, highq SANS comparison with magnetostriction. Highq SANS was averaged along 30° sectors between $0.045 < q < 0.14$ Å^{-1}. Lowq SANS was circularly averaged between $0.001 < q < 0.015$ Å^{-1}.

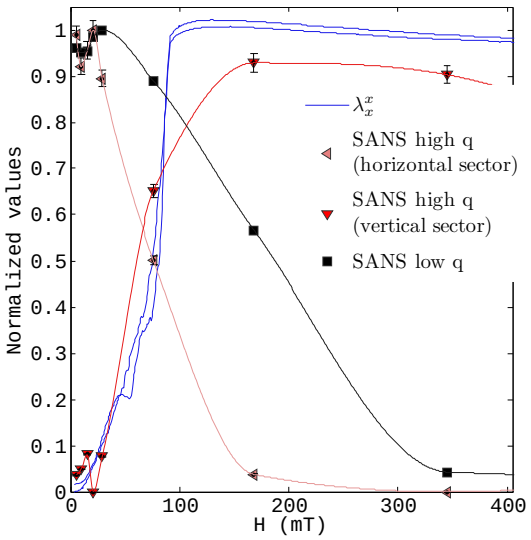

Figure 4.72: 17S lowq, highq SANS comparison with magnetostriction. Highq SANS was averaged along 30° sectors between $0.045 < q < 0.14$ Å^{-1}. Lowq SANS was circularly averaged between $0.001 < q < 0.015$ Å^{-1}.

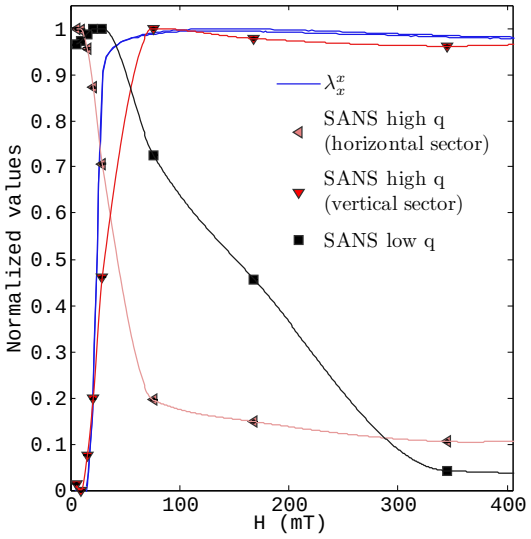

Figure 4.73: 20S lowq, highq SANS comparison with magnetostriction. Highq SANS was averaged along 30° sectors between $0.029 < q < 0.14$ Å^{-1}. Lowq SANS was circularly averaged between $0.001 < q < 0.015$ Å^{-1}.

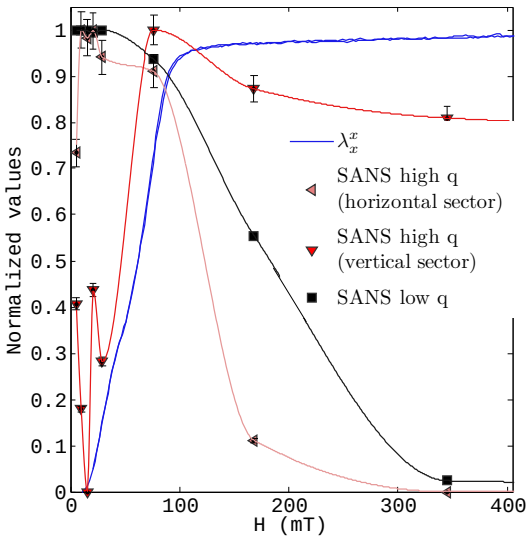

Figure 4.74: 20Q lowq, highq SANS comparison with magnetostriction. Highq SANS was averaged along 30° sectors between $0.029 < q < 0.14$ Å^{-1}. Lowq SANS was circularly averaged between $0.001 < q < 0.015$ Å^{-1}.

magnetic field. If both the lowq and highq scattering changes are compared to the magnetostriction, then for all samples, the highq scattering agrees well with the magnetostriction i.e., they both saturate nearly at the same magnetic field. The lowq scattering, which represents the domain walls scattering on the other hand saturates at a higher magnetic field than the magnetostriction. So, it appears that the magnetization of the sample as a whole does not saturate with the magnetostriction of the sample. However, the highq scattering representing the magnetization of the heterogeneities indicates that the heterogeneities and the magnetostriction of the whole sample saturate at the same magnetic field. Therefore, it appears that the magnetostriction has a very strong relation to the heterogeneities and it was thought that they play a crucial role [63, 65].

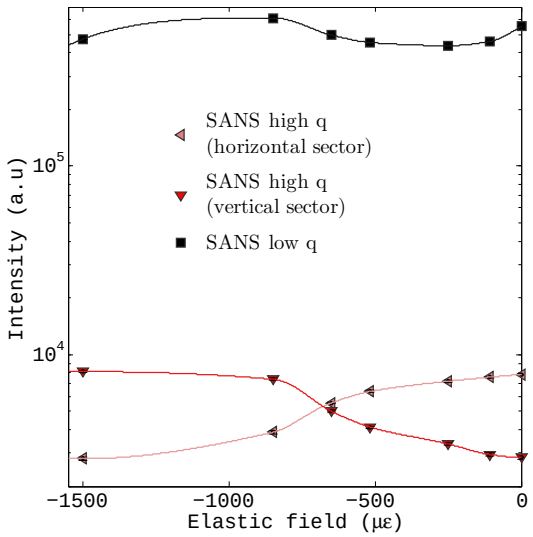

Figure 4.75: 19Qe lowq, highq SANS response to elastic field. Highq SANS was averaged along 30° sectors between $0.019 < q < 0.051$ Å^{-1}. Lowq SANS was circularly averaged between $0.0069 < q < 0.0195$ Å^{-1}.

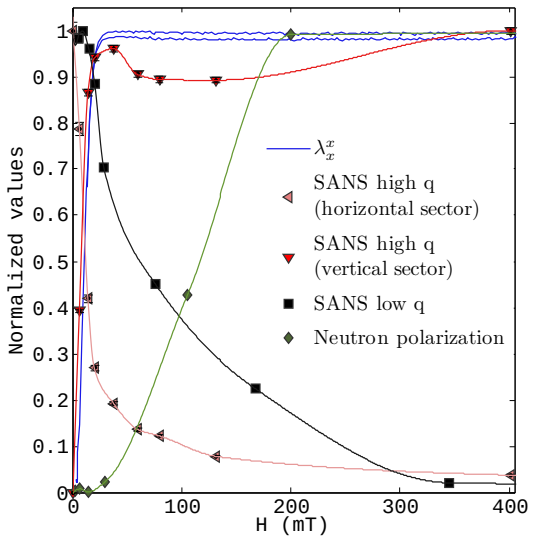

Figure 4.76: 19Qe neutron polarization data superimposed on to the data shown in figure 4.67.

In figure 4.75, the lowq and highq SANS response to elastic field are plotted. The highq scattering clearly responds to the elastic field. The scattering along the

vertical sector increases while that in the horizontal sector decreases. The critical field where both of them become equal was $-650\mu\epsilon$. On the other hand, the lowq scattering does not show any significant changes with the applied compressive elastic fields. This indicates that, somehow, the domain walls are not as responsive to the elastic field as the heterogeneities are, which again seems to indicate that the existence of the heterogeneities perhaps is crucial to the magnetostriction of these alloys.

The SANS results appear to contradict not only the intrinsic notion of magnetostriction but also the extrinsic notion. Even if the magnetostriction is engendered from the heterogeneities, it is expected they are magnetically coupled to the matrix and hence the magnetization of heterogeneities, the magnetostriction, and the magnetization of the matrix should all saturate at the same field. Previous characterization of Fe–Ga samples [29, 31, 38, 99, 110, 111] show that is indeed the case. However, the SANS results portray a different picture.

Figure 4.76 shows the neutron polarization data of 19Qe superimposed on the figure 4.67 to compare with the lowq, highq, and magnetostriction of the same sample. The lowq SANS, representing the magnetic domain walls, and neutron polarization data, representing the magnetization, both show that the sample saturates at a much higher magnetic field compared to the magnetostriction or the magnetization of the heterogeneities.

Figures 4.77 - 4.80 show the USANS intensity change with varying magnetic fields and compares that to the magnetostriction for 19Qe, 20S, 17Q, and 17S samples. The intensity values used in these plots were measured at $q = 1.7 \times 10^{-4}$

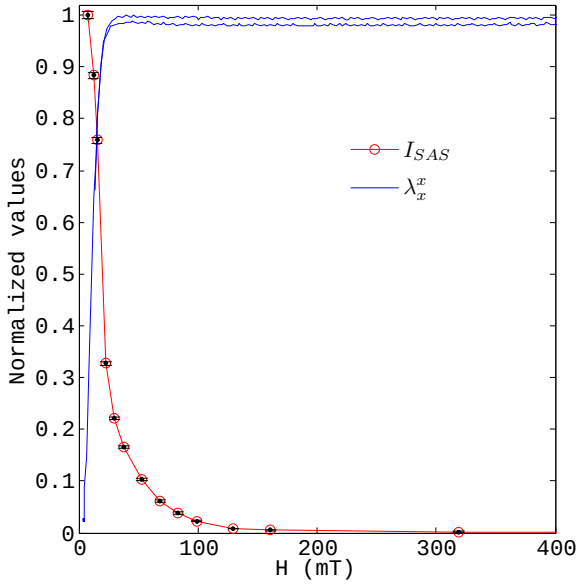

Figure 4.77: Comparison of USANS intensity at $q = 1.7 \times 10^{-4}$ Å^{-1} and magnetostriction of 19Qe

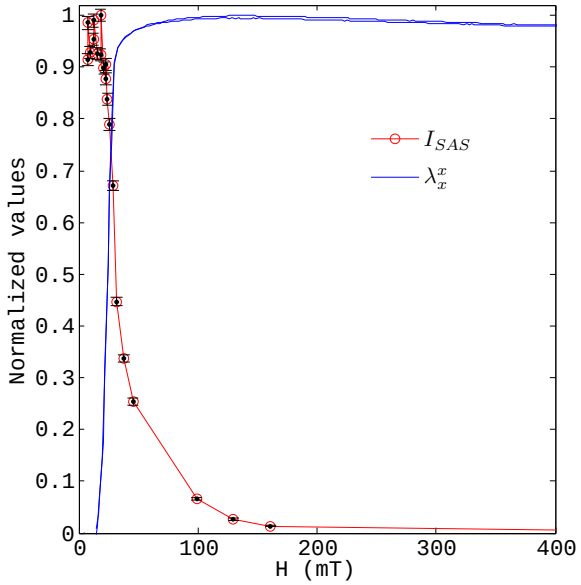

Figure 4.78: Comparison of USANS intensity at $q = 1.7 \times 10^{-4}$ Å^{-1} and magnetostriction of 20S

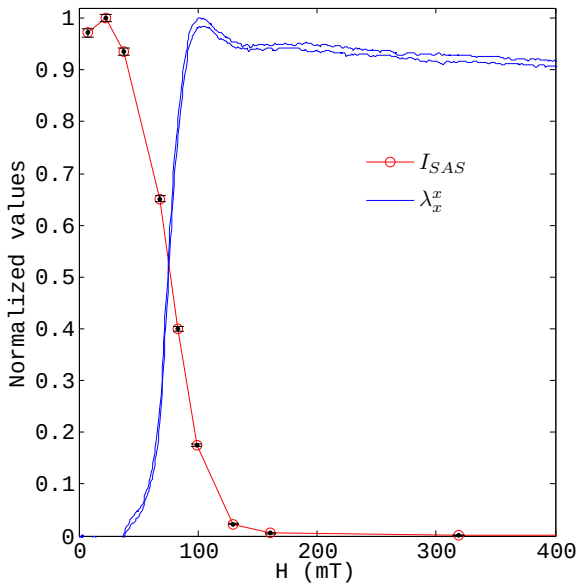

Figure 4.79: Comparison of USANS intensity at $q = 1.7 \times 10^{-4}$ Å^{-1} and magnetostriction of 17Q

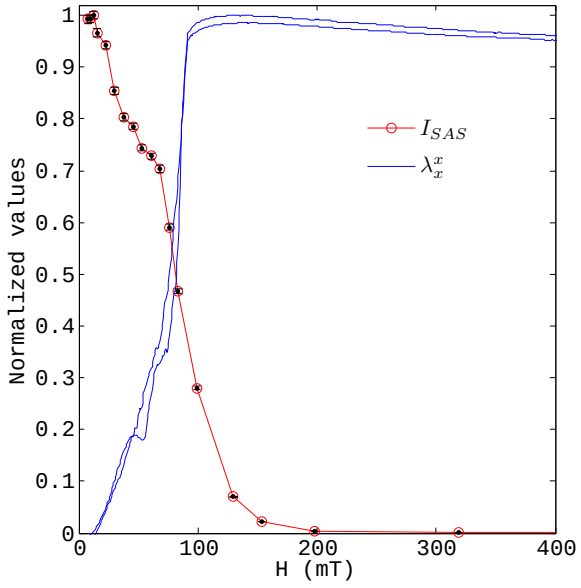

Figure 4.80: Comparison of USANS intensity at $q = 1.7 \times 10^{-4}$ Å^{-1} and magnetostriction of 17S

$Å^{-1}$, which corresponds to the length scales of $\sim$3.7 μm. These length scales are much larger than the heterogeneity length scales (seperated by $\sim$15 nm). Therefore, USANS intensity should truly correspond to the magnetic domain wall scattering. However, as with the SANS lowq intensity and neutron polarization measurements, USANS intensity also saturates at higher magnetic fields than at which the magnetostriction saturates.

Broad peaks in the USANS intensity at $q \approx 1 \times 10^{-4}$, corresponding to the length scales of $\sim$6 μm that shift with the magnetic field, indicate that the scattering could be originating from the surface domain walls. From figures 3.13 and 3.14 on pages 66 and 66 respectively show the domain structure on an unpolished or badly polished surfaces. The periodicity of domain walls in these images correspond to approximately the same length scales at which broad peaks were measured with USANS.

In order to verify if the SANS and USANS results were affected by the surface conditions of the samples, 17Q and 17S were polished on both sides so that neutron interaction with domains formed due to surface stresses could be minimized. Comparing the transmission measurements after polishing both sides (see figure 4.59 on page 169) with those measured before polishing (see figure 4.54 on page 165), it can be seen that polishing both sides of the samples increased transmissions. Comparing the USANS intensitites before and after polishing in figures 4.57 and 4.60 for 17Q sample and in figures 4.58 and 4.61 for 17S sample shows that the scattering was reduced significantly by merely polishing the samples on both sides.

Further, the USANS intensity measured at $q = 1.7 \times 10^{-4}$ $Å^{-1}$ in figures

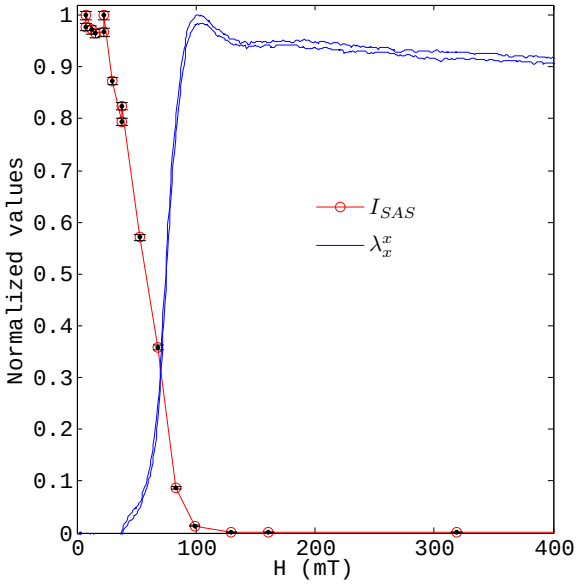

Figure 4.81: Comparison of USANS intensity at $q = 1.7 \times 10^{-4}$ Å^{-1} and magnetostriction of 17Q that was polished on both sides

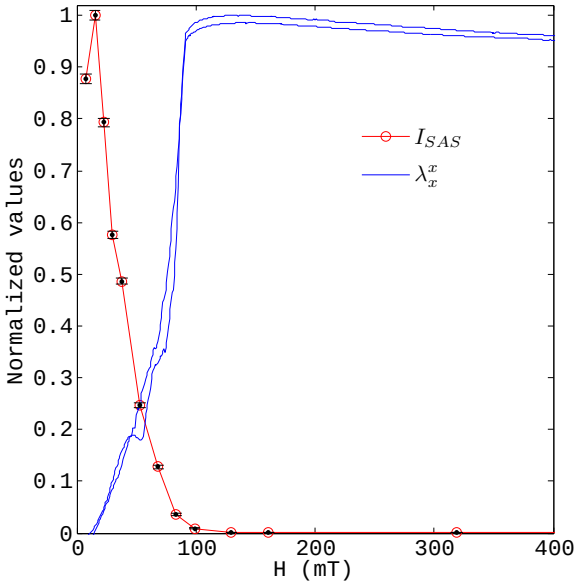

Figure 4.82: Comparison of USANS intensity at $q = 1.7 \times 10^{-4}$ Å^{-1} and magnetostriction of 17S that was polished on both sides

Table 4.5: Saturation magnetic fields in mT

Sample	λ_x^x	local magnetization	*highq* SANS	*lowq* SANS	USANS
15S	290	–	–	350	–
17S	100	100	∼100	350	180
17Q	100	100	∼100	350	150
18S	120	–	105	300	–
18Q	155	–	150	>300	–
19Qe	30	30	30	350	100
20S	50	–	∼50	350	150
20Q	100	–	80	350	–
After polishing both sides					
17S	100	100	–	–	100
17Q	100	100	–	–	100

4.81 and 4.82 for 17Q and 17S respectively after they were polished on both sides show that the USANS intensity now saturates with the magnetostriction at the same magnetic field. Therefore, surface conditions of the samples have a significant effect on the USANS results. Extending this logic, one could say that the lowq SANS intensities too were likely affected by the irregular surface domains. All these results are summarized in table 4.5. This is contrary to the expectation that since the neutrons interact with the bulk of the sample, surface finishing is not quite

important.

As discussed in chapter 3, the irregular surface domains form due to an out-of-plane anisotropy induced by the surface stresses. To overcome this anisotropy, a large magnetic field is required and hence such irregular domains are known to saturate at much higher magnetic fields than the bulk domains [79]. Further, the size of these irregular domains is about 2 - 5 μm whereas the true domains are much larger in size, on the order of 100 μm. Therefore, the density of domain walls for the irregular surface domains is much larger than the bulk domains although they are restricted to few tens of microns in depth [79]. This explains the reason why magnetic domain wall scattering (lowq SANS and USANS) and the neutron polarization saturate at a higher magnetic field than either magnetostriction or magnetization of the samples.

Therefore, though it appeared that the magnetostriction is closely connected to the magnetic moments of the heterogeneities, with lowq SANS not representing the true domains, such a conclusion can not be made. Nonetheless, the highq SANS, which is not affected by the irregular domains (due to much smaller length scales) shows that the heterogeneities exist in every sample that was studied. A large scattering, indicating a higher volume fraction of heterogeneities, was measured in 19Qe and 20S samples. However, the volume fraction of heterogeneities is much lower in other samples, including 20Q. The heterogeneities are expected to be lower in number in 20Q than 20S because it is known that when the sample at this composition is slow-cooled, DO3 phase precipitates. The unusually high volume fraction of heterogeneities in 19Qe, which is similar to 20S, coupled to the fact that the

maximum magnetostriction measured on this sample is 270 $\mu\epsilon$ hints that the sample might have actually been slow-cooled rather than quenched. If it was quenched then the quenching might not have been performed properly. Apart from the 19Qe sample, all other samples are consistent with their heat-treatment histories and magnetostriction values. As said before, the highq SANS shows that the heterogeneities exist in all the samples from 15S to 20Q. To understand if these heterogeneities are engendering the magnetostriction in Fe–Ga the nature of the heterogeneities must be identified and then compared with the SANS and magnetostriction results.

Identifying to which of the possible phases the heterogeneity belongs to is difficult using SANS due to the weak nuclear contrast. Therefore, neutron diffraction was employed to identify the phase of the heterogeneities. The neutron diffraction results showed (100) peak for all the samples except for 15S, which suggests the phase of the heterogeneities to be one of the ordered phases - DO3, $D0_{22}$, B2, or $L1_2$. The presence of (1/2 1/2 1/2) peak suggests that the heterogeneities could be of DO3 or $D0_{22}$ phase. This does not, however, rule out the presence of $B2$ and $L1_2$ phase heterogeneities. Recent results by Du et al. [66] show that the (100) peak has contributions from both DO3 and B2-like phases. To estimate the relative presence of DO3 and B2 phases, the intensities of (1/2 1/2 1/2), which has only DO3 contribution, and (100), which has DO3+B2 contribution could be compared. However, this cannot be done with the data acquired in this study because the diffraction intensities measured has both nuclear and magnetic contributions. While nuclear form factor is known, magnetic form factor is required to compare the two intensities. Alternately, magnetic field could be applied perpendicular to the scattering

plane and magnetic contribution to the intensity can be suppressed [93]. Whatever may be the phase of the heterogeneities, to find out if they engender the magnetostriction in Fe–Ga, the results from the macroscopic measurements from chapter 2 are pooled together with SANS and neutron diffraction results in table 4.6. From

Table 4.6: Comparison of SANS and neutron diffraction results with the magnetostriction

Sample	Discernible peak in $0.001 < q < 0.2$ Å^{-1}	SANS highq anisotropy	(100) peak	$\lambda(\mu\epsilon)$
15S	No	Weak	Indiscernible	215
17S	No	Weak	Diffuse	303
17Q	No	Weak	Weak + diffuse	280
18Q	No	Weak	Weak	280
19Qe	Yes	Strong	Sharp + diffuse	266
20S	Yes	Strong	Sharp + diffuse	242
20Q	No	Weak	Diffuse	317

table 4.6, it can be observed that the sample 15S, which has a magnetostriction of 215 $\mu\epsilon$, shows no peak in the SANS intensity, a very weak anisotropy in the SANS intensity, and no (100) peak. Therefore the heterogeneities, DO3, $D0_{22}$, B2, or $L1_2$, could be too small to yield a Bragg or diffuse peak in 15S. It is important to note that this sample shows magnetostriction of 215 $\mu\epsilon$ without any significant presence of heterogeneities.

The 17S, 17Q, 18Q, and 20Q samples show no peak in the SANS intensity,

weak anisotropy in the SANS intensity, and weak (100) peaks that suggest that the presence of the heterogeneities in these samples is small. Of these samples, 17Q and 18Q show a well defined, though weak, (100) peaks and their magnetostriction is 280 $\mu\epsilon$. In addition, 17Q shows a diffuse (100) peak. Samples 17S and 20Q show broad diffuse (100) peaks and both show magnetostriction in access of 300 $\mu\epsilon$. Samples 19Qe and 20S show well defined peaks in the SANS intensity, large anisotropy in the SANS intensity, and sharp (100) peaks superimposed on to the diffuse (100) peaks. They show magnetostriction of 266 and 242 $\mu\epsilon$ respectively. Taking all these results into account, the heterogeneities in 19Qe and 20S could be DO3 precipitates that degrade the magnetostriction. The diffuse (100) peaks in 17S and 20Q seem to suggest that if these precipitates are short range ordered then the magnetostriction in excess of 300 $\mu\epsilon$ is possible. However, the fact that 15S shows 215 $\mu\epsilon$ without any significant presence of the heterogeneities suggests that the short range ordering in 17S and 20Q resulting in diffuse (100) peak might not be as important to the magnetostriction as previously suggested [59, 61]. It could be possible that the precipitates present in 17S and 20Q are DO3 in their nascent stage of formation. If this is true, then the magnetostriction should decrease with the appearance of the (100) peak (diffuse, weak, or sharp). Therefore, one can expect two regimes in the magnetostriction vs. Ga at% curves - one before and the other after the onset of the (100) peak i.e., 15 at% Ga. Figure 4.83 shows the quadratic fit to the first four data points - 0, 4, 6, 8.7 at% Ga. As expected, the higher at% Ga shows the magnetostriction below the quadratic curve. It is possible that the intrinsic magnetostriction is quadratically dependent on the Ga at% [58] while the

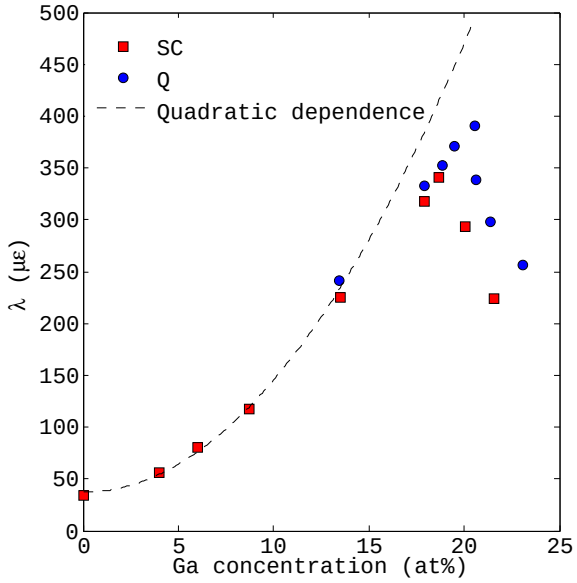

Figure 4.83: Magnetostriction of slow-cooled (SC) and quenched (Q) Fe-Ga. Data points were taken from [26]. First four data points were used for quadratic fit.

reduction in the magnetostriction from the predicted value beyond ∼14 at% Ga could be due to the precipitation of the DO3 phase. Of course, what is presented here is just a hypothesis and not an affirmative conlucsion. Further data with good confidence levels is needed to test the veracity of this thought.

Chapter 5

Conclusions

Fe–Ga alloys demonstrate extraordinary enhancement in their magnetostriction with the addition of Ga. Understanding the origin of the magnetostriction in these alloys has been the focus of many recent studies [55, 59–61, 63, 65]. With the intention of finding out the nature of the magnetostriction in Fe–Ga alloys, specifically if the magnetostriction is intrinsic as suggested by [55, 56, 58, 60] or extrinsic as suggested by [59, 61, 63, 65, 67, 68], magnetic domain studies and neutron studies were conducted.

It has been shown that due to the increased magnetostriction in Fe–Ga, compared to Fe or Fe-Si, a large stress-induced anisotropy could result from small stresses on the surface, which induce maze-like irregular domain patterns. The importance of preparing a stress-free surface has been demonstrated for visualizing the "true" domain patterns. Studying magnetic domains under magnetic and elastic fields using Kerr microscopy, SANS, and USANS, and heterogeneities under magnetic and elastic fields using SANS, no direct evidence has been found to attribute the enhanced magnetostriction in Fe–Ga to tetragonal heterogeneities as proposed by the extrinsic theory [67, 68]. However, there is evidence of magnetic heterogeneities in all samples.

A research summary and the contributions of this dissertation are provided in

the subsequent sections followed by recommendations for future work.

5.1 Summary of Research

Single crystal samples of varying composition and heat treatments were used in this study. Each sample was carefully characterized. In Chapter 2, macroscopic characterization of the samples was discussed. First, the composition of the samples was measured using EDS. The crystallographic orientation of the samples for which the orientation is not known was measured using EBSD. Magnetization of 15S, 18S, and 19Qe samples was measured using VSM. Strains along [100] and [010] were measured using resistive strain gages with the magnetic field applied along [100] and [010]. It was found that the measured magnetic strains have a volume magnetostriction component ($< 70\ \mu\epsilon$). Finally, using all the strain values, the magnetostriction of the samples was calculated and their remanent states were estimated. This macroscopic characterization is very important. For example, 17S sample shows the presence of an anisotropy that strongly favors [100] to [010] or [001]. Such a knowledge helps in understanding and analyzing the results from magnetic domain and SANS studies.

In Chapter 3, the magnetic domain studies were discussed. It has been shown that all the magnetic domain study results on Fe–Ga in literature suffer from insufficient polishing. The maze-like irregular domains imaged previously [57, 62, 87, 88] were a result of surface stresses induced by mechanical polishing. The higher sensitivity of Fe–Ga (compared to pure iron, Fe-Si, or Fe-Al) to the surface stresses was

explained as being due to the increased magnetostriction. The maze-like domain patterns form due the presence of a uniaxial anisotropy. This uniaxial anisotropy was attributed to the stress-induced surface anisotropy. Since the stress-induced anisotropy is proportional to the magnetostriction, an increase in magnetostriction leads to an increase in stress-induced anisotropy, thus making Fe–Ga more susceptible to stresses induced from mechanical polishing. An additional polishing step using silica gel proved to be effective in removing the stressed surface layers. After the additional polishing step, the expected domain structure with $\langle 100 \rangle$ magnetized domains and straight 90° and 180° domain walls were imaged. High resolution MFM images did not reveal any subdomain structure as reported by [88].

Using Kerr microscopy, magnetic domains were imaged while applying a magnetic field. Thus measured magnetic domain images were compared with the magnetostriction measurements and the remanent states estimated in chapter 2. The information from the domain images was used to extract the local magnetization of the sample. The magnetostriction, magnetic domain images, remanent states, and the magnetization extracted from the domain images, compared well for all the samples except 17Q. Polishing the 17Q sample on both sides revealed a complicated domain structure in which the magnetization of the domains was oriented along the width of the sample on the top surface while it was oriented along the length on the bottom surface, possibly flipping in direction through the thickness. Such a domain structure with magnetization oriented along the thickness was also suggested by the remanent state of this sample.

Next, the samples were subjected to elastic fields using a custom built device

and the magnetic domains under the influence of these elastic fields were imaged. 19Qe sample showed elastic saturation in which the magnetization of the sample was aligned perpendicular to the compressive elastic field direction with two kinds of domains separated by 180° domain walls. It appeared that for 17S sample, the maximum applied elastic field was not sufficient to elastically saturate it as at the maximum elastic field, there were still some domains with magnetization parallel to the compressive elastic field direction. However, it was shown that these domains were possibly restricted to the surface and the bulk domain structure has out-of-plane domains.

The magnetic domain studies showed that the domain structure in Fe–Ga, which is a cubic material with positive magnetocrystalline anisotropy, is similar to the domain structure in materials of its class - like Fe and Fe-Si. The maze-like domain patterns that were reported in literature and that were claimed to be as a result of tetragonal precipitates enhancing the magnetostriction in Fe–Ga, were shown to be limited to the surface and form due to residual stresses from mechanical polishing. Magnetic domain imaging under magnetic and elastic fields revealed no unusual behavior and they compared well with the remanent state estimates and magnetostriction measurements from chapter 2.

Neutron experiments conducted on the samples were discussed in chapter 4. First, the results from Small-Angle Neutron Scattering experiments were discussed. The experiments were conducted both under applied magnetic and elastic fields. The SANS results fall under two regimes, lowq and highq. Lowq scattering showed behavior consistent with the magnetic domain wall scattering. The scattering in the

highq regime was different in behavior from that of the lowq. In the highq regime, the scattering was dominated by the heterogeneities present in the sample. 19Qe and 20S samples showed a clear peak in the highq scattering intensity corresponding to the average separation between the heterogeneities. In 19Qe, the average separation was 15 nm, while in the 20S it was 35 nm. There was no perceptible peak in the SANS intensity for any other sample. However, the anisotropy in the SANS intensity that had a $\sin^2\theta$ dependence on the azimuthal angle indicated that there were heterogeneities in all the samples but far less in 15S, 17S, 17Q, 18Q, and 20Q compared to 19Qe or 20S. Discerning the SANS anisotropy in 15S and 20Q proved to be difficult. In 15S, the highq SANS scattering was also dominated by nuclear scattering, possibly from the grain boundaries (although it is supposed to be a single crystal, neutron diffraction showed that it contained many crystals that are slightly mis-oriented from each other). This made it difficult to identify the anisotropy in SANS intensity. In 20Q, there was no nuclear scattering dominating at the highq but it nonetheless proved to be difficult to discern the anisotropy in SANS intensity.

Comparing the changes in the highq SANS scattering, which corresponds to the magnetization of the heterogeneities, lowq scattering, which corresponds to the magnetic domain wall density, to the magnetostriction of the samples revealed an interesting behavior. While lowq scattering saturated at much higher fields compared to the magnetostriction, highq scattering changes resembled that of the magnetostriction. This appeared to indicate that the magnetization of the heterogeneities saturate at much lower field than the overall magnetization of the sample. Moreover, the magnetostriction seemed to correspond with the magnetization of the

heterogneities. SANS under elastic field on 19Qe also indicated similar behavior. The highq scattering responded as expected to the elastic fields whereas there were no significant changes in the lowq scattering. This again appeared to indicate that the heterogeneities were more responsive to the elastic fields than the magnetic domain walls or magnetization of the sample. Neutron polarization experiments on 19Qe also showed that the sample saturated at much higher magnetic field than the magnetostriction. The magnetic domain images obtained in chapter 3, however, show that this is not the case. Magnetic domains were indeed chased out of the sample and the magnetization of the sample saturates with the magnetostriction of the sample. To resolve this discrepancy, Ultra Small-Angle Neutron Scattering (USANS) experiments were conducted. Even USANS experimental results showed similar behavior as that of SANS lowq results. The USANS intensity saturated at much higher magnetic fields than is expected for the samples. In order to understand if these strange results were as a result of sample's surface finish, 17S and 17Q samples were polished on both sides so that the neutrons don't interact with any irregular domain walls. The results from USANS after polishing the samples on both sides demonstrated that the USANS intensity, lowq SANS intensity, and neutron polarization measurements were all affected by the irregular domain walls on the sample's surface. As found in chapter 3 from magnetic domain studies, these irregular domain walls form due to the anisotropy induced by the surface stresses that result from mechanical polishing or scratches. It takes enormous field to overcome this anisotropy and thus these irregular domain walls take much larger fields to be chased out of the sample. Also, the density of these irregular domain walls

is much higher than the real domain walls. Typically, the irregular domains are less than 2 μm in size whereas the real domains are about 100 μm in size. This explained why USANS and SANS lowq intensities, and neutron polarization measurements saturated at much higher fields compared to the heterogeneities or the magnetostriction. A peak was observed in the USANS intensity after 17S was polished on both sides. It could be due to the irregular domains that still remained on certain areas of the surface that may not be polished as well as the rest. From SANS and USANS experiments it was found that there were heterogeneities in all the samples and the behavior of the magnetic domains and the heterogeneities both agree with the magnetostriction behavior in all the studied samples.

Next, neutron diffraction experiments were conducted to identify different phases present in the samples. The (200) reciprocal point rocking curves showed the presence of multiple crystals in all the samples. Sample 15S showed exceptionally large number of crystals, which explained the nuclear scattering seen in the SANS experiments. It was observed that a peak at the (100) reciprocal point was present in all the samples except 15S. While 19Qe and 20S showed sharp (100) peaks, 17Q and 18Q showed weak (100) peaks. Samples 17S and 20Q showed weak and diffuse (100) peaks. Further, the presence of (1/2 1/2 1/2) reciprocal points indicated that the phase of the precipitates could be either DO3 or $D0_{22}$. However, the presence of B2 or $L1_2$ could not be ruled out completely.

In order to understand if these heterogeneities are the source of magnetostriction in Fe–Ga alloys as suggested by the extrinsic magnetostriction model, the neutron diffraction measurements were compared to the SANS and magnetostriction

measurements. Samples 19Qe and 20S, which showed higher volume fraction of the heterogeneities, also show sharp (100) peaks. Also, the magnetostriction of these samples was measured to be 266 and 242 $\mu\epsilon$ respectively. Samples 17Q and 18Q showed weak (100) peaks, weak SANS anisotropy, and magnetostriction of 280 $\mu\epsilon$ each. Samples 17S and 20Q showed diffuse (100) peaks, weak SANS aninsotropy, and magnetostriction of 303 and 317 $\mu\epsilon$ respectively. Sample 15S showed no (100) peak at all, very weak SANS anisotropy, and magnetostriction of 215 $\mu\epsilon$. Piecing together these results indicated that the heterogeneities were most likely DO3 precipitates that are detrimental to the magnetostriction. It is certainly possible that there are all kinds of heterogeneities - DO3, $D0_{22}$, B2, and $L1_2$. It was argued in the past [61], that the diffuse (100) peak does correspond to the $D0_{22}$ tetragonal phase, supporting the extrinsic magnetostriction model. However, the absence of any (100) peak in 15S with magnetostriction as high as 215 $\mu\epsilon$ does not lend support to this hypothesis.

5.2 Contributions of this research

- A systematic study has been conducted on various Fe–Ga samples of varying composition and heat treatment covering the first peak in magnetostriction. One of the key contributions of this research is to conduct all the experiments on the same set of samples and at different length scales.
  - Macroscopic characterization - Composition, crystal orientation, magnetization, and magnetostriction were carefully measured. From the mag-

netostriction measurements in two directions with field also applied along two directions, the remanent states of the samples were estimated.

  - Microscopic - Magnetic domains were imaged using wide field Kerr microscope and their response to magnetic and elastic fields was studied.
  - Nanoscopic - Using Small-Angle Neutron Scattering (SANS) the heterogeneities were identified and their response to magnetic and elastic fields was studied
  - Lattice level - Neutron diffraction was used to identify the phase of the heterogeneities present in the samples.

- The real magnetic domains in Fe–Ga were imaged for the first time. It has been shown that all the previously published magnetic domain images in Fe–Ga were due to improper polishing. As a consequence, previous claims about the notion of tetragonal precipitates inducing the formation of irregular domains have been disproved.

- The response of the magnetic domains to magnetic and elastic fields was studied. A method to estimate the magnetization of the sample from its magnetic domain images has been described. The magnetic domain images, magnetization estimates, and the magnetostriction measurements have been shown to agree with each other quite well. This study found the expected magnetic domain behavior in all the samples.

- Small-Angle Neutron Scattering (SANS) were conducted for the first time on

Fe–Ga samples. These studies revealed the existence of the heterogeneities supporting the findings of previous TEM studies [59]. These studies also revealed that the heterogeneities are magnetically distinct from the matrix.

- The magnetic domain wall scattering observed from SANS and and Ultra SANS (USANS) experiments were observed to saturate at higher magnetic fields than the magnetostriction of the sample or the magnetization of the heterogeneities observed by SANS. The source of this discrepancy was identified to be the surface finishing of the sample. The high density of irregular magnetic domain walls on the surface were found to dominate the SANS and USANS scattering. The importance of polishing both sides of the sample for reliable lower q SANS and USANS results was demonstrated.

- Through neutron diffraction, the reciprocal space of the samples was probed. It has been shown that although the samples were considered to be single crystals, they are not perfectly single crystals. Multiple crystallites that were slightly mis-oriented from each other were observed. It has also been shown that ordered phases are present in all the samples except 15S by measuring the (100) peak. The lack of the (100) peak in 15S indicated that the phase precipitates, if there are any, were too small to yield either a Bragg or diffuse peak. From (1/2 1/2 1/2) peak measurements, it has been shown that this ordered phase could be either DO3 or $D0_{22}$.

- By piecing together the results from all the experiments conducted, it has been shown that DO3 heterogeneities in 19Qe, 20S, 17Q, and 18Q are likely

detrimental to the magnetostriction. The absence of the (100) peak in 15S from the neutron diffraction experiments indicated that the phase precipitates, if there are any, were too small to yield either a Bragg or diffuse peak. It has been proposed that the diffuse peaks observed in 17S and 20Q samples could be due to the DO3 in its early stages of formation. Quadratic curve that predicts the lower at% Ga magnetostriction was shown to not fit the higher at% Ga. The reduced magnetostriction observed at higher at% Ga was proposed to be due to the precipitation of the DO3 phase. Further, no evidence has been found in this study that directly supports the proposed extrinsic magnetostriction model [67, 68].

5.3 Recommendations and future work

Magnetic domains in Fe–Ga alloys with Ga at% less than 20% were investigated under static magnetic and elastic fields in this study. As the wide field Kerr microscopy technique allows real time visualization of the magnetic domains, studies can be conducted to investigate the magnetic domains under dynamic fields. The results from such a study could be used to develop a dynamic magnetoelastic model.

The magnetocrystalline anisotropy of Fe–Ga decreases with composition and becomes almost negligible close to 20 at% Ga [53]. If the magnetocrystalline anisotropy become negative above 20 at% Ga, then $\langle 111 \rangle$ should the easy axes. In such a case, interesting domain patterns form on the $\{100\}$ surfaces. The maximum composition for which the domains have been imaged in this study was 19 at% Ga. Therefore,

further domain studies could be carried out on samples with 20 and greater at% Ga. Also, magnetic domains in samples beyond 25 at% Ga upto 29 at% Ga could yield information about the second peak in the magnetostriction.

It was shown that the surface condition of the samples has a profound impact on neutron scattering. The SANS experiments reported in this thesis were conducted on samples that were either unpolished or polished on one side. Although it is expected that this will affect the lower q SANS and not the higher q SANS, repeating SANS experiments with samples polished on both sides should be done to ensure the validity of the higher q SANS data.

The current study could not ascertain the phase of the heterogeneities conclusively. It is possible that heterogeneities of multiple phases exist within the sample [66]. To determine all the phases present, neutron diffraction experiments could be conducted such that the diffraction intensity has only nuclear contribution. This can be achieved by using polarized neutrons. From the nuclear diffraction intensity, comparing various peaks would be easy, which can be used to identify all the phases present in the sample.

A recent study reported [61] the presence of tetragonal heterogeneities in Fe–Ga sample. They reported a peak at $(\frac{11}{4}00)$ and that it splits. It has been found later that this data was not reproducible [112]. The maximum reciprocal point that was investigated in their study was $(h00) < (300)$. The TriCS neutron diffraction instrument used in this study is capable of reaching reciprocal lattice points beyond (300). Therefore, using TriCS the (300) peak and a possible tetragonal splitting of this peak can be re-investigated. Further, by conducting neutron diffraction

experiments under magnetic field the response of the reciprocal lattice points, and hence different phases in the materials could be studied.

It was shown that the magnetostriction of higher at% Ga does appear to deviate from the quadratic enhancement at lower at% Ga. More data with good confidence intervals need to be measured to verify if this is indeed true.

In the present study, the main focus was on the first peak. The second peak is more complex with a mix of several phases. Not many studies were conducted to investigate the reason for this second peak. Therefore, a similar approach taken in this thesis could be taken to investigate the second peak thoroughly and understand its origins.

Bibliography

[1] S. Chikazumi, *Physics of Ferromagnetism*, ser. Physics of Ferromagnetism. New York: Claredon Press, Oxford, 1997.

[2] P. Weiss, "Hypothesis of the molecular field and ferromagnetic properties," *J. Phys. Theor. Appl.*, vol. 6, no. 1, pp. 661–690, 1907.

[3] W. Heisenberg, "Zur Theorie des Ferromagnetismus," *Zeitschrift für Physik A Hadrons and Nuclei*, vol. 49, pp. 619–636, 1928, 10.1007/BF01328601.

[4] E. Kneller, *Ferromagnetismus*. Springer-Verlag, 1962.

[5] L. Néel, "Anisotropie magnétique superficielle et surstructures d'orientation," *J. Phys. Radium*, vol. 15, no. 4, pp. 225–239, 1954.

[6] J. P. Joule, "On a new class of magnetic forces," *The Annals of Electricity, Magnetism, and Chemistry*, vol. 8, pp. 219–224, 1842.

[7] C. Kittel, "Physical theory of ferromagnetic domains," *Reviews of Modern Physics*, vol. 21, no. 4, pp. 541–583, 1949.

[8] E. W. Lee, "Magnetostriction and magnetomechanical effects," *Reports on Progress in Physics*, vol. 18, no. 1, pp. 184–229, 1955.

[9] E. Villari, "Change of magnetization by tension and by electric current," *Annalen der Physik und Chemie*, vol. 126, pp. 87–122, 1865.

[10] C. Mudivarthi, S. Datta, J. Atulasimha, P. G. Evans, M. J. Dapino, and A. B. Flatau, "Anisotropy of constrained magnetostrictive materials," *Journal of Magnetism and Magnetic Materials*, vol. 322, no. 20, pp. 3028 – 3034, 2010.

[11] C. Mudivarthi, S. Datta, J. Atulasimha, A. B. Flatau, P. Evans, and M. Dapino, "Equivalence of magnetoelastic and elastic energies with stress-induced anisotropy and its use in the armstrong model for magnetostriction," in *proceedings of SPIE: Smart Structures and Materials*, San Diego, CA, USA, 2008.

[12] C. Bormio-Nunes, M. A. Tirelli, R. S. Turtelli, R. Grössinger, H. Müller, G. Wiesinger, H. Sassik, and M. Reissner, "Volume magnetostriction and structure of copper mold-cast polycrystalline Fe-Ga alloys," *Journal of Applied Physics*, vol. 97, no. 3, p. 033901, 2005.

[13] C. B. Jiang, J. H. Liu, F. Gao, and H. B. Xu, "Large linear and volume magnetostriction in Fe-Ga alloys," *Materials Science Forum*, vol. 561-565, pp. 1117–1122, 2007.

[14] E. Secemski and J. C. Anderson, "Magnetic anisotropy in single-crystal nickel films," *Journal of Physics D: Applied Physics*, vol. 4, no. 4, pp. 574–585, 1971.

[15] S. Kuriki, "Strain effects on magnetic anisotropies in (110) Ni films," *Journal of Applied Physics*, vol. 48, no. 7, pp. 2992–2997, 1977.

[16] H. Barkhausen, "Two phenomena uncovered with help of the new amplifiers," *Z. Phys.*, vol. 20, p. 401, 1919.

[17] F. Bitter, "On inhomogeneities in the magnetization of ferromagnetic materials," *Phys. Rev.*, vol. 38, no. 10, pp. 1903–1905, Nov 1931.

[18] S. Kaya, "Pulverfiguren des magnetisierten eisenkristalls," *Zeitschrift für Physik A Hadrons and Nuclei*, vol. 90, pp. 551–558, 1934, 10.1007/BF01333142.

[19] H. J. Williams, R. M. Bozorth, and W. Shockley, "Magnetic domain patterns on single crystals of silicon iron," *Phys. Rev.*, vol. 75, no. 1, pp. 155–178, Jan 1949.

[20] S. Chikazumi and K. Suzuki, "On the maze domain of silicon-iron crystal (I)," *J. Phys. Soc. Jpn.*, vol. 10, no. 7, pp. 523–534, 1955.

[21] A. E. Clark, *Ferromagnetic Materials*. North-Holland Publishing Company, 1980, vol. 1, ch. 7, pp. 531–589.

[22] A. Clark and D. Crowder, "High temperature magnetostriction of $TbFe_2$ and $Tb_{.27}Dy_{.73}Fe_2$," *Magnetics, IEEE Transactions on*, vol. 21, no. 5, pp. 1945–47, 1985.

[23] G. Engdahl, *Handbook of Giant Magnetostrictive Materials*, G. Engdahl, Ed. Academic Press, New York, 2000.

[24] see:www.etrema usa.com/products/terfenol, "Terfenol-d, Etrema products, inc, Ames, IA, USA."

[25] A. E. Clark, J. B. Restorff, M. Wun-Fogle, T. A. Lograsso, and D. L. Schlagel, "Magnetostrictive properties of body-centered cubic Fe-Ga and Fe-Ga-Al alloys," *Magnetics, IEEE Transactions on*, vol. 36, no. 5, pp. 3238–3240, 2000.

[26] A. E. Clark, K. B. Hathaway, M. Wun-Fogle, J. B. Restorff, T. A. Lograsso, V. M. Keppens, G. Petculescu, and R. A. Taylor, "Extraordinary magnetoelasticity and lattice softening in bcc Fe-Ga alloys," *Journal of Applied Physics*, vol. 93, no. 10, pp. 8621–8623, 2003.

[27] S. Datta, "Quasi-static characterization and modeling of the bending behavior of single crystal galfenol for magnetostrictive sensors and actuators," Ph.D. dissertation, University of Maryland, College Park, MD, USA, 2009.

[28] R. C. Hall, "Magnetostriction of aluminum-iron single crystals in the region of 6 to 30 atomic percent aluminum," *Journal of Applied Physics*, vol. 28, no. 6, pp. 707–713, 1957.

[29] R. A. Kellogg, "Development and modeling of iron-gallium alloys," Ph.D. dissertation, Iowa State University, 2003.

[30] R. A. Kellogg, A. M. Russell, T. A. Lograsso, A. B. Flatau, A. E. Clark, and M. Wun-Fogle, "Tensile properties of magnetostrictive iron-gallium alloys," *Acta Materialia*, vol. 52, no. 17, pp. 5043–5050, 2004.

[31] J. Atulasimha, A. B. Flatau, and J. R. Cullen, "Analysis of the effect of gallium content on the magnetomechanical behavior of single-crystal FeGa alloys using an energy-based model," *Smart Materials and Structures*, vol. 17, no. 2, p. 025027, 2008, 0964-1726.

[32] S.-M. Na and A. B. Flatau, "Secondary recrystallization, crystallographic texture and magnetostriction in rolled Fe–Ga based alloys," *Journal of Applied Physics*, vol. 101, no. 9, p. 09N518, 2007.

[33] H. Chun, S.-M. Na, C. Mudivarthi, and A. B. Flatau, "The role of misorientation and coincident site lattice boundaries in goss-textured galfenol rolled sheet," *Journal of Applied Physics*, vol. 107, no. 9, p. 09A960, 2010.

[34] T. Ueno, E. Summers, and T. Higuchi, "Machining of iron-gallium alloy for microactuator," *Sensors and Actuators A: Physical*, vol. 137, no. 1, pp. 134 – 140, 2007.

[35] T. Ueno, E. Summers, M. Wun-Fogle, and T. Higuchi, "Micro-magnetostrictive vibrator using iron-gallium alloy," *Sensors and Actuators A: Physical*, vol. 148, no. 1, pp. 280 – 284, 2008.

[36] P. R. Downey and A. B. Flatau, "Bending of iron-gallium (galfenol) alloys for sensor applications," in *Proceedings of Material Research Society*, vol. 0888-V06-11, 2004.

[37] P. Downey and A. B. Flatau, "Magnetoelastic bending of galfenol for sensor applications," *Journal of Applied Physics*, vol. 97, pp. 10R505–3, 2005.

[38] S. Datta, J. Atulasimha, and A. B. Flatau, "Modeling of magnetostrictive galfenol sensor and validation using four point bending test," *Journal of Applied Physics*, vol. 101, no. 9, pp. 09C521–3, 2007.

[39] S. Datta, J. Atulasimha, C. Mudivarthi, and A. B. Flatau, "The modeling of magnetomechanical sensors in laminated structures," *Smart Materials and Structures*, vol. 17, no. 2, p. 025010 (9pp), 2008.

[40] F. T. Calkins, A. B. Flatau, and M. J. Dapino, "Overview of magnetostrictive sensor technology," *Journal of Intelligent Material Systems and Structures*, vol. 18, no. 10, pp. 1057–1066, 2007.

[41] M. J. Parsons, S. Datta, C. Mudivarthi, S. M. Na, and A. Flatau, "Torque sensing using rolled galfenol patches," W. Ecke, K. J. Peters, and N. G. Meyendorf, Eds., vol. 6933, no. 1. SPIE, 2008, p. 693314.

[42] C. Mudivarthi, S. Datta, J. Atulasimha, and A. B. Flatau, "A bidirectionally coupled magnetoelastic model and its validation using a galfenol unimorph sensor," *Smart Materials and Structures*, vol. 17, no. 3, p. 035005 (8pp), 2008.

[43] U. Marschner, F. Graham, C. Mudivarthi, J.-H. Yoo, H. Neubert, and A. B. Flatau, "Finite element model-simulation-based characterization of a magnetostrictive gyrosensor," *Journal of Applied Physics*, vol. 107, no. 9, p. 09E705, 2010.

[44] P. D. McGary, L. Tan, J. Zou, B. J. H. Stadler, P. R. Downey, and B. F. Alison, "Magnetic nanowires for acoustic sensors," *Journal of Applied Physics*, vol. 99, p. 08B310, 2006.

[45] P. R. Downey, A. B. Flatau, P. D. McGary, and B. J. H. Stadler, "Effect of magnetic field on the mechanical properties of magnetostrictive iron-gallium nanowires," *Journal of Applied Physics*, vol. 103, no. 7, p. 07D305, 2008.

[46] C. Mudivarthi, P. Downey, and A. B. Flatau, "Elastic and magneto-elastic modeling of galfenol nanowires," in *Proceedings of SPIE, Nanosensors, Microsensors, and Biosensors and Systems*, vol. 6528, San Diego, CA, USA, 2007, pp. 652 803–11.

[47] J. J. Park, M. Reddy, C. Mudivarthi, P. R. Downey, B. J. H. Stadler, and A. B. Flatau, "Characterization of the magnetic properties of multilayer magnetostrictive iron-gallium nanowires," *Journal of Applied Physics*, vol. 107, no. 9, p. 09A954, 2010.

[48] T. Massalski, Ed., *Binary Alloy Phase Diagrams*, 2nd ed. Materials Park, Ohio, USA: ASM International, 2002.

[49] O. Ikeda, R. Kainuma, I. Ohnuma, K. Fukamichi, and K. Ishida, "Phase equilibria and stability of ordered b.c.c phases in the Fe-rich portion of the Fe-Ga system," *Journal of Alloys and Compounds*, vol. 347, pp. 198–205, 2002.

[50] T. A. Lograsso, A. R. Ross, D. L. Schlagel, A. E. Clark, and M. Wun-Fogle, "Structural transformations in quenched Fe-Ga alloys," *Journal of Alloys and Compounds*, vol. 350, no. 1-2, pp. 95 – 101, 2003.

[51] E. Summers, T. Lograsso, and M. Wun-Fogle, "Magnetostriction of binary and ternary FeGa alloys," *Journal of Materials Science*, vol. 42, pp. 9582–9594, 2007, 10.1007/s10853-007-2096-6.

[52] N. Kawamiya, K. Adachi, and Y. Nakamura, "Magnetic properties and mössabauer investigations of Fe-Ga alloys," *Journal of the Physical Society of Japan*, vol. 33, no. 5, pp. 1318–1327, 1972.

[53] S. Rafique, J. R. Cullen, M. Wuttig, and J. Cui, "Magnetic anisotropy of FeGa alloys," *Journal of Applied Physics*, vol. 95, no. 11, pp. 6939–6941, 2004.

[54] M. Wuttig, L. Dai, and J. Cullen, "Elasticity and magnetoelasticity of Fe-Ga solid solutions," *Applied Physics Letters*, vol. 80, no. 7, pp. 1135–1137, 2002.

[55] Q. Xing, Y. Du, R. J. McQueeney, and T. A. Lograsso, "Structural investigations of Fe-Ga alloys: Phase relations and magnetostrictive behavior," *Acta Materialia*, vol. 56, no. 16, pp. 4536–4546, 2008.

[56] J. R. Cullen, A. E. Clark, M. Wun-Fogle, J. B. Restorff, and T. A. Lograsso, "Magnetoelasticity of Fe-Ga and Fe-Al alloys," *Journal of Magnetism and Magnetic Materials*, vol. 226-230, pp. 948 – 949, 2001.

[57] F. Bai, J. Li, D. Viehland, D. wu, and T. A. Lograsso, "Magnetic force microscopy investigation of domain structures in Fe-x at. % Ga single crystals ($12 < x < 25$)," *Journal of Applied Physics*, vol. 98, no. 2, pp. 023 904–1–4, 2005.

[58] J. Cullen, P. Zhao, and M. Wuttig, "Anisotropy of crystalline ferromagnets with defects," *Journal of Applied Physics*, vol. 101, no. 12, p. 123922, 2007.

[59] S. Bhattacharyya, J. R. Jinschek, A. Khachaturyan, H. Cao, J. F. Li, and D. Viehland, "Nanodispersed DO3-phase nanostructures observed in magnetostrictive Fe–19% Ga galfenol alloys," *Physical Review B (Condensed Matter and Materials Physics)*, vol. 77, no. 10, p. 104107, 2008.

[60] S. Pascarelli, M. P. Ruffoni, R. S. Turtelli, F. Kubel, and R. Grossinger, "Local structure in magnetostrictive melt-spun $Fe_{80}Ga_{20}$ alloys," *Physical Review B (Condensed Matter and Materials Physics)*, vol. 77, no. 18, pp. 184 406–8, 2008.

[61] H. Cao, P. M. Gehring, C. P. Devreugd, J. A. Rodriguez-Rivera, J. Li, and D. Viehland, "Role of nanoscale precipitates on the enhanced magnetostriction of heat-treated galfenol ($Fe_{1-x}Ga_x$) alloys," *Physical Review Letters*, vol. 102, no. 12, p. 127201, 2009.

[62] F. Bai, H. Zhang, J. Li, and D. Viehland, "Magnetic force microscopy investigation of the static magnetic domain structure and domain rotation in Fe-x at.%Ga alloys," *Applied Physics Letters*, vol. 95, no. 15, pp. 152 511–1–3, 2009.

[63] M. Laver, C. Mudivarthi, J. Cullen, A. Flatau, W.-C. Chen, S. Watson, and M. Wuttig, "Magnetostriction and magnetic heterogeneities in Iron-Gallium," *Physical Review Letters*, vol. 105, no. 2, pp. 027 202–1–4, 2010.

[64] C. Mudivarthi, S.-M. Na, R. Schaefer, M. Laver, M. Wuttig, and A. B. Flatau, "Magnetic domain observations in Fe-Ga alloys," *Journal of Magnetism and Magnetic Materials*, vol. 322, no. 14, pp. 2023–2026, 2010, doi: 10.1016/j.jmmm.2010.01.027.

[65] C. Mudivarthi, M. Laver, J. Cullen, A. Flatau, and M. Wuttig, "Origin of magnetostriction in Fe-Ga," *Journal of Applied Physics*, vol. 107, no. 9, p. 09A957, 2010.

[66] Y. Du, M. Huang, S. Chang, D. L. Schlagel, T. A. Lograsso, and R. J. McQueeney, "Relation between Ga ordering and magnetostriction of Fe-Ga alloys studied by x-ray diffuse scattering," *Phys. Rev. B*, vol. 81, no. 5, p. 054432, Feb 2010.

[67] A. G. Khachaturyan and D. Viehland, "Structurally heterogeneous model of extrinsic magnetostriction for Fe-Ga and similar magnetic alloys: Part I. decomposition and confined displacive transformation," *Metallurgical and Materials Transactions A*, vol. 38, no. 13, pp. 2308–2316, 2007, doi: 10.1007/s11661-007-9253-z.

[68] A. Khachaturyan and D. Viehland, "Structurally heterogeneous model of extrinsic magnetostriction for Fe-Ga and similar magnetic alloys: Part II. giant magnetostriction and elastic softening," *Metallurgical and Materials Transactions A*, vol. 38, pp. 2317–2328, 2007, 10.1007/s11661-007-9252-0.

[69] R. Wu, "Origin of large magnetostriction in FeGa alloys," *Journal of Applied Physics*, vol. 91, no. 10, pp. 7358–7360, 2002.

[70] R. Wu, Z. Yang, and J. Hong, "First-principles determination of magnetic properties," *Journal of Physics: Condensed Matter*, vol. 15, no. 5, p. S587, 2003.

[71] R. A. Dunlap, N. C. Deschamps, R. E. Mar, and S. P. Farrell, "Mössbauer effect studies of $Fe_{100-x}Ga_x$ films prepared by combinatorial methods," *Journal of Physics: Condensed Matter*, vol. 18, no. 20, p. 4907, 2006.

[72] M. Huang and T. A. Lograsso, "Short range ordering in Fe–Ge and Fe–Ga single crystals," *Applied Physics Letters*, vol. 95, no. 17, p. 171907, 2009.

[73] Y. N. Zhang, J. X. Cao, and R. Q. Wu, "Rigid band model for prediction of magnetostriction of iron-gallium alloys," *Applied Physics Letters*, vol. 96, no. 6, p. 062508, 2010.

[74] T. Khmelevska, S. Khmelevskyi, and P. Mohn, "Magnetism and structural ordering on a bcc lattice for highly magnetostrictive Fe–Ga alloys: A coherent potential approximation study," *Journal of Applied Physics*, vol. 103, no. 7, pp. 073 911–5, 2008.

[75] see: www.mpc.ameslab.gov, "Single crystals synthesized at the materials preparation center, Ames laboratory, USDOE basic energy sciences, Ames, IA, USA."

[76] J.-H. Yoo, S.-M. Na, J. Restorff, M. Wun-Fogle, and A. Flatau, "The effect of field annealing on highly textured polycrystalline galfenol strips," *Magnetics, IEEE Transactions on*, vol. 45, pp. 4145 –4148, 2009.

[77] M. Wun-Fogle, J. B. Restorff, and A. E. Clark, "Magnetostriction of stress-annealed Fe-Ga and Fe-Ga-Al alloys under compressive and tensile stress," *Journal of Intelligent Material Systems and Structures*, vol. 17, no. 2, pp. 117–122, 2006.

[78] J. Restorff, M. Wun-Fogle, A. Clark, and K. Hathaway, "Induced magnetic anisotropy in stress-annealed galfenol alloys," *Magnetics, IEEE Transactions on*, vol. 42, no. 10, pp. 3087 –3089, oct. 2006.

[79] A. Hubert and R. Schäfer, *Magnetic Domains*. Springer Verlag, 1998.

[80] R. Jain, "Design and packaging of an iron-gallium (galfenol) nanowire acoustic sensor for underwater applications," Master's thesis, University of Maryland, College Park, 2007.

[81] Z. N. Bulycheva, S. I. Svezhova, V. P. Makarov, and B. A. Kornienkov, "Domain structure and magnetostriction of Fe–Al alloys," *Metal Science and Heat Treatment*, vol. 21, pp. 299–302, 1979, 10.1007/BF00775115.

[82] U. Hartmann, "Magnetic force microscopy," *Annual Review of Materials Science*, vol. 29, no. 1, pp. 53–87, 1999.

[83] J. Kerr, "On rotation of the plane of polarization by reflection from the pole of a magnet," *Philosophical Magazine Series 5*, vol. 3, no. 19, pp. 321 – 343, 1877.

[84] J. Atulasimha, A. B. Flatau, and J. R. Cullen, "Energy-based quasi-static modeling of the actuation and sensing behavior of single-crystal iron-gallium alloys," *Journal of Applied Physics*, vol. 103, no. 1, p. 014901, 2008.

[85] R. V. Coleman and G. G. Scott, "Magnetic domain patterns on single-crystal iron whiskers," *Physical Review*, vol. 107, no. 5, p. 1276, 1957.

[86] D. J. Craik and R. S. Tebble, "Magnetic domains," *Reports on Progress in Physics*, vol. 24, no. 1, pp. 116–166, 1961, 0034-4885.

[87] J. K. Zhou, D. D. Li, and J. G. Li, "Magnetic force microscopy observation of undercooled $Fe_{81}Ga_{19}$ magnetostrictive alloys," *Journal of Physics D: Applied Physics*, vol. 41, p. 205405 (4pp), 2008.

[88] H. Z. Song, Y. X. Li, K. Y. Zhao, H. R. Zeng, S. X. Hui, G. R. Li, Q. R. Yin, and G. H. Wu, "Influence of stress on the mangetic domain structure in $Fe_{81}Ga_{19}$ alloys," *Journal of Applied Physics*, vol. 105, no. 1, pp. 013 913–1–4, 2009.

[89] R. Carey and E. D. Isaac, "Chapter 4: The colloid technique," in *Magnetic domains and techniques for their observation.* Academic Press, 1966.

[90] L. Hua, J. E. L. Bishop, and J. W. Tucker, "Simulation of transverse and longitudinal magnetic ripple structures induced by surface anisotropy," *Journal of Magnetism and Magnetic Materials*, vol. 163, no. 3, pp. 285–291, 1996, 0304-8853 doi: DOI: 10.1016/S0304-8853(96)00345-9.

[91] L. J. Dijkstra and U. M. Martius, "Domain pattern in silicon-iron under stress," *Rev. Mod. Phys.*, vol. 25, no. 1, pp. 146–150, Jan 1953.

[92] V. Hoffmann, R. Schäfer, E. Appel, A. Hubert, and H. Soffel, "First domain observations with the magneto-optical Kerr effect on Ti-ferrites in rocks and their synthetic equivalents," *Journal of Magnetism and Magnetic Materials*, vol. 71, no. 1, pp. 90–94, 1987, 0304-8853 doi: DOI: 10.1016/0304-8853(87)90336-2.

[93] G. L. Squires, *Introduction to the theory of thermal neutron scattering.* Cambridge University Press, 1978.

[94] R. Pynn, "Neutron scattering: A primer," *Los Alamos Science*, vol. 19, pp. 1–31, 1990.

[95] O. Halpern and M. H. Johnson, "On the magnetic scattering of neutrons," *Phys. Rev.*, vol. 55, no. 10, pp. 898–923, May 1939.

[96] R. M. Moon, T. Riste, and W. C. Koehler, "Polarization analysis of thermal-neutron scattering," *Physical Review*, vol. 181, no. 2, pp. 920–931, 1969.

[97] Y. Zhu, *Modern techniques for characterizing magnetic materials*, Y. Zhu, Ed. Springer, 2005.

[98] V. F. Sears, "Neutron scattering lengths and cross sections," *Neutron News*, vol. 3, no. 3, pp. 29–37, 1992.

[99] J. Atulasimha, "Characterization and modeling of the magnetomechanical behavior of Iron-Gallium alloys," Ph.D. dissertation, University of Maryland, College Park, 2006.

[100] G. D. Wignall and Y. B. Melnichenko, "Recent applications of small-angle neutron scattering in strongly interacting soft condensed matter," *Reports on Progress in Physics*, vol. 68, no. 8, p. 1761, 2005.

[101] C. J. Glinka, J. G. Barker, B. Hammouda, S. Krueger, J. J. Moyer, and W. J. Orts, "The 30 m Small-Angle Neutron Scattering Instruments at the National Institute of Standards and Technology," *Journal of Applied Crystallography*, vol. 31, no. 3, pp. 430–445, Jun 1998.

[102] "NG3 30-m Small Angle Neutron Scattering Instrument," January 2010. [Online]. Available: http://www.ncnr.nist.gov/instruments/ng3sans/

[103] J. G. Barker, C. J. Glinka, J. J. Moyer, M. H. Kim, A. R. Drews, and M. Agamalian, "Design and performance of a thermal-neutron double-crystal diffractometer for USANS at NIST," *Journal of Applied Crystallography*, vol. 38, no. 6, pp. 1004–1011, Dec 2005.

[104] "Perfect Crystal Diffractometer for Ultra Small-Angle Neutron Scattering," January 2010. [Online]. Available: http://www.ncnr.nist.gov/instruments/usans/

[105] "Investigation of the structure of coarse fibrin clots," NIST Center for Neutron Resarch, Tech. Rep., 2008, summer School on Small Angle Scattering and Neutron Reflectometry.

[106] "TriCS, Laboratory for Neutron Scattering (LNS), Paul Scherrer Institut." [Online]. Available: http://trics.web.psi.ch

[107] W. R. Busing and H. A. Levy, "Angle calculations for 3- and 4-circle x-ray and neutron diffractometers," *Acta Crystallographica*, vol. 22, no. 4, pp. 457–464, 1967.

[108] S. R. Kline, "Reduction and analysis of SANS and USANS data using IGOR Pro," *Journal of Applied Crystallography*, vol. 39, no. 6, pp. 895–900, Dec 2006.

[109] A. Michels, F. Dobrich, M. Elmas, A. Ferdinand, J. Markmann, M. Sharp, H. Eckerlebe, J. Kohlbrecher, and R. Birringer, "Spin structure of nanocrystalline gandolinium," *Europhysics Letters*, vol. 81, pp. 66 003–1–6, 2008.

[110] J. Atulasimha, A. B. Flatau, and E. Summers, "Characterization and energy-based model of the magnetomechanical behavior of polycrystalline iron-gallium alloys," *Smart Materials and Structures*, vol. 16, no. 4, pp. 1265–1276, 2007.

[111] J. Atulasimha, A. B. Flatau, and R. A. Kellogg, "Sensing behavior of varied stoichiometry single crystal Fe-Ga," *Journal of Intelligent Material Systems and Structures*, vol. 17, no. 2, pp. 97–105, 2006.

[112] D. Viehland, "personal communication," 201 Holden Hall (0237), Virginia Tech, Blacksburg, VA 24061, 2010.